CRANFIELD UNIVERSITY

JAMES JACKMAN

PRE-EMPTIVE INFRARED COUNTERMEASURES

CRANFIELD DEFENCE AND SECURITY

PhD
Academic Year: 2011

Supervisor: Mark Richardson
November 2011

CRANFIELD UNIVERSITY

CRANFIELD DEFENCE AND SECURITY

PhD

Academic Year 2011

JAMES JACKMAN

PRE-EMPTIVE INFRARED COUNTERMEASURES

Supervisor: MARK RICHARDSON

November 2011

ABSTRACT

The aim of this PhD is to investigate pre-emptive flare release compared to reactive flare release and their efficacy as a countermeasure device in the protection of fast jet and transport aircraft against the MANPAD threat. Implicit in this is to study the optimum release time of the flare decoy. Consequently, this also raises the question of whether flares of reduced payload size can be as effective as standard flares when released at this optimum time.

To achieve these aims the initial step is to develop models for the different types of Man-Portable Air-Defence (MANPAD) systems and the IR seekers they utilise. This also requires the simulation of the full pre-launch process, namely the acquisition of the target to obtain lock-on then the application of lead and super elevation to give a more realistic model of the firing sequence. Two target models are also developed, a fast jet (AMX-A1) and a transport aircraft (C130), with realistic positions and ejection characteristics for the countermeasure (CM) dispensers.

The next stage includes a counter-countermeasure (CCM) capability in the IR seekers. The first is a track angle bias with values optimised for the two aircraft models. Second is the development of a two-colour seeker with signal processors designed for both a spinscan and a conscan system.

Using all MANPAD models flares are released at intervals throughout the engagements to find the optimum firing time and the simulations repeated for flares with reduced peak intensity and burn time. The results show that flare release around the time of missile launch is effective against most threats, even the more advanced MANPADs with CCMs. Also, that for reduced performance flares maintaining the burn time is perhaps more important than the peak intensity.

Keywords:

MANPAD, flare, simulation, electro-optics, seeker, reticle

ACKNOWLEDGEMENTS

I would like to offer my sincerest thanks and gratitude to Mark Richardson, whose supervision has been vital in the completion of the PhD. His generous support and always friendly advice has made the work possible and also an enjoyable experience.

I would also like to thank Chemring Countermeasures Ltd for funding the research and especially Brian Butters, Roy Walmsley and Nic Millwood. Their help and assistance has always been forthcoming and valuable counsel given whenever needed.

TABLE OF CONTENTS

LIST OF FIGURES

LIST OF TABLES

LIST OF EQUATIONS

GLOSSARY

AGC	Automatic gain control
AM	Amplitude modulation
CAT	Crossed array tracker
CCM	Counter-countermeasure
CDAS	Common defensive aids suite
CM	Countermeasure
CPU	Central processing unit
DIRCM	Directional infrared countermeasure
FM	Frequency modulation
FOV	Field of view
GPU	Graphics processing unit
HWIL	Hardware in the loop
IFF	Identification friend or foe
IIR	Imaging infrared
MANPAD	Man-Portable Air-Defence
MAWS	Missile approach warning system
MODTRAN	Moderate resolution atmospheric radiance and transmittance model
MTV	Magnesium Teflon Viton
MWIR	Mid-wavelength infrared
NEP	Noise equivalent power
PEH	Probability of escaping a hit
PN	Proportional navigation
POST	Passive optical seeker technique
RMP	Reprogrammable microprocessor
SAM	Surface to air missile
SWIR	Short-wavelength infrared
TAB	Track angle bias

1 INTRODUCTION

1.1 The MANPAD Threat

Man-Portable Air-Defence systems (MANPADs) are shoulder launched surface-to-air missiles (SAM), the majority of which passively track the infrared (IR) emissions of an aircraft(1). They can be carried by one man and can typically be made operational in under a minute. Once fired they require no more input from the operator giving a fire-and-forget capability.

It is estimated that more than 500,000 systems have been produced worldwide and of these 6,000 are outside of any government control(2,3). Most are early generation systems that can be bought for as little as a few thousand dollars but later systems, although more expensive, are available. Approximately 20 countries have manufactured MANPADs but 56 countries reportedly possess derivatives of the SA-7(3). As of 2002 coalition forces in Afghanistan had reportedly capture 5,592 systems, some of which were the U.S. Stinger(3). From the Wikileaks release of classified DoD documents the International Security Assistance Force (ISAF) has recovered or seen Chinese HN-5 MANPADs, an improved version of the SA-7(4). Iraqi press reports indicated that 4,000 to 5,000 systems were available to insurgent forces(5). Also, there are large quantities in Africa left over from civil wars and Cold War sponsorship. Table 1-1 gives a list of non-state groups believed to possess MANPADs in the 1996-2001 time period, reproduced from reference(6).

Table 1-1 Non-state groups with MANPADs in the period 1996-2001.

Group	Location	Missile Type
Armed Islamic Group (GIA)	Algeria	Stinger (c)
Chechen rebels	Chechnya, Russia	SA-7 (c), Stinger (c), Blowpipe (r)
Democratic Republic of the Congo (DRC) rebel forces	Democratic Republic of Cong	SA-16 (c)
Harkat ul-Ansar (HUA)	Kashmir	SA-7 (c)
Hizbullah	Lebanon	SA-7 (c), QW-1 (r), Stinger (r)

Hizbul Mujahedin (HM)	Kashmir	Stinger (r)
Hutu militiamen	Rwanda	Unspecified type (r)
Jamaat e Islami	Afghanistan	SA-7 (c), SA-14 (c)
Jumbish-i-Milli	Afghanistan	SA-7 (c)
Khmer Rouge	Thailand/Cambodia	Unspecified type (r)
Kosovo Liberation Army (KLA)	Kosovo	SA-7 (r)
Kurdistan Workers Party (PKK)	Turkey	SA-7 (c), Stinger (c)
Liberation Tigers of Tamil Eeelam	Sri Lanka	SA-7 (r), SA-14 (r), Stinger (c), HN-5 (c)
Oromo Liberation Front (OLF)	Ethiopia	Unspecified type (r)
Palestinian Authority (PA)	Palestinian autonomous areas and Lebanon	SA-7 (r), Stinger (r)
Popular Front for the Liberation of Palestine-General Command (PFLP-GC)	Palestinian autonomous areas and Lebanon	Unspecified type (r)
Provisional Irish Republican Army (PIRA)	Northern Ireland	SA-7 (c)
Revolutionary Armed Forces of Colombia (FARC)	Colombia	SA-7 (r), SA-4 (r), SA-16 (r), Redeye (r), Stinger (r)
Rwanda Patriotic Front (RPF)	Rwanda	SA-7 (r), SA-16 (r)
Somali National Alliance (SNA)	Somalia	Unspecified types (r)
Al Qaeda/Taliban	Afghanistan	SA-series (c), Stinger (c), Blowpipe (c)
National Liberation Army (ELN)	Colombia	Stinger (r), Unspecified types (r)
National Liberation Army	Macedonia	SA-18 (c)
National Union for the Total Independence of Angola (UNITA)	Angola	SA-7 (c), SA-14 (r), SA-16 (r), Stinger (c)
United State Wa Army	Myanmar	SA-7 (c), HN-5N (c)
United Somali Congress – Somali Salvation Alliance (USC-SSA)	Somalia	Unspecified types (r)

(c) possession confirmed, (r) reported but not confirmed

Since their first use, a kill percentage of 70% has been recorded for MANPADs fired at unprotected aircraft. It is also claimed that they account for 80% of all combat aircraft losses(1). Recent military encounters show that that missile defence systems are not always effective. In December 2003 a U.S. Air Force Globemaster III cargo aircraft was struck by a SAM when it had just departed Baghdad International Airport(5). Also, in January 2004 a C-5 Galaxy transport

aircraft was hit by a shoulder fired SAM. Both had missile defence systems that did not counter the attacks. It was reported that sensor placement and aircraft altitude and manoeuvring could have been the cause(3). In January 2005 a Royal Air Force (RAF) C-130 Hercules was lost to a suspected MANPAD attack(7) and in May 2007 a US Chinook cargo helicopter shot down killing all on board(4).

1.2 Aim

It is evident that these systems pose a significant threat to all types of aircraft, even those with a Defensive Aids Suite (DAS). An important factor in this scenario may be that the majority of current countermeasures to a MANPAD attack are reactive, i.e. after the missile has been launched. In my research I will investigate the use of pre-emptive countermeasures against first and second generation MANPADs. The aim is to show that pre-emptive countermeasures prove to be more robust, even against more advance MANPADs with counter-countermeasure (CCM) capabilities.

2 INFRARED RADIATION

2.1 Introduction

The infrared part of the electromagnetic spectrum has a wavelength that lies between 0.75 and 1000 μm, Figure 2-1. Any heated object radiates energy in the infrared and the intensity depends on the objects temperature and surface properties.

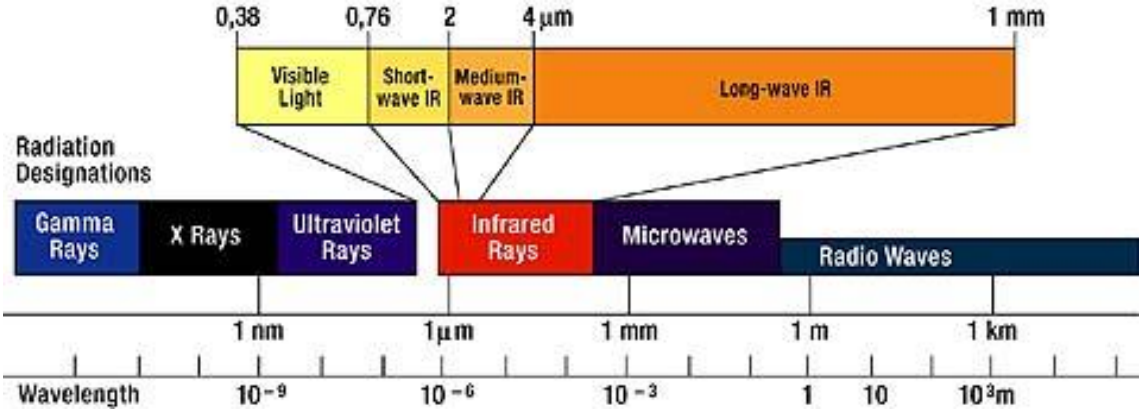

Figure 2-1 Infrared part of the electromagnetic spectrum(8).

2.2 Blackbody Radiation

A blackbody is an idealised object which absorbs all incident radiant energy upon it, and by definition is also the most efficient radiator. Planck's radiation law defines the spectral composition of radiation emitted from a blackbody source of temperature *T* (in Kelvin), Figure 2-2, as(9,10)

$$W_\lambda = \frac{c_1}{\lambda^5\left[e^{\frac{c_2}{\lambda T}} - 1\right]} \qquad \textbf{(2-1)}$$

where W_λ is the spectral radiant emittance $Wm^{-2}\mu m^{-1}$

T is the absolute temperature K

λ is the wavelength μm

$c_1 = 2\pi hc^2$ is the first radiation constant 3.7418×10^8 $Wm^{-2}\mu m^4$

$c_2 = ch/k$ is the second radiation constant 1.4388×10^4 μmK.

The total radiant emittance is calculated by integrating Planck's law over all wavelengths from 0 to infinity; this is given by the Stefan-Boltzman law

$$\int_0^\infty W_\lambda d\lambda = W = \sigma T^4 \qquad \textbf{(2-2)}$$

where σ is Stefan-Boltzmann constant 5.6697 x 10^{-12} $Wcm^{-2}K^{-4}$. This clearly shows that the radiant emittance increases with temperature. Differentiating Planck's law and solving for the maximum gives Wien's displacement law

$$\lambda_m T = a = 2898 \mu m K \qquad \textbf{(2-3)}$$

which describes how the wavelength of maximum radiant emittance decreases as temperature increases.

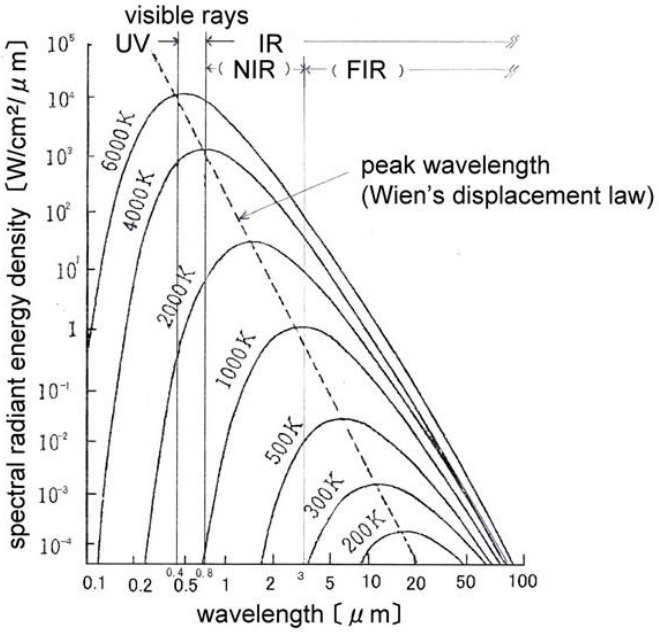

Figure 2-2 Blackbody radiation curves(11).

2.3 Radiant Properties

To apply the formulas to a real object, or greybody, a factor called emissivity is introduced which is defined as the ratio between the radiant emittance of the source W' and radiant emittance of a blackbody at the same temperature(9,10)

$$\varepsilon = \frac{W'}{W}. \qquad \textbf{(2-4)}$$

For a blackbody the emissivity would equal 1, whereas for a greybody it can take a constant value between 0 and 1. A selective radiator is defined so that the spectral emissivity varies with wavelength, Figure 2-3. There are three processes that occur when radiant energy is incident on a body; absorptance *α*, reflectance ρ and transmittance τ. From the conservation of energy they are related by

$$\alpha + \rho + \tau = 1. \qquad \textbf{(2-5)}$$

For a blackbody, by definition, the absorptance is 1 and the reflectance and transmittance are 0. For an object in thermal equilibrium Kirchhoff's law shows that $\varepsilon = \alpha$, so for an opaque material which doesn't transmit(9)

$$\varepsilon = (1 - \rho). \qquad \textbf{(2-6)}$$

For an infrared source where most of the radiant energy is from emission there will be minimal reflectance.

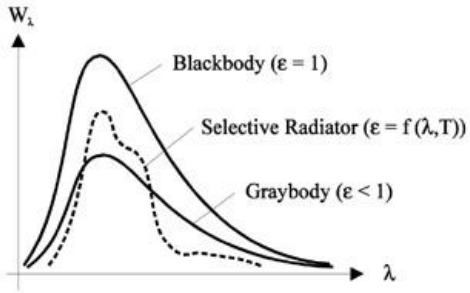

Figure 2-3 Spectral emissivities(9).

2.4 Power

A point source in three dimensions has a radiant intensity J that is equal to the total power radiated divided by the solid angle.

$$J = \frac{P_{Total}}{4\pi}(Wsr^{-1}). \qquad \textbf{(2-7)}$$

For a real object which is an extended source the radiance N is defined as the energy radiated per steradian per apparent area as seen by the observer

$$N = \frac{P}{A\Omega}(Wsr^{-1}m^{-2}). \quad \textbf{(2-8)}$$

If the radiance does not vary with the angle at which the object is viewed then it is defined as a Lambertian source and the radiance is given by

$$N = \frac{W}{\pi}(Wsr^{-1}m^{-2}), \quad \textbf{(2-9)}$$

where W is the radiant emittance.

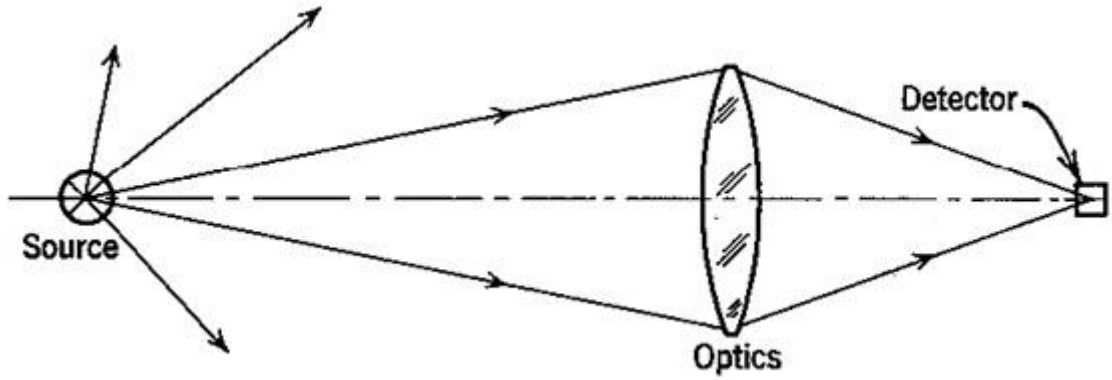

Figure 2-4 Power received at detector(9).

The total power radiated by an object is equal to the radiant emittance multiplied by the area. To calculate the power received at an infrared detector, Figure 2-4, properties of the optical system have to be defined. In terms of the transmission of the optics T_o the power density on the detector is

$$P_d = \frac{\pi N T_o}{4}\left(\frac{1}{f_\#}\right)^2, \quad \textbf{(2-10)}$$

where the f number, $f_\#$, is the focal length of the optics divided by the diameter and there is no transmission loss through the atmosphere.

2.5 Detector Performance

The most basic descriptor of a detectors performance is its responsivity, defined as the output signal per watt of radiant power absorbed(9)

$$R = \frac{V_s}{P}(VW^{-1}). \qquad \textbf{(2-11)}$$

To give an indication of the minimum incident power from a source that can be detected it is necessary to introduce noise equivalent power (NEP). It is defined as the incident power which gives an output signal equal to the detector noise, *S/N=1*(12). As it is difficult to measure signal-to-noise ratios of unity, the measurement is made at higher *S/N* ratios. If the signal output of the detector is a linear function of the input then the *NEP* can be calculated from

$$NEP = \frac{P}{(V_s/V_n)} = \frac{V_n}{R}(W). \qquad \textbf{(2-12)}$$

The inverse of *NEP* is defined as the detectivity

$$D = \frac{1}{NEP}(W^{-1}). \qquad \textbf{(2-13)}$$

This is because the detector with the best performance will have the lowest *NEP* and therefore the highest detectivity. To be able to compare one detectors performance with another the area and bandwidth of the detector is normalised out giving specific detectivity(13)

$$D^* = \frac{(A_d \Delta f)^{\frac{1}{2}}}{NEP} = \frac{(A_d \Delta f)^{\frac{1}{2}} R}{V_n}\left(cmHz^{\frac{1}{2}}W^{-1}\right), \qquad \textbf{(2-14)}$$

where A_d is the area of the detector and Δf is the bandwidth.

There are two classes of IR detectors, thermal and photon. In a thermal detector the energy from the incident radiation produces a change in a physical property of the detector, i.e. expansion of the mercury inside a thermometer(10). In a photon detector incident photons interact directly with the electrons of the detector material. Because of this a photon detector will have a shorter response time than a thermal detector and a greater detectivity(9).

For a Lead Sulphide (PbS)(14) detector if an incident photon has an energy greater than the band gap energy then an electron will be excited from the valance band to the conduction band, Figure 2-5. This can be measured through the change in the materials electrical resistance. At a temperature of 300*K* Lead Sulphide has a band gap energy, E_g, of 0.37eV. This gives a cut off wavelength of 3.4μm which, from Wien's displacement law, is the peak wavelength of radiation from a black body source of 850*K*.

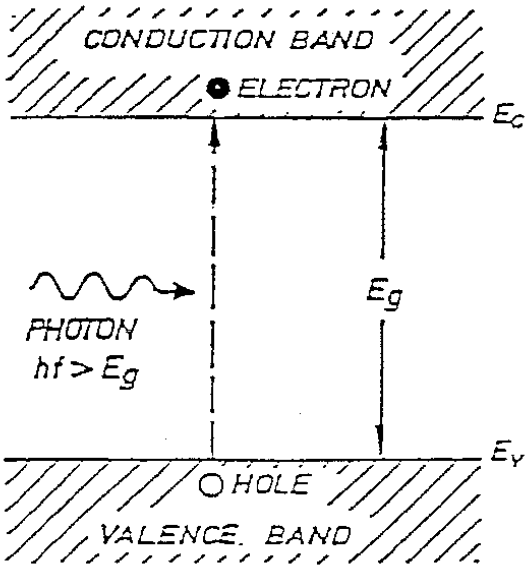

Figure 2-5 Band gap energy for semiconductor detector(13).

For a thermal detector the specific detectivity is independent of wavelength as the energy per unit wavelength is constant. For photon detectors the photon energy is inversely proportional to the wavelength giving a gradient up to the high wavelength cut off due to the band gap energy.

2.6 Range Equation

Having defined properties of the detector, optical system and radiation source it is now possible to calculate the range at which objects can be detected(13).

$$R = \sqrt{\frac{\pi D_o^2 J D^* T_o T_a}{4\left(A_d \Delta f\right)^{\frac{1}{2}} \left(\frac{V_s}{V_n}\right)}}, \qquad \textbf{(2-15)}$$

where D_o is the diameter of the optics, T_o the transmittance of the optics and the atmospheric transmittance given by

$$T_a = e^{-\sigma R}, \qquad \textbf{(2-16)}$$

which is also a function of the range *R*.

2.7 Sources of IR radiation

The IR radiation sources of interest to this research are target aircraft that have to be distinguished from background sources such as the sun, sky and solar reflectance from clouds. On an aircraft the engine produces a large amount of radiant energy which infrared systems are able to detect(15,16). The parts of the jet aircraft with the largest infrared signatures are the tailpipe and exhaust plume with peak temperatures in the near and middle infrared wave bands. A tailpipe can be modelled as a greybody with an emissivity of 0.9(9). Radiation from the tailpipe is dominant; however, if an afterburner is used then the plume can become the main source, Figure 2-6.

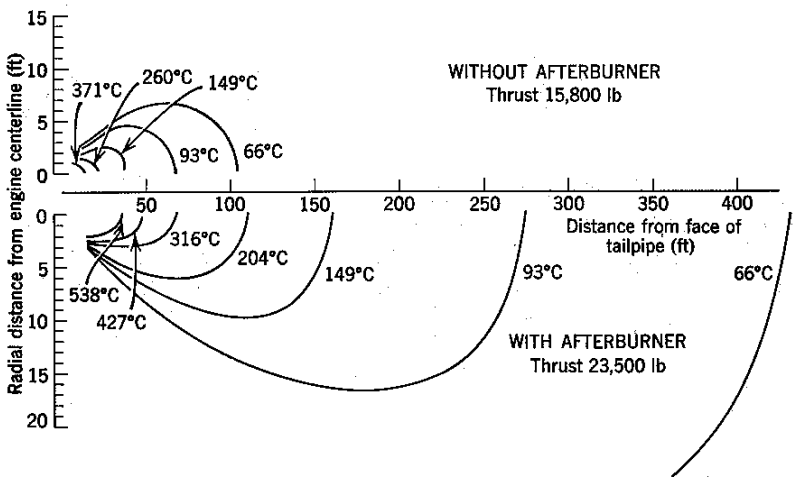

Figure 2-6 Plume temperature contours of a jet aircraft(9).

Another source of radiation from an aircraft can be solar reflection from the canopy and other metal parts, Figure 2-7. In the case of fast jets aerodynamic heating also plays an important role(17).

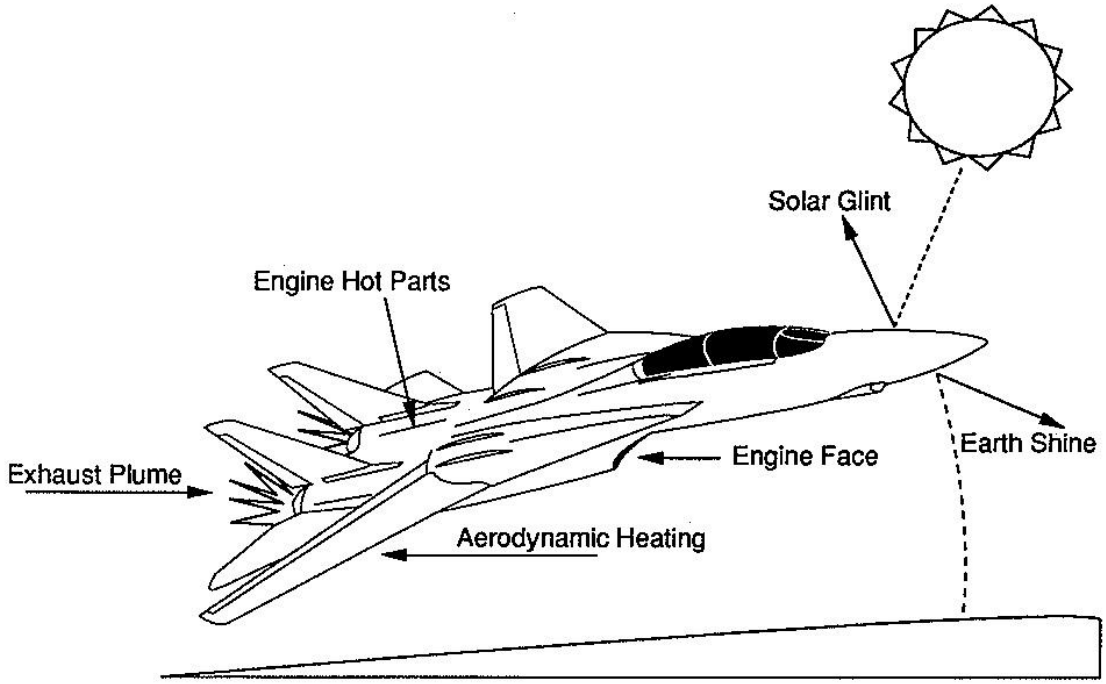

Figure 2-7 Sources of radiation from a target aircraft(17).

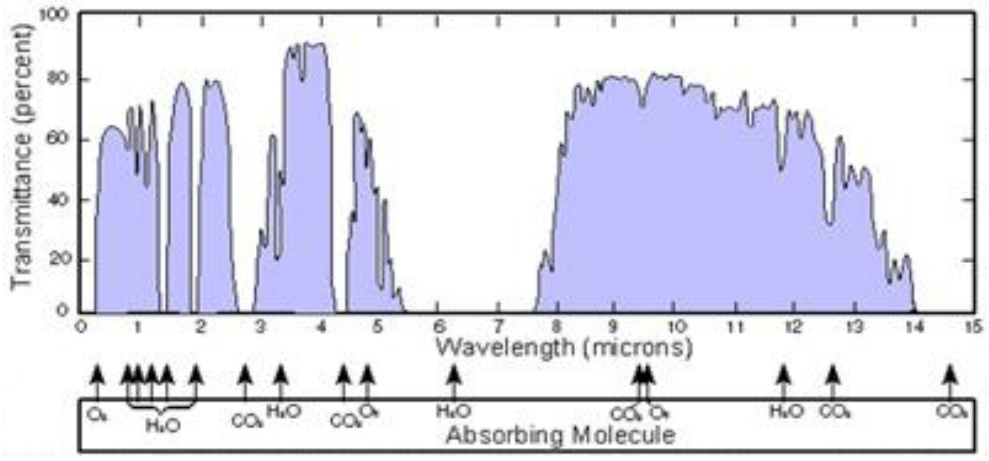

Figure 2-8 Transmittance of the atmosphere at sea level(18).

A major effect on the plume radiance is atmospheric absorption(9,19). This is because the plume constituents carbon dioxide and water vapour are also present in the atmosphere, where the amount is highly dependent on altitude, ambient temperature and location. Absorption and scattering by the CO_2 and

H_2O molecules in the Earth's atmosphere mean that the transmittance of the exhaust plume at certain wavelengths is zero, Figure 2-8. This imposes boundaries on the wavelengths in which IR guided missiles can operate.

3 IR GUIDED MISSILES

IR guided missiles were first developed in the 1960s and used rotating reticles as optical modulators. The purpose of optical modulation is to provide tracking information for the IR seeker. Reticles are also able to suppress background emission with regards to the target by a process known as spatial filtering. For a fuller background on the use of reticles in electro-optical devices see references(9,10,12,20,21,22,23).

3.1 Spatial Filtering

If an object has a radiant distribution $N(\underline{r})$ *(W sr^{-1} m^{-2})* which is a function of a two-dimensional angle defined as $\underline{r} = (x, y)$, then the power distribution in the image plane is(24)

$$P(\underline{r}) = N(\underline{r})A_0 (Wsr^{-1}), \quad \textbf{(3-1)}$$

where A_0 is the area of the optics entrance. In the image plane there is positioned a spatial filter, which takes the form of a rotating reticle. The power incident on the IR detector is then defined as

$$H = \int N(\underline{r}) f(\underline{r}) d^2 \underline{r} (Wm^{-2}), \quad \textbf{(3-2)}$$

where $f(\underline{r})$ is the reticle function which describes the transmittance of the reticle at the point $\underline{r}$. As the reticle rotates it is more convenient to use polar coordinates (r, θ) defined by

$$r = |\underline{r}| = \sqrt{x^2 + y^2}, \theta = \tan^{-1} \frac{x}{y}. \quad \textbf{(3-3)}$$

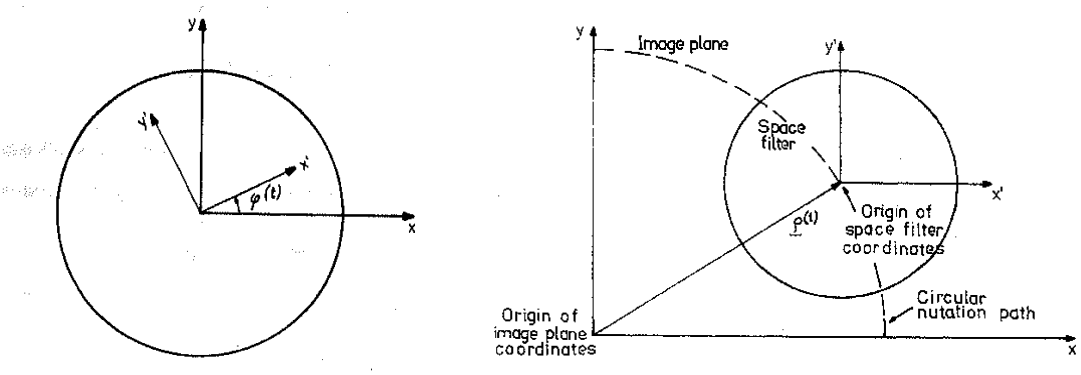

Figure 3-1 Rotation and translatory motion of a reticle(25).

If the rotation of the reticle is described by $\varphi(t)$, Figure 3-1, then the power incident on the detector is

$$H(t)=\int_0^{2\pi}\int_0^{\infty} N(r,\theta)f\left(r,\theta-\varphi(t)\right)rdrd\theta\,. \qquad \textbf{(3-4)}$$

For a nutating reticle with translatory motion described by $\underline{\rho}(t)$ then

$$H(t)=\int N(\underline{r})f\left(\underline{r}-\underline{\rho}(t)\right)d^2\underline{r}\,. \qquad \textbf{(3-5)}$$

The purpose of spatial filtering is to maximise the signal to noise ratio of the target with regard to the background radiation. As the target is a hot point source its signal will be a series of pulses with a chopping frequency of $f_c = nf_r$, where n is the number of pairs of opaque and transparent spokes of the reticle and f_r is its rotational frequency(9). The background will cover many spokes so it will be seen as an extended source with no chopping. The signal is then amplified and electrically filtered with a band-pass filter centred at the chopping frequency suppressing the background radiation. This produces an error signal giving guidance information in the form of polar coordinates projected onto the image plane.

3.2 First Generation MANPADs

The simplest IR seekers and the most widely proliferated have rotating reticles(26,27). They are known as spinscan seekers and use un-cooled Lead Sulphide detectors that work in the 2-2.7μm atmospheric window. This means they can only detect the high temperature tailpipe and exhaust plume essentially limiting them to tail chasers. The dome of the seeker needs to be made of an IR transmitting material, usually silicon, Germanium or a variant of Irtran(14). Once the IR radiation passes through the dome a Catadioptric telescope reflects the signal onto a rotating reticle shown in Figure 3-2.

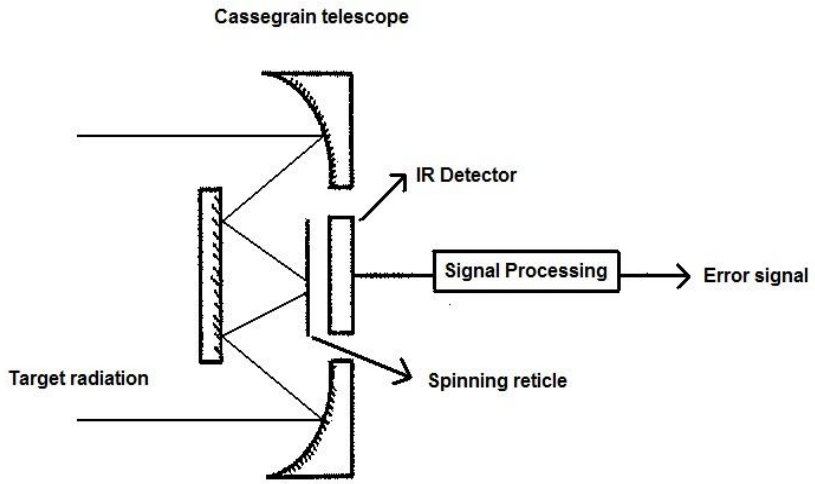

Figure 3-2 Layout of a first generation seeker(28).

The reticle has a rising sun pattern with a 50% transmission portion which modulates the amplitude of the signal from the target, shown in Figure 3-3. The amplitude of the signal from the target when it is in the wagon wheel section is proportional to the radial distance of the target image from the centre of the reticle(9). This is due to more of the target image being visible the further the radial distance from the centre of the reticle. The phase variation is achieved through a pick-off at every rotation from the 50% transmission portion. This can also be used to set the automatic gain control (AGC), which uses the average signal level to regulate the gain of the system.

A gimballed head gives the seeker a field of regard of typically 120^{o}. These systems give the unique position of the target within the field of view but are insensitive to on axis targets due to a loss of amplitude modulation (AM) when the target image is at the centre of the reticle(21,29,30,31,32).

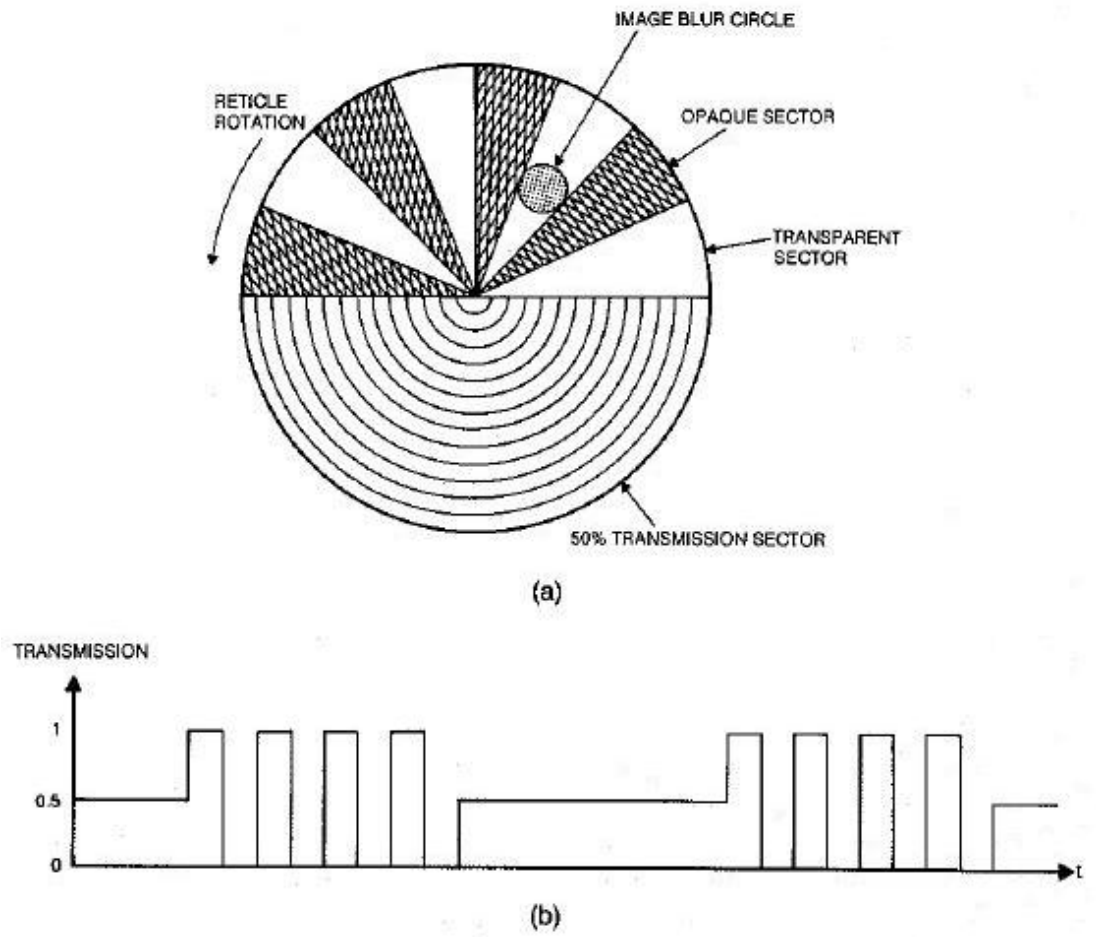

Figure 3-3 (a) Rising sun reticle pattern and (b) AM signal(33).

An example of a MANPAD that utilises this type of seeker is the Russian SA-7b, Figure 3-4. The original SA-7(34), based on and reverse engineered from the US Redeye, entered service in 1968. At this time an improved version, the SA-7b, was designed with small differences that increased the operational envelope of the missile(34,35,36,37). It entered service in 1970 along with series production.

Figure 3-4 Russian SA-7b MANPAD.

The system consists of the launch tube, gripstock, battery and the missile itself(38). To engage a target there is a process of actions that must be performed by the operator. First, the battery is inserted to power the seeker head. The operator can then use the sights on the launch tube to aim at a target. If a signal is detected this produces a lock-on tone that alerts the operator. Next, the trigger on the gripstock is pulled to the first position which uncages the seeker head. This allows super elevation to be applied and any lead needed in the case of crossing target. Super elevation aims the missile above the target and lead aims ahead of the target. Finally, pulling the trigger to the second position launches the missile. The lock-on tone needs to be maintained throughout for the launch to occur.

On launch the missile is initially ejected from the tube by a small charge. Once the missile is a safe distance from the operator the boost motor ignites taking the missile to its top speed then a sustain motor to maintain that speed. The warhead of the missile is fully armed at this point. The missile has stabilising tail fins and two control fins to manoeuvre the missile to the target. There is an impact fuse on the warhead and a delayed self destruct mechanism set from the time of missile launch.

There are several problems associated with the SA-7b. Because of the detector waveband it tracks the hottest part of the target, usually tailpipes of jet engines. Therefore, even in a successful engagement, the aircraft could still land as the small warhead may fail to damage the engine. Also, it can lose target tracking due to solar reflectance/emission and be easily defeated by expendable off board countermeasures.

The SA-7b has been produced in large numbers, proliferated worldwide and seen use in nearly every conflict since it first entered service. Because of this several countries have produced their own variant through reverse engineering. Copies include; the Chinese HN-5, Pakistani Anza MKI, Egyptian Sakr Eye, Yugoslav Strela 2M2J Sava and the North Korean Hwasung-Chong. These variants may have different missile characteristic, e.g. greater thrust to increase speed or improved signal processing for better tracking.

3.3 Second Generation MANPADs

Second generation seekers overcame the problem of on-axis insensitivity by rotating the optics instead of the reticle, which is known as conscan(21,39). In this arrangement the secondary mirror is tilted and the reticle is a full wagon wheel which produces a nutation circle and frequency modulation (FM)(27,40,41,42) of the image, Figure 3-5. The magnitude of the frequency modulation gives the off-axis distance and a pick-off gives phase variation to yield the position of the target in the field of view(9). Instead of the uncooled PbS detectors used in earlier models second generation seekers use cooled PbS or Indium Antimonide (InSb)(14) detectors which allowed them to operate in the 3-5μm wave band seeing cooler parts of the plume and hot components of the aircraft widening the tracking aspect. To cool the detector a Joule-Thomson cooler with argon or nitrogen is used.

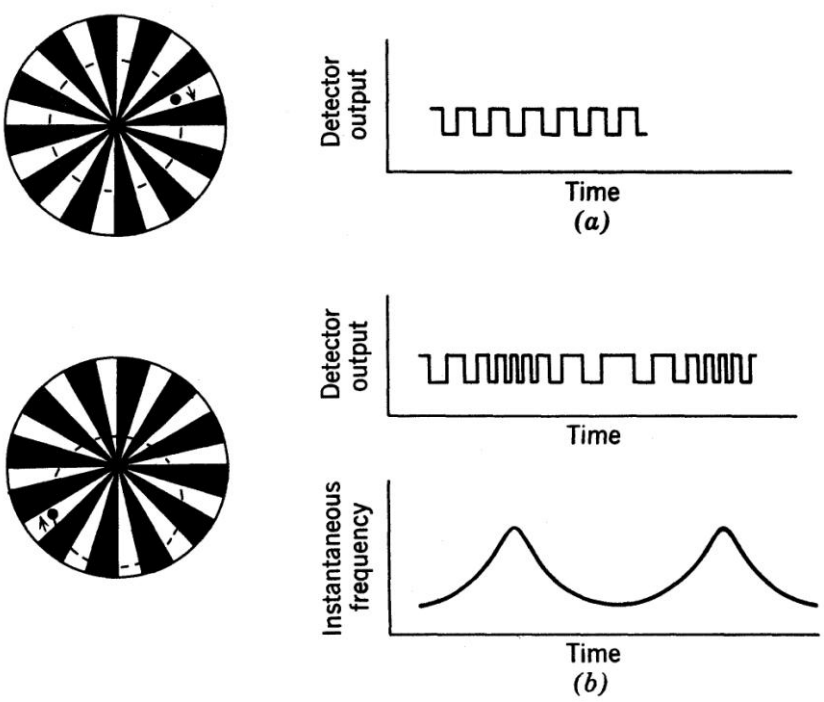

Figure 3-5 FM con-scan reticle system(9).

An example of this type of system is the Russian SA-14(43,44,45) which is an improved version of the SA-7b with better tracking and a wider aspect capability. It could track cooler targets at greater ranges and engage faster moving targets. The SA-14 entered service in 1974 but at this time Russia was already developing another second generation MANPAD designated SA-16(46,47,48). Brought into service in 1981 it had several improvements over the SA-14 but was still based on the same conscan IR seeker. An Identification Friend or Foe (IFF) receiver prevented it from firing on friendly aircraft and an improved rocket motor extended the range and speed. The impact fuse had a delay along with another charge to detonate the remaining rocket fuel. Coupled with a terminal manoeuvre to hit cooler parts of the aircraft the SA-16 achieved a greater level of lethality.

While the Russians were developing their second generation MANPADs the US produced the Stinger Basic(49,50). It was introduced in 1981 and has similar capability to the SA-16.

Both the SA-14 and SA-16 have been exported to over 30 countries and as in the case with the SA-7b some countries have reverse engineered their own variant. The Chinese have developed the QW-1 which is their version of the SA-16 but it also incorporates some design elements of the US Stinger Basic. Also, Pakistan has developed the Anza MK II and the Iranians a version called Misagh-1.

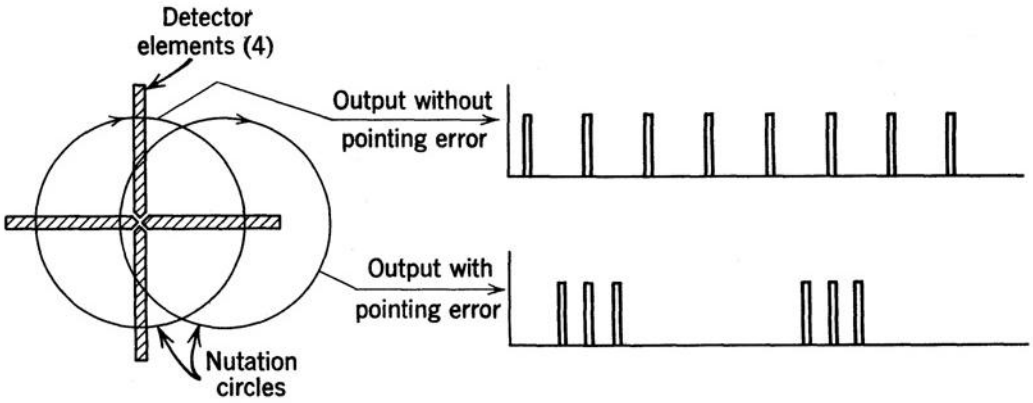

Figure 3-6 Crossed array tracker (CAT)(9).

Another type of seeker uses four detectors in an open-cross formation instead of a reticle, shown in Figure 3-6. It still uses a nutation circle to give frequency modulation by producing four equally spaced detector outputs for an on-axis target and unequal spacing for off-axis targets(9). An example of this type of system is the original French Mistral(51).

All the variants of second generation MANPADs have different maximum slant range, altitude and speed. Some may contain a counter-countermeasure capability. Any aircraft countermeasure system needs to be able to deal with these diverse threats.

3.4 Third Generation MANPADs

The main advancement in third generation seekers was the development of more robust counter-countermeasures. This made them much more resistant to any countermeasures deployed by the aircraft. To achieve this, new scanning techniques were used rather than the conventional reticle system.

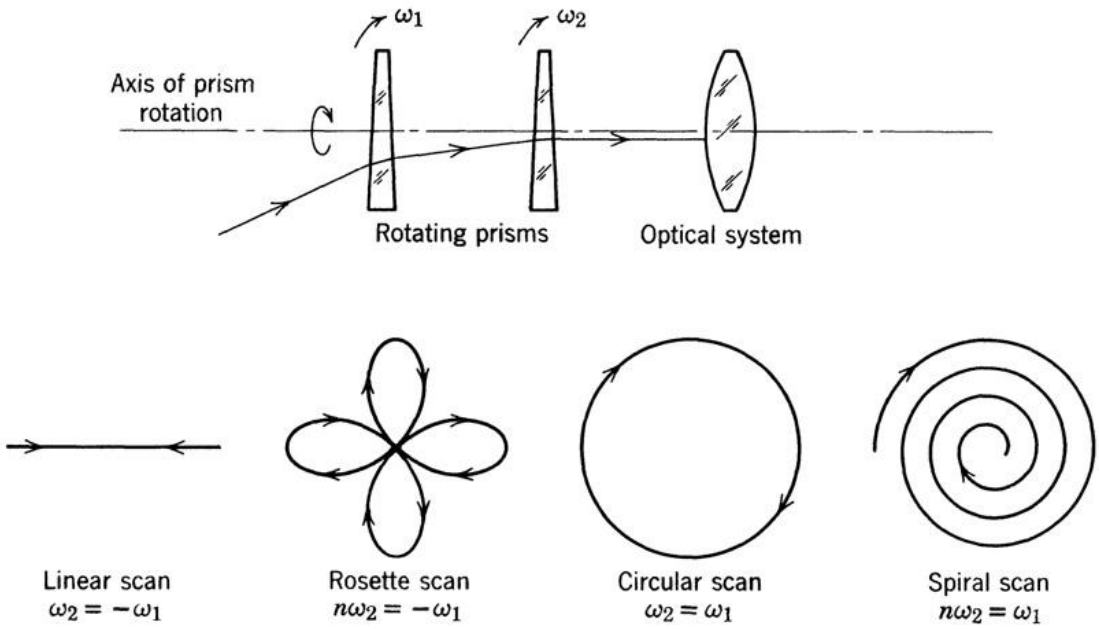

Figure 3-7 Scan generation with rotating prisms(13).

The seekers are termed pseudo-imaging as they create a simulated image of the target by moving the infrared signal over the detector. Two offset mirrors rotate to produce a specified pattern, the most common one being the rosette scan as this visits the axis multiple times for each rotation, Figure 3-7. They can discriminate targets from clutter and countermeasures but use digital signal processing to cope with the large amount of data.

Along with new scanning techniques dual band detectors were also incorporated. They could be ultraviolet (UV)/IR or short wave and medium wave IR (SWIR/MWIR). This ability to detect at different wavelengths made the discrimination between target and countermeasure much easier. They were also more resistance to jamming, a directed infrared countermeasure discussed in the next chapter.

Examples of third generation MANPADs are the Russian SA-18(52,53,54) and SA-24(55), US Stinger Passive Optical Seeker Technique (POST) and the Stinger Reprogrammable Micro Processor (RMP)(49,50). The US Stinger RMP gave the added ability to reprogram the IRCCM without a retrofit if a new countermeasure evolved(56). Two other countries have produced their own

variant, the Chinese QW-18 and Iranian Misagh 2. Knowing exactly what CCM each missile has, its operational envelope and maximum speed is unlikely. Therefore, any countermeasure must be fully tested against a range of threats that an aircraft is likely to face.

3.5 Fourth Generation MANPADs

Fourth generation seekers, or imaging seekers, produce an image of the target on a focal plane array. This is either done by a linear array which is scanned across the scene or a 2-d staring array, see Figure 3-8 and Figure 3-9.

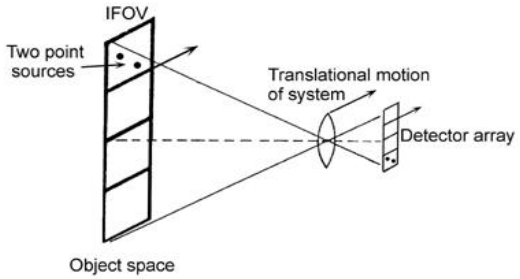

Figure 3-8 Scanned image array(57).

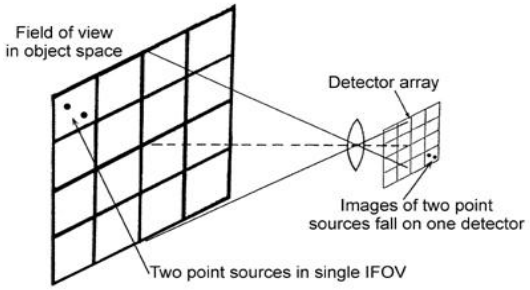

Figure 3-9 Staring focal plane array imaging system(57).

The cost of obtaining the required image size for sufficient resolution and the computing power needed for the image processing in real time is extremely high. As of 2004 the Chinese are developing the QW-4 reported to contain a focal plane array. Also, the US were developing the Stinger RMP Block II, it would have had an imaging infrared (IIR) seeker but was cancelled in 2001.

3.6 Missile Guidance

MANPAD systems use Proportional Navigation (PN) guidance to track and hit their target. The PN law(58) issues acceleration commands which are proportional to the line of sight rate and the closing velocity, stated as

$$n_c = kV_c\dot{\lambda}. \qquad \textbf{(3-6)}$$

The acceleration command, n_c, is perpendicular to the instantaneous missile to target line of sight, k is the PN constant, V_c, the missile to target closing velocity and $\dot{\lambda}$ is the rate of change of the line of sight angle. As the IR seeker will not know the closing velocity an estimate has to be incorporated into the PN law. This can be based on the known maximum velocity of the missile and the likely target velocity.

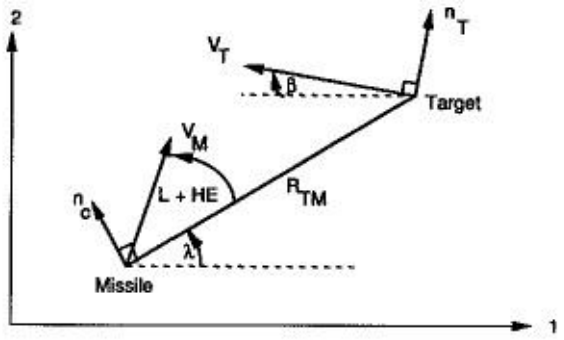

Figure 3-10 Two-dimensional missile target engagement geometry(58).

Figure 3-10 shows the case for two-dimensions with the missile and target travelling at constant velocity. The velocity magnitude of the missile, V_M, has a heading of L + HE which represents missile lead angle plus heading error. The lead angle is the angle that the missile needs to be on to result in a collision. If this is the case the rate of change of the line of sight angle will be zero and no acceleration commands are needed for the missile to hit the target. The heading error is the initial error in the missiles line of sight angle from the lead angle.

4 IR COUNTERMEASURES

The development of IR guided missiles necessitated the need for aircraft to also develop some kind of countermeasure capability(33). The first defence used against heat seeking missiles was expendable decoys, i.e. flares. They provide another hot point source for the IR seeker to track that will hopefully seduce it from the target. The use of flares also usually requires some kind of warning system in order to cue their reactive release.

4.1 Missile Approach Warning System

A missile approach warning system (MAWS) is designed to detect an incoming threat, which is then used to activate an aircrafts countermeasure system(59). The MAWS can operate in different parts of the EM spectrum depending on the missile characteristic it is trying to detect. For IR and UV warners they look for the emissions from the missile rocket motor and plume, with a MANPAD having a distinctive thrust profile from the boost and sustain motors(33). For radar systems they detect the Doppler shift of an approaching missile. Each system will have varying detection ranges, directional information about the threat, response time and false alarm rates. Optimisation of the MAWS will depend on the type of threat you are trying to detect and the type of aircraft you are trying to protect.

4.2 Conventional Flares

Conventional flares have pellets made from Magnesium, Teflon and Viton (MTV) and provide a point source of around 2000 K, Figure 4-1. Figure 4-2 shows the typical spectra for a target and a decoy. It illustrates why flares are more effective against a first generation MANPAD as the relative intensity is much greater at shorter wavelengths.

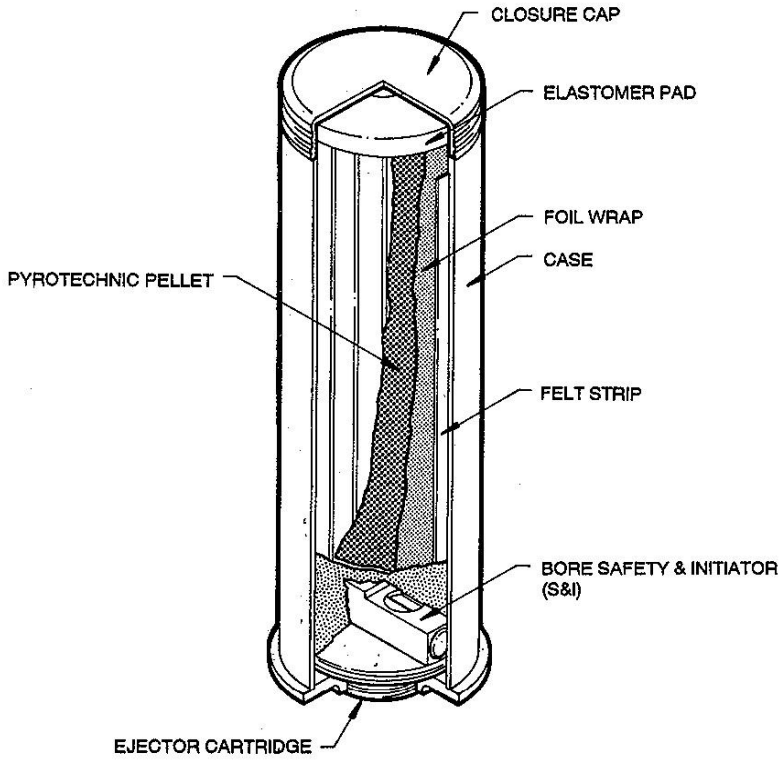

Figure 4-1 Components of a conventional flare(33).

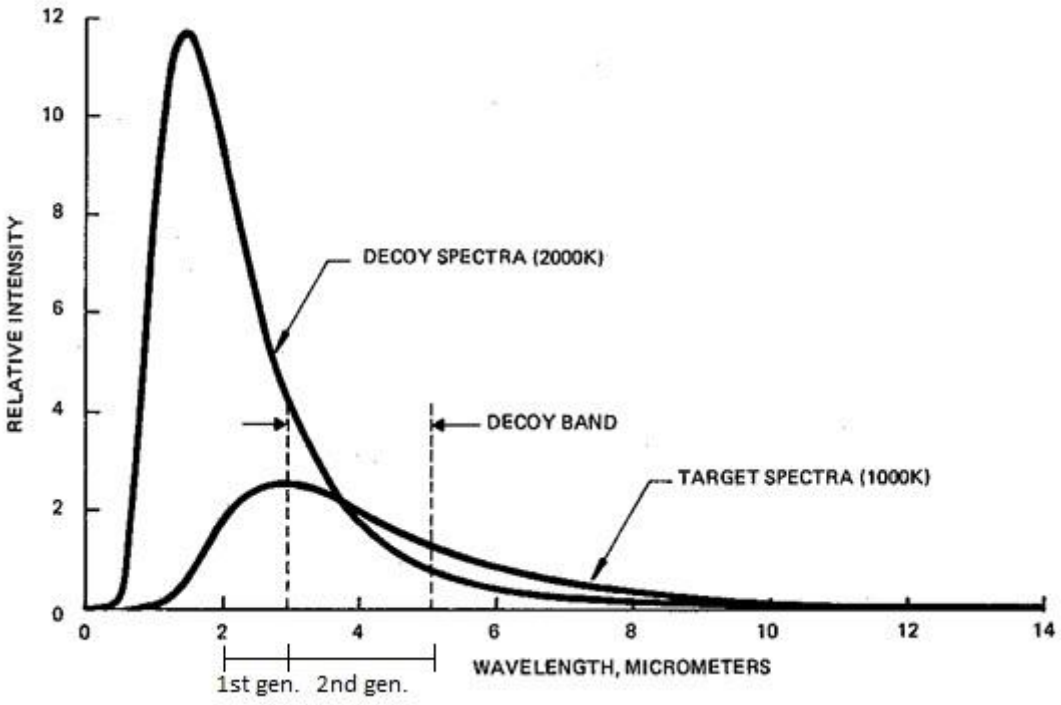

Figure 4-2 Typical decoy/target spectra(33).

Figure 4-3 Square format 218 flare(60).

A conventional flare comes in either a round format or square format, Figure 4-3, depending on the manufacturer and which dispenser it will be housed in. The flare also needs to have certain characteristics to effectively decoy the missile(61,62). The peak intensity has to exceed that of the aircraft in the waveband of the IR seeker, usually 2-2.7µm or 3-5µm. It must also reach this peak intensity in a very short period of time before the flare has exited the field of view (FOV), usually less than 1 second. The burn time of the flare has to be long enough, around 4 seconds, so there is no chance of the seeker reacquiring the target after the flare is extinguished. Also, the flare may have an ejection velocity coupled with some aerodynamic property to prevent it quickly leaving the seeker FOV.

4.3 Counter-Countermeasures

In response to the effectiveness of flares against first generation MANPADs, later systems incorporated counter-countermeasures (CCMs) into the IR seeker(63,64,65). The CCM looks for the inherent differences between the aircraft and flare to reject the decoy and still track the target.

To initiate a CCM there needs to be an event that triggers it. This can be due to a rapid rise in the IR emission incident on the detector because of a flare. Also, because a flare quickly separates from an aircraft there will be an increase in the rate of change of the line of sight angle in the PN guidance. Having detected one of these the seeker could apply a track angle bias. In this instance the seeker turns off the tracking and applies a forward angle to the gimbal for a

specified duration. The seeker will have effectively pushed forward and when the tracking is turned back on the flare will have exited the FOV. Another option is to apply a track memory. Again, the tracking will be turned off for a specified duration, but will continue on its current PN guidance course applying the same rate of turn.

A more sophisticated CCM is two colour where the seeker can detect in two parts of the EM spectrum, either UV/IR or SWIR/MWIR(66,67,68,69). The signatures of the aircraft and flare will not match in the two wavebands so the seeker could look at the ratio between the two wavebands and be able to reject the flare.

4.4 Advanced Flares

To counteract the CCMs incorporated into missile seekers more advanced flares were developed. An aerodynamic flare, Figure 4-4, is designed to have an improved trajectory so it will stay in the FOV longer and mitigate against a track angle bias CCM.

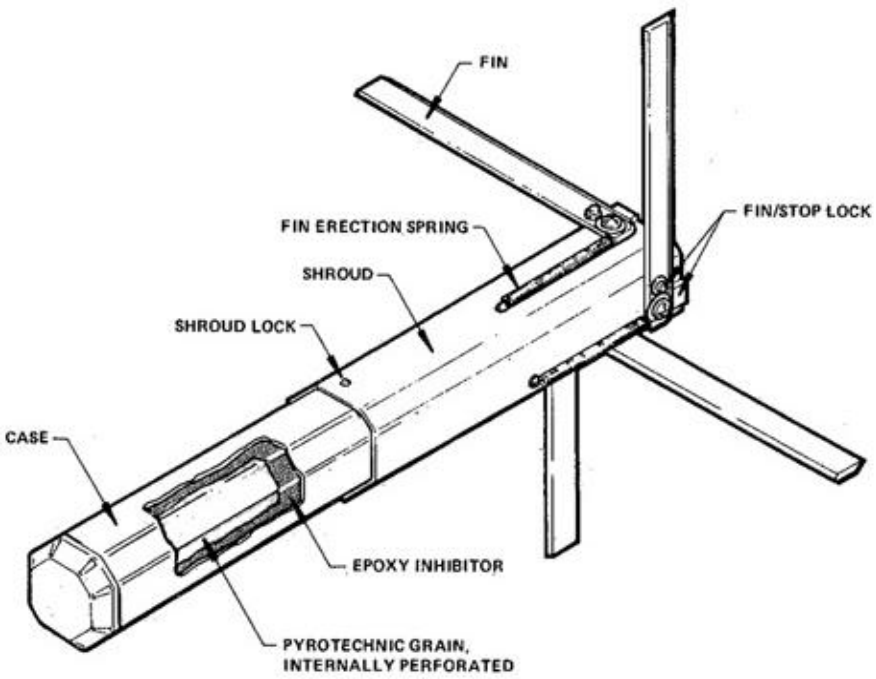

Figure 4-4 MJU-31/B aerodynamic flare(33).

Figure 4-5 Chemring Countermeasures K7 propelled flare(60).

Another type of flare that is designed to work against a track angle bias is a propelled flare, Figure 4-5. It has an aerodynamic front, stabilising fins and a small rocket motor to propel the flare forward to maintain its presence in the seeker FOV(70).

The latest types of flares are spectral flares and multileaf decoys. A spectral flare is designed to work against a two colour CCM by matching an aircrafts signature in multiple wavebands. Instead of behaving similar to a greybody like a conventional flare, a spectral flare is a selective radiator and emits radiation in different temperature bands. A multileaf decoy consists of pyrophoric wafers that when released react with the atmosphere. They create a large cloud in the IR spectrum instead of a hot point source and are designed to be effective against imaging seekers.

4.5 Directional Infrared Countermeasure

Another type of countermeasure is the DIRCM (Directional Infrared Countermeasure)(71,72) which produces a jamming signal that confuses the seekers guidance system. It can be a laser based on a turret that tracks an incoming threat and sends a pulsed beam to interrupt the modulated signal. The applicability of these systems to fast jets is questionable given their size and effects on aerodynamics at high speeds. For transport aircraft a combined solution of DIRCM and flares may be appropriate(73).

5 MODELLING AND SIMULATION

5.1 Software

The software used to model the missile and target engagement is called CounterSim(74), Figure 5-1. This is designed and developed by Chemring Countermeasures and allows the user to specify the type of missile, aircraft and environment in which the simulation takes place. Parameters have been taken from open sources in order to model different MANPAD models(61,75,76). For the targets generic aircraft models have been used with engine and plume signatures taken from the open literature(9).

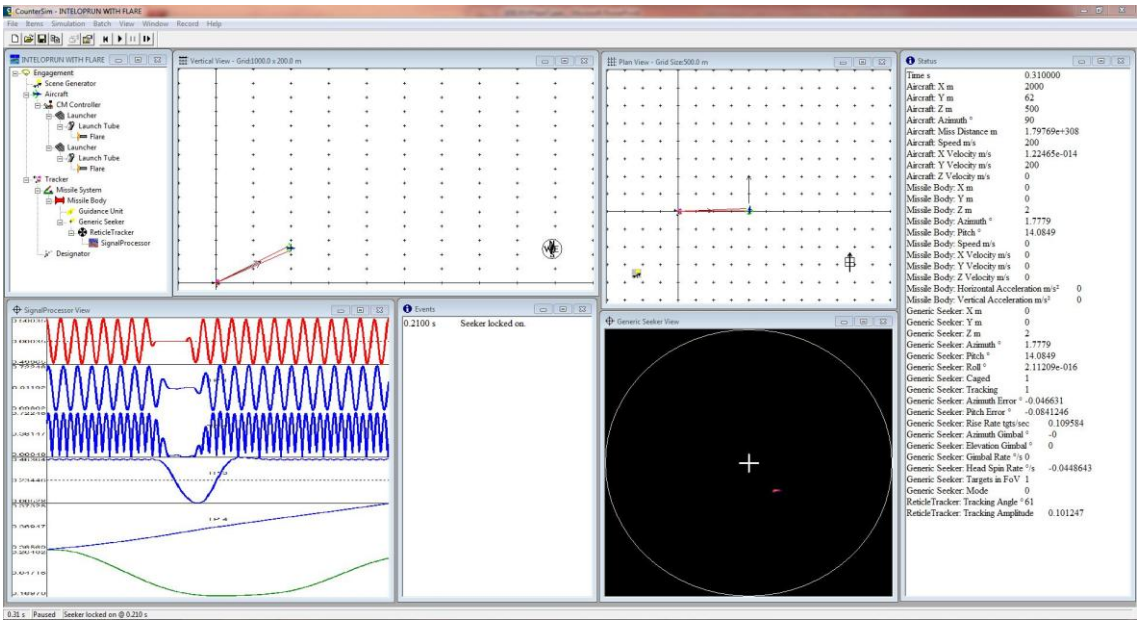

Figure 5-1 Screenshot of CounterSim.

CounterSim is a discrete event simulation tool that is designed to be modular and capable of being tailored to the end users' requirements. A simulation consists of a list of items, Figure 5-2, where the inputs and outputs are specified by the user. The inputs depend on the type of scenario trying to be modelled, e.g. a MANPAD attack on a fast jet. The outputs from the simulation can be chosen by the user, e.g. target position, missile acceleration. Each output is logged at time intervals in the simulation and the information saved in a data file.

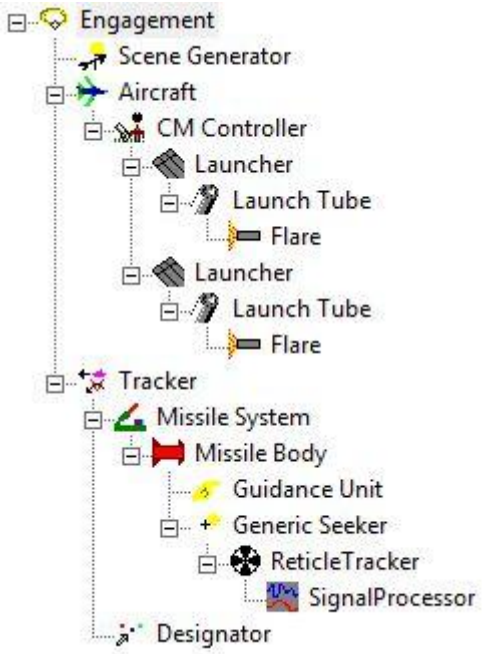

Figure 5-2 Hierarchy of items in CounterSim.

Previously MANPADS have been modelled in CounterSim with the scenario starting either at launch or with a missile assumed to be already in flight(77,78,79,80,81). In order to model the full pre-launch phase of an engagement it was necessary to identify and add some additional options - particularly to the existing CounterSim Missile System item. The MANPAD system parent item is the Tracker which models the operator of the MANPAD tracking the target to obtain lock-on. The Tracker uses an Alpha, Beta, Gamma track filter(82). The Designator merely identifies an object to track – in this case the Aircraft. Once the Tracker is tracking the Aircraft and the Generic Seeker is locked-on, the advanced options in the Missile System simulate the different stages in the firing sequence.

The classification of a lock-on in CounterSim is defined in the signal processor. If the signal amplitude is above a certain threshold then the seeker is locked-on and the advanced options in the missile system are initiated. An audio tone is also produced mimicking the tone heard by an operator of a MANPAD.

The advanced options in the missile system start with the seeker being uncaged a user defined time after lock-on. Next, the lead and super elevation angles are

applied. These are either fixed or are related to the calculated crossing rate. The missile is then launched at a set time after applying the launch angles assuming that lock-on is maintained. Pre-launch horizontal and vertical gimbal rates set in the Generic Seeker affect the time taken to fire the missile. Maximum pre-launch gimbal limits are also set and therefore if these are exceeded the seeker will lose lock. Preset logic choices in the Generic seeker may cause the seeker to be re-caged until track is resumed or the seeker may remain uncaged. When track is resumed the lead and super elevation angles are reapplied and the launch is again attempted.

5.2 Hardware

The hardware used for the simulations are two PCs with multicore Intel CPUs and NVidia GPU graphics cards with 1GB of memory.

The processing time for a simulation depends on its complexity. In a simple scenario with one target, one missile and no countermeasures or noise a simulation time of 9s relates to a real time of 90s. To obtain greater realism Modtran(83) can be included in the CounterSim scene generator. It is a narrow band model atmospheric radiative transfer code that simulates transmission loss due to molecular absorption/emission. However, this can greatly increase the processing time and make large batch runs unfeasible.

5.3 First Generation MANPAD

Parameters for the missile body such as size and weight have been taken from open sources. The dimensions are quoted in Table 5-1 along with values for the spinscan IR seeker head. For the boost and sustain thrust timings were taken from a video of a MANPAD firing. The forces were then calculated to give an acceptable velocity profile, Figure 5-3. There is an initial ejection at 30m/s with a 0.5s delay before the boost thrust ignites so the missile is a safe distance from the operator.

Table 5-1 Parameters for first generation MANPAD.

Missile diameter	70mm
Missile mass	9.6kg
Latax limit	15g
Drag coefficient	0.3
Field of view (FOV)	1.9°
Gimbal rate	6°/s
Pre-launch gimbal limit	90°
Max gimbal limit	120°
Detector waveband	2-2.7µm
F number	1.6
Focal length	25mm

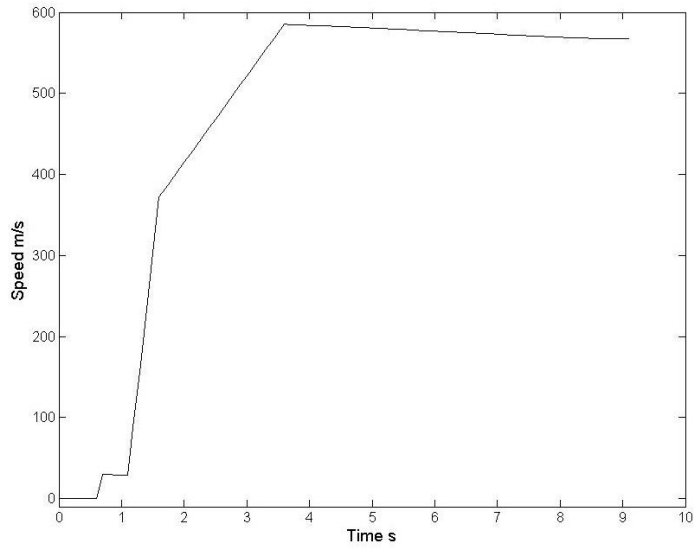

Figure 5-3 Velocity profile of the missile.

The pre-launch gimbal limit is reduced because the missile sits inside the tube, Figure 5-4, with the seeker dome not flush to the opening. The transmission of the seeker dome, Figure 5-5, shows a peak that corresponds with the detector waveband. The result is from an infrared spectrometer using a piece of the dome from an SA-7b. The reticle design is a rising pattern with a 50% transmissive portion which produces an AM signal. Figure 5-6 shows a comparison of the design used in the simulations and a picture of the reticle from an SA-7b(84). The modification from the rising sun reticle design, Figure 3-3, is because straight lines in a reticle design generate a larger signal when

chopping a line image than a point image(9). The signal processor design is shown in Figure 5-7 which also defines if the seeker is locked-on to the target, mentioned earlier. In the simulations the operational envelope of the MANPAD is considered to cover distances from 1km up to 5.5km and altitudes from 100m up to 3km.

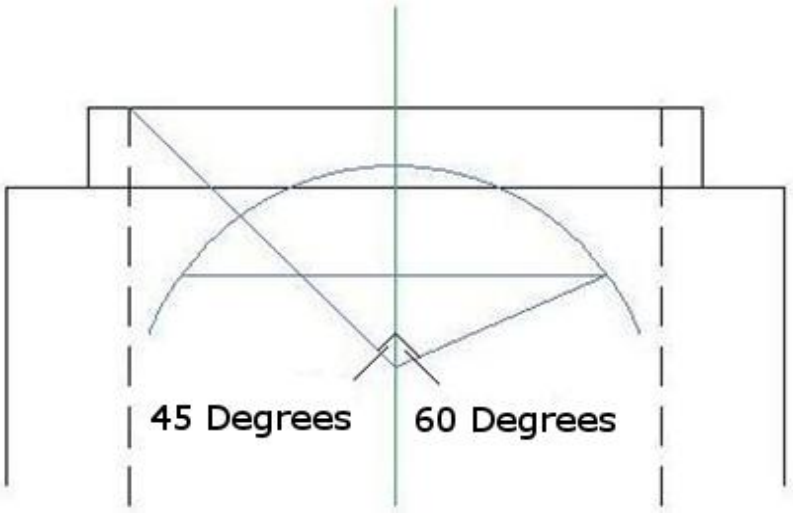

Figure 5-4 Seeker gimbal limits, pre-launch and general.

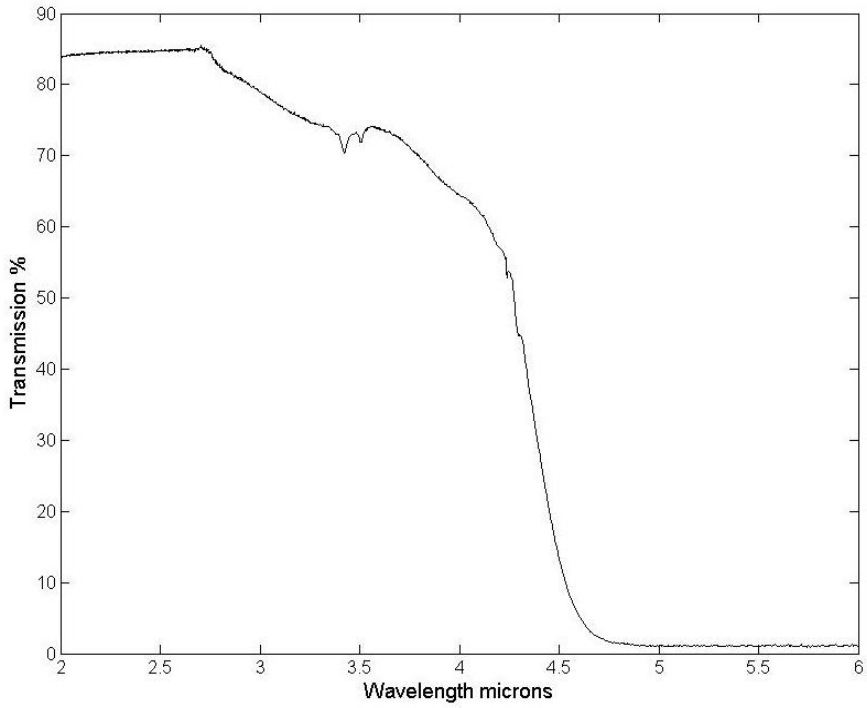

Figure 5-5 Transmission of seeker dome of an SA-7b.

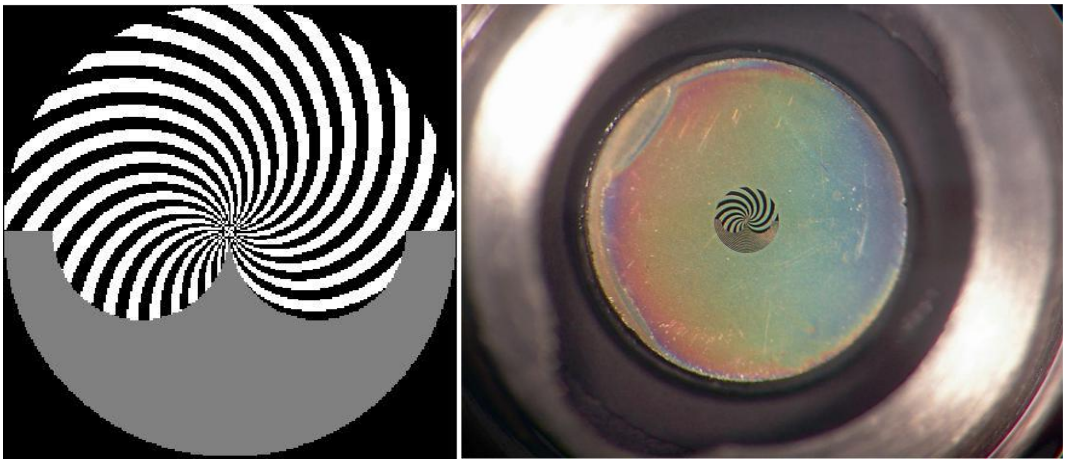

Figure 5-6 Reticle design for the spinscan IR seeker and a picture of the reticle from an SA-7b(84).

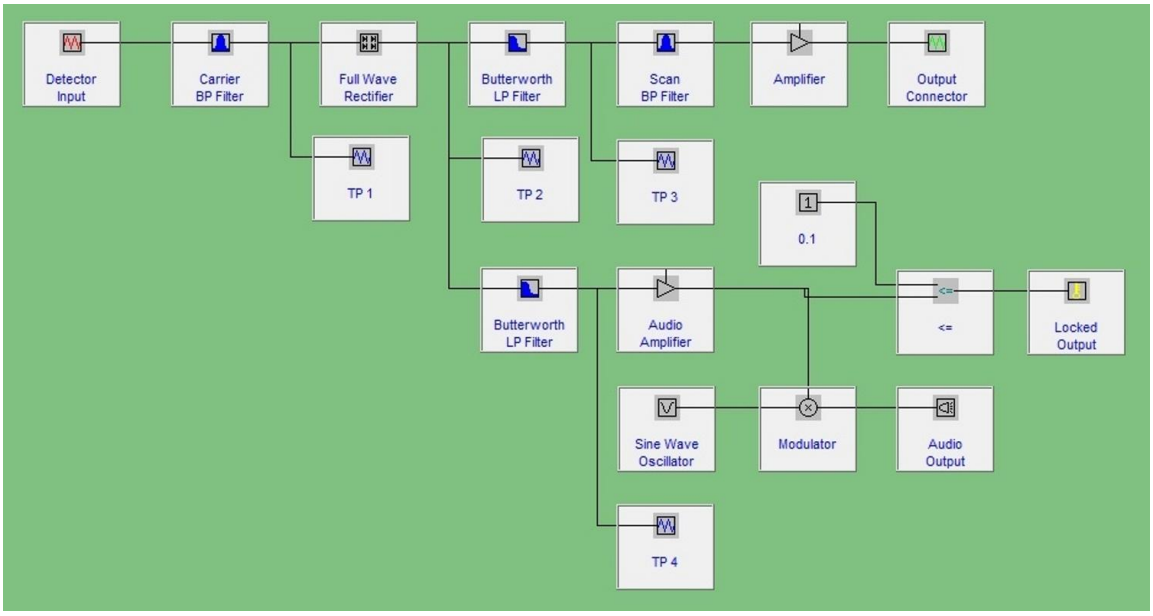

Figure 5-7 Signal processor design.

Previous work has modelled a spinscan seeker using the same reticle design and signal processor(77,78,80). Therefore, it was decide to not run test simulations for the model of a first generation MANPAD.

5.4 Second Generation MANPAD

The parameters for the missile body are the same as the first generation MANPAD but the IR seeker is improved from a spinscan system to a conscan.

The gimbal rates are increased to 18°/s which allows the missile to turn at a greater rate. Also, the detector waveband is increased to 3-5µm so cooler parts of the aircraft and plume are detectable giving an all aspect capability. As a conscan seeker produces a FM signal a new design for the signal processor is needed and a different reticle pattern. Four reticle designs were investigated, Figure 5-8, and a signal processor based on a design from reference(21), Figure 5-9. The signal processor is essentially a FM detector and a frequency demodulator. The band pass filter converts the FM signal to AM then the two low pass filters act as an envelope detector and a demodulator. The resulting demodulated signal gives the tracking error which is a measure of the missile to target line of sight rate. This simple design is able to process both the FM signal for small tracking errors and the AM signal for large tracking errors(21).

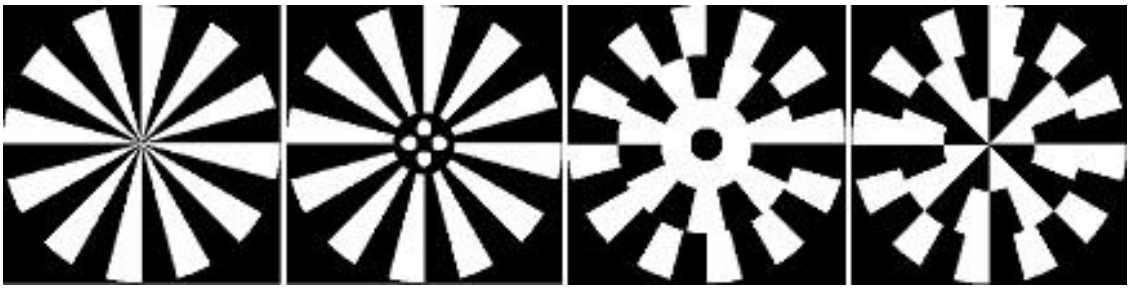

(a) (b) (c) (d)

Figure 5-8 Four reticle patterns.

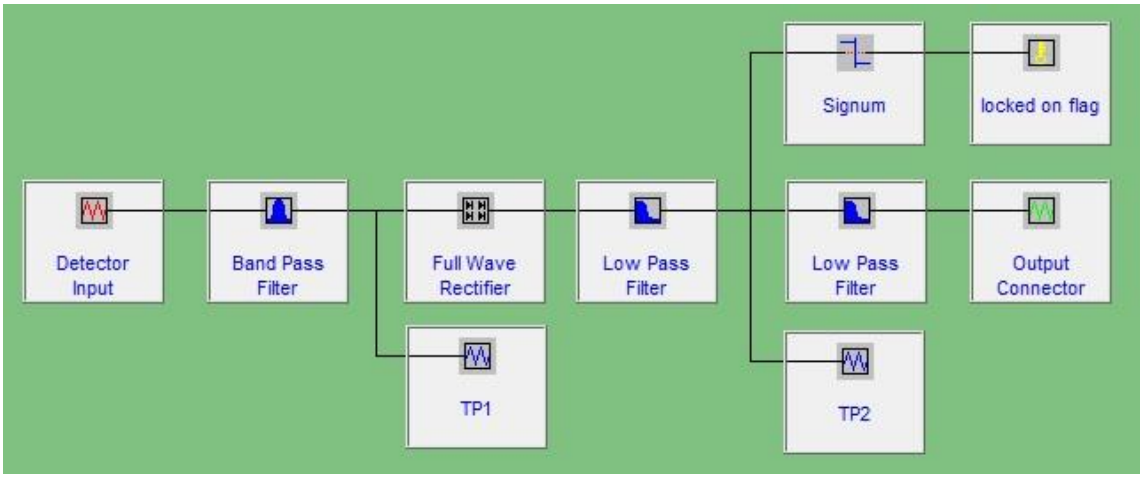

Figure 5-9 FM signal processor.

Two signal processor designs were investigated. The first had an offset band pass filter; the second had the centre frequency equal to the carrier frequency. The carrier frequency is the rotational speed of the optics times the number of spokes on the reticle. Parameters for the low pass filters were optimised to give the smoothest tracking error signal which would then give the best tracking. The results for each signal processor and reticle design are represented as static gain curves; a typical static gain curve for a conscan seeker is shown in Figure 5-10. In a real IR seeker the static gain curve represents the voltage produced with regards to the boresight error(21). In the simulations the amplitude of the error signal is used. The results for each signal processor and reticle design are shown in Figure 5-11 and Figure 5-12.

As the band pass filter should be offset to convert the FM signal to AM then signal processor 1 should give the best results. Also, the combination with the modified wagon wheel reticle should produce good results as this closely resembles the real reticle from an SA14, Figure 5-13.

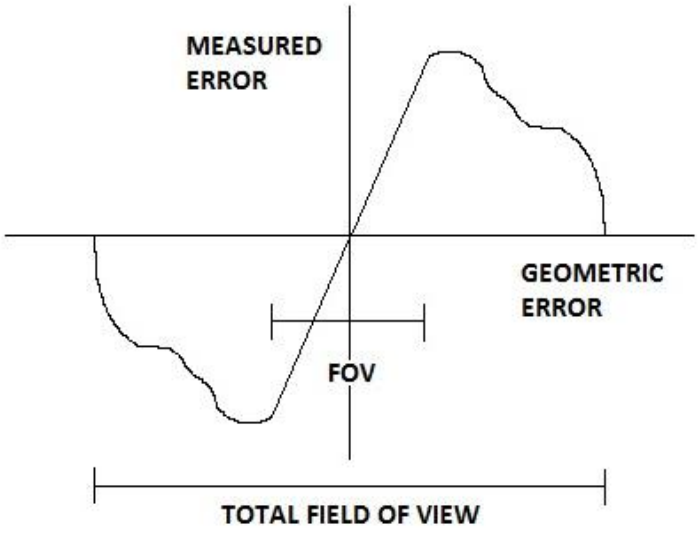

Figure 5-10 Typical static gain curve for a conscan seeker, reproduced from reference(21).

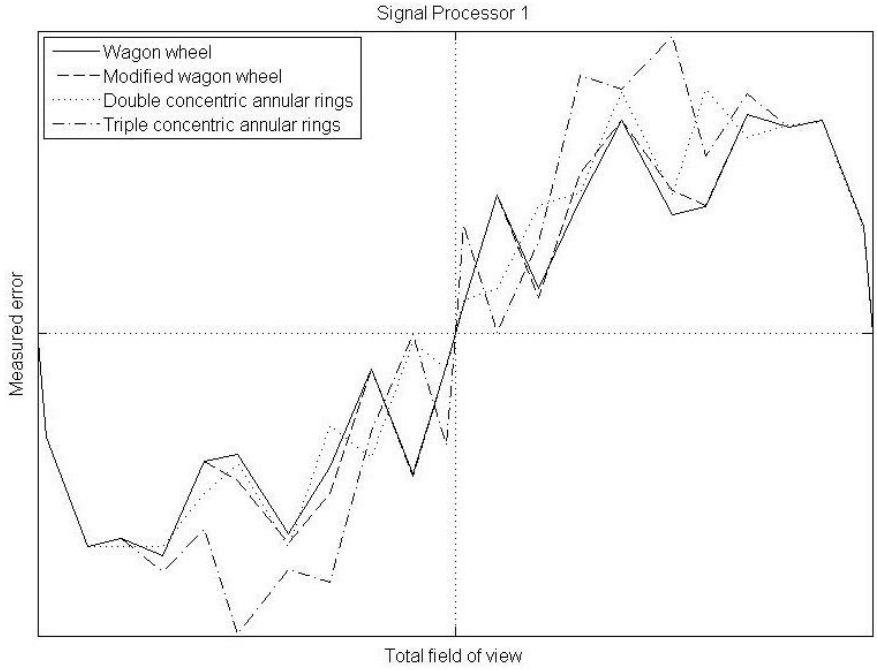

Figure 5-11 Static gain curve for signal processor 1.

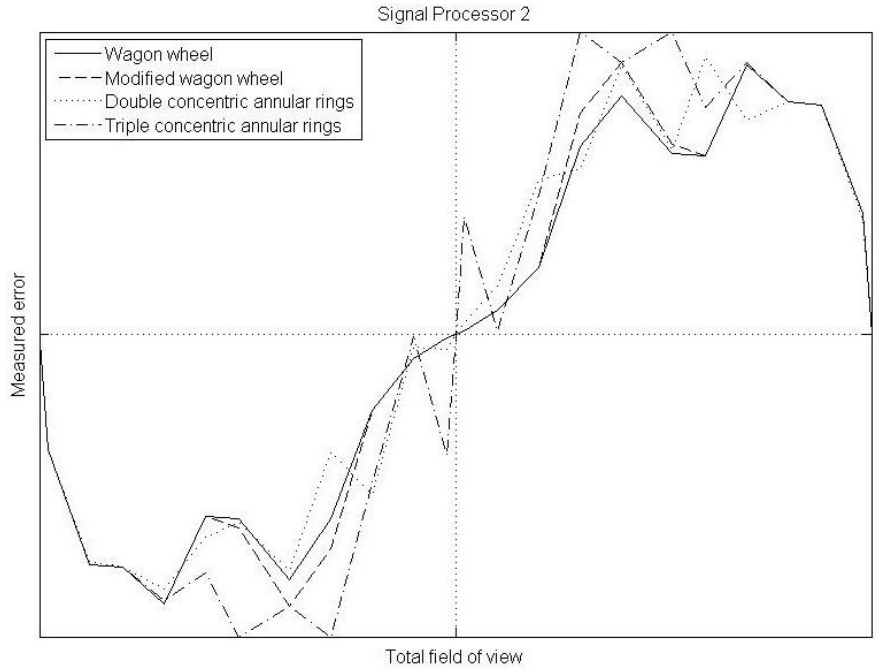

Figure 5-12 Static gain curve for signal processor 2.

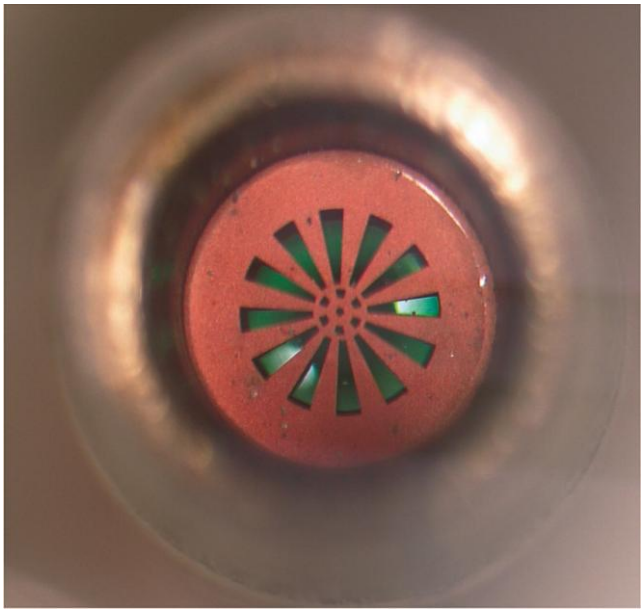

Figure 5-13 Picture of the reticle from an SA-14(85).

As this is a new untested model for a second generation MANPAD initial test simulations were carried out where different aircraft distance and azimuths were used to cover the operational envelope of a MANPAD; the results are shown in Table 5-2. Each set of simulations covered one aircraft altitude and various distances and azimuths totalling 240 separate engagements. It gives the percentage hit rate for each reticle design and signal processor.

Table 5-2 Percentage hit rates for different signal processors and reticles.

Signal Processor	Wagon Wheel Fig 5.8a	Modified Wagon Wheel Fig 5.8b	Double Concentric Fig 5.8c	Triple Concentric Fig 5.8d
1	87.5	88.8	72.1	80.8
2	29.6	34.6	38.8	56.7

The modified wagon wheel and signal processor design 1 give the highest percentage hit rates so they were chosen for the conscan seeker used in the second generation MANPAD model.

5.5 Aircraft Models

The first aircraft model used is a generic fast jet based on a 3D model of the AMX-A1. The plume is modelled as three concentric cones each with a transparency of 0.5 and temperature set according to open source literature(9). It is therefore an unclassified model and results should not be interpreted as representative of the AMX-A1. Figure 5-14 shows the model seen in the 3-5µm wave band. In the simulations in the proceeding chapters the aircraft was set on a constant bearing at a speed of 200m/s and performed no manoeuvre.

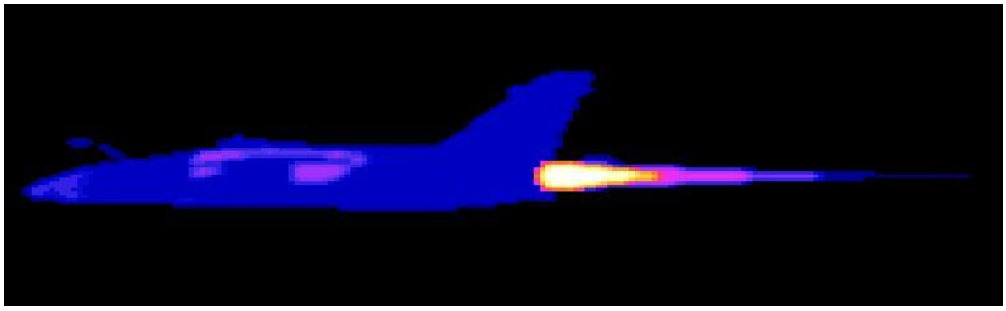

Figure 5-14 AMX-A1 model in the 3-5µm waveband.

Ejection characteristics for the flares are based on a configuration which has four dispensers located on each side of the airframe between the wings and the tail(81), as shown in Figure 5-15 where the large oval covers the front two dispensers. The results should not be interpreted as indicative of the AMX-A1 countermeasure system performance.

Figure 5-15 Positions of the four flare dispensers on the AMX-A1(86).

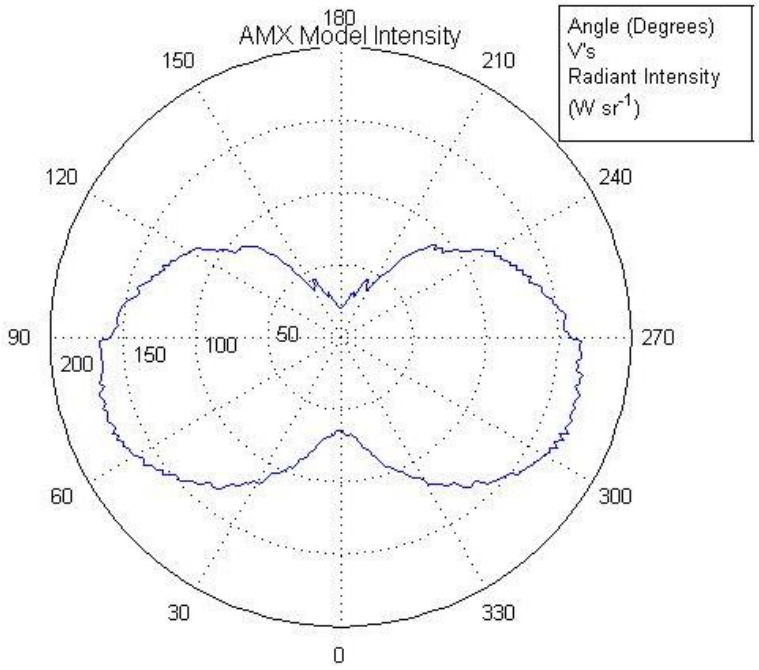

Figure 5-16 Polar intensity plot of the AMX-A1 model.

Figure 5-16 shows a polar plot of the radiant intensity in Wsr^{-1} for the AMX-A1 model where 0° represents tail-on. It was produced by placing a Mid-Wave thermal imager level with the aircraft then rotating the model through 360°. For a MANPAD that is placed on the ground the signature would be altered as it is not level with the aircraft. However, it is useful to compare the signature of different types of aircraft.

The second aircraft model used is a generic transport plane that is based on the C130. It has four engines and again the plume signatures are set according to the open source so should not be interpreted as representative of the C130(9).

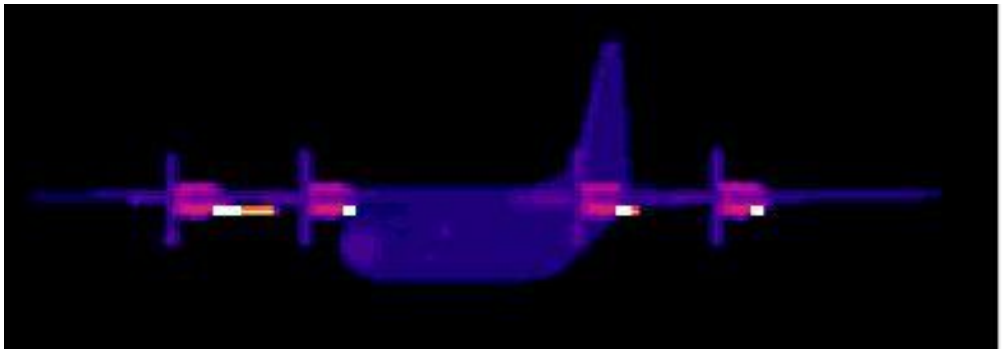

Figure 5-17 C130 model in the 3-5μm waveband.

Figure 5-17 shows the C130 model in the 3-5µm waveband. In the simulations in the proceeding chapters the aircraft was set on a constant bearing at a speed of 150m/s and performed no manoeuvre. Ejection characteristics for the flares are based on open source images from references(87,80) which show four flare dispensers. They are positioned under the aircrafts nose and in the aft end of the main landing gear fairings, yellow circles in Figure 5-18 and Figure 5-19.

Figure 5-18 Position of flare dispensers on C130 shown by yellow circles(87).

Figure 5-19 Position of flare dispensers in the aft end of the main landing gear fairings(87).

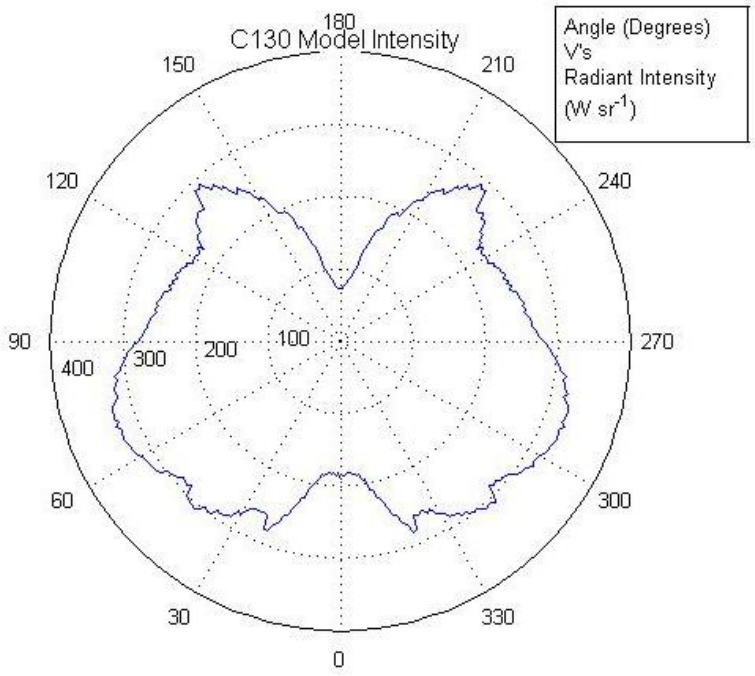

Figure 5-20 C130 model radiant intensity.

Figure 5-20 shows a polar plot of the radiant intensity of the C130 model which was produced in the same way as the AMX-A1. Both plots show the smallest signature at 180° which is head-on, as expected. There are peaks close to beam on as the full extent of the plume is visible at this angle.

5.6 Flare Models

The countermeasures used in the simulations are based on the square format 218 and 118 flares(60). For the simulations with the generic fast jet a 218 flare was used. This is because fast jets carry the larger type flares for when an afterburner is used as a flare with greater intensity is needed. Flares with reduced performance were then used in the simulations. Based on the 218 they had reduced peak intensity or reduced burn time. The four variants used were half intensity, half burn time, quarter intensity and quarter burn time.

For the simulations with the C130 transport aircraft model the 118 format flare was used. The smaller payload means more can be carried and the greater intensity of the 218 is not needed as the engines have no afterburner. Again,

the same flares with reduced performance were utilised, but this time based on the 118.

Figure 5-21 shows the two aircraft models releasing two flares simultaneously in a tail-on engagement. The waveband is 3-5µm and for the C130 model both the front and side dispensers are used.

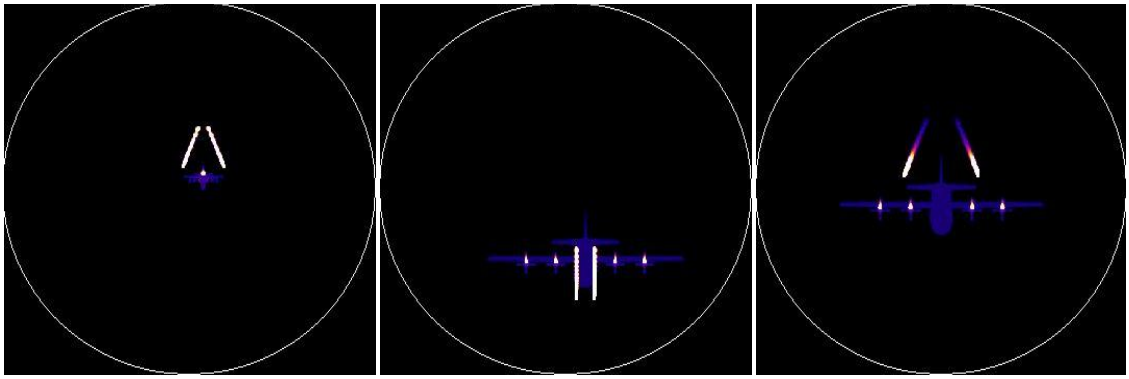

Figure 5-21 The simulated seeker FOV in CounterSim showing the two aircraft models and the flare ejection characteristics in a tail-on engagement.

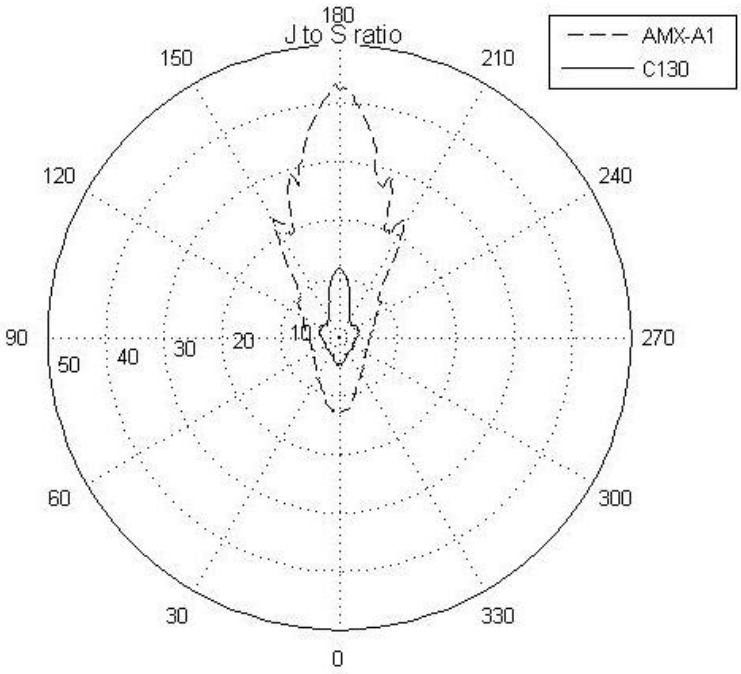

Figure 5-22 J to S ratio for the two aircraft models against a 218 flare.

The radiant intensity of the 218 flare was compared with both the AMX-A1 and C130 models to produce J/S ratios (jamming to signal). Figure 5-22 shows a polar plot of the J/S ratio for both models with 0° representing tail-on. For the AMX-A1 model in a head on engagement the 218 flare has a signature 40 times that of the aircraft. This is reduced to 10 for the C130 model, again compared to a 218 flare. The lowest ratio is in a beam on engagement where for both aircraft it is 5 or less.

6 BASE RUNS

For each MANPAD model base run simulations were carried out where the aircraft released no countermeasures giving an indication of the missiles performance(88). These covered the full operational envelope as quoted in open sources. To achieve this at the start of the simulation the horizontal distance of the MANPAD operator from the aircraft ranged from 1km to 5.5km in 500m steps. The aircraft altitude ranged from 100m to 3km in 100m steps. Also, the azimuth angle of the MANPAD operator is varied over 360° in 15° steps with 0° representing tail-on.

6.1 First Generation MANPAD and AMX-A1 Model

For the first generation MANPAD the parameters used for the missile system were to uncage the seeker 0.1s after lock-on, apply a super elevation of 5° at a rate of 6°/s and launch 0.1s after super elevation. A test run was undertaken for one altitude to study the effect of applying a lead angle based on the crossing rate. Taking the gimbal rate and the time for the firing sequence the maximum possible lead angle applied in a beam on engagement was estimated to be 10°. This value was used to calculate the lead angle, L, for each aircraft azimuth based on the sinusoidal law where

$$L = 10\sin(180^{o} - AircraftAzimuth)\,. \qquad \textbf{(6-1)}$$

The results of this test were exactly the same as when no lead angle was applied. Other test runs were also carried out with varying amounts of lead angle but the results were always the same. With first generation missiles the open source value for gimbal rates is low and is quoted as 6°/s. This limits the lead angle that can be applied in the time it takes to fire. The results for each aircraft altitude using the AMX-A1 model are shown in Table 6-1 where the values represent the probability of the aircraft escaping a hit (PEH). For each altitude there is 240 simulation; 24 aircraft azimuths times 10 aircraft distances. A hit is defined as a miss distance of less than 2m so the PEH represents the number of simulations out of the 240 that do not result in a hit. A near miss is

between 2m and 10m and a miss is more than 10m. There was no noise or atmospheric attenuation so the results give the best possible values that a first generation MANPAD could achieve.

Table 6-1 Base runs for 1st generation MANPAD and AMX-A1 model.

Altitude m	PEH	Altitude m	PEH	Altitude m	PEH
100	1.00	**1100**	0.20	**2100**	0.10
200	0.95	**1200**	0.18	**2200**	0.09
300	0.85	**1300**	0.16	**2300**	0.10
400	0.60	**1400**	0.16	**2400**	0.10
500	0.43	**1500**	0.14	**2500**	0.11
600	0.32	**1600**	0.13	**2600**	0.12
700	0.25	**1700**	0.13	**2700**	0.10
800	0.23	**1800**	0.13	**2800**	0.11
900	0.20	**1900**	0.11	**2900**	0.12
1000	0.19	**2000**	0.11	**3000**	0.11

The results for an aircraft altitude of 1km are shown as a polar plot in Figure 6-1. Each point of the wheel plot represents the position where the MANPAD is placed with regard to the aircraft at the start of the simulations, i.e. when the tracker item is trying to obtain lock-on.

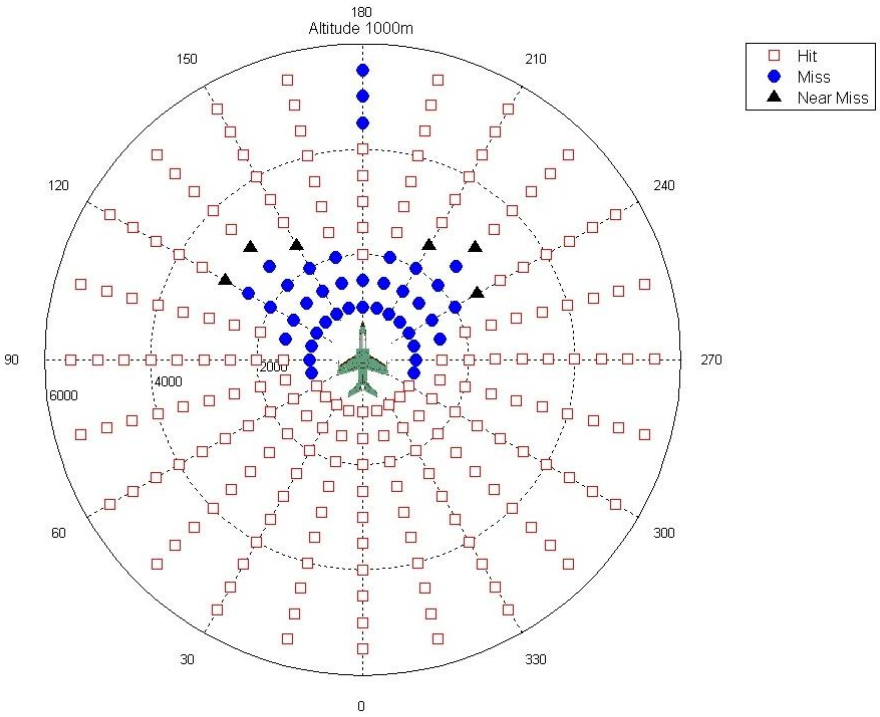

Figure 6-1 Results of the base run simulations for an altitude of 1km.

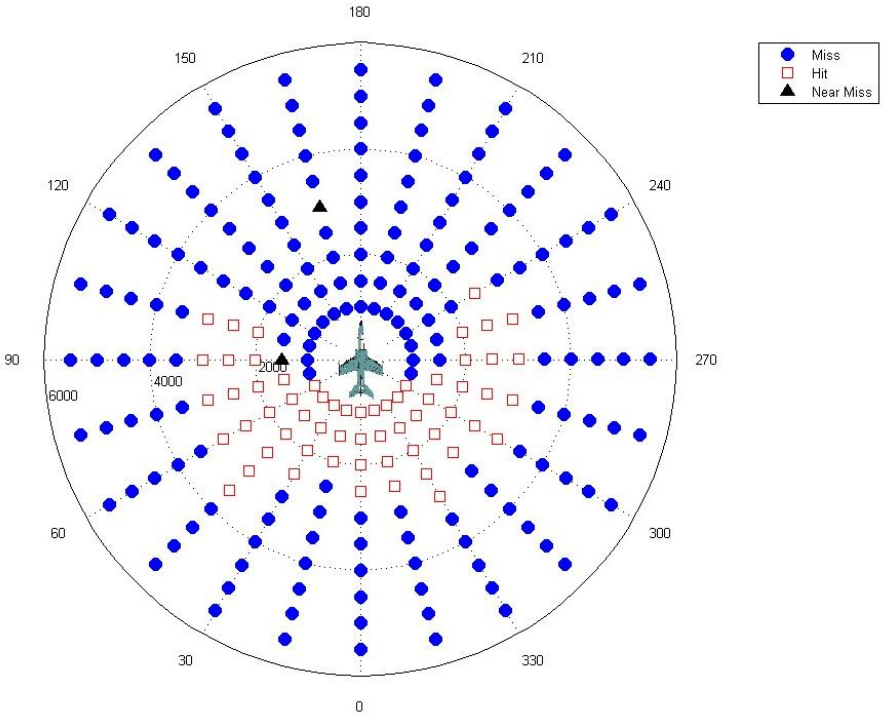

Figure 6-2 Results for an altitude of 1km with noise.

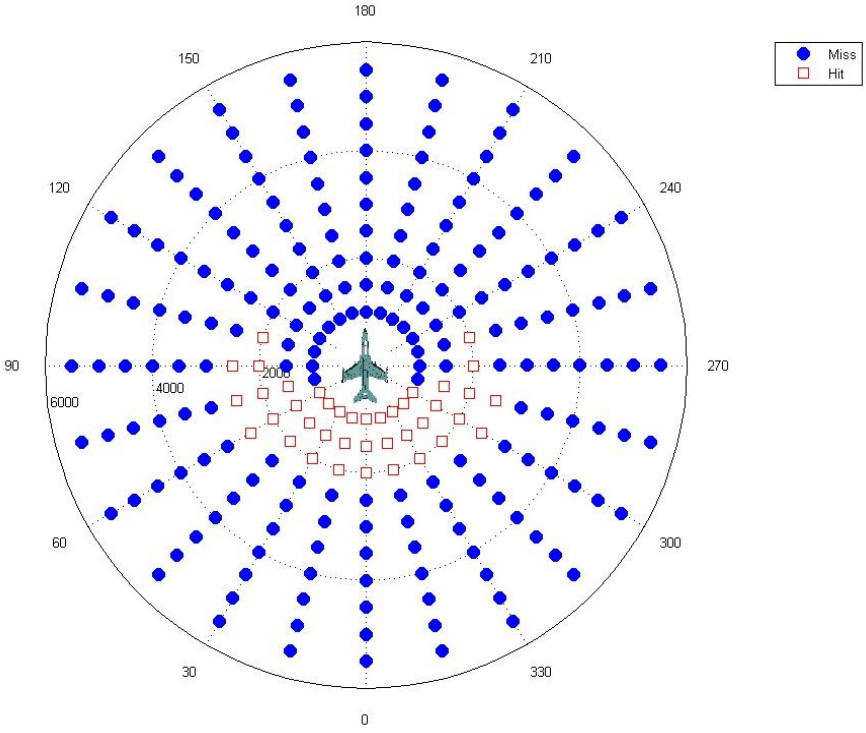

Figure 6-3 Results for an altitude of 1km with noise and Modtran.

To investigate the effect of noise on the outcome of the simulations a low level of noise was included in the seeker for one aircraft altitude. The dark noise included is assumed to be random with a normal distribution about a mean of zero with a standard deviation equal to one. The units are in photons and the noise is signal independent; the results are shown in Figure 6-2. Next, Modtran was also included to simulate transmission loss through the atmosphere. The results are shown in Figure 6-3 and are consistent with a first generation MANPAD being limited to close engagements in the rear aspect due to the limitations of its detector. (Appendix A looks at the asymmetry of polar plots and why certain engagements result in a hit or miss.)

6.2 First Generation MANPAD and C130 Model

The results for each aircraft altitude using the C130 model are shown in Table 6-2. Figure 6-4 shows a polar plot of the results for an aircraft altitude of 1km. Again, a super elevation of 5° was applied at a rate of 6°/s and no lead angle was used. The C130 model has lower values for the PEH up to an altitude of 500m compared to the AMX-A1 model as expected for a larger and slower target. However, the C130 model performs better at altitudes over 500m, i.e. has higher PEH values. One reason for this might be that in the 2-2.7 waveband the C130 shows as 4 distinct targets as the missile approaches, one for each of the engines/plumes. The tracking of the spinscan seeker may not be adequate to deal with this complicated scenario of multiple targets in the FOV.

Table 6-2 Base runs for 1st generation MANPAD and C130 model.

Altitude m	PEH	Altitude m	PEH	Altitude m	PEH
100	0.96	**1100**	0.27	**2100**	0.32
200	0.88	**1200**	0.29	**2200**	0.31
300	0.71	**1300**	0.30	**2300**	0.32
400	0.58	**1400**	0.31	**2400**	0.31
500	0.43	**1500**	0.30	**2500**	0.30
600	0.38	**1600**	0.29	**2600**	0.30
700	0.30	**1700**	0.32	**2700**	0.29
800	0.27	**1800**	0.35	**2800**	0.30
900	0.24	**1900**	0.33	**2900**	0.28
1000	0.27	**2000**	0.33	**3000**	0.28

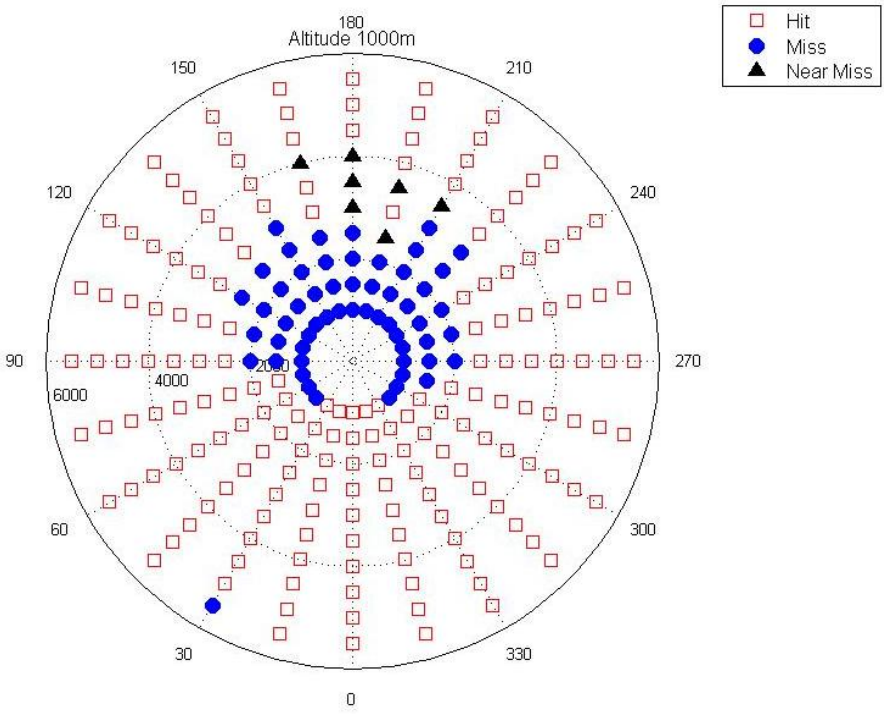

Figure 6-4 Results of the base runs for an altitude of 1km and C130 model.

6.3 Second Generation MANPAD and AMX-A1 Model

For the second generation MANPAD the parameters used for the missile system were to uncage the seeker 0.1s after lock-on, apply a super elevation of 5° at a rate of 10°/s and launch 0.1s after super elevation. As the gimbal rates are higher a lead angle could be applied in a shorter amount of time. Test simulations were run to find the optimum values and the best results were for a lead, L, given by the equation

$$L = 5\sin(180^o - AircraftAzimuth). \qquad \textbf{(6-2)}$$

The lead angle was also applied at a rate of 10°/s. Results for each aircraft altitude are shown in Table 6-3. Figure 6-5 shows a polar plot for an aircraft altitude of 1km.

Table 6-3 Base runs for 2nd generation MANPAD and AMX-A1 model.

Altitude m	PEH	Altitude m	PEH	Altitude m	PEH
100	0.63	**1100**	0.11	**2100**	0.07
200	0.38	**1200**	0.11	**2200**	0.08
300	0.31	**1300**	0.10	**2300**	0.08
400	0.23	**1400**	0.10	**2400**	0.08
500	0.18	**1500**	0.09	**2500**	0.10
600	0.17	**1600**	0.08	**2600**	0.11
700	0.15	**1700**	0.07	**2700**	0.12
800	0.15	**1800**	0.08	**2800**	0.12
900	0.14	**1900**	0.07	**2900**	0.13
1000	0.11	**2000**	0.06	**3000**	0.13

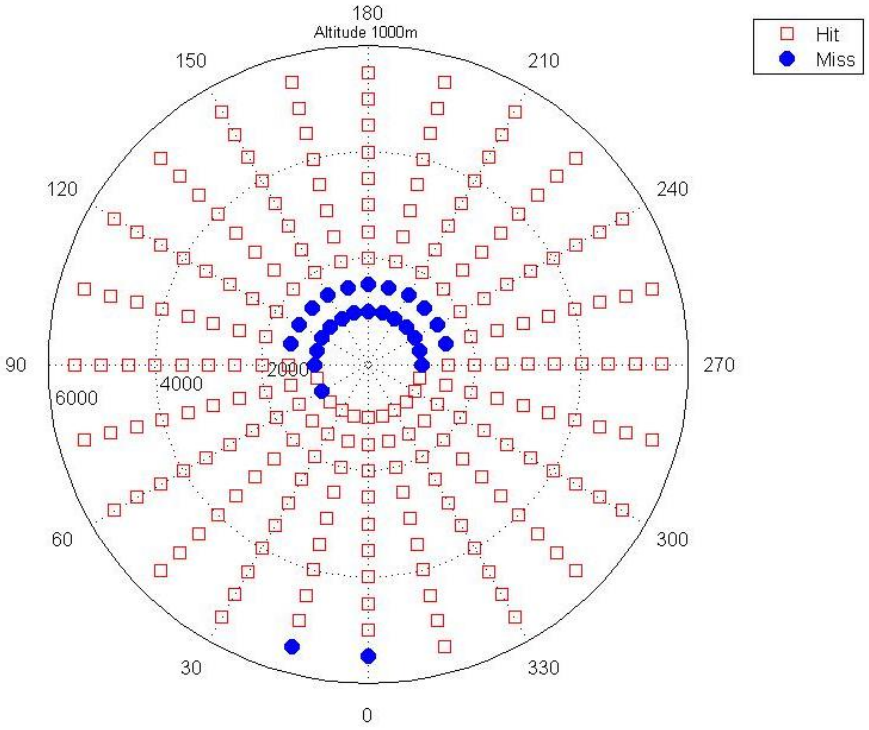

Figure 6-5 Results of the base runs for an altitude of 1km and AMX-A1 model.

6.4 Second Generation MANPAD and C130 Model

For the base runs with the C130 model the same amount of super elevation and lead were applied but at a lower rate of 6°/s as the target was moving at a slower speed. If lead was still applied at 10°/s then the target was lost from the seeker FOV. Results for each aircraft altitude are shown in Table 6-4. The

results for the C130 model give lower values for the PEH compared to the AMX-A1 model as expected. The only misses are for close range head-on scenarios. Both models have lower PEH values for the second generation conscan MANPAD compared to the first generation spinscan MANPAD. This is a confirmation of the improved tracking achieved with a conscan IR seeker.

Table 6-4 Base runs for 2nd generation MANPAD and C130 model.

Altitude m	PEH	Altitude m	PEH	Altitude m	PEH
100	0.64	**1100**	0.05	**2100**	0.03
200	0.25	**1200**	0.04	**2200**	0.04
300	0.11	**1300**	0.03	**2300**	0.05
400	0.08	**1400**	0.03	**2400**	0.04
500	0.07	**1500**	0.03	**2500**	0.05
600	0.07	**1600**	0.02	**2600**	0.05
700	0.08	**1700**	0.03	**2700**	0.06
800	0.07	**1800**	0.03	**2800**	0.09
900	0.06	**1900**	0.03	**2900**	0.08
1000	0.05	**2000**	0.03	**3000**	0.08

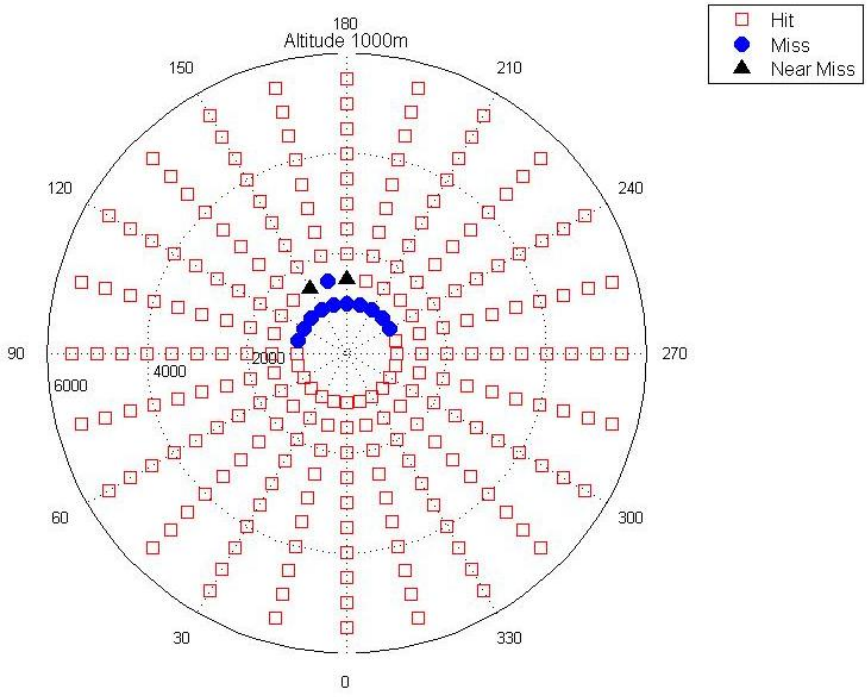

Figure 6-6 Results of the base runs for an altitude of 1km and C130 model.

6.5 Δd Analysis

From the base run simulations with a first generation MANPAD and the AMX-A1 model individual scenarios were chosen to analyse in greater detail. A new variable, Δd, the projected miss distance is introduced and calculated for individual runs. Also, other missile parameters are logged to investigate their effect on an engagements outcome.

At each time step in the simulation the aircraft and missile velocity vectors are used to calculate their intersect point. The difference between this intersect point and the actual impact point of a hit or point of closest approach for a miss is defined as the projected miss distance Δd, Figure 6-7. A1 and M1 are the positions of the aircraft and missile at time t1, likewise for time t2.

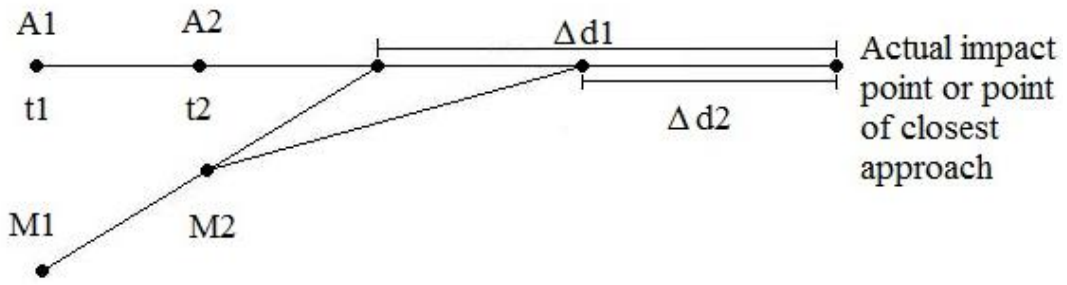

Figure 6-7 Definition of the projected miss distance Δd.

It is unlikely that two lines in three dimensions will intersect exactly, however they can be connected by a unique shortest line segment(89), Figure 6-8. Given two lines in three dimensions with endpoints p_1, p_2 and p_3, p_4 a point on the two lines will be defined by the following two equations

$$p_a = p_1 + \mu_a(p_2 - p_1) \quad \textbf{(6-3)}$$

$$p_b = p_3 + \mu_b(p_4 - p_3). \quad \textbf{(6-4)}$$

The parameters μ_a and μ_b can only have values between 0 and 1.

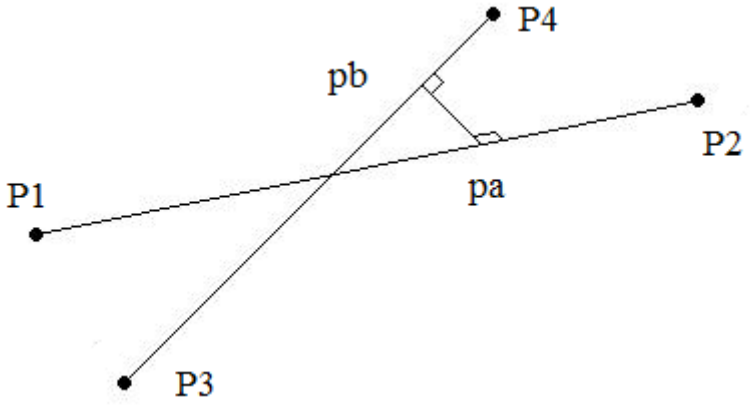

Figure 6-8 Shortest line segment between two lines in three dimensions(89).

Because the shortest line segment will be perpendicular to the two lines, two equations can be written for the dot product

$$(p_a - p_b)\cdot(p_2 - p_1) = 0 \qquad \textbf{(6-5)}$$

$$(p_a - p_b)\cdot(p_4 - p_3) = 0\,. \qquad \textbf{(6-6)}$$

Then, substituting for p_a and p_b and expanding gives μ_a and μ_b.

The point to use for the projected intersect point has to be chosen. Point p_a will lie on the aircraft velocity vector, p_b which will lie on the missile velocity vector or the midpoint of the line segment $p_a p_b$ can be used. The results are nearly identical and because the aircraft is on a constant trajectory in two-dimensions the point p_a has been chosen for the projected hit point.

Graphs of Δd can be classified into different types depending on the angle of attack of the missile. For tail on engagements that result in a hit, shown by the dashed curve in Figure 6-9, the graphs are similar in shape. When the missile misses it is due to the fact that the aircraft is too far away to lock-on to the signal. For head on engagements all the misses occur because the missile is unable to lock-on to the target. This is because of the geometry of the scenario whereby the seeker cannot see the plume of the jet and no signal is detected. The graphs of Δd for head on hits all closely resemble the solid curve in Figure

6-9. The missile is launched at 1.5s, from 1.5s to 2s is the ignition delay, from 2s to 2.5s is the boost motor and from 2.5s to 3.5s is the sustain motor.

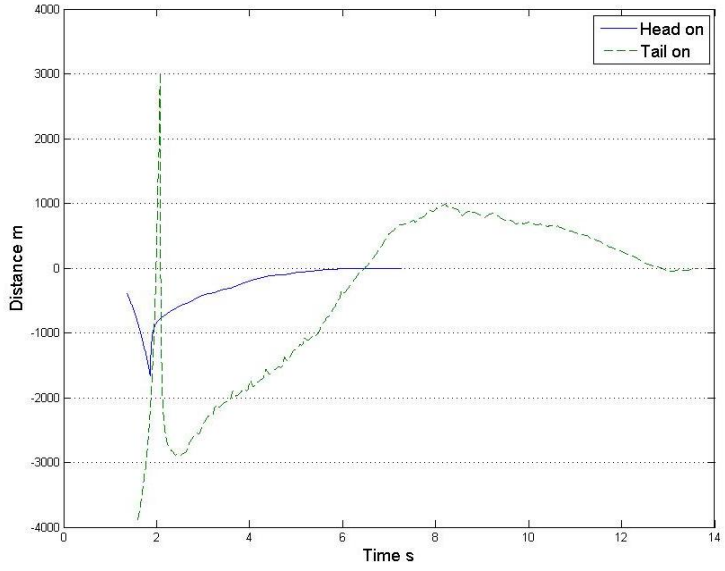

Figure 6-9 Graphs of ∆d for head on and tail on hits.

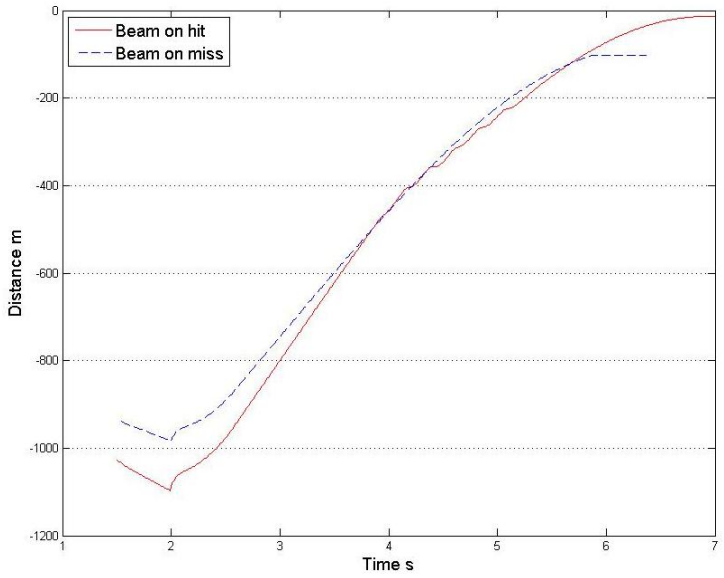

Figure 6-10 Graphs of ∆d for a beam on hit and beam on miss.

To study the differences in plots of ∆d for hits and misses it is necessary to look at beam on engagements. In these cases it is possible that the missile misses due to the limitations of its design and not due to a lack of signal from the target. Figure 6-10 shows plots of ∆d for two engagements where only the missile

range from the aircraft changed by 500m but the simulations ended with different results. The two graphs are similar up until 4s into the simulation at which point the plot for a miss shows a continuous smooth curve whereas the plot for a hit shows small fluctuations before attaining a zero miss distance.

The missile body and seeker behaviour during each simulation was examined to determine which factors most affected the outcome of an engagement. The most significant factor was the missile acceleration.

Figure 6-11 shows two engagements; the first is a beam on engagement for a distance of 1500m, altitude 1500m and aircraft azimuth 120^{o} that results in a miss. The horizontal component of the missiles acceleration shows a steady increase as the missile tries to use proportional navigation to aim ahead of the aircrafts current position. Once the missile reaches its latax limit it can no longer keep the target in the seeker FOV and so loses signal. This can also be seen in the graph of Δd, Figure 6-10, which exhibits a smooth curve. The second engagement in Figure 6-11 shows a beam on engagement for a distance of 2000m, altitude 1500m and aircraft azimuth 120^{o} that results in a hit. The horizontal component of the acceleration is the same until 4s into the simulation. At this time the missile starts alternating between zero and the latax limit as it goes through a process of acquiring the target, then the target moving to the edge of the FOV and finally reacquires the target in the centre of the seeker view. The large fluctuations in the lateral acceleration appear as small fluctuations in the graph of Δd, Figure 6-10.

Figure 6-12 shows the differences in plots of Δd for a hit and a miss caused by pre-emptive flare deployment when the flares are fired at simulation time t=0s. The two plots are very similar up to the time of missile launch, around 1.5s, so Δd cannot be used to classify the outcome of an engagement when studying pre-emptive countermeasures.

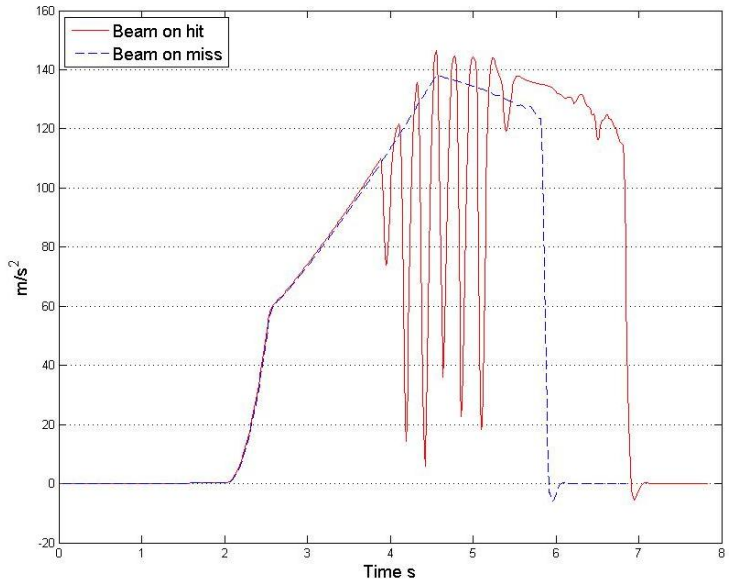

Figure 6-11 Horizontal component of the missile acceleration for a beam on hit and beam on miss.

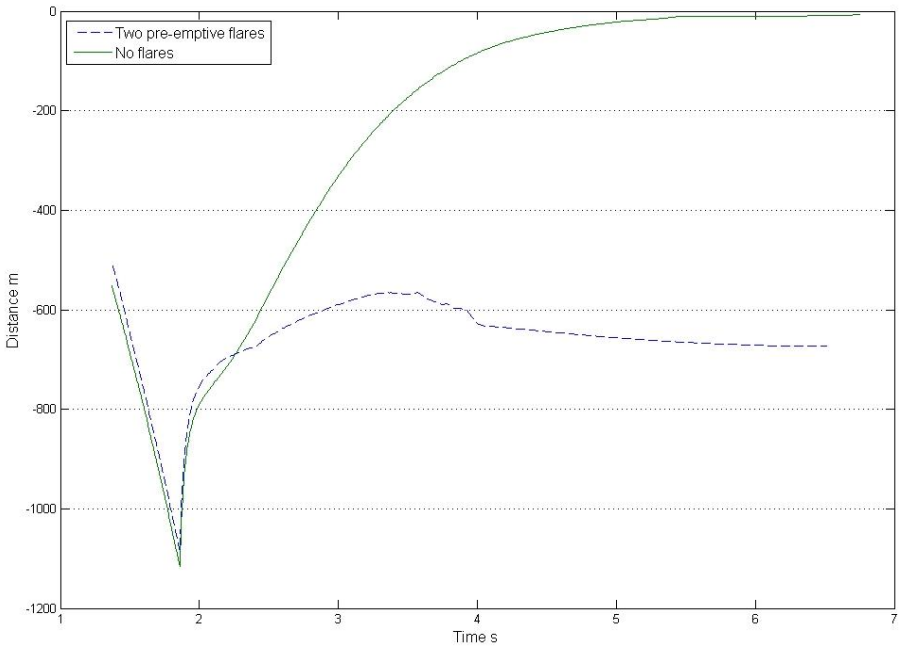

Figure 6-12 Plots of Δd for no flares and pre-emptive flares.

6.6 Conclusions

A first generation spinscan MANPAD and a second generation conscan MANPAD have been modelled and tested against a fast jet and a transport

aircraft. When noise and Modtran were included in the simulations the results confirmed the accepted view of a first generation MANPAD being described as a tail-chaser. The lowest values for the PEH occurred in the simulations with a second generation MANPAD and the C130 model as expected. The results represent the best possible case for the MANPAD and are a good basis for future simulations to test IR countermeasures.

A new variable Δd was introduced which can be used to classify the angle of attack in an engagement but not the outcome when studied prior to missile launch. As this thesis is interested in the analysis of pre-emptive countermeasures Δd will not be used in future chapters.

7 PRE-EMPTIVE COUNTERMEASURES

In this chapter all flares are released pre-emptively by the aircraft models, i.e. before missile launch(90). All the flares are fired in pairs from dispensers on either side of the airframe. Flares with reduced performance will be used with the AMX-A1 model and for the C130 model different flare dispensers will be tested(91).

7.1 First Generation MANPAD and AMX-A1 Model

For the first pre-emptive flare deployment scenario, two flares were fired at the start of the simulation, t=0s, when the tracker is trying to lock-on to the target. To represent the operational envelope of the MANPAD, the simulation start distance between the missile system and the aircraft ranges from 1km to 5.5km in steps of 500m. The aircraft altitude ranges from 100m to 3000m in steps of 100m and the aircraft azimuth angle with respect to the missile launch position ranges from 0° to 345° in steps of 15°. An aircraft azimuth of 0° represents a tail-on engagement where the aircraft is flying directly away from the missile operator position. In each simulation the aircraft is travelling at a constant speed of 200 m/s.

Two flares are fired at the simulation start time (t=0), one each from the first dispenser on both sides of the airframe. At this time the tracker item is not pointing at the target but simulates the operator manoeuvring the MANPAD onto the target to obtain lock-on. Once lock-on has occurred, the seeker head is uncaged then lead and super elevation are applied. Finally, the missile is launched, which is dependent on maintaining lock-on throughout the procedure. Typically it takes about 1.5s from the simulation start until the missile is launched. Therefore any flares fired up to this time can be regarded as pre-emptive. If pre-emptive flares are in the FOV as the seeker locks-on then they represent an immediate target in addition to the aircraft.

There are a total of 240 simulations for each aircraft altitude, 10 missile launch ranges (1km to 5.5km in steps of 500m) and 24 aircraft azimuths (0° to 345° in

steps of 15°). This gives a total of 7200 simulations for each type of flare (240 x 30 altitudes – 100m to 3km in steps of 100m).

Table 7-1 Results for a full 218 flare, overall PEH of 0.81.

Altitude m	PEH	Altitude m	PEH	Altitude m	PEH
100	1.00	**1100**	0.80	**2100**	0.75
200	0.99	**1200**	0.79	**2200**	0.72
300	0.96	**1300**	0.79	**2300**	0.76
400	0.92	**1400**	0.78	**2400**	0.77
500	0.88	**1500**	0.77	**2500**	0.78
600	0.88	**1600**	0.77	**2600**	0.78
700	0.88	**1700**	0.74	**2700**	0.78
800	0.88	**1800**	0.74	**2800**	0.77
900	0.84	**1900**	0.72	**2900**	0.78
1000	0.83	**2000**	0.73	**3000**	0.79

Table 7-2 Results for a half intensity 218 flare, overall PEH of 0.69.

Altitude m	PEH	Altitude m	PEH	Altitude m	PEH
100	1.00	**1100**	0.71	**2100**	0.58
200	1.00	**1200**	0.71	**2200**	0.57
300	0.93	**1300**	0.67	**2300**	0.57
400	0.88	**1400**	0.65	**2400**	0.56
500	0.83	**1500**	0.63	**2500**	0.55
600	0.79	**1600**	0.62	**2600**	0.58
700	0.79	**1700**	0.59	**2700**	0.56
800	0.79	**1800**	0.57	**2800**	0.62
900	0.75	**1900**	0.57	**2900**	0.61
1000	0.73	**2000**	0.56	**3000**	0.65

Table 7-3 Results for a half burn time 218 flare, overall PEH 0.69.

Altitude m	PEH	Altitude m	PEH	Altitude m	PEH
100	1.00	**1100**	0.73	**2100**	0.54
200	0.99	**1200**	0.71	**2200**	0.53
300	0.93	**1300**	0.70	**2300**	0.55
400	0.87	**1400**	0.65	**2400**	0.55
500	0.84	**1500**	0.64	**2500**	0.56
600	0.80	**1600**	0.61	**2600**	0.56
700	0.79	**1700**	0.61	**2700**	0.60
800	0.78	**1800**	0.60	**2800**	0.60
900	0.79	**1900**	0.58	**2900**	0.62
1000	0.74	**2000**	0.56	**3000**	0.65

Table 7-4 Results for a quarter burn time 218 flare, overall PEH 0.56.

Altitude m	PEH	Altitude m	PEH	Altitude m	PEH
100	1.00	**1100**	0.54	**2100**	0.39
200	0.99	**1200**	0.55	**2200**	0.41
300	0.93	**1300**	0.55	**2300**	0.42
400	0.83	**1400**	0.53	**2400**	0.41
500	0.73	**1500**	0.52	**2500**	0.42
600	0.70	**1600**	0.49	**2600**	0.43
700	0.68	**1700**	0.49	**2700**	0.38
800	0.62	**1800**	0.45	**2800**	0.39
900	0.63	**1900**	0.47	**2900**	0.39
1000	0.58	**2000**	0.43	**3000**	0.40

Table 7-5 Results for a quarter intensity 218 flare, overall PEH 0.59.

Altitude m	PEH	Altitude m	PEH	Altitude m	PEH
100	1.00	**1100**	0.60	**2100**	0.45
200	0.98	**1200**	0.58	**2200**	0.47
300	0.93	**1300**	0.58	**2300**	0.45
400	0.86	**1400**	0.58	**2400**	0.44
500	0.78	**1500**	0.58	**2500**	0.43
600	0.75	**1600**	0.51	**2600**	0.43
700	0.75	**1700**	0.50	**2700**	0.44
800	0.70	**1800**	0.48	**2800**	0.44
900	0.63	**1900**	0.44	**2900**	0.42
1000	0.63	**2000**	0.43	**3000**	0.42

Results for each aircraft altitude with a standard 218 flare are shown in Table 7-1. The process of firing pre-emptive flares at t=0s was repeated for the reduced performance flares and the results are shown in Table 7-2, Table 7-3, Table 7-4 and Table 7-5 respectively.

As well as presenting the results with regard to aircraft altitude some more insights can be gained by plotting the PEH versus aircraft azimuth. The results are shown in Figure 7-1, where the PEH for each aircraft azimuth is out of 300 simulations (30 aircraft altitudes x 10 missile launch ranges). The results show that the PEH is dependent on aircraft azimuth. All flare types perform best in tail-on or close to tail-on engagements with a full 218 giving the best results overall. The half intensity and half burn time flares demonstrate similar results to each other. This is not surprising since the half burn time and half intensity flare

pellets are very similar in size and mass and the total energy is therefore similar. The same applies to the quarter burn time and quarter intensity flares.

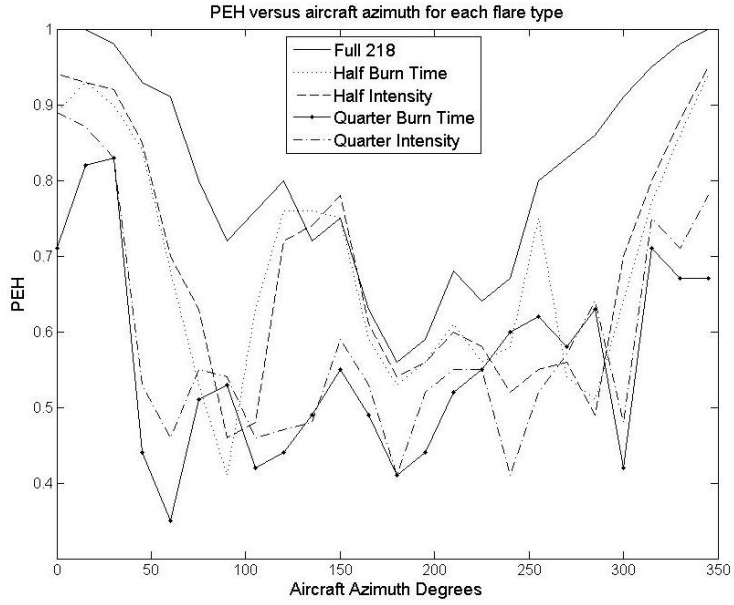

Figure 7-1 PEH versus aircraft azimuth.

There are clear differentiations between the full, half and quarter flare types throughout the azimuth range. Engagements with the largest crossing rates, around 90° and 270°, have the greatest separation rate of target and flare. The tracker follows the aircraft and loses the flare from the seeker FOV before lock-on has been achieved. There is an interesting asymmetry with the half flares where they match the full flare results from about 120° to 180° and do less well thereafter. The quarter flare performance is clearly worse in the head on region. In the real world, head-on hits are not likely with a first generation MANPAD because the hot parts of the engine and plume are less likely to be detected.

The next set of simulations looked at the firing time of pre-emptive flares as releasing at t=0s can sometimes be a test of the tracker and not the IR seeker for certain engagement geometries. One aircraft altitude of 1km was chosen using all the missile ranges and azimuth angles, giving 240 simulations for each flare release time. Flares were released from simulation time t=0s up to t=1s in steps of 0.1s and the simulations were repeated for all flare types.

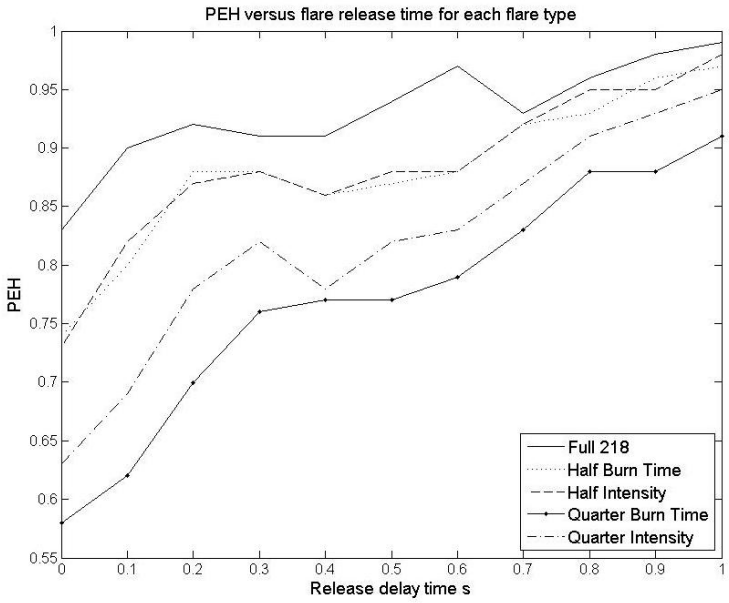

Figure 7-2 PEH versus flare release time delayed from the start of the simulation.

The results are presented in Figure 7-2 which shows that when the release of pre-emptive flares is delayed from the start of the simulation the PEH for all flare types increases. Therefore, delaying the deployment of flares of all types until the seeker has obtained lock-on and is in the pre-launch firing sequence is significantly more effective. The greatest PEH values for all flare types occurs at t=1s which is when the MANPAD has achieved lock-on and is in the process of applying lead and super elevation. For the full 218 the PEH is 0.99 and for the half intensity and half burn time flares the results are similar. The largest difference is between the quarter flares with the quarter intensity flare performing better than the quarter burn time flare. This is because the quarter burn time flare only lasts for 1s and given some engagement geometries, such as tail-on or close to tail-on, the target is still in the seeker FOV when the flare burns out.

To further demonstrate the effect of delaying the release of pre-emptive countermeasures Figure 7-3 shows a polar plot for an altitude of 1km and a full 218 flare released at t=0s. The aircraft is at the origin with 0° tail-on and each point represents where a MANPAD is placed with regard to the aircraft at the

beginning of each simulation. In Figure 7-3 hits can be seen for the beam on scenarios with the largest crossing rates, mentioned earlier, where the tracker loses the flare from the seeker FOV before lock-on has occurred. If the time of flare release is delayed until t=1s, when the MANPAD is in the process of applying lead and super elevation, then only 2 out of the 240 engagements resulted in a hit.

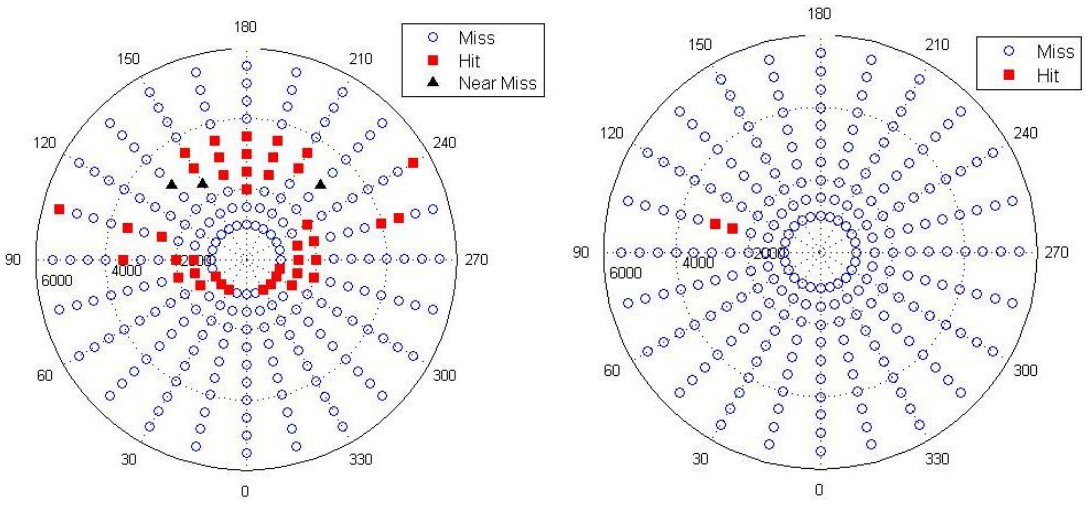

Figure 7-3 Results for an aircraft altitude of 1km and full 218 flare fired at time (a) t=0s and (b) t=1s.

7.2 First Generation MANPAD and C130 Model

For the simulations with the C130 model the full 118 flare was used and released from the front dispensers, side dispensers and both sets of dispensers. From the previous section firing flares at simulation time t=0s is sometimes a test of the tracker item given engagement geometries with the largest crossing rates. As this thesis concerns the effect of pre-emptive flares on the IR seeker it was decide not to carry out all the base run simulations with flares fired at t=0s. One aircraft altitude of 1km was chosen using all the missile ranges and azimuth angles, giving 240 simulations for each flare release time. Flares were released up to simulation time t=1s in steps of 0.1s and the

simulations were repeated for the different dispensers. The results are shown in Figure 7-4.

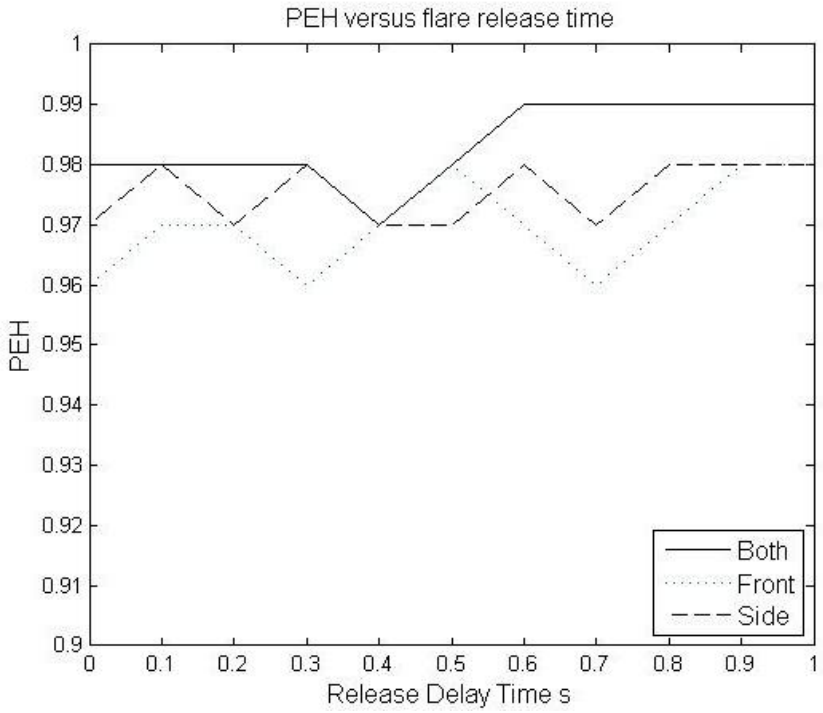

Figure 7-4 PEH versus flare release delay time for different flare dispensers.

Figure 7-4 shows that a high PEH is achieved irrespective of which dispensers are used and that the value is roughly constant across the different delay times, i.e. between 0.96 and 0.99. This is higher than the scenario with the AMX-A1 model and the full 218 flare, which again maybe due to the more complicated target signature in the 2-2.7µm waveband as stated previously in section 6.2.

When the data is plotted with regard to the aircraft azimuth, Figure 7-5, there are some difference depending on which dispenser is used. All perform badly in the tail-on scenario, 0°, giving lower values for the PEH with the front dispensers being the worst. The side dispensers have a dip at 105° but give similar results for all other aircraft azimuths with the PEH between 0.95 and 1.

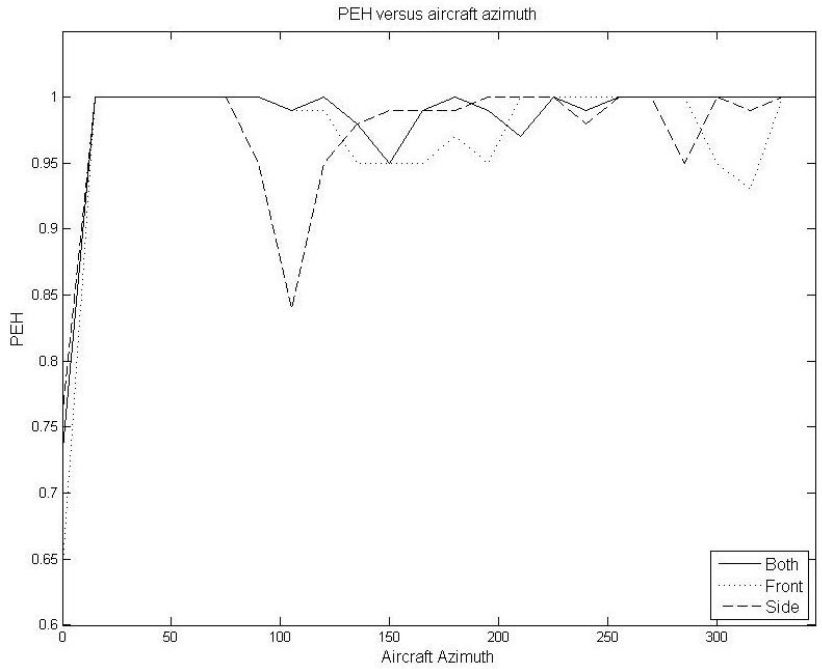

Figure 7-5 PEH versus aircraft azimuth for different flare dispensers.

7.3 Second Generation MANPAD and AMX-A1 Model

For the second generation MANPAD and the AMX-A1 model the simulations were repeated where all flare types are released from t=0s to t=1s in steps of 0.1s. Again, this was for an aircraft altitude of 1km and using all launch ranges and azimuth angles, the results are shown in Figure 7-6.

The results show that for a conscan seeker delaying the firing of pre-emptive flares until after the MANPAD has achieved lock-on and is in the process of applying lead and super elevation increases the effectiveness of all flare types. The full 218 flare performs the best and the quarter burn time flare is the worst as expected. However, the half intensity and quarter intensity flares give nearly identical results with the quarter intensity performing better than the half burn time flare.

Comparing the results with those for a first generation MANPAD, Figure 7-2, with flare release at t=1s the biggest difference is with the quarter burn time flare. For a conscan seeker the total FOV is larger due to the nutating optics so

there is a greater chance of the target staying in the FOV after the flare has burned out.

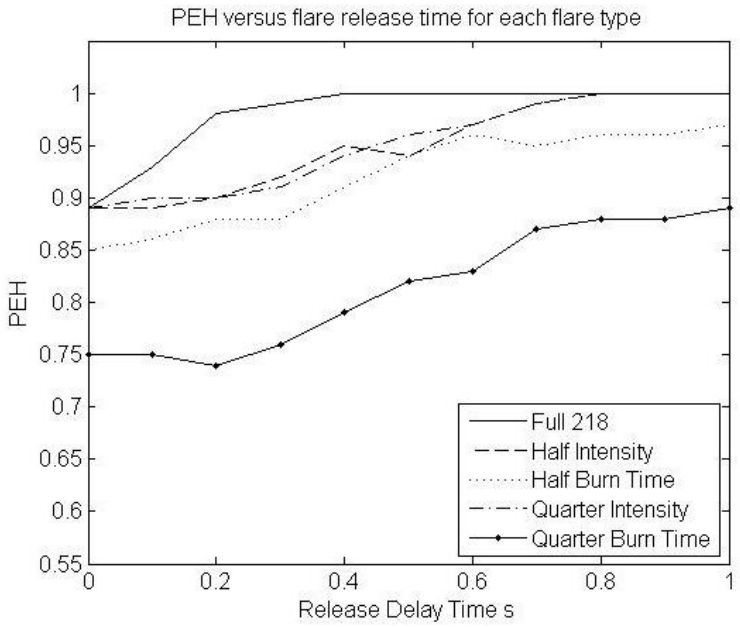

Figure 7-6 The PEH of all flare types for an aircraft altitude of 1km and delayed flare release time.

7.4 Second Generation MANPAD and C130 Model

For the second generation MANPAD and the C130 model the simulations were repeated for an aircraft altitude of 1km and all missile launch ranges and azimuth angles. Full 118 flares were released from t=0s to t=1s in steps of 0.1s from the different dispensers; the results are shown in Figure 7-7.

From Figure 7-7 it appears that firing flares pre-emptively from the side dispensers is the most effective. However, if the data is plotted with regards to aircraft azimuth instead of flare release time then they are only more effective for certain engagements; this is shown in Figure 7-8. The front dispensers perform badly in head-on and tail-on engagements but are effective in any engagement with a crossing rate. The side dispensers perform well in the head-on and tail-on engagements but less well in the regions of aircraft azimuth between 90°-135° and 210°-270°. Interestingly, firing from both sets of

dispensers gives similar results to the front dispensers so releasing more flares seems to be ineffective.

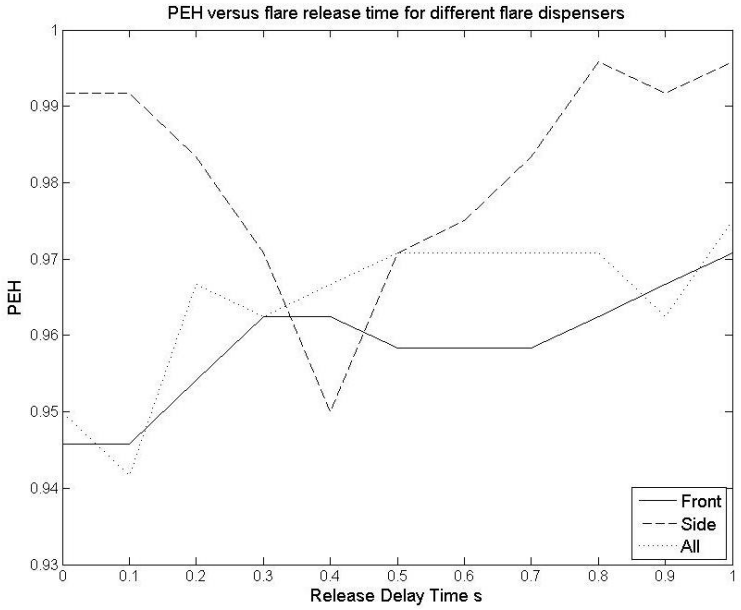

Figure 7-7 PEH versus flare release delay time for different flare dispensers.

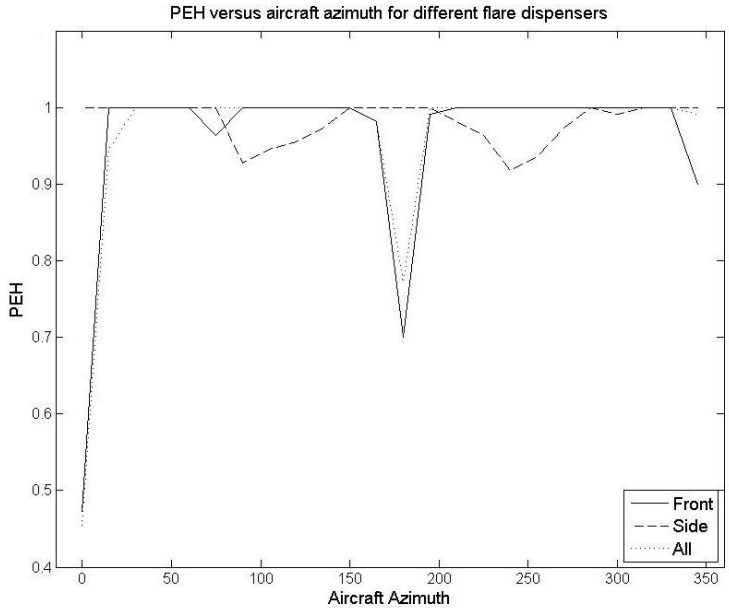

Figure 7-8 PEH versus aircraft azimuth for different flare dispensers.

7.5 Conclusions

For the first generation MANPAD and the AMX-A1 model flares were fired at t=0s for all aircraft altitudes with the simulations repeated for the reduced performance flares. The results for the half intensity and half burn time flares were similar, as were the quarter flares. This was expected given that they have the same total energy. On closer analysis firing flares at t=0s is sometimes a test of the Tracker item which mimics the MANPAD operator.

To study the effect of pre-emptive flares on the IR seeker it was chosen to look at delaying the flare release time from the start of the simulation. This was carried out for an aircraft altitude of 1km as repeating for all altitudes was unfeasible. For a first generation MANPAD and the AMX-A1 model the results showed that delaying flare release until 1s from the start of the simulation improved the PEH for all flare types. This was also the case with a second generation MANPAD and the AMX-A1 model. However, the quarter burn time flare performed much worse due to the larger total FOV of a conscan seeker.

For the C130 model the simulations were repeated for flare release from the front dispensers, side dispensers and both sets of dispensers. When the results are plotted with regard to aircraft azimuth, the side dispensers are generally better in tail-on and head-on scenarios, and the front dispensers are better when there is a crossing rate.

The next chapter looks at comparing pre-emptive flare release with reactive. This is for MANPAD models with and without a track angle bias (TAB) CCM.

8 REACTIVE VERSUS PRE-EMPTIVE FOR AMX-A1 MODEL

This chapter compares reactive with pre-emptive flare deployment against different MANPAD models with and without a CCM capability. The first model (M1) is a first generation MANPAD with an IR spin scan seeker. The second MANPAD model (M2) is a second generation MANPAD with a conscan seeker system. A track angle bias (TAB) CCM is then included in the IR seekers using two different triggers; rise rate and head spin rate(92,93).

8.1 No CCM

In the first set of simulations for each MANPAD model base runs were done where an aircraft altitude of 1km was chosen where the aircraft released no flares. Next, reactive flares were fired at a detection range of 1500m with a half second firing delay for each model with no CCM. In each case there were 240 simulations based on the set of ranges and azimuth angles. PEH is calculated as the fraction of misses in 240 simulations. The results for no flares and reactive flares are shown in Table 8-1. This confirms the effectiveness of reactive flares against a MANPAD with no CCM capability.

Table 8-1 PEH for each MANPAD model for no flares and reactive flares.

	M1	M2
No flares	0.19	0.11
Reactive flares	1.00	1.00

8.2 Track Angle Bias CCM

The two triggers used to initiate the TAB CCM are rise rate and head spin rate (line of sight rate). The levels for the triggers were calculated by running a simulation with flares released reactively and the values logged; in target-levels/s and degrees/s. The results are shown in Figure 8-1 for rise rate and Figure 8-2 for head spin rate with flares showing as spikes at 8.5s. From these

it was decided to set the rise rate at 20 target-levels/s and the head spin rate at 4°/s. The large spikes in the rise rate before 1s are prior to missile launch.

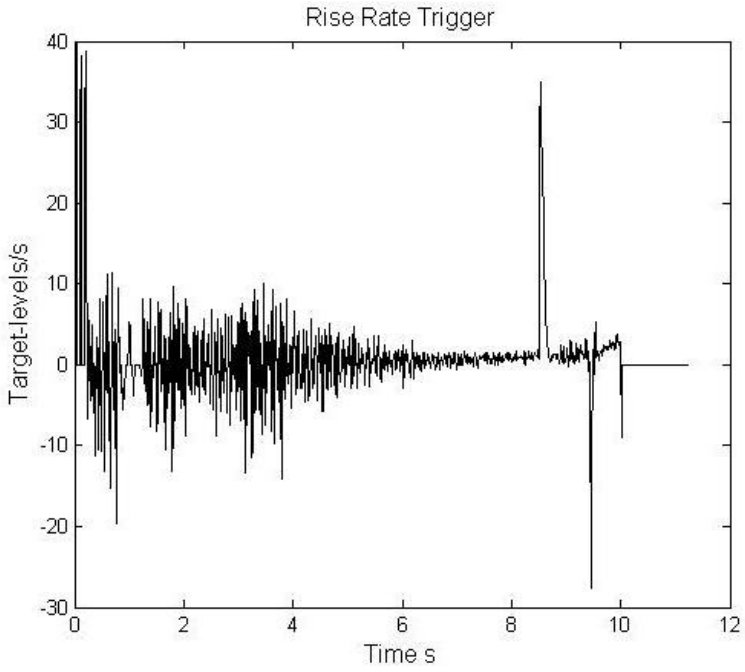

Figure 8-1 Rise rate in target-levels/s.

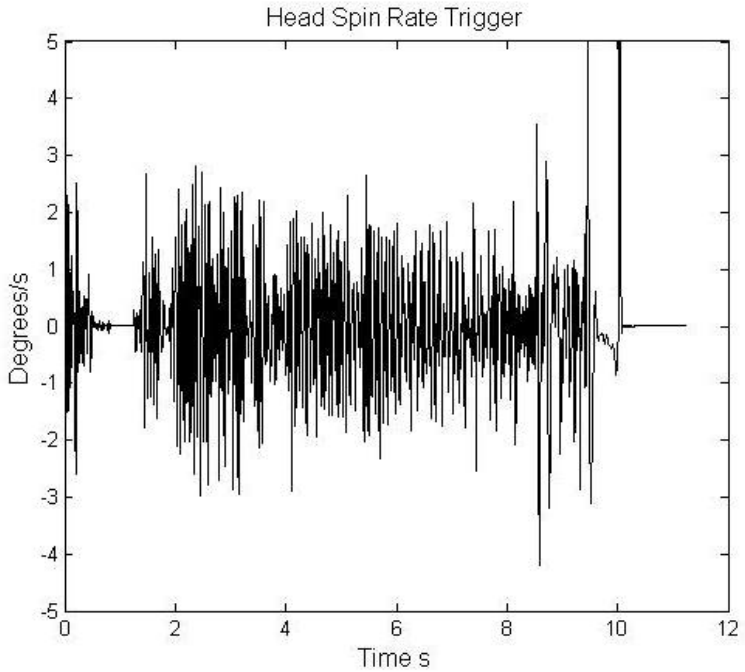

Figure 8-2 Head spin rate in degrees/s.

To investigate the amount of bias needed for the CCM, a range of angles were applied for various durations with the rise rate trigger on after launch. These simulations covered all aircraft azimuths and ranges with the number of hits determining the best combination. The optimum values were found to be a track angle bias of 1^{o} for 0.5s. Table 8-2 shows the PEH for these values of track angle bias and time using each of the two CCM triggers enabled after launch and with reactive flares fired 0.5s after a detection range of 1500m.

Table 8-2 PEH for each MANPAD model with a track angle bias CCM using the rise rate or the head spin rate trigger.

	M1	M2
Rise rate trigger	0.53	0.47
Head spin rate trigger	0.88	0.71

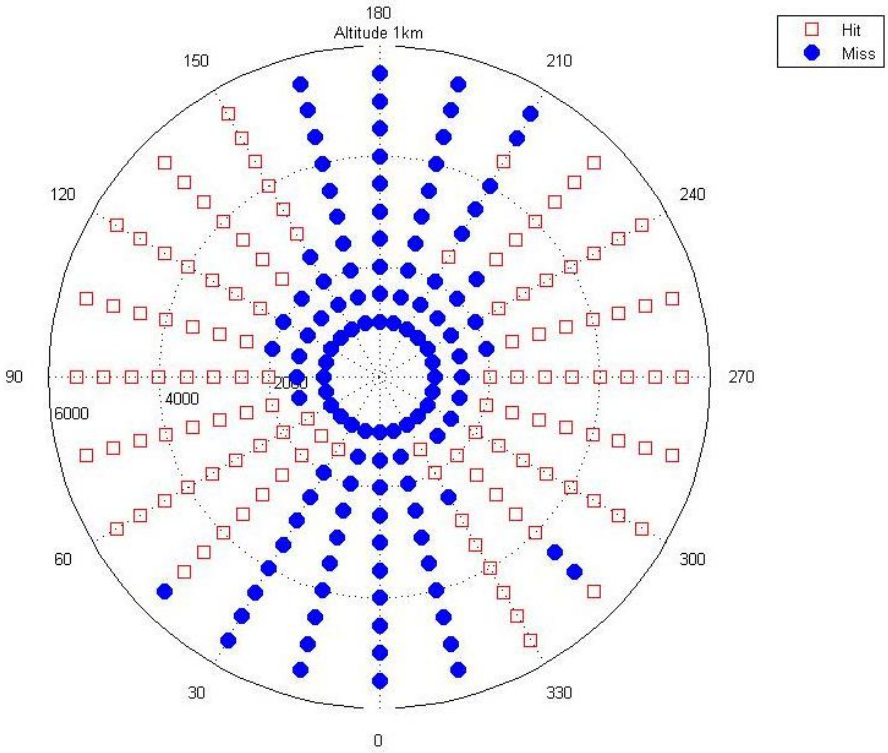

Figure 8-3 Reactive flares fired against M2 with a TAB and rise rate trigger.

The rise rate trigger is more effective achieving hits reflected by the lower PEH because of the more clearly defined spike, seen in Figure 8-1, due to flare release. Therefore, the rise rate was adopted as the trigger in all of the following

simulations. Figure 8-3 shows a wheel plot of model M2 with a TAB and rise rate trigger. The consequence of the CCM can be seen in the engagements with a crossing rate as they result in a hit and the reactive flares are ineffective. Reactive flares still work in tail-on and head-on scenarios against a TAB CCM as expected because of the slower separation rate in these geometries.

The next set of simulations looked at the use of pre-emptive flares by varying the flare release time from t=0s to t=2s in steps of 0.2s. Table 8-3 shows the PEH for the two MANPAD models with the rise rate trigger active from uncaging.

Table 8-3 PEH for each MANPAD model with different flare release times.

Release Delay	0.0	0.2	0.4	0.6	0.8	1.0	1.2	1.4	1.6	1.8	2.0
M1	0.84	0.92	0.71	0.72	0.80	0.88	0.98	1.00	0.99	1.00	1.00
M2	0.45	0.46	0.55	0.72	0.81	0.90	0.80	0.63	0.92	0.88	1.00

Table 8-3 suggests that flare release around 1-2s after simulation start offers greater protection to the aircraft compared to reactive flares (PEH values of 0.53 for M1 and 0.47 for M2).

Since the PEH results in Table 8-3 are from a set of 24 azimuth angles, a smaller set of engagements was chosen to further investigate specific azimuth angles and the flare release time. The aircraft was positioned at an altitude of 1km and a range of 2km and the aircraft azimuth varied from tail on at 0^{o} to 135° in steps of 45°. Flares were released in half second intervals from the start of the simulation. Figure 8-4 shows the miss distances versus flare release times for different aircraft azimuths and the 2 MANPAD models. M1 has no CCM and the simulations with M2 were repeated for no CCM and with a TAB of 1° for 0.5s and a rise rate trigger active after launch.

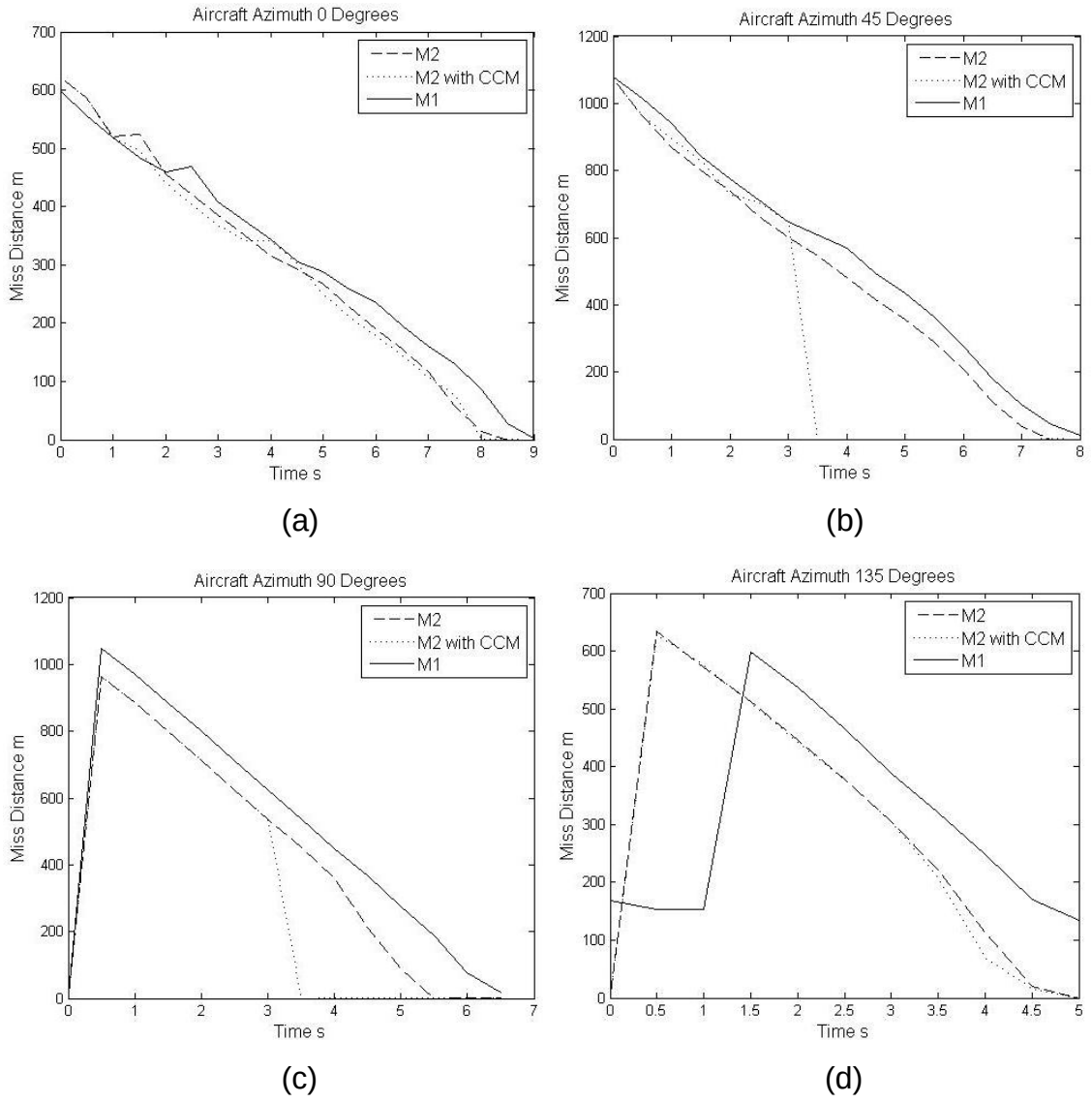

Figure 8-4 Miss distance versus flare release time for aircraft azimuth of (a) 0°, (b) 45°, (c) 90° and (d) 135°.

The tail on azimuth results, Figure 8-4 (a), show a linear decrease in miss distance with flare release time. This is not surprising because there is little angular separation of the flare and the aircraft and the track angle bias has no effect. At an azimuth of 45° the CCM has an effect and flare release after 3s is too late, shown by the dotted line in Figure 8-4 (b). At 90° azimuth, Figure 8-4 (c), it is apparent in all cases that release at t=0 is too early but for M2 with the CCM flare release after 3.5s is too late. At 135°, Figure 8-4 (d), M1 misses without flares due to the low gimbal rates and M2 with and without the CCM perform similarly.

Further results were produced at the 4 azimuth angles - 0°, 45°, 90° and either 105° or 135° depending on the line of sight distance; 105° for the shorter engagements and 135° for the longer engagements. A set of simulations was carried out at each azimuth angle with parameters derived by setting a constant slant range and using different aircraft altitudes, starting at 300m and increasing at 100m intervals, Figure 8-5. The MANPAD elevation angle was calculated for each aircraft height and a 60° limit was applied. This therefore confined the set of aircraft altitudes and the number of simulations at each azimuth angle.

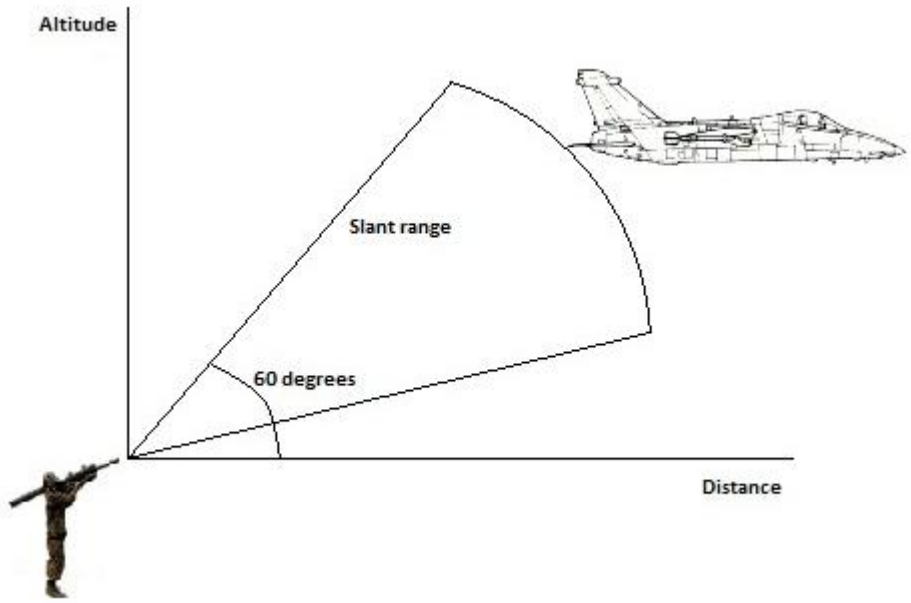

Figure 8-5 Scenario for simulations with a constant slant range.

PEH was again evaluated based on the 2m miss distance criterion. This was done for slant ranges of 2km, 3km and 4km with M2 using a track angle bias of 1° for 0.5s and a rise rate trigger active after launch. For the slant range of 2km the maximum aircraft azimuth was 105° because the shorter engagements at 135° resulted in a miss even when no flares were released due to the increase demand on the rate of turn. A set of simulations was carried out as a reference set where M2 had no CCM capability; the results are shown in Figure 8-6. The results for M2 with the CCM in use and at slant ranges of 2km, 3km and 4km are shown in Figure 8-7 and Figure 8-8.

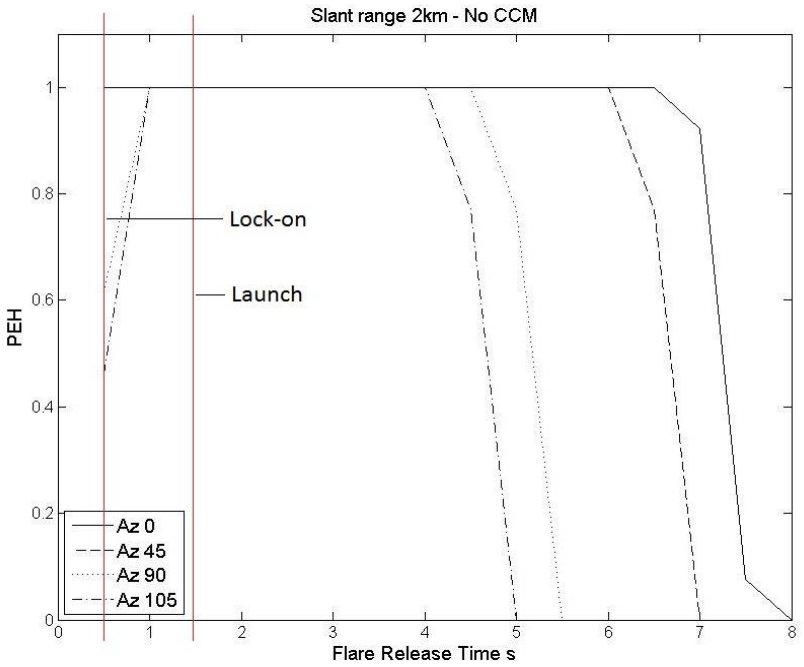

Figure 8-6 PEH versus flare release time for a slant range of 2km with no CCM.

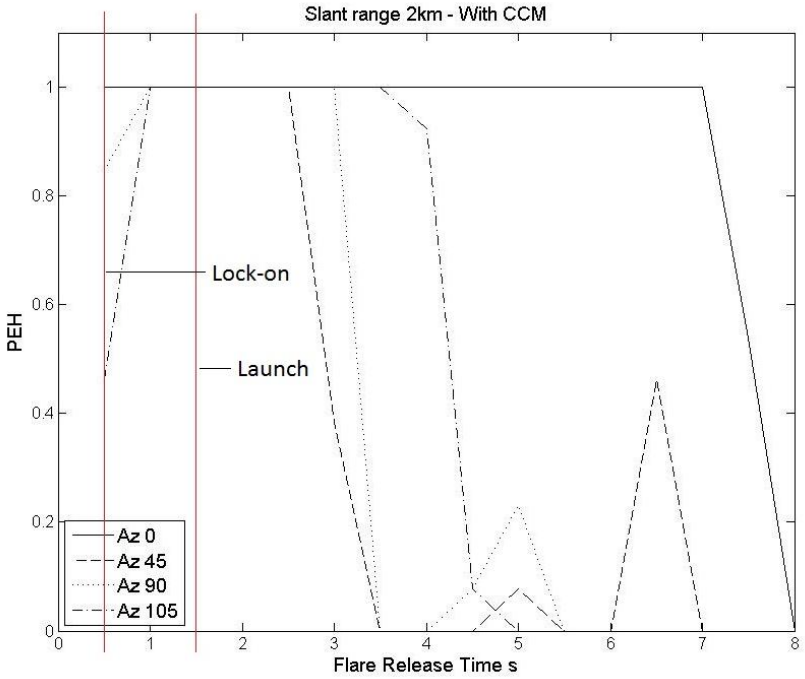

Figure 8-7 PEH versus flare release time for a slant range of 2km with CCM.

In Figure 8-6 at 0° azimuth and with no CCM there is a period from 1s to 6.5s where PEH=1. This period includes the half second prior to missile launch. At 45° the period is reduced to a 5s interval and is shortest at 105° azimuth. This is due to the geometry of the engagement resulting in a shorter missile flight time.

In Figure 8-7 the introduction of the CCM has no significant effect on the 0° azimuth result but narrows the interval where PEH=1 for the other 3 cases. Interestingly, the 45° and 105° azimuths have changed position with respect to the 90° result. The 105° azimuth is approaching so a TAB applied at a faster rate may be needed for this angle and short distance. However, this will cause the 45° and 90° azimuths to push ahead too much and loose the target from the FOV. This illustrates the compromise in designing a TAB CCM if it assumed that the crossing rate of the target is unknown. The interval where PEH=1 for the 45° azimuth is reduced from 5s to 1.5s; this covers the half second prior to missile launch and the first second after. The first second after missile launch includes the half second ignition delay and the half second boost thrust. Flare release after 2.5s will likely be ineffective and the engagement will result in a hit. The spikes in the PEH at 5s and 6.5s are due to near misses. For near misses the miss distances are less than 10m and if a greater hit/miss criterion was used the PEH would be zero.

Figure 8-8 shows the results for a slant range of (a) 3km and (b) 4km. The longer distances means the flare release times are extended to 12s and 14s respectively. With the longer slant ranges the 1.5s interval where the PEH is 1 irrespective of aircraft azimuth is still present. Again, it covers the half second prior to missile launch and the first second after. The results for azimuths 90° and 135° are similar for both slant ranges with flare release after 2.5s too late. In contrast to the 2km slant range the 45° azimuth has a longer interval where the PEH=1. Again, this is due to the values of the TAB CCM. For longer slant ranges and 45° azimuth there is less separation between the aircraft and flares when the flares are released earlier in an engagement. Increasing the time the TAB is applied for would help loose the flares from the FOV but will also influence the results for the 90° and 135 azimuths°.

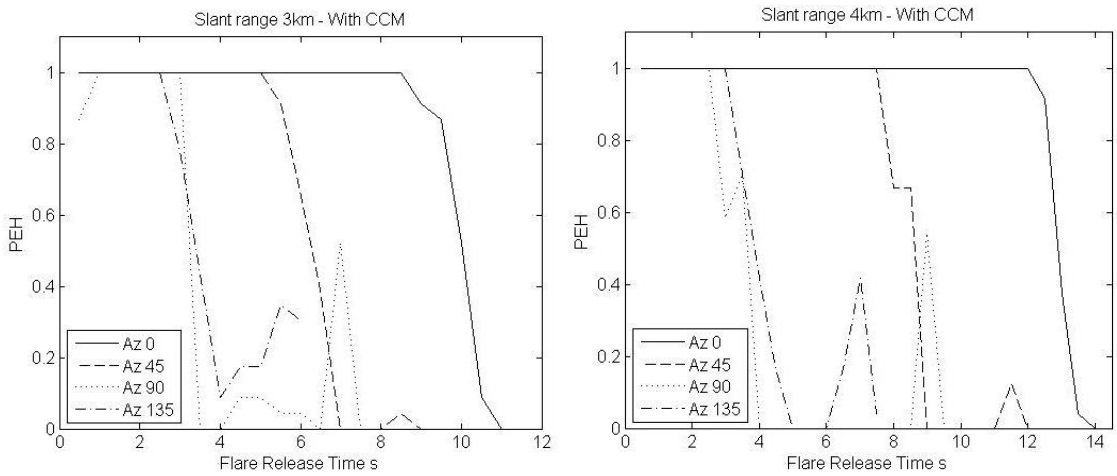

(a) (b)

Figure 8-8 PEH versus flare release time for a slant range of 3km and 4km with CCM.

As in the simulations two flares are fired, one from each side of the aircraft, this represents a symmetrical situation. To see if the model agrees, by producing symmetrical results, one slant range of 3km was chosen and a single flare was fired, first from the left side for all the simulations then repeated for the right side. The results are shown in Figure 8-9 for the left side and Figure 8-10 for the right side. MANPAD model M2 was used with a track angle bias CCM and rise rate trigger.

The results are not identical, showing slight differences in the PEH. A single flare fired from the right side gives lower PEH when there is a crossing rate between aircraft and missile, e.g. azimuths 45°, 90° and 135°. However, as the electro-optical system modelled in the IR seeker has inherent asymmetry, rotation of the reticle or optics counter-clockwise, slight differences are expected.

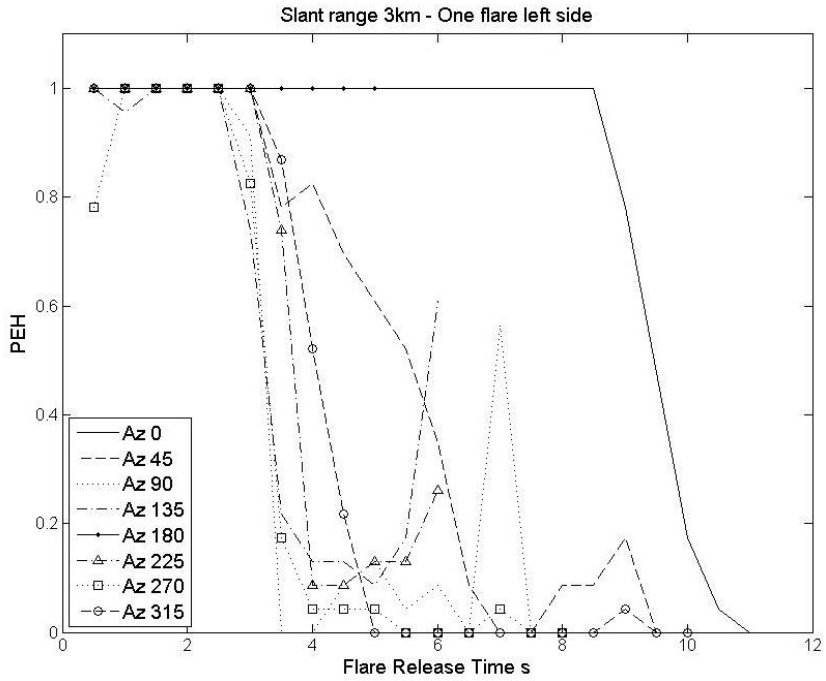

Figure 8-9 PEH versus flare release time for slant range of 3km and one flare fired from the left side .

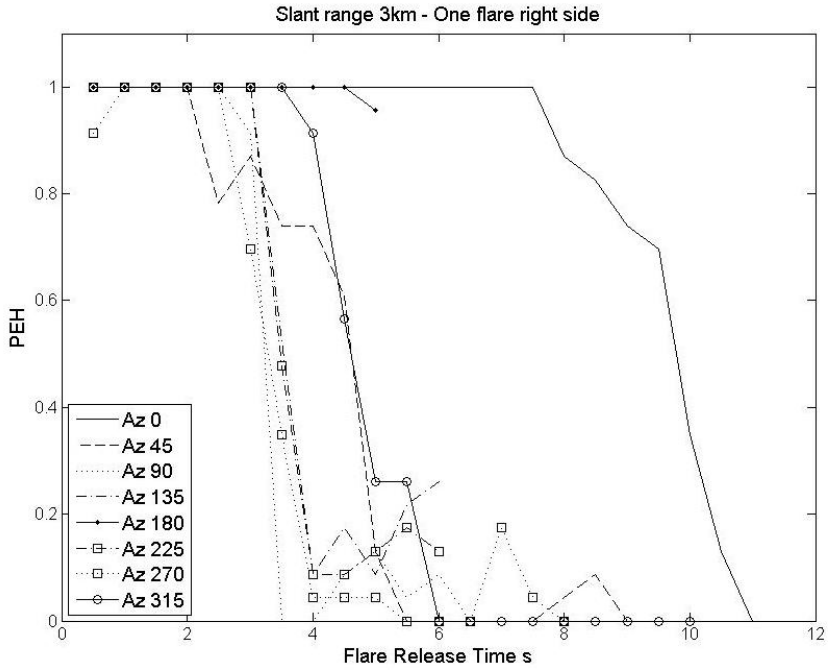

Figure 8-10 PEH versus flare release time for slant range of 3km and one flare fired from the right side .

8.3 Reduced Flares

The simulations were repeated for the scenarios with constant slant ranges and with the reduced flare models. MANPAD model M2 was used with a track angle bias CCM and a rise rate trigger active after launch. This is because M2 with the TAB CCM gave the lowest values for the PEH and it was chosen to test the IR countermeasures against the best MANPAD model. The results for slant ranges 2km, 3km and 4km are shown in Figure 8-11, Figure 8-12 and Figure 8-13 respectively.

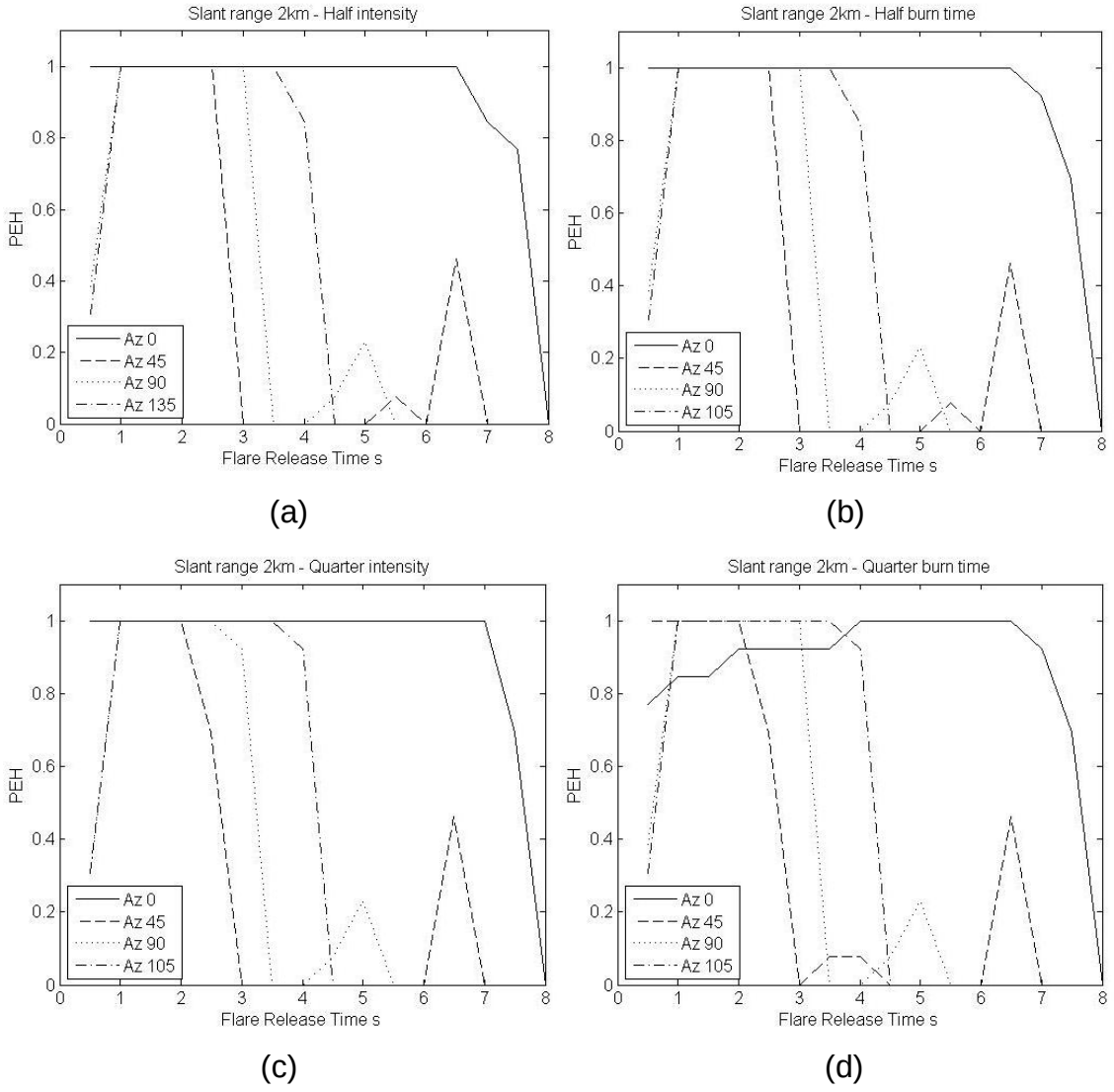

Figure 8-11 PEH versus flare release time for a slant range of 2km and reduced flare models.

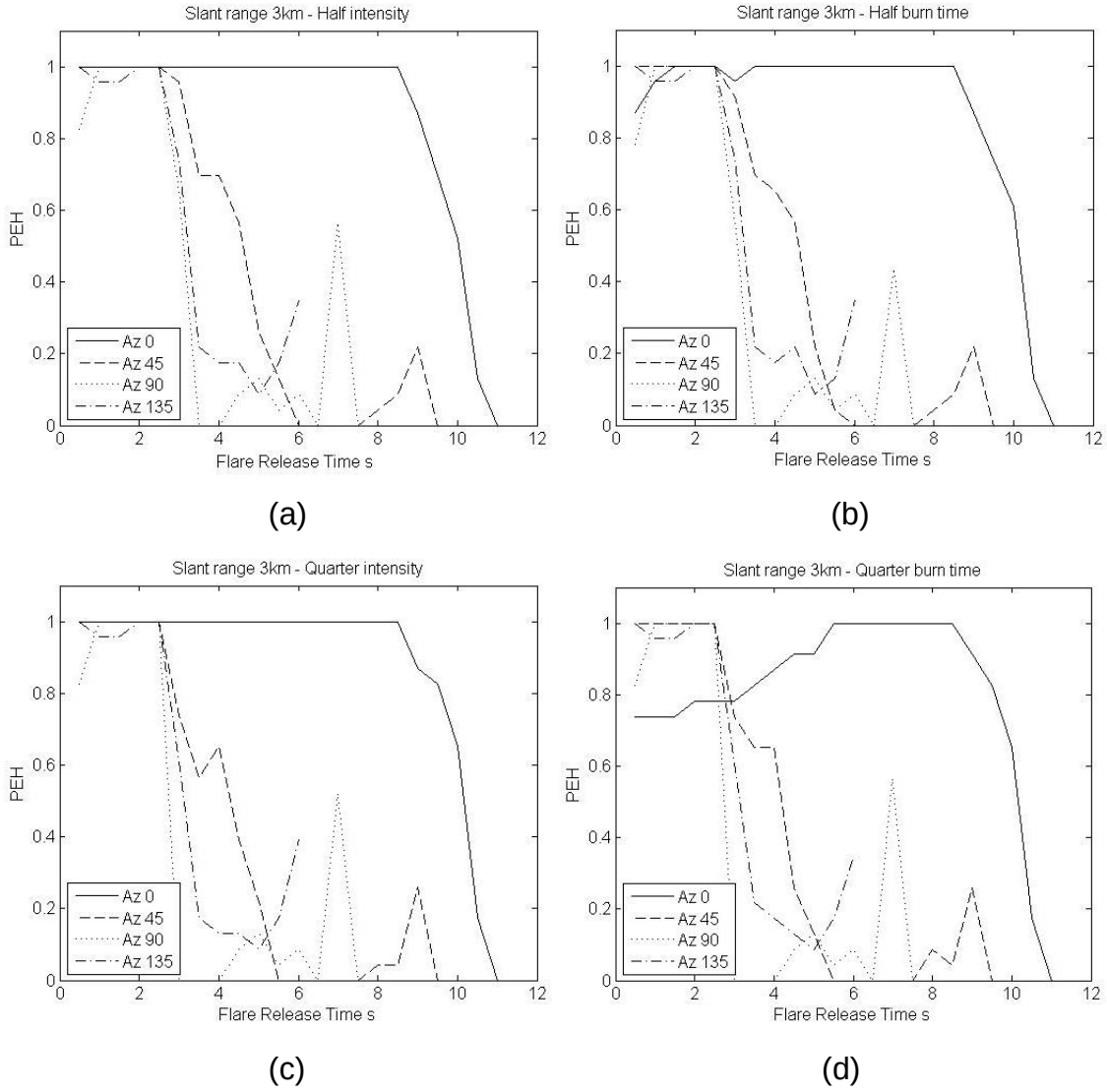

Figure 8-12 PEH versus flare release time for a slant range of 3km and reduced flare models.

For a slant range of 2km the reduced intensity flares, Figure 8-11 (a) and (c), give similar results to the standard 218 flare, Figure 8-7. The 1.5s interval where the PEH=1 irrespective of aircraft azimuth is still present and covers the flare release time of 1-2.5s. This is also the case for the half burn time flare, Figure 8-11 (b). However, for the quarter burn time flare, Figure 8-11 (d), the PEH is less than 1 for the tail-on engagement (0°) in that 1.5s interval. For 0° azimuth the quarter burn time flares still give a PEH=1 if they are released later in the simulation, between 4s and 6s.

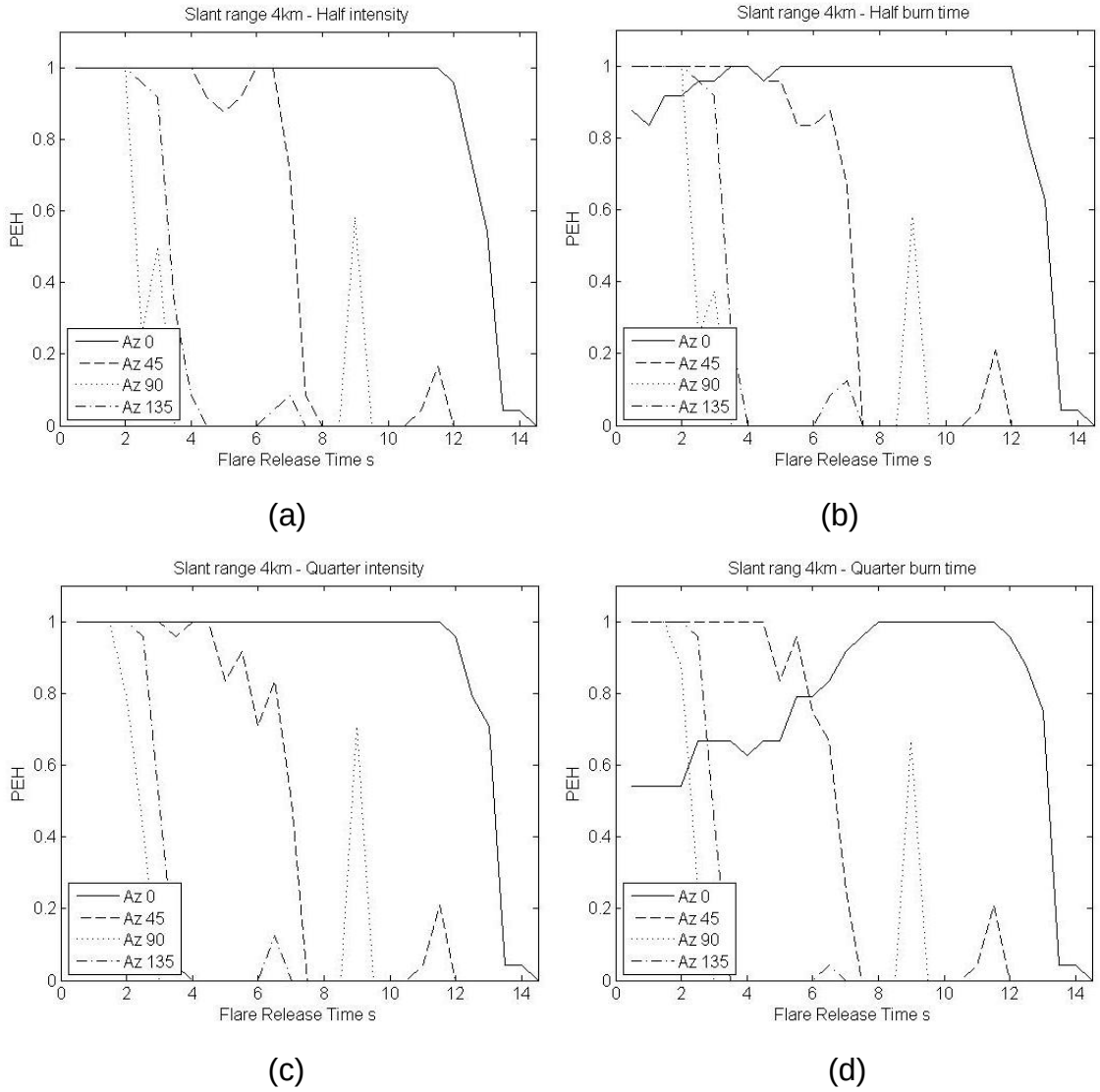

Figure 8-13 PEH versus flare release time for a slant range of 4km and reduced flare models.

For a slant range of 3km the half flares and quarter intensity flare, Figure 8-12 (a) (b) and (c), all show similar results for each aircraft azimuth. Again, the quarter burn time flare, Figure 8-12 (d), shows a reduced PEH for 0° azimuth in the 1.5s interval covering the half second prior to missile launch and the first second after.

For the 4km slant range the reduced intensity flares, Figure 8-13 (a) and (c), show similar results for each aircraft azimuth. The quarter burn time flare, Figure 8-13 (d), has a PEH of just above 0.5 for the 1.5s interval which is

reducing at longer slant ranges. At the longer distance of 4km the half burn time flare, Figure 8-13 (b), also shows a reduced PEH in the 1.5s interval.

8.4 Conclusions

Two MANPAD models, a first generation and second generation, were fired at the fast jet model releasing against reactive flares. This confirmed the effectiveness of reactive flares against MANPADs without a CCM capability. A TAB CCM was then included in the MANPAD models and two triggers were tested. The rise rate trigger performed better as the rise rate showed a clear increase upon flare release. Therefore, this trigger was chosen to use with the TAB CCM.

The timing of flare release was then investigated by releasing flares throughout an engagement. The simulations showed that flares have to be fired in a 1.5s interval covering the half second before missile launch and the first second after to maintain a PEH=1 irrespective of aircraft azimuth.

For the reduced intensity flares the interval was still present but not for the half burn time flare at a slant range of 4km and not for the quarter burn time flare at all slant ranges. This was due to a reduced PEH in the tail-on engagements. However, PEH=1 is achieved for the reduced burn time flares if they are released later in the engagement. For engagements with a crossing rate releasing the flares later in the simulation will considerably reduce the PEH.

9 REACTIVE VERSUS PRE-EMPTIVE FOR C130 MODEL

This chapter compares reactive with pre-emptive flare deployment against a second generation MANPAD model (M2) with and without a TAB CCM capability for the C130 aircraft model. The first simulations look at reactive flare release from different dispensers then a TAB CCM is optimised for the C130 model to see the effect on reactive flare deployment. Finally, flares are released throughout an engagement with the simulations repeated for reduced performance flares.

9.1 No CCM

The first simulations compared no flare release with reactive flare release from the front and side dispensers against MANPAD model M2. An aircraft altitude of 1km was chosen using all missile ranges and aircraft azimuths; this gives the PEH out of 240 simulations (10 ranges x 24 azimuths). Reactive flares were released at a detection range of 1500m. The results are shown in Table 9-1 confirming the effectiveness of flares against MANPADs without a CCM capability.

Table 9-1 PEH for no flares and reactive flares.

	No Flares	Reactive Flares (Dispensers)	
		Front	Side
PEH	0.05	1.00	1.00

9.2 Track Angle Bias CCM

For the C130 model the parameters have been adjusted for the TAB CCM to take into account the slower moving target and the 118 flare. Again, test simulations were carried with the best values found to be a rise rate trigger of 15 target-levels/s and a TAB of 0.6° for 0.5s. Using these parameters the simulations were repeated where reactive flares are released from the front and side dispensers; the results are shown in Figure 9-1 and Figure 9-2 respectively.

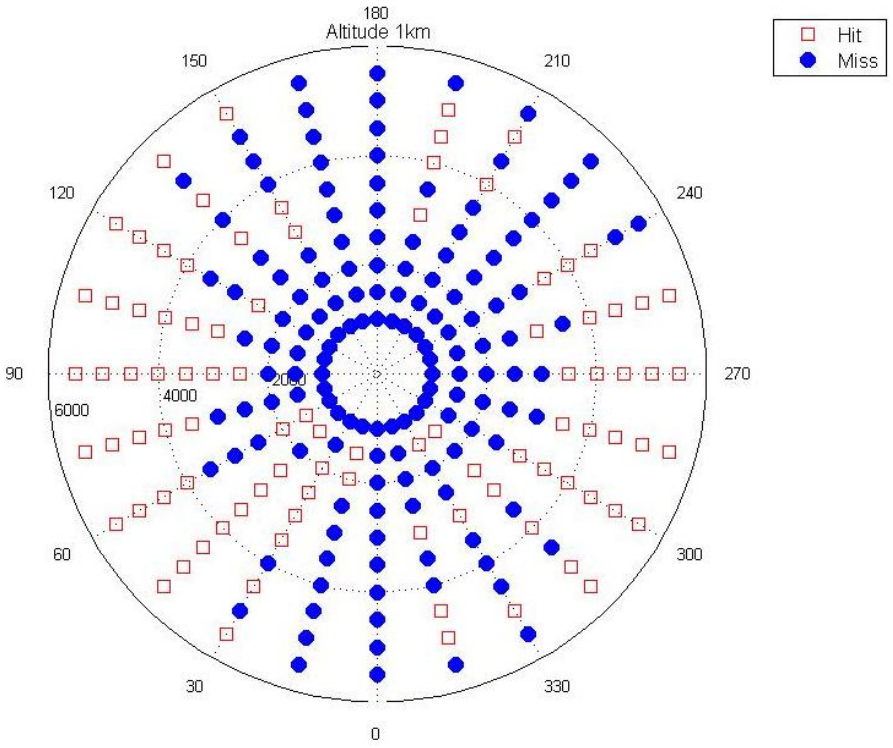

Figure 9-1 Reactive flares released from the front dispensers.

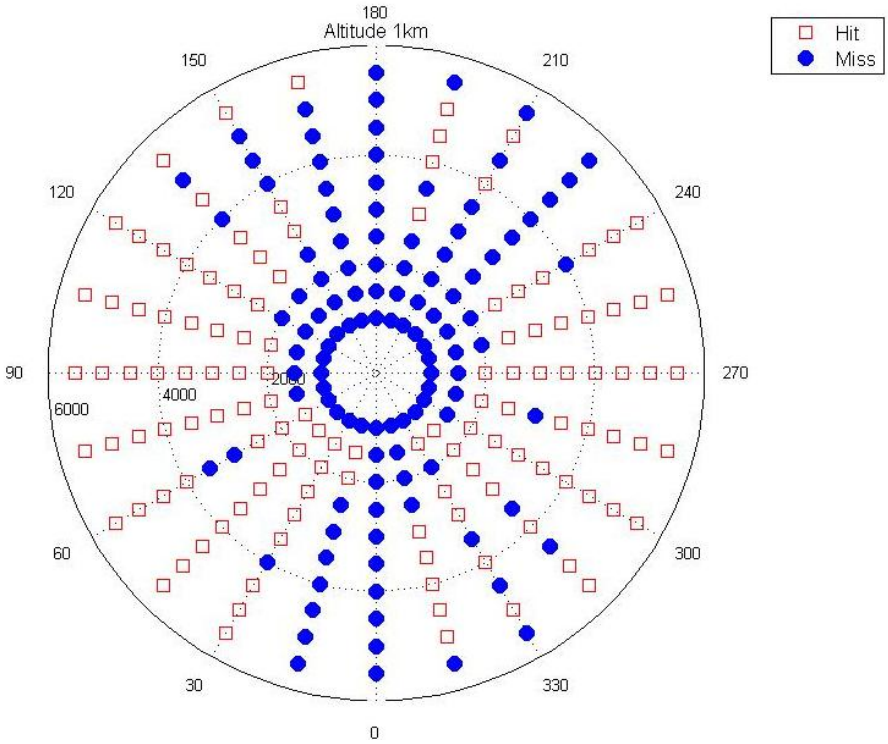

Figure 9-2 Reactive flares released from the side dispensers.

The PEH is reduced from 1.00 to 0.61 for the front dispensers and from 1.00 to 0.48 for the side dispensers. The two sets of dispensers show similar results in the tail-on and head-on aspects but the front dispensers produce fewer hits in beam-on engagements where there is a crossing rate. This is due to the ejection angle of the front dispensers giving a reduced separation rate between the aircraft and flares. Therefore, there is a greater chance of the flares still being in the FOV when the TAB is cleared.

The next simulations looked at scenarios with a constant slant range and flares released at 0.5s intervals throughout an engagement up to the hit point. The results for a constant slant range of 2km are shown in Figure 9-3 where the simulations are repeated for the front, side and all dispensers. Figure 9-3 (a), (c) and (e) are for no CCM in the MANPAD model and (b), (d) and (f) are for the TAB CCM included. The inclusion of the CCM shortens the window where the PEH=1 irrespective of aircraft azimuth.

For tail-on engagements, 0°, the front dispensers perform worst than the side dispensers; shown by the PEH being less than 1 for more flare release times. Using both sets of dispensers gives similar results to the front dispensers, meaning releasing more flares in not necessarily effective. For engagements with a crossing rate, azimuths 45°, 90° and 135°, the TAB CCM reduces the PEH for flare release after 3s from the start of the simulations.

The simulations were repeated for slant ranges of 3km and 4km for flare release from the front and side dispensers against the MANPAD model with a TAB CCM. The results are shown in Figure 9-4. For any engagement with a crossing rate, azimuths 45°, 90° and 135°, they again show that flare release after 3s is too late. This indicates that against a MANPAD with a TAB CCM flares have to be released within 1.5s of missile launch irrespective of the distance between the MANPAD and target.

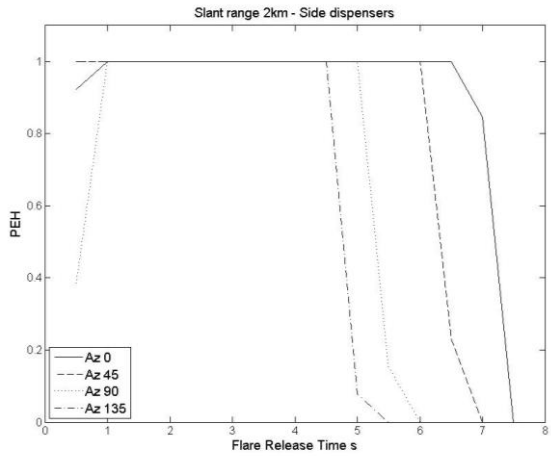

(a)

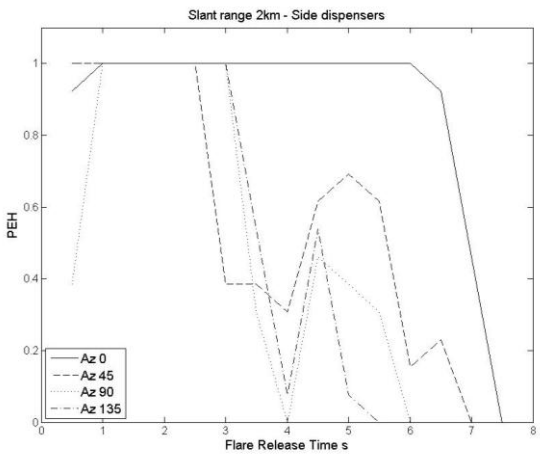

(b)

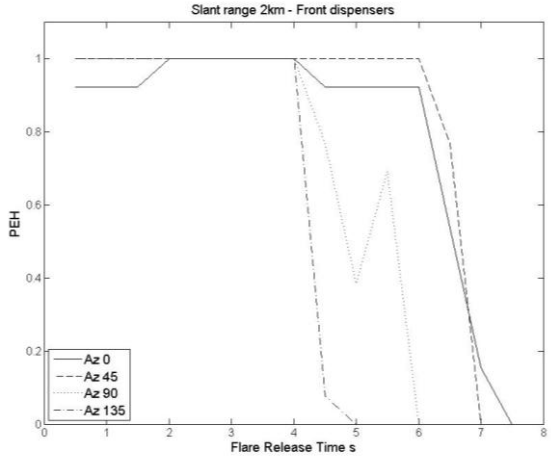

(c)

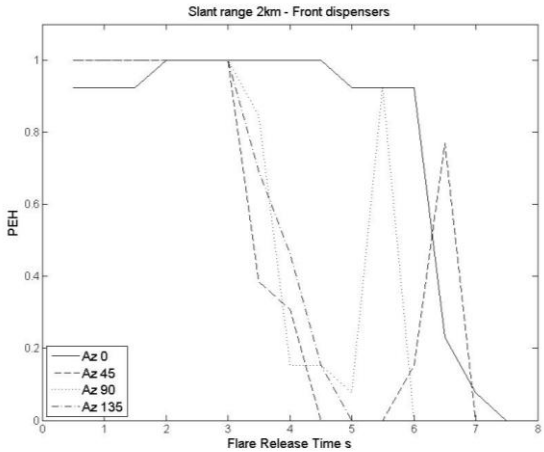

(d)

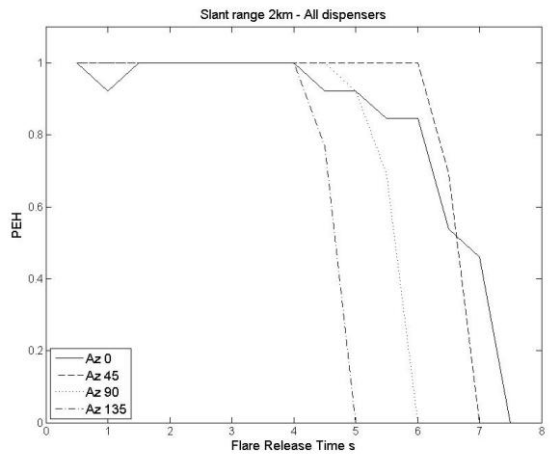

(e)

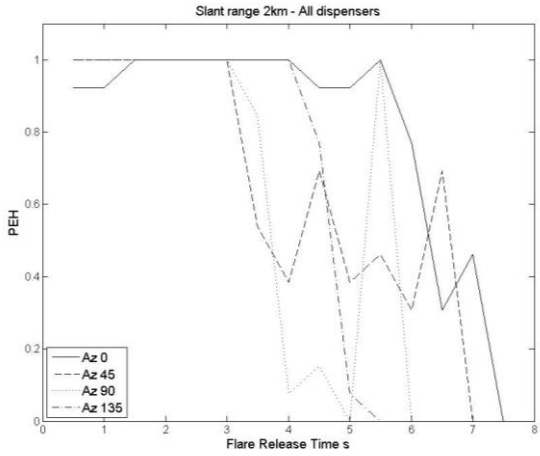

(f)

Figure 9-3 PEH versus flare release time for the side, front and all dispensers.

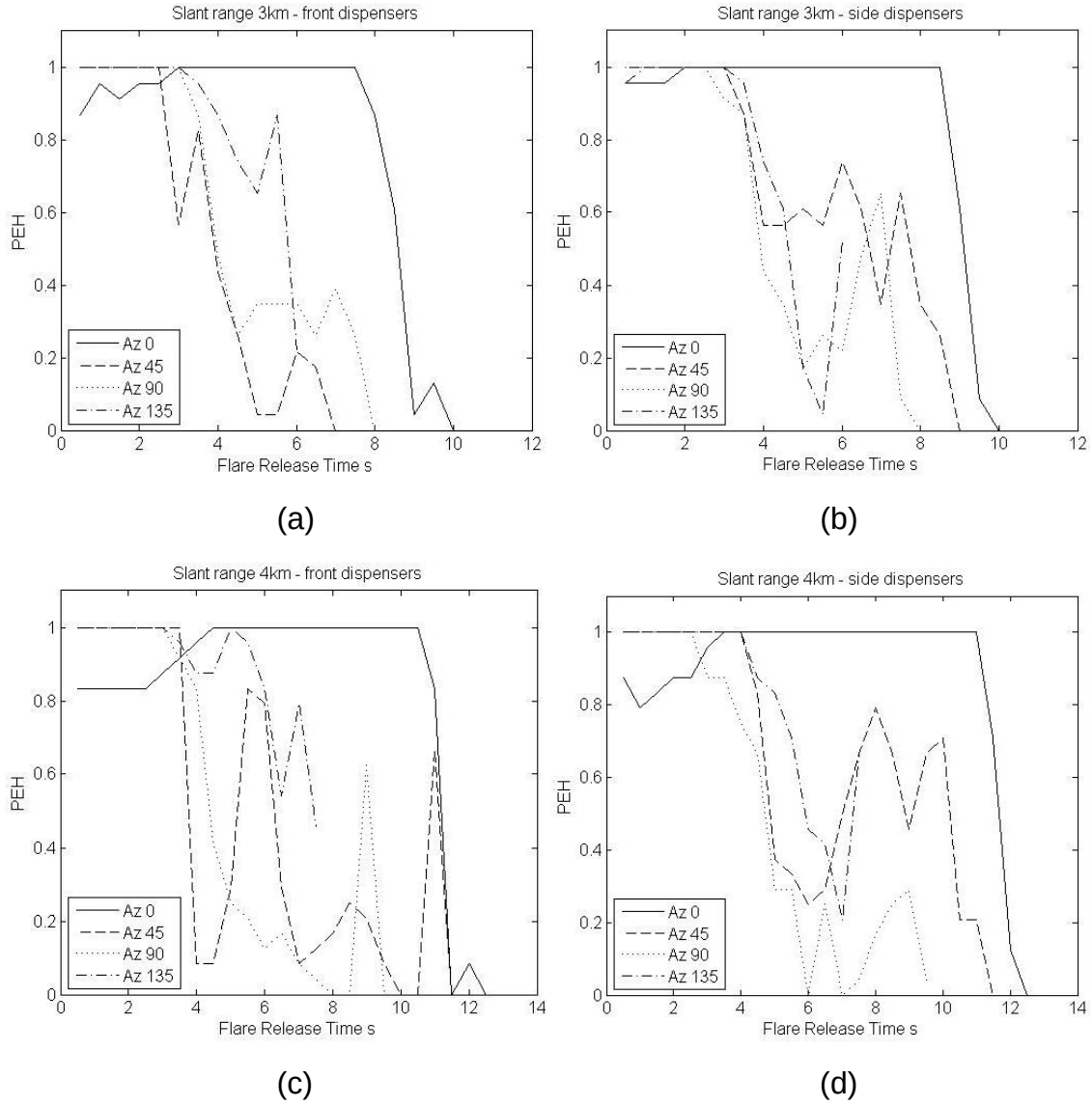

Figure 9-4 PEH versus flare release time for slant ranges 3km and 4km.

9.3 Reduced Flares

The simulations with constant slant ranges of 2km, 3km and 4km were repeated for the flares with reduced performance. They were half intensity, half burn time, quarter intensity and quarter burn time; all in relation to the standard 118 flare. In the first instance no TAB CCM was included in the MANPAD model for a slant range of 2km with flares released from the front and side dispensers. The results are shown in Figure 9-5 and Figure 9-6 respectively.

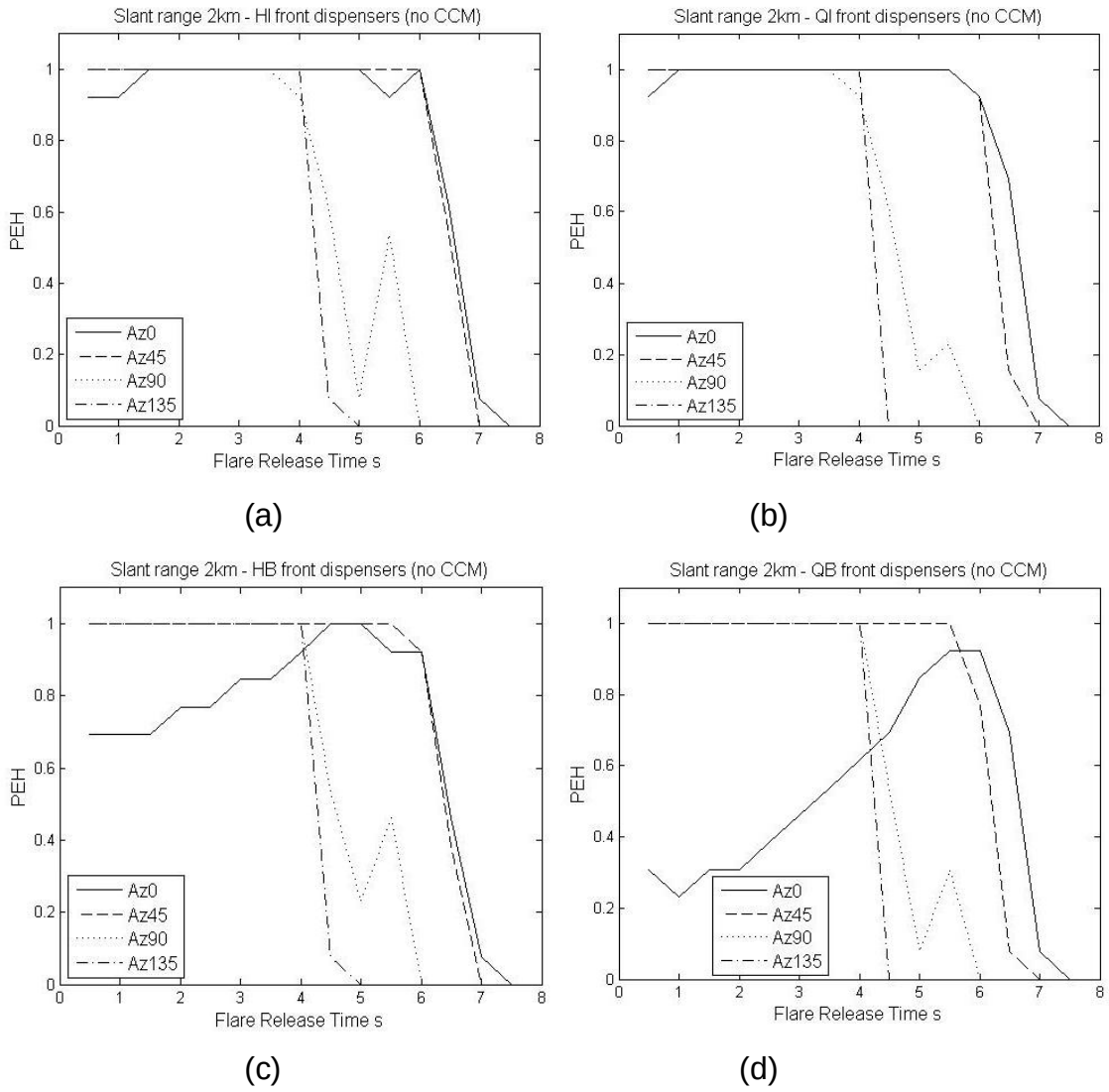

Figure 9-5 PEH versus flare release time for a slant range of 2km with flares released from the front dispensers.

The results for the front dispensers show that the reduced burn time flares, Figure 9-5 (c) and (d), perform worse in tail-on engagements if they are released too early. For all other aircraft azimuths the four reduced flare types give similar results to each other and the full118, Figure 9-3 (c). Again, for the side dispensers the reduced burn time flares, Figure 9-6 (c) and (d), perform worse in tail-on engagements but have a higher PEH than the front dispensers. The results for all other aircraft azimuths are similar for each flare type and also when compared to the full 118, Figure 9-3 (a).

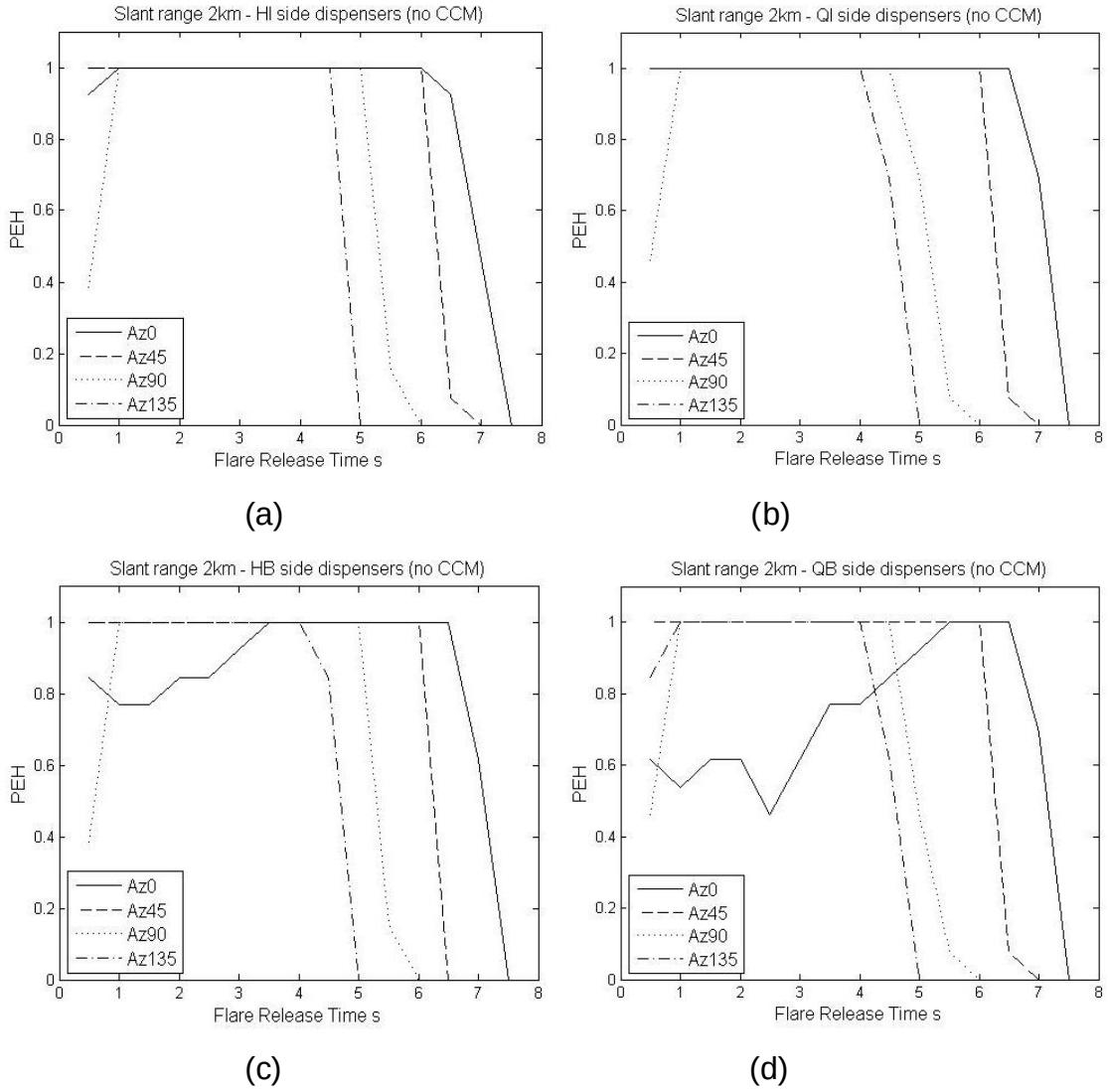

Figure 9-6 PEH versus flare release time for a slant range of 2km with flares released from the side dispensers.

The next simulations included a TAB CCM in the MANPAD model and repeated the scenarios with a constant slant range for each flare type using the front and side dispensers. The results for the half intensity, half burn time, quarter intensity and quarter burn time are shown in Figure 9-7, Figure 9-8, Figure 9-9 and Figure 9-10 respectively.

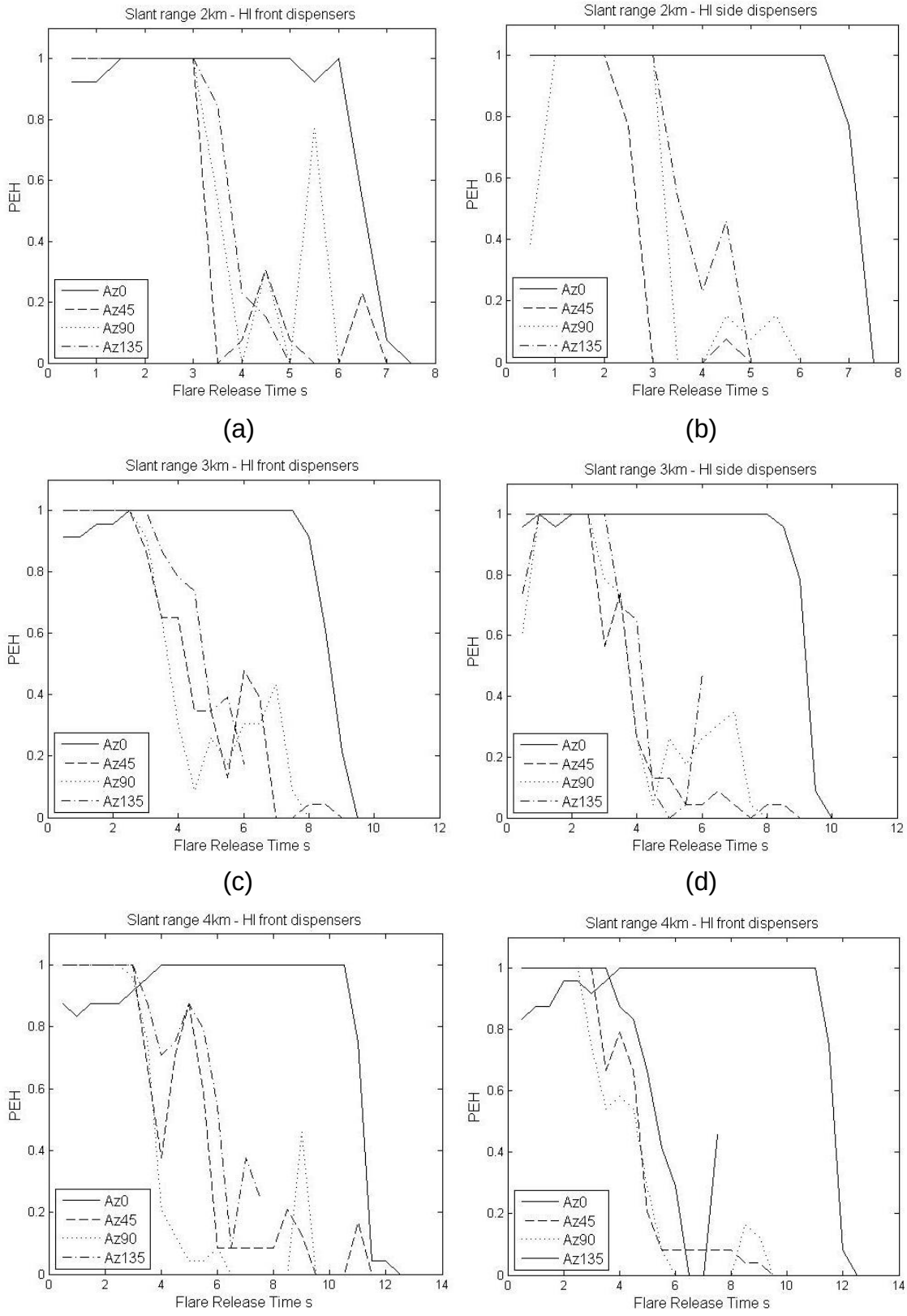

Figure 9-7 PEH versus flare release time for the half intensity flare.

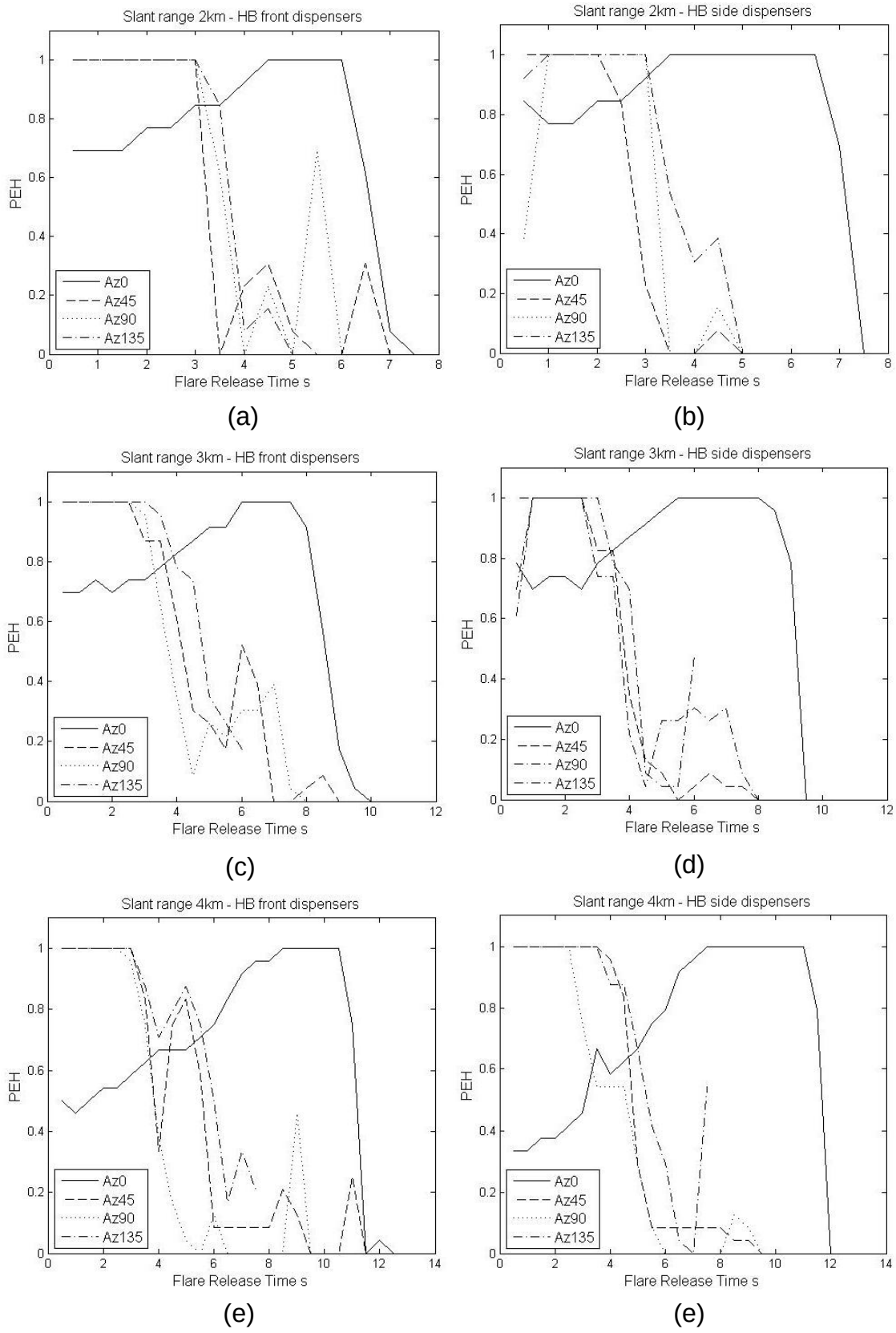

Figure 9-8 PEH versus flare release time for the half burn time flare.

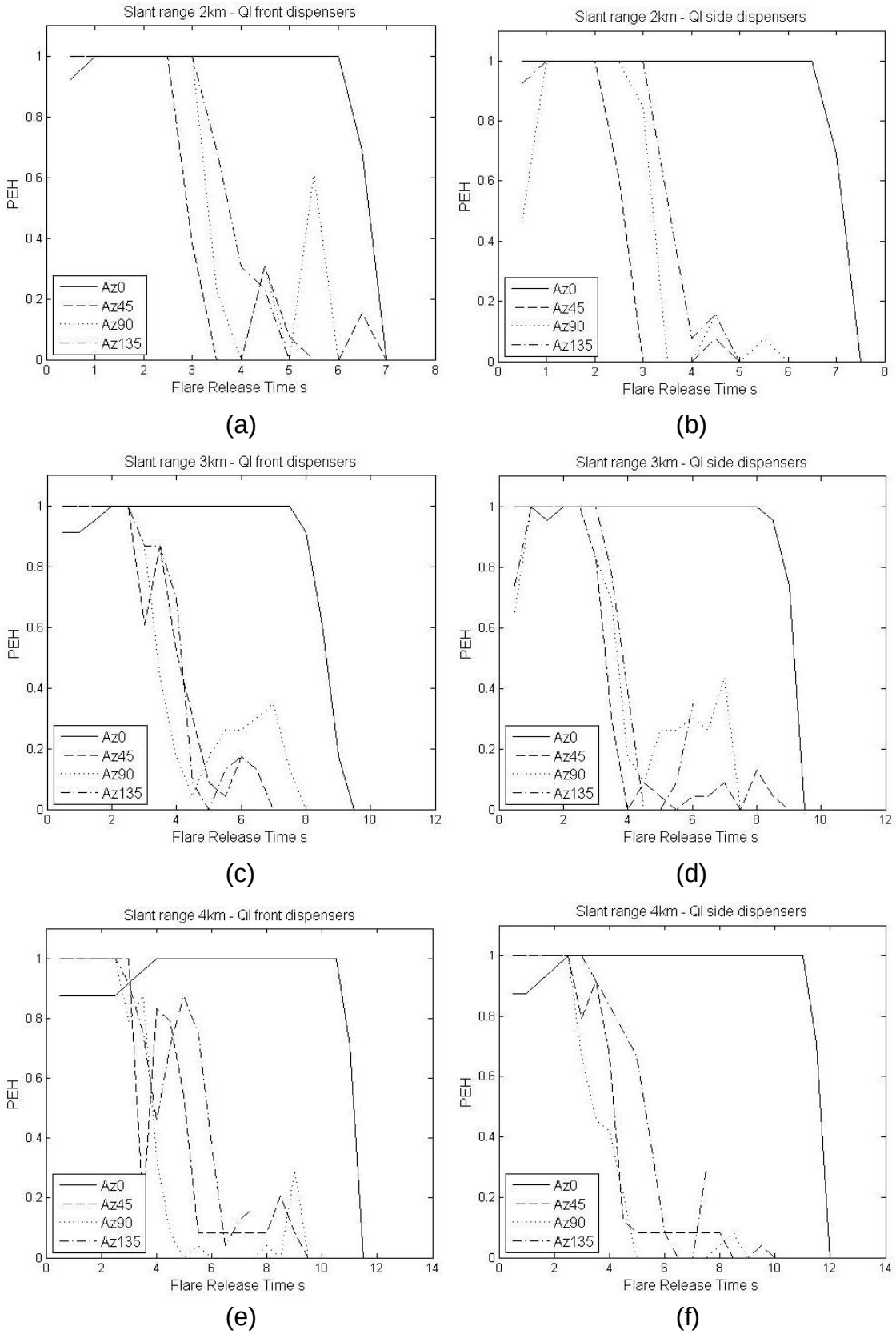

Figure 9-9 PEH versus flare release time for the quarter intensity flare.

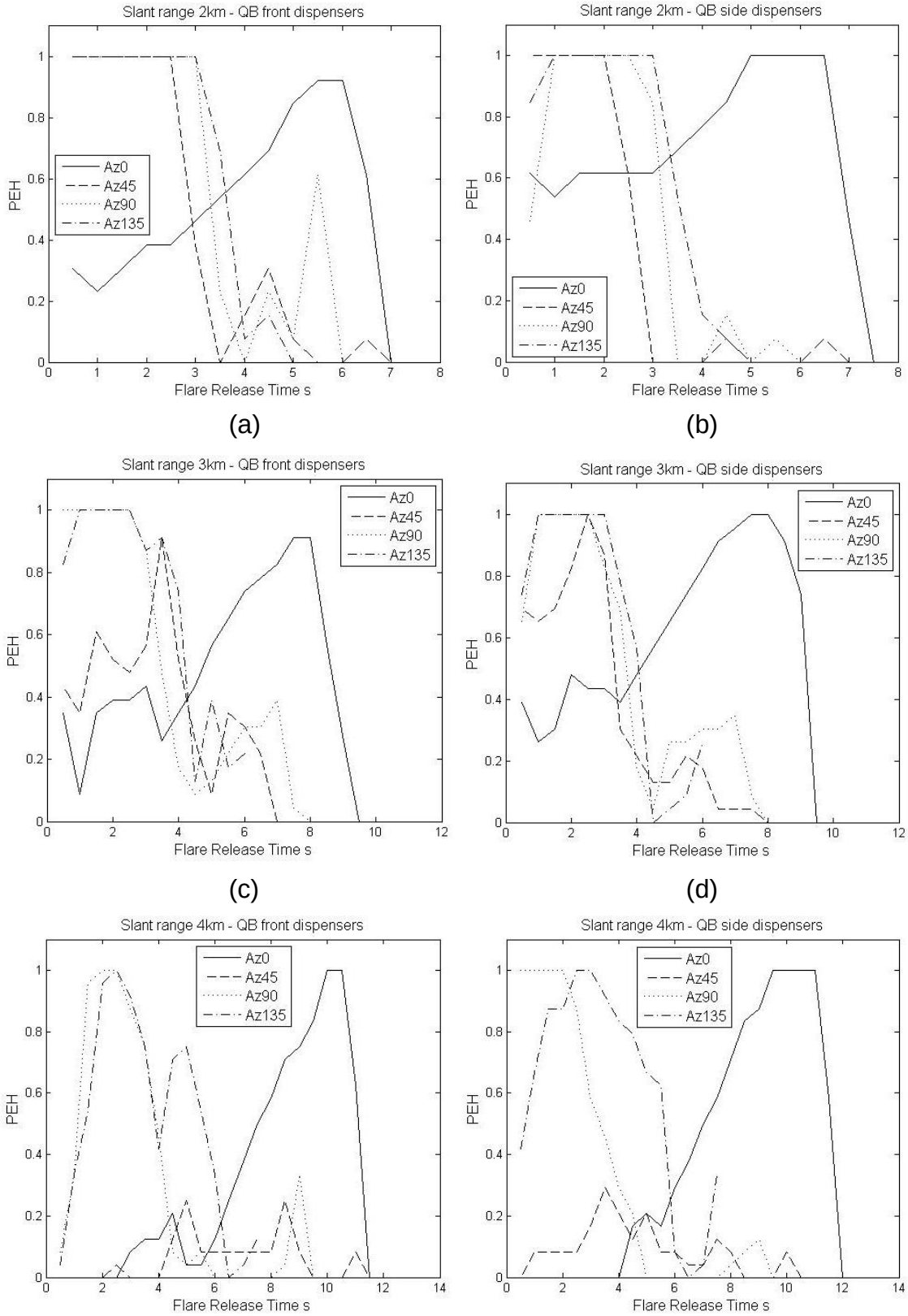

Figure 9-10 PEH versus flare release time for the quarter burn time flare.

The reduced intensity flares, Figure 9-7 and Figure 9-9, give similar results to the standard 118 flare Figure 9-4. Again they show that flare release after 3s is too late for any engagement with a crossing rate. This is also the case for the half burn time flare, Figure 9-8. However, for tail-on engagements, 0°, the maximum PEH occur around 5s, 7s and 9s respectively for slant ranges 2km, 3km and 4km. For the quarter burn time flare, Figure 9-10, and 0° azimuth the maximum PEH is 2s before the hit point. At 2km slant range, Figure 9-10 (a) and (b), there is still a high PEH for the other azimuths. At 3km slant range, Figure 9-10 (c) and (d), and 45° azimuth the PEH is decreased for flare release before 3s. At 4km slant range, Figure 9-10 (e) and (f), and 45° azimuth the PEH is low for all flare release times. The PEH is also reduced for an azimuth of 135° for flare release from either set of dispensers and for 90° for flare release from the front dispensers.

9.4 Conclusions

A TAB CCM has been optimised for the C130 aircraft model and shows that reactive flare release in engagements with a crossing rate is less effective compared to a MANPAD with no CCM. Initial simulations with a constant slant range indicate that releasing more flares, i.e. from both sets of dispensers, does not give more protection for the aircraft. Instead, for each aircraft range and azimuth the timing of flare release and which dispenser to use is critical. Flares with reduced performance were also used and the results indicate that maintaining the burn time is the most important factor. However, the simulations are an ideal scenario and the quarter intensity flare still has a J/S ratio of greater than 2 to 1.

10 TWO-COLOUR SPINSCAN

The previous CCM modelled was track angle bias which requires there to be some amount of crossing rate in the engagement. This limitation means that it is not designed for tail-on or head-on scenarios. However, the easiest scenario for the missile to obtain lock-on and track an aircraft is in the rear aspect due to the greater emissions from the hot tail pipe and the exhaust plume.

An improved CCM that was designed to be more robust and work for all engagement geometries is two-colour. In this instance the IR seeker can detect in two separate wavebands (SWIR/MWIR) and exploit the different spectral characteristics of the target and flare. The seeker can then either compare the ratio of the signal in the two wavebands or try and null the signal received from a flare; both of which can be incorporated into the signal processing of the reticle tracker. Modelling a two-colour seeker allows the chance to test current countermeasures against this type of threat. Also, a two-colour CCM is more likely to be active prior to missile launch.

10.1 Modelling

The modelling of a two-colour CCM is implemented in the signal processor item where the block diagram detail is designed, Figure 10-1. It allows the user to apply any design of their choosing; the following describes the method chosen in this work. In the simulations the main band is 4-5µm and the guard band is 2-3µm.

Input 1 is the main band and input 2 is the guard band. A band-pass filter centred on the carrier frequency (or chopping frequency) is applied to the two waveforms of the signals separately. Next, a full wave limiter is applied to the two signals set to the maximum signal level received from the aircraft. Then, a full wave rectifier turns both waveforms positive. The two low-pass filters applied to each waveform act as envelope detectors, essentially smoothing out the signal.

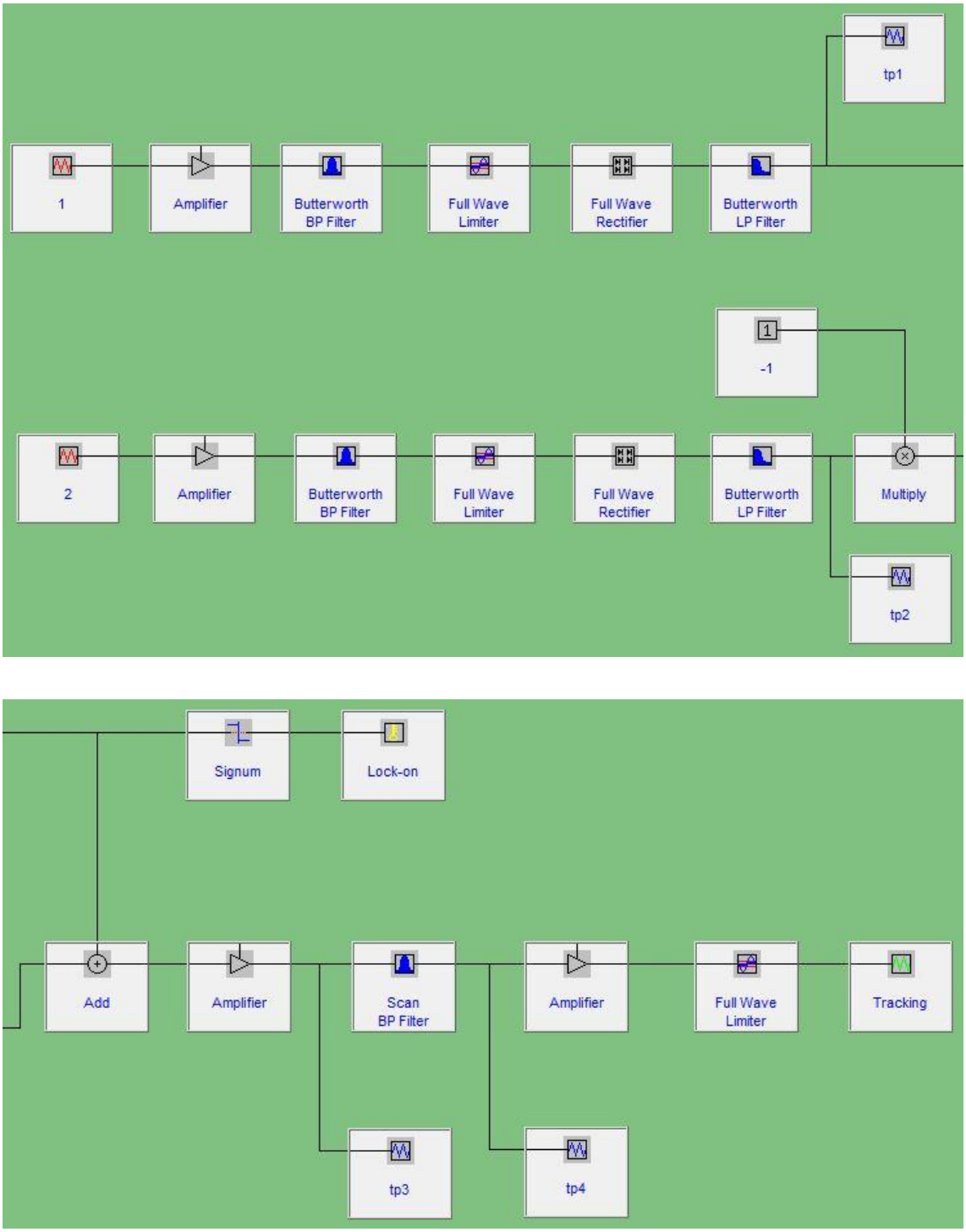

Figure 10-1 Block diagram design of the signal processor

As the shape of input 2 is a mirror image of input 1, due to alternate reticle spokes being transparent to the different wavebands, input 2 is multiplied by minus 1. After this the two resulting waveforms are added together and another filter applied to further smooth out the signal. Finally, another full wave limiter set to the maximum signal level received from the aircraft, gives the tracking signal. The amplitude of the tracking waveform gives the radial distance, r, and the phase variation the polar angle, θ, in polar coordinates. The parameters for the filters and limiters were calculated by running simulations with just the aircraft and no flares then just the flares with no target signature.

Figure 10-2 shows the signal processor view when (a) just the target aircraft is in the FOV and (b) when the aircraft and flares are in the FOV. In Figure 10-2 (b) tp3 is the combined signal from the two detectors showing the suppression of the signal tp2 from detector 2, the guard band. This detects in the 2-3µm waveband and therefore will be dominated by the flare as it burns at a higher temperature than the target.

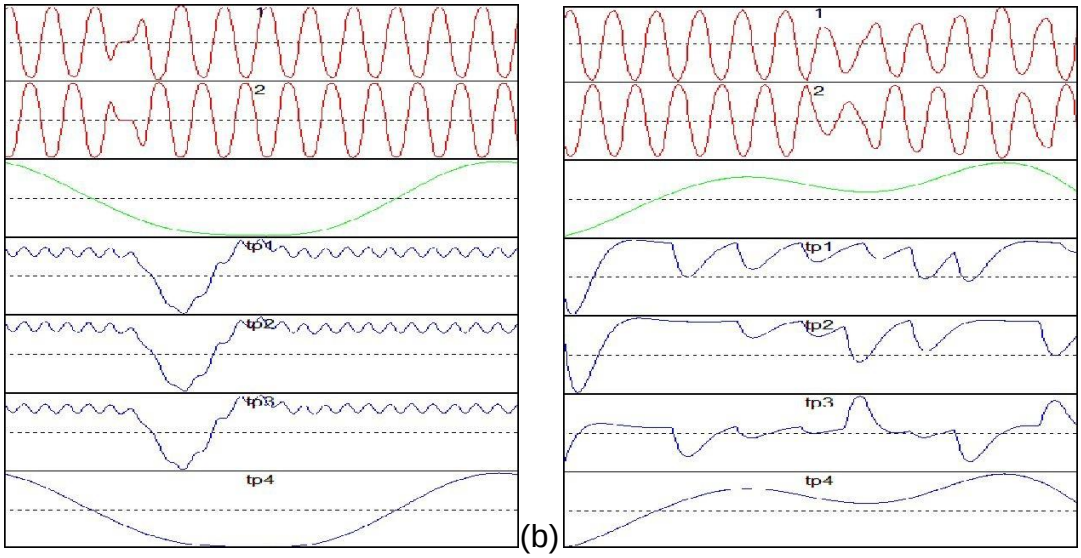

Figure 10-2 Signal processor view for (a) aircraft and (b) aircraft and flares.

Another effect of the suppression of the signal from the highest temperature region in the FOV is that during the end game of an engagement the missile will aim away from the hot tail pipe and exhaust plume towards the cooler metal parts of the aircraft. This can be a desirable result because the aircraft will most likely suffer more structural damage and be unable to land safely.

10.2 Two-Colour Spinscan CCM and AMX-A1 Model

In the first set of simulations the AMX-A1 travels at 200 m/s, straight and level, and on a constant bearing at an altitude of 1km. To represent the operational envelope of the MANPAD, the simulation start distance between the missile system and the aircraft ranges from 1km to 5.5km in steps of 0.5km. Also, the aircraft azimuth angle with respect to the missile launch position ranges from 0° to 345° in steps of 15°. An aircraft azimuth of 0° represents a tail-on engagement where the aircraft is flying directly away from the MANPAD operator position. This gives a total of 240 simulations (24 aircraft azimuths x 10 aircraft distances). In the simulations the aircraft releases flares reactively at a detection range of 1500m, one from the dispenser on each side of the airframe.

In the second set of simulations flares are released every 0.5s throughout an engagement up to the hit point. The slant range is kept constant and the aircraft azimuth varied from 0° to 180° in steps of 45°. Again, an aircraft azimuth of 0° represents a tail-on scenario. The simulations were repeated for constant slant ranges of 2km, 3km and 4km. A limit was set on the aircraft altitude by a maximum launch elevation of 60°.

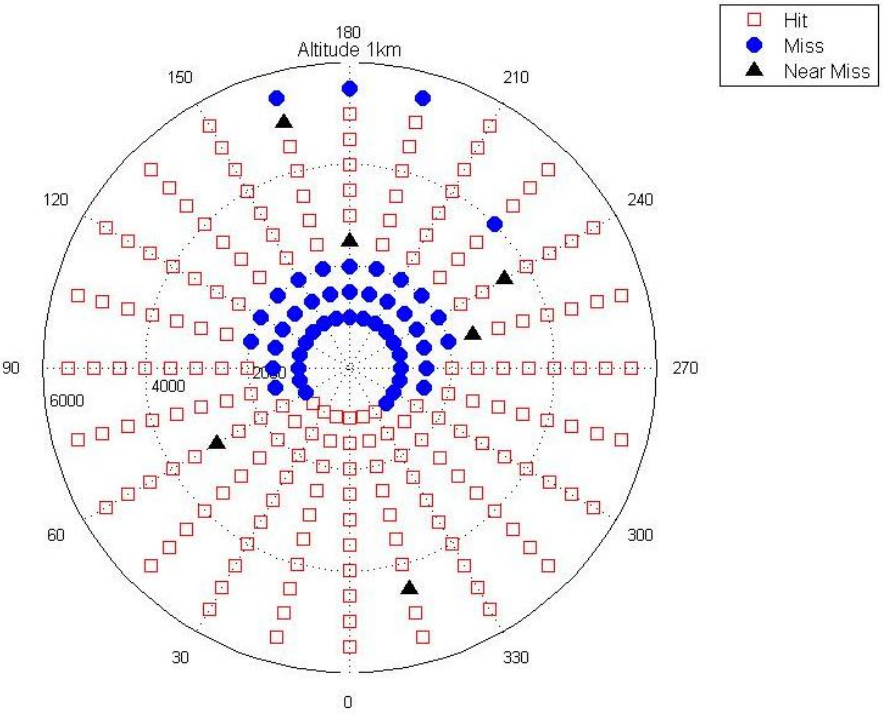

Figure 10-3 Aircraft altitude of 1km with no countermeasures.

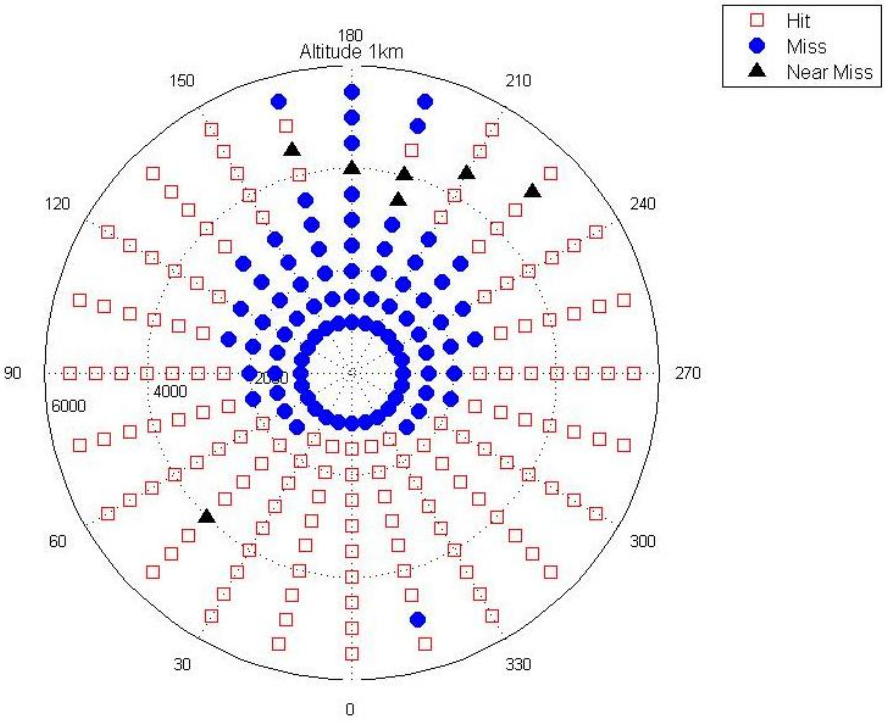

Figure 10-4 Aircraft altitude of 1km with reactive flares.

The results for the first set of simulations are shown in Figure 10-3 where the aircraft is at the centre of the polar plot and each point represents where the MANPAD is placed in relation to the aircraft at the start of the simulation.

Figure 10-3 shows the results for the AMX-A1 releasing no countermeasures. Of the 240 simulations, 186 were hits, giving a probability of escaping a hit (PEH) of 0.23. This compares to previous simulations of a spinscan IR seeker detecting only in the 2-2.7μm waveband where the PEH was 0.19. Therefore, the results are slightly worse for the two-colour seeker, but the large improvement occurs when the aircraft deploys countermeasures. When flares are released reactively, Figure 10-4, the PEH is 0.38, compared to 1.00 for the single detector IR seeker. This is also an improvement for the IR seeker compared to previous simulations where a track angle bias CCM was modelled. For a spinscan seeker detecting in the 2-2.7μm waveband the PEH was 0.53, and for a conscan seeker detecting in the 3-5μm waveband the PEH was 0.47.

The results for the second set of simulations for the AMX-A1 model are shown in Figure 10-5, where (a), (b) and (c) are for the slant ranges 2km, 3km and 4km respectively. The graphs show the PEH for each flare release time for different aircraft azimuths. For the 2km slant range there is no aircraft azimuth of 90° or 135° because all the engagements resulted in a miss even when no flares were released. This is due to the faster target having a greater crossing rate and the missile being unable to apply the required rate of turn for a successful PN course.

Figure 10-5 clearly shows that the timing of flare release is critical if you want maximum protection for the aircraft. Firing after 4s is too late for any engagement with a crossing rate. The worst performing is 0° azimuth, tail-on, where flares need to be fired prior to 2s from the start of the simulation. Also, in head-on engagements, 180° azimuth, releasing flares before 1s is too early. This leaves a very short window in which releasing flares gives the highest values of PEH. The time is around 1s, which corresponds to the period of missile launch, and shows that a flare can still be effective against a two-colour CCM if released at this time.

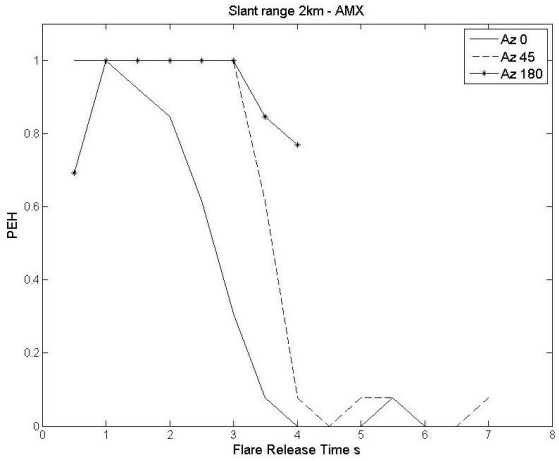

(a)

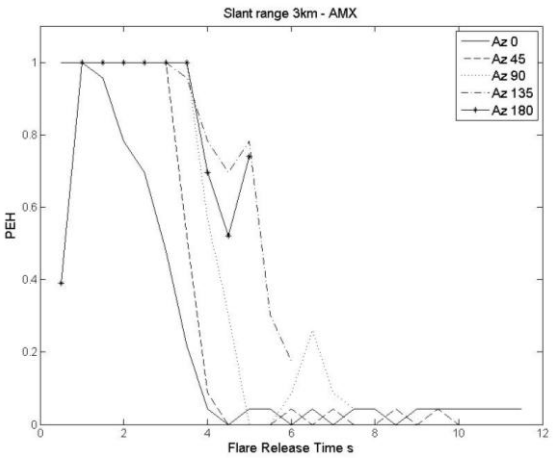

(b)

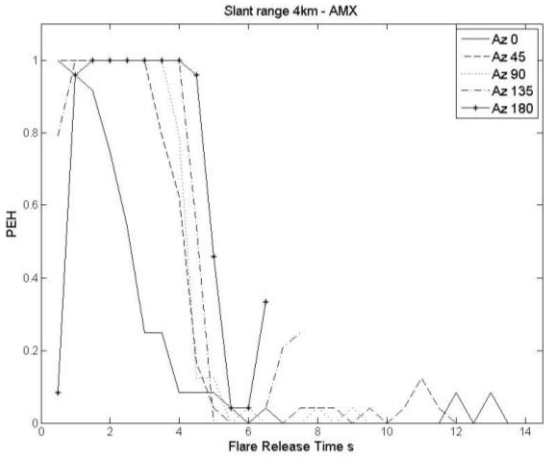

(c)

Figure 10-5 PEH versus flare release time for slant ranges 2km, 3km and 4km.

The simulations with a constant slant range were repeated for the flares with reduced performance. Figure 10-6 show the results for the half intensity and half burn time flares and Figure 10-7 shows the results for the quarter intensity and quarter burn time flares. All flare types give similar results for each aircraft azimuth. The only exception is the quarter burn time flare in a tail-on engagement for the 4km slant range, azimuth 0° in Figure 10-7 (f), which gives a lower PEH for flare release before 2s.

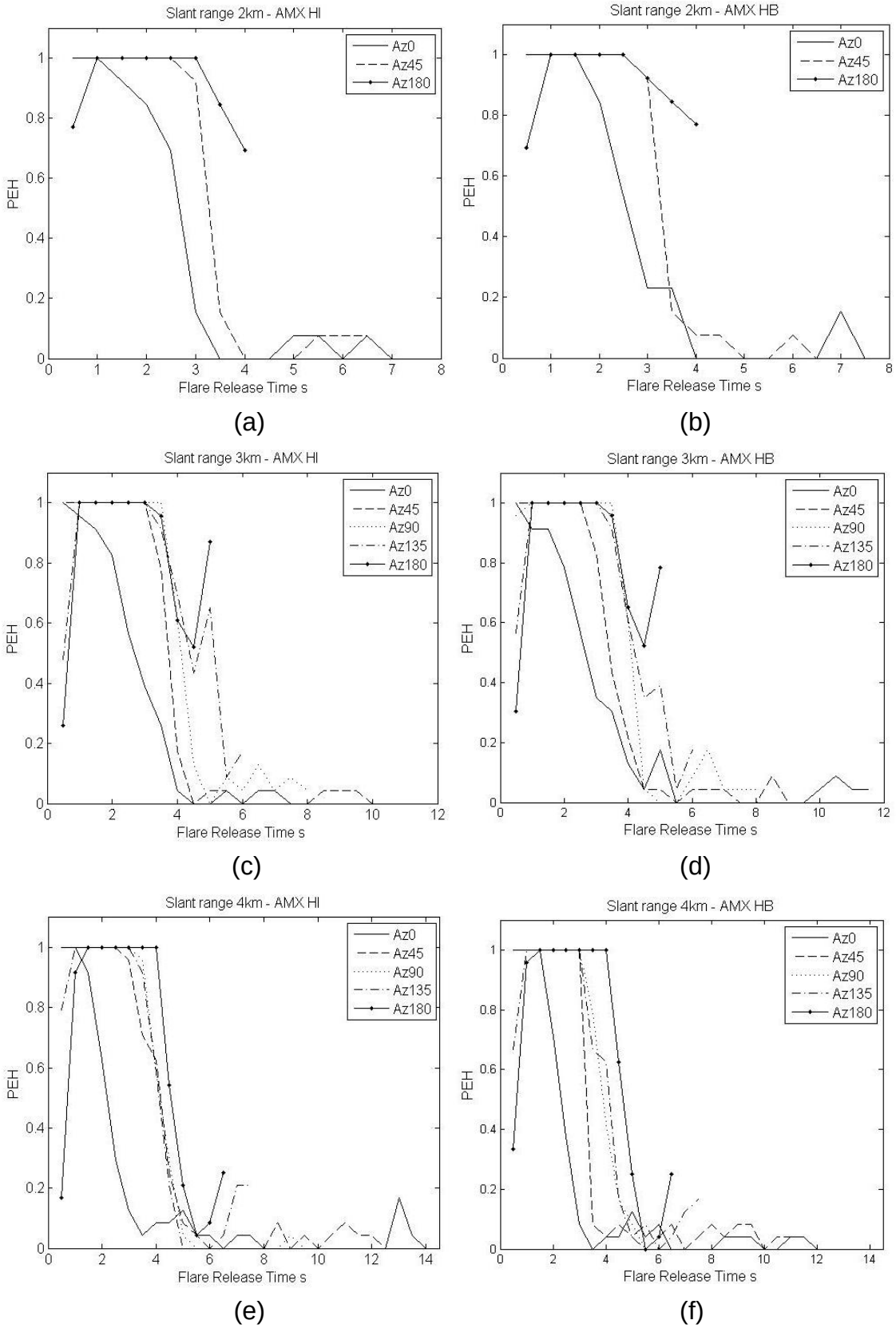

Figure 10-6 PEH versus flare release time for half intensity and half burn time flares.

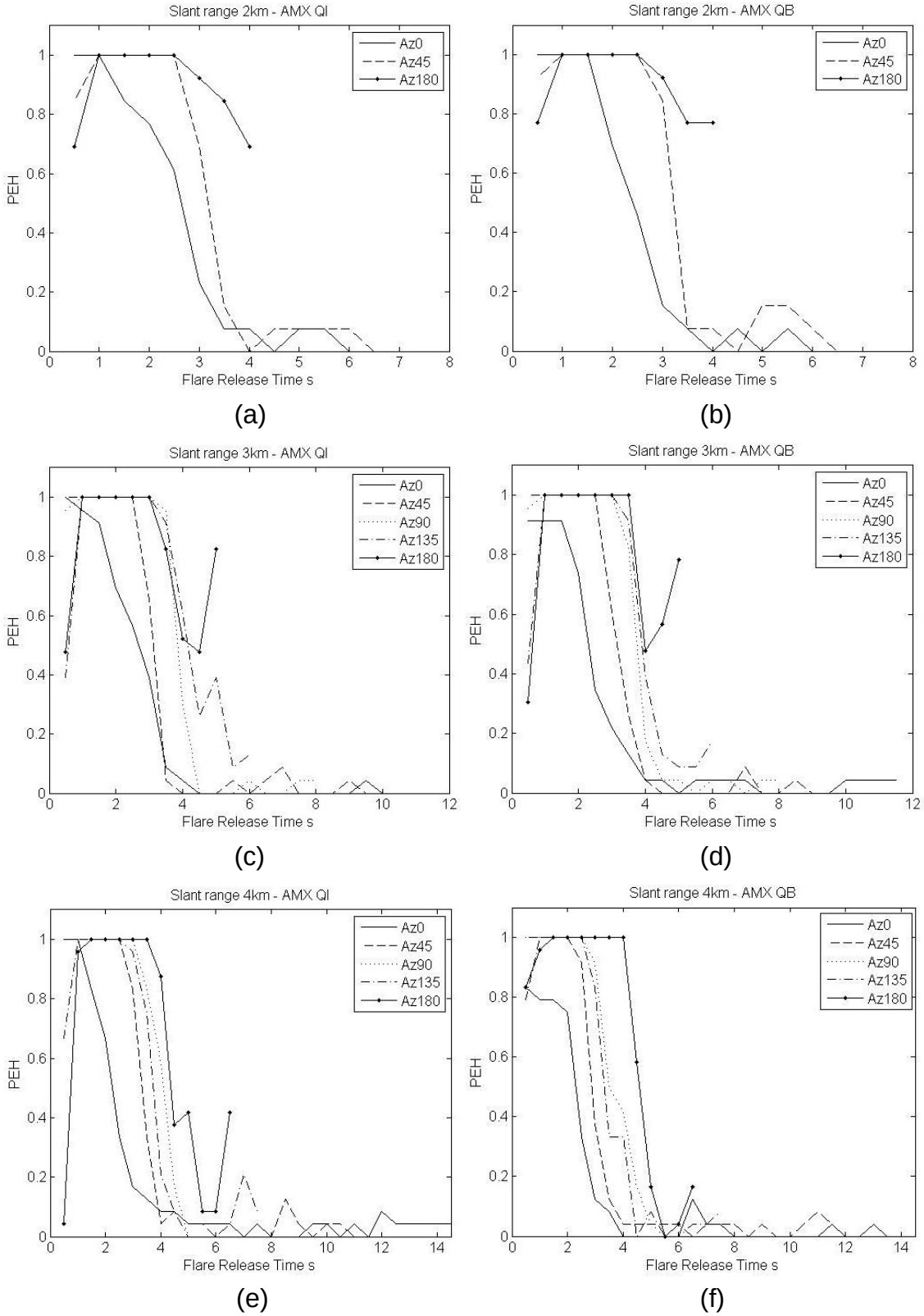

Figure 10-7 PEH versus flare release time for quarter intensity and quarter burn time flares.

10.3 Two-Colour Spinscan CCM and C130 Model

The results for the first set of simulations and the C130 aircraft model when no countermeasures are released are shown in Figure 10-8. There are 199 hits, giving a PEH of 0.17. This compares to previous simulations of a spinscan IR seeker detecting only in the 2-2.7µm waveband where the PEH was 0.27. When flares are fired reactively from the front dispensers, Figure 10-9, the PEH is 0.63. When flares are fired reactively from the side dispensers, Figure 10-10, the PEH is 0.45. Again, this compares to a PEH of 1.00 for both the front and side dispensers when reactive flares are fired against a spinscan 2-2.7µm single detector IR seeker.

The front dispensers perform much better than the side dispensers in engagements with a crossing rate. The angle of ejection for the front dispensers means that the flares stay in the FOV longer compared to the side dispensers and are therefore harder to reject. This is similar to the results for a MANPAD with a TAB CCM.

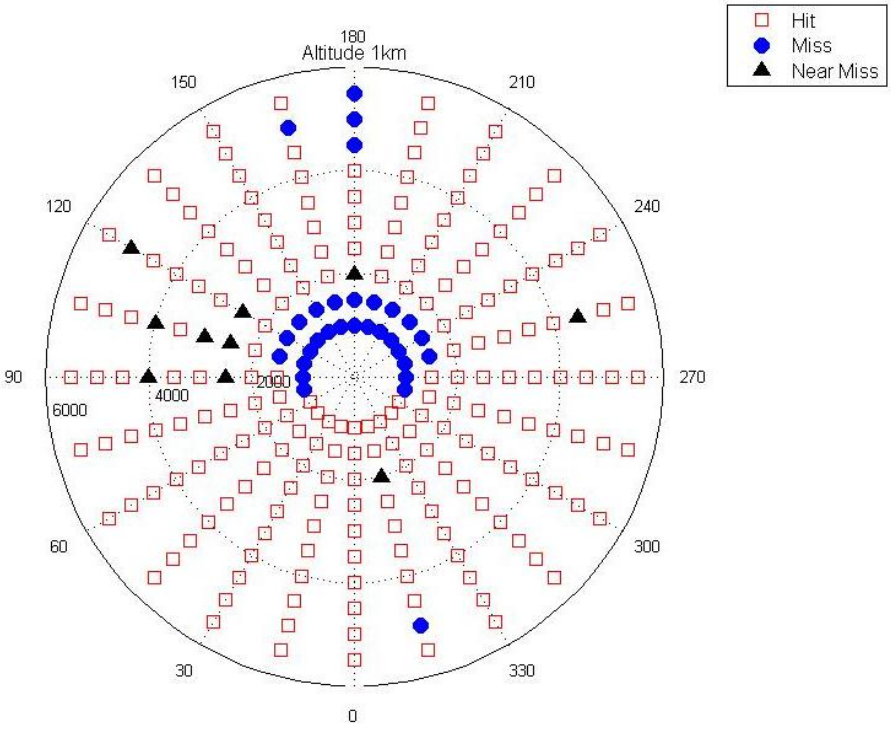

Figure 10-8 Aircraft altitude of 1km with no countermeasures.

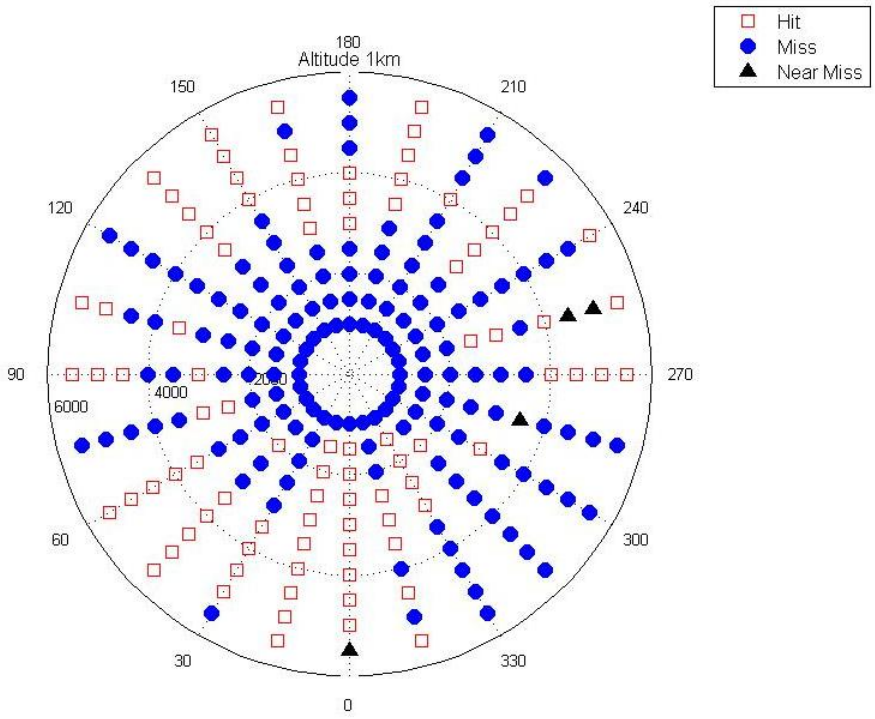

Figure 10-9 Aircraft altitude of 1km with reactive flares released from the front dispensers.

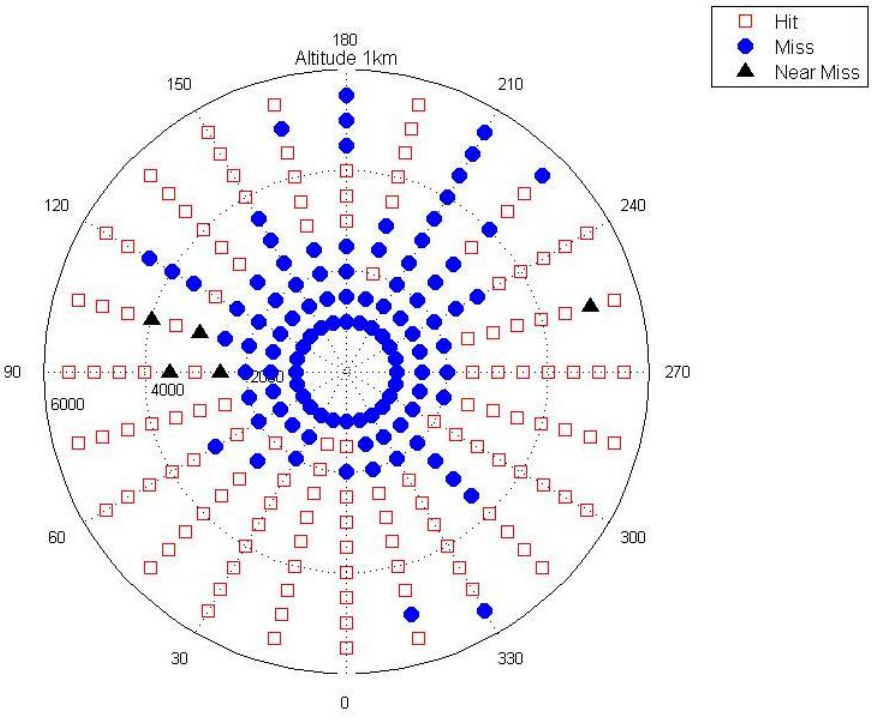

Figure 10-10 Aircraft altitude of 1km with reactive flares released from the side dispensers.

The results for the second set of simulations with a constant slant range and the C130 model are shown in Figure 10-11. Figure 10-11 (a) and (b) are for a slant range of 2km with flares fired from the front and side dispensers respectively. Figure 10-11 (c) and (d) are for a 3km slant range, and (e) and (f) for 4km slant range. For a slant range of 2km the worst performing countermeasure is flares fired from the front dispensers in a tail-on engagement. For the side dispensers there is still the window around 1s in which releasing flare gives maximum protection to the aircraft.

For slant ranges of 3km and 4km there is no flare release time when the PEH=1 irrespective of flare dispenser or aircraft azimuth. However, the highest values for the PEH still occur between the times of 1s and 2s from the start of the simulation. This stage of the simulations covers the period just prior to missile launch and the half second ignition delay on the boost thrust. At this time the missile is either stationary or travelling at a low velocity. The presence of flares in the seeker FOV at this time is likely to have an effect on the PN guidance course implemented by the seeker as it has to estimate the closing velocity. Overall, the deployment flares around the time of missile launch gives the best results for the aircraft independent of which flare dispenser is used, distance and angle of attack.

The simulations with a constant slant range were repeated for the flares with reduced performance. The results for the half intensity, half burn time, quarter intensity and quarter burn time are shown in Figure 10-12, Figure 10-13, Figure 10-14 and Figure 10-15 respectively. All flare types give similar results for engagements with a crossing rate, azimuth 45°, 90° and 135°, and head-on engagements, azimuth 180°. Again, the only clear difference is the reduced protection offered by the quarter burn time flare, Figure 10-15, in tail-on engagements, azimuth 0°.

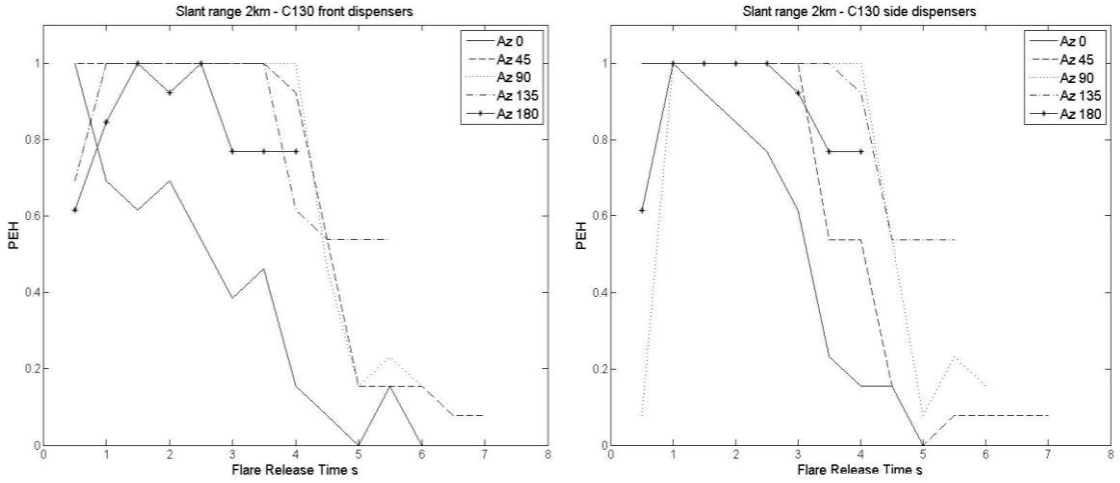

(a)

(b)

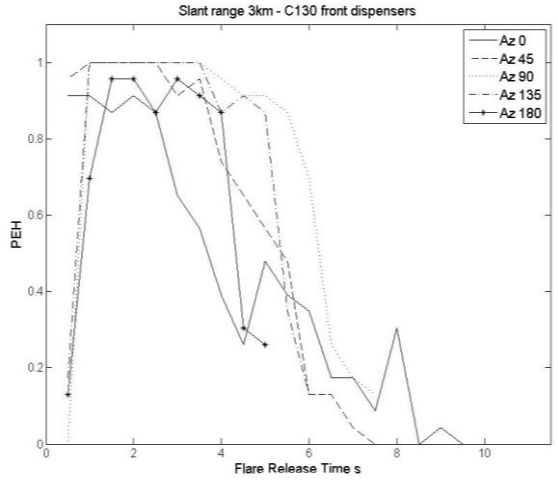

(c)

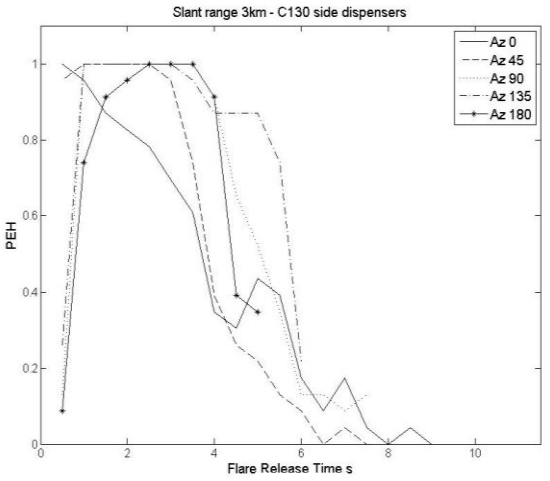

(d)

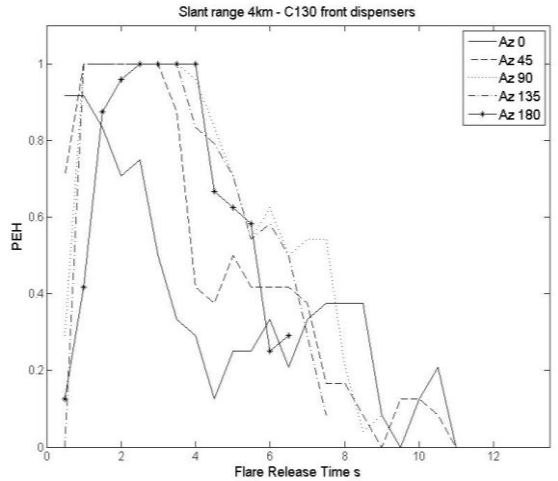

(e)

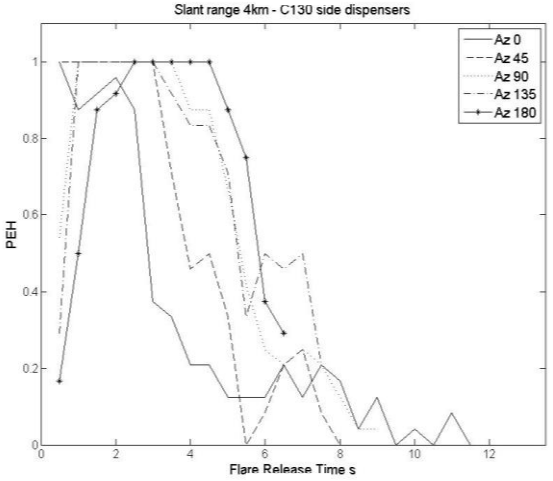

(e)

Figure 10-11 PEH versus flare release time for slant ranges 2km, 3km and 4km for flare release from the front and side dispensers.

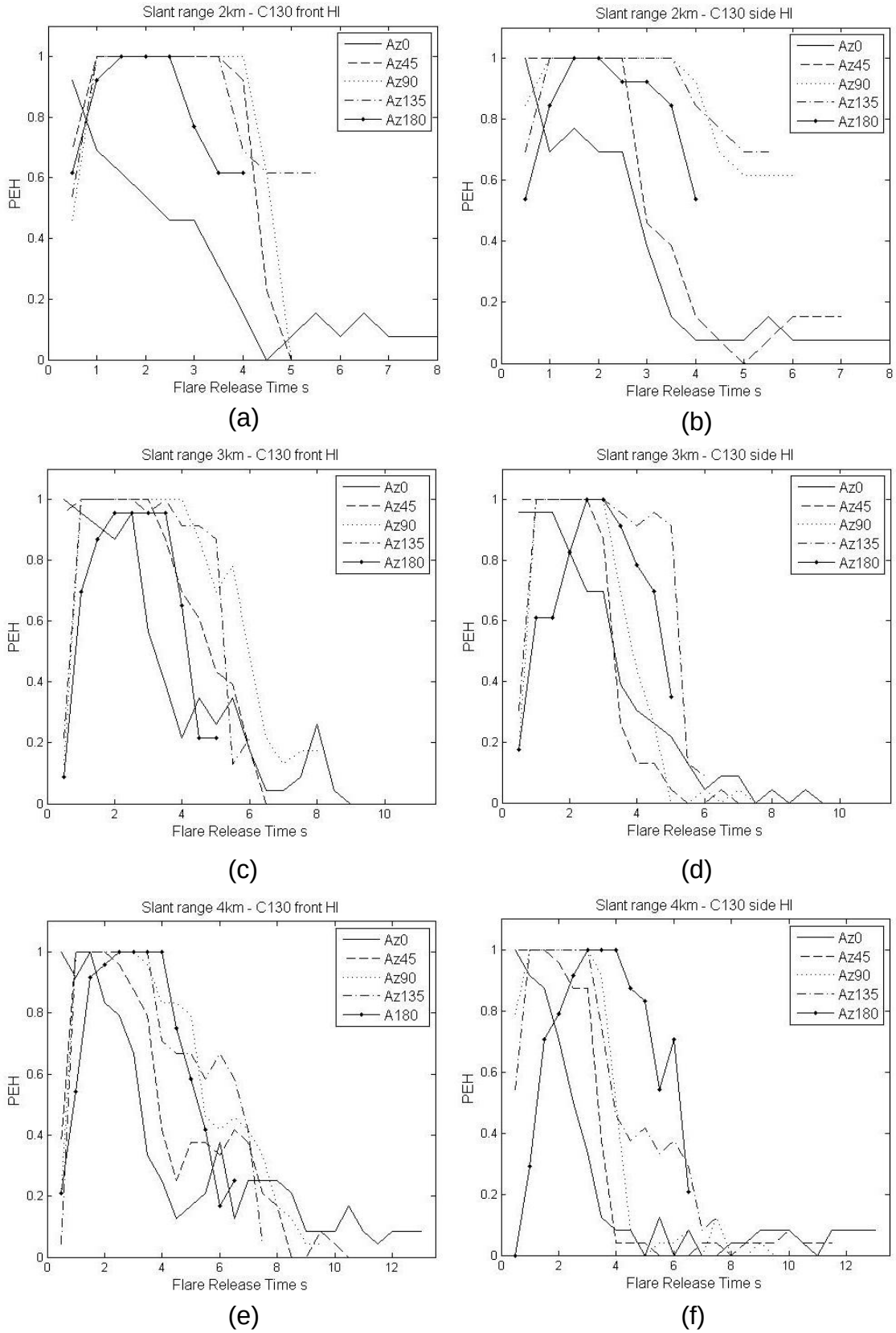

Figure 10-12 PEH versus flare release time for slant ranges 2km, 3km and 4km for half intensity flares.

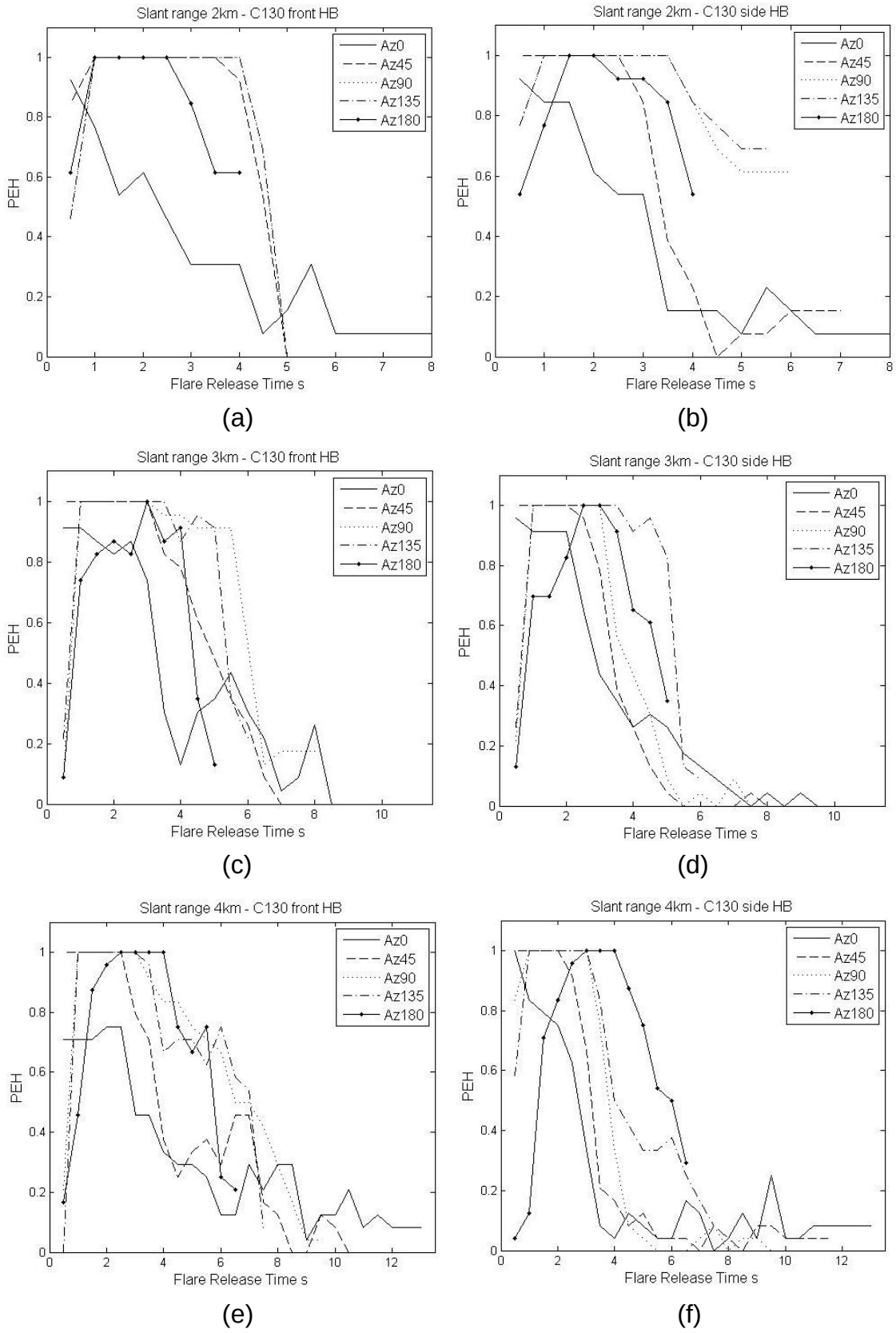

Figure 10-13 PEH versus flare release time for slant ranges 2km, 3km and 4km for half burn time flares.

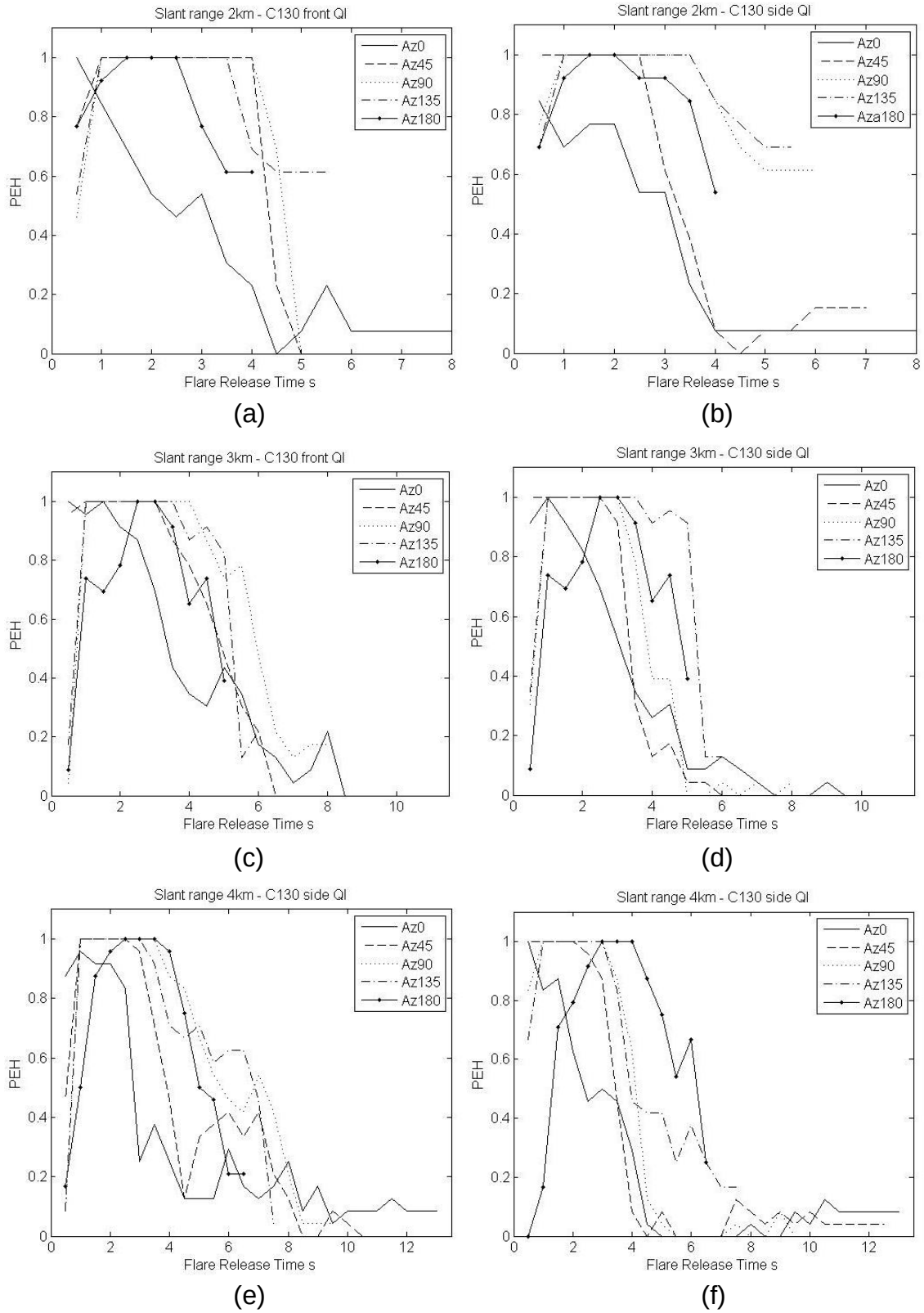

Figure 10-14 PEH versus flare release time for slant ranges 2km, 3km and 4km for quarter intensity flares.

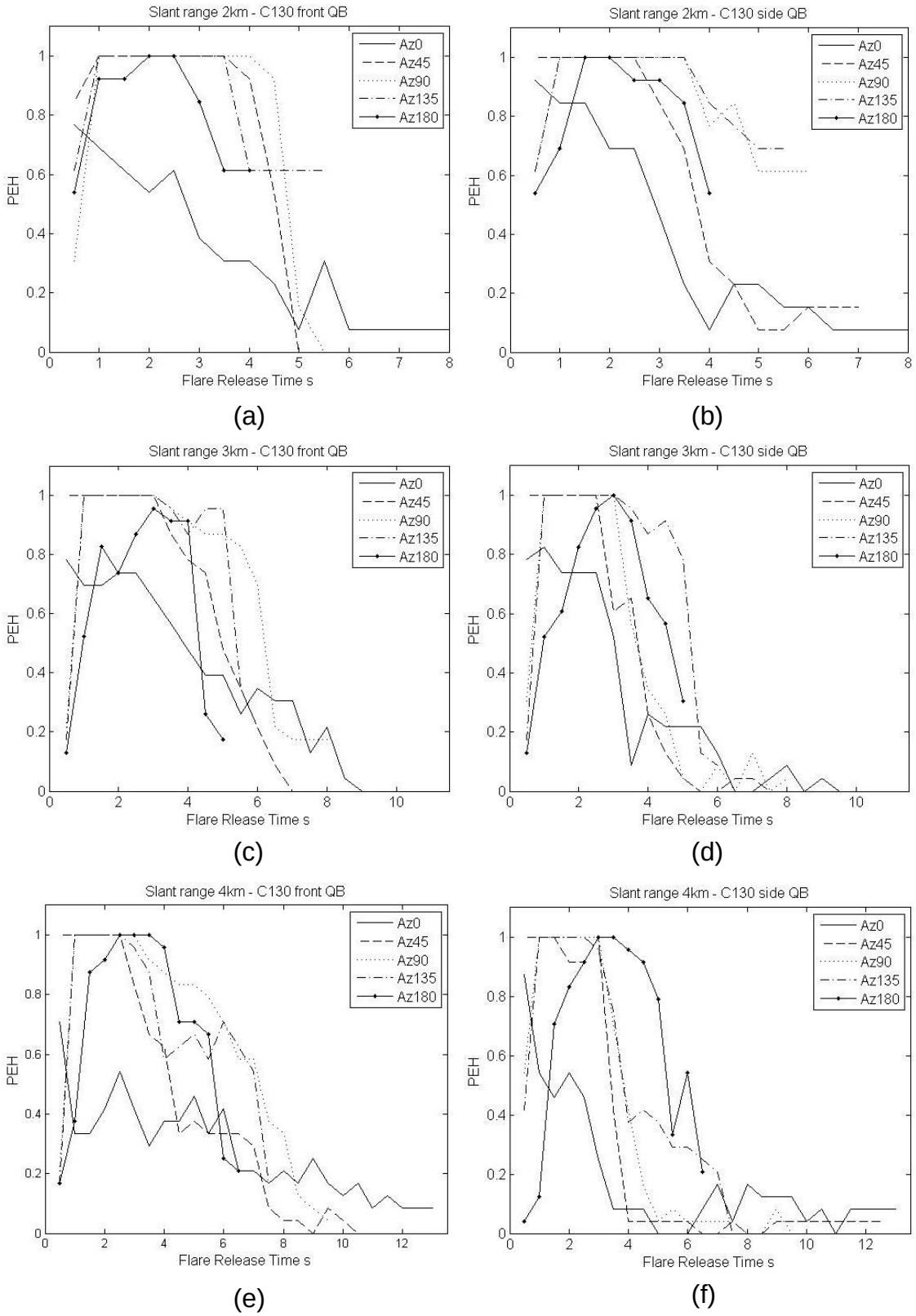

Figure 10-15 PEH versus flare release time for slant ranges 2km, 3km and 4km for quarter burn time flares.

10.4 Conclusions

A two-colour spinscan CCM has been modelled and has reduced the effectiveness of reactive flares. The PEH for the AMX-A1 releasing no countermeasures is 0.23 compared to 0.38 for reactive flares. The PEH for the C130 releasing no countermeasures is 0.17 compared to 0.63 for reactive flares released from the front dispensers and 0.45 for reactive flares released from the side dispensers.

Flares were then released throughout an engagement for different slant ranges and aircraft azimuths. For the AMX-A1 model flare release between 1 and 2s gives the highest PEH for all aircraft azimuths with similar results for the reduced performance flares. For the C130 model the same flare release time gives the highest PEH whether using the front or side dispensers. With the reduced performance flares the results are similar for the half intensity and quarter intensity flares. The only difference with the reduced burn time flares is in tail-on engagements where the PEH is lower compared to the other flares. However, the maximum values still occur at flare release between 1 and 2s.

11 TWO-COLOUR CONSCAN

In this chapter another two-colour CCM is modelled but this time for a conscan seeker. The CCM is again implemented in the signal processor but a new design is needed for the FM signal compared to the AM signal for a spinscan seeker.

11.1 Modelling

The signal processor design for the two-colour conscan CCM is shown in Figure 11-1. There are two inputs; the first from the main band of 4-5µm, the second from the guard band of 2-3µm. Both signals are limited to the maximum level received from just the aircraft, tp1 and tp2 in Figure 11-2, then the two waveforms are added together. After the two waveforms are added together the same filters are applied as described in section 5.4 for the one-colour conscan seeker, tp3 and tp4 in Figure 11-2. This then gives the tracking signal which is represented by the final waveform in Figure 11-2.

The effect of the CCM is that the seeker will track cooler extended targets rather than hot point sources. This is probably not how a real two-colour CCM would be implemented in a real system; it would most likely compare the ratio of intensities in the two wavebands. However, this design can reject flares and serves as a good test for aircraft countermeasures.

To test the signal processing static gain curves were produced for different targets. The targets were placed at the same distance from the MANPAD system and were stationary with the missile set not to launch. The targets used were a hot sphere, a 218 flare and the AMX-A1 aircraft model. For the simulations with the flare, it was released with a zero ejection velocity to maintain it within the FOV and there was no aircraft signature. The simulations with the aircraft were repeated for the modified wagon wheel design in section 5.4 and a new design from reference(21), as shown in Figure 11-3.

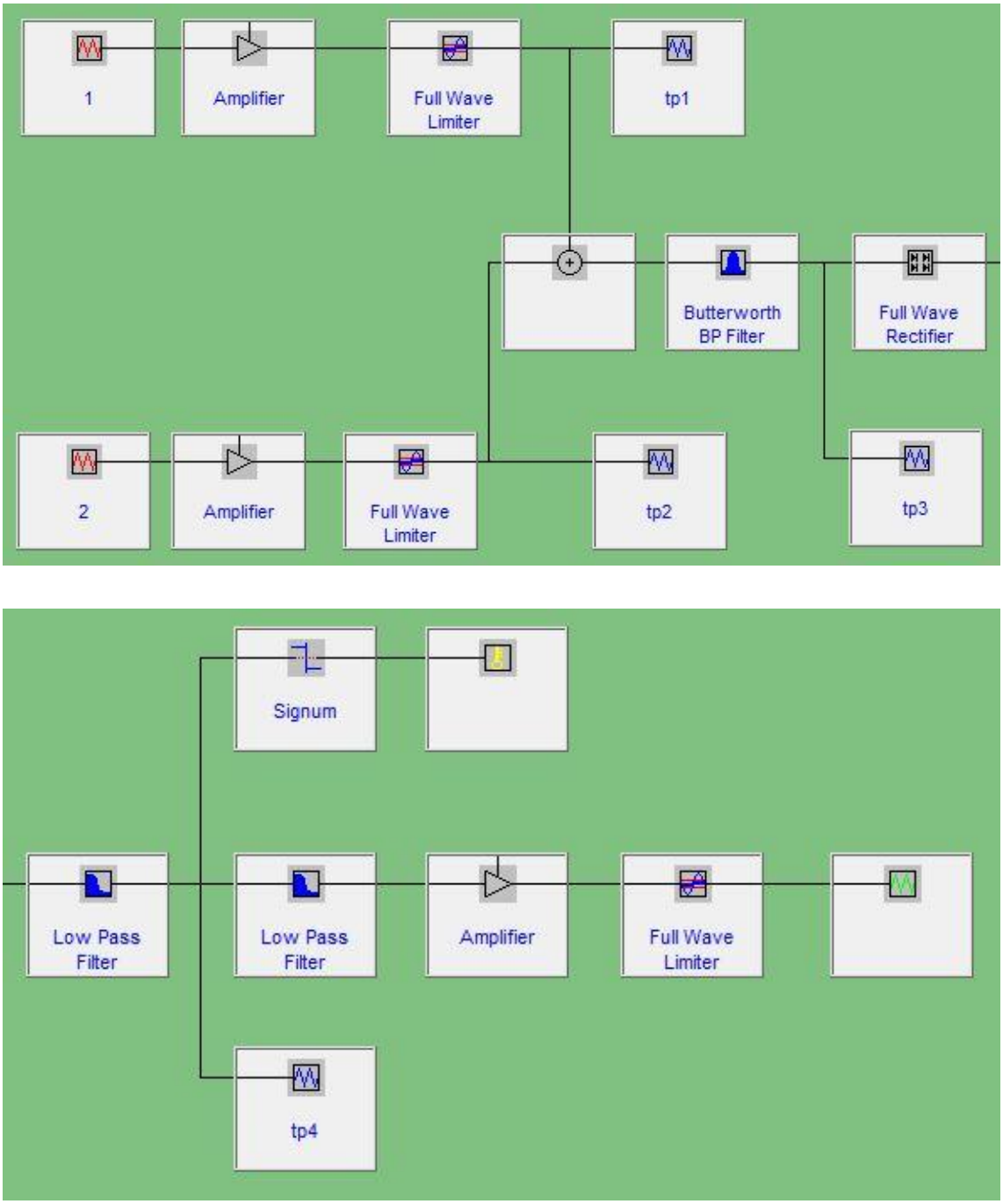

Figure 11-1 Signal processor design for the two-colour conscan CCM.

The results for the static gain curves are shown in Figure 11-4. The curve for the aircraft with the new reticle design was from half the data points. This was to illustrate that static gain curves in open sources, such as that shown in Figure 5-10, are most likely best fits of nosier data. The results for the hot sphere and flare are very similar, as expected. The results for the aircraft show a much

larger gain for on-axis targets and also across the majority of the total FOV; this is the effect of the two-colour CCM.

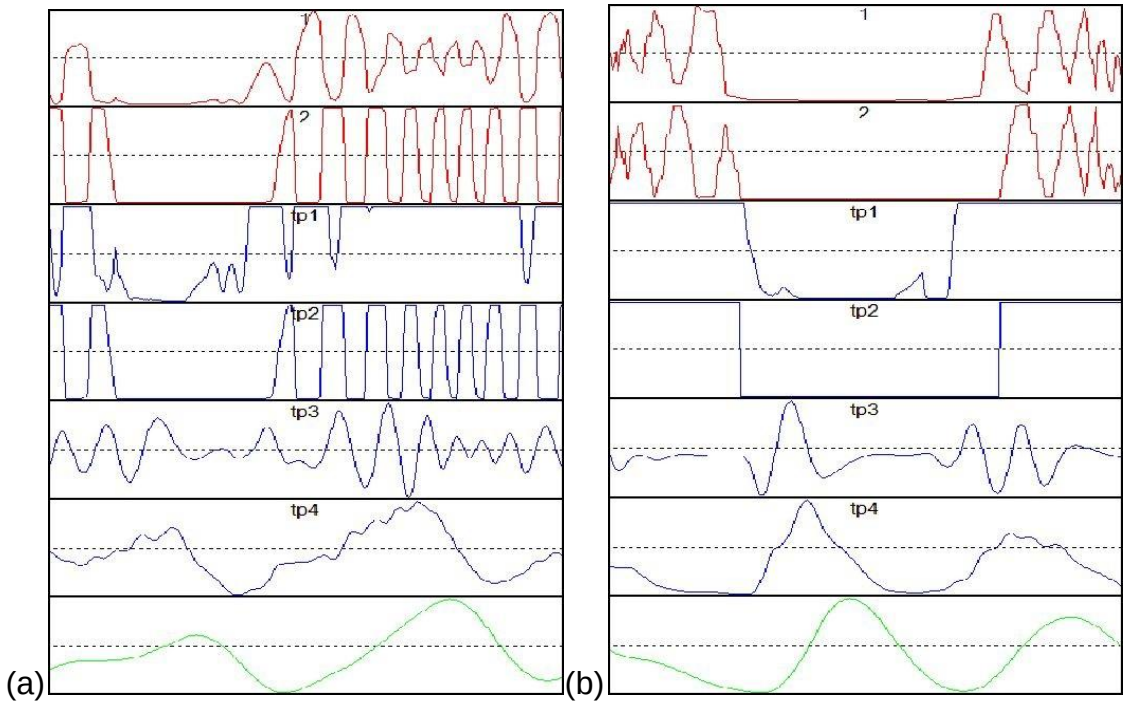

Figure 11-2 Signal processor view for (a) aircraft and (b) aircraft and flares.

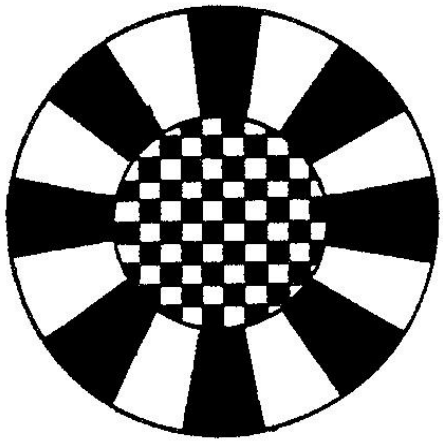

Figure 11-3 New reticle design for the conscan seeker.

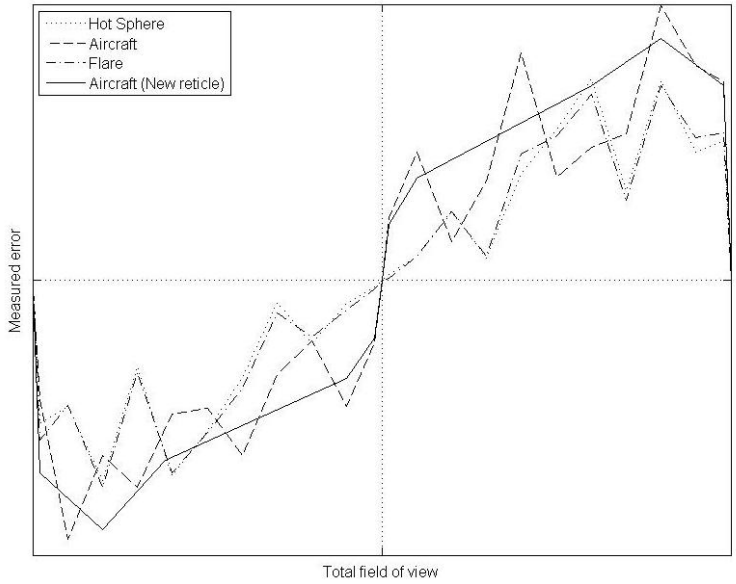

Figure 11-4 Static gain curves for the three targets.

11.2 Two-Colour Conscan CCM and AMX-A1 Model

The first simulations for the AMX-A1 model were for an aircraft altitude of 1km, all missile ranges and azimuths, and the aircraft releasing no countermeasures; the results are shown in Figure 11-5. Next, the simulations were repeated but this time the aircraft released flares reactively at a detection range of 1500m; the results are shown in Figure 11-6. The PEH when no flares are release is 0.20, compared to 0.11 for a single detector conscan seeker. The difference is due to the two-colour CCM always being active in the signal processing. The additional simulations that result in a miss are the long range head-on engagements that can be seen in Figure 11-5.

The PEH when reactive flares are released is 0.34, compared to 1.00 for a single detector conscan seeker with no CCM. This is a substantial improvement and is the best performing model for a MANPAD with a CCM. Given that reactive flares do not offer a high level of protection for the aircraft against this threat the next simulations investigate the effect of flare release time.

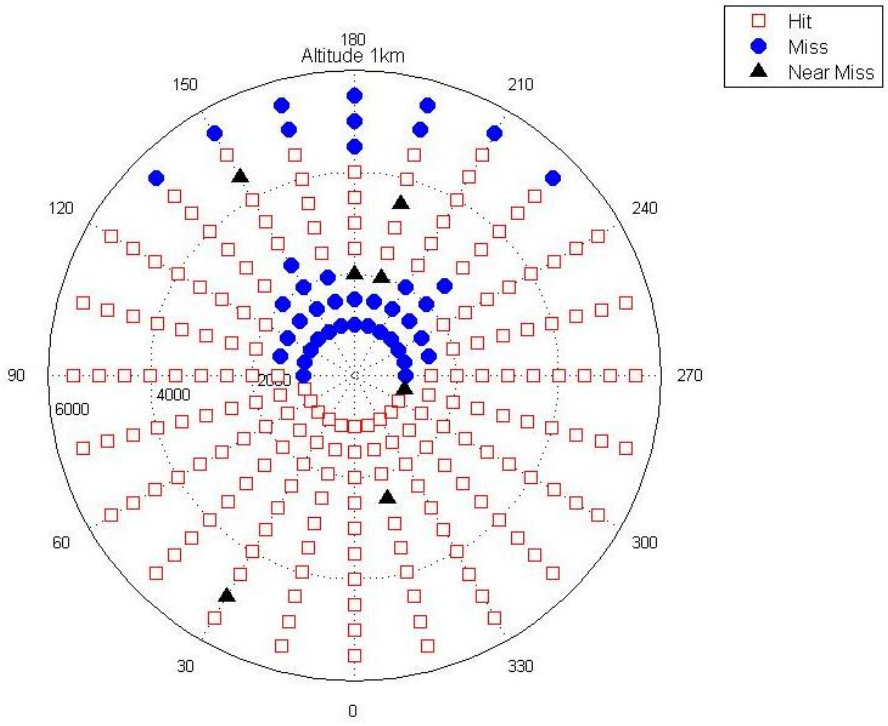

Figure 11-5 Aircraft altitude of 1km with no countermeasures.

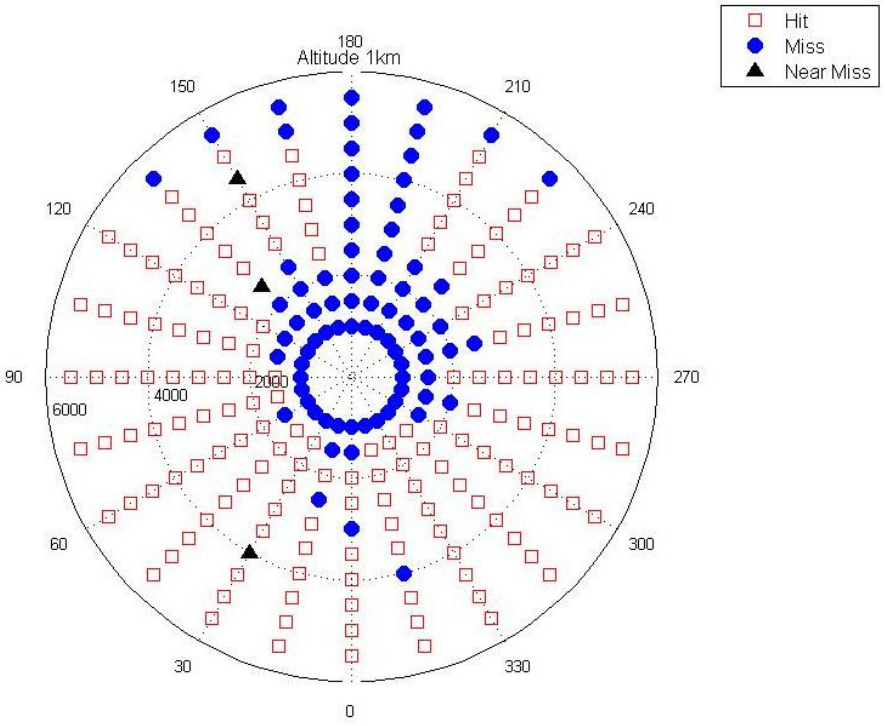

Figure 11-6 Aircraft altitude of 1km with reactive flares.

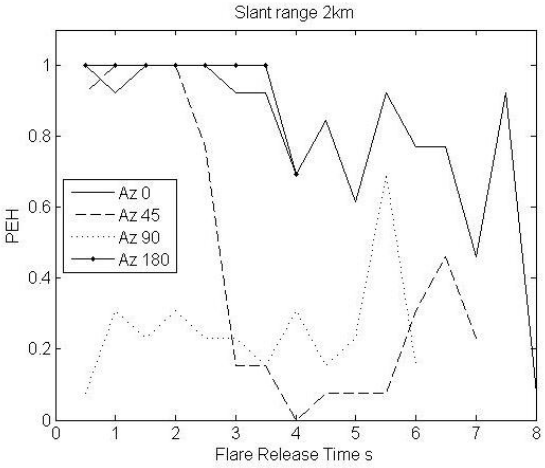

(a)

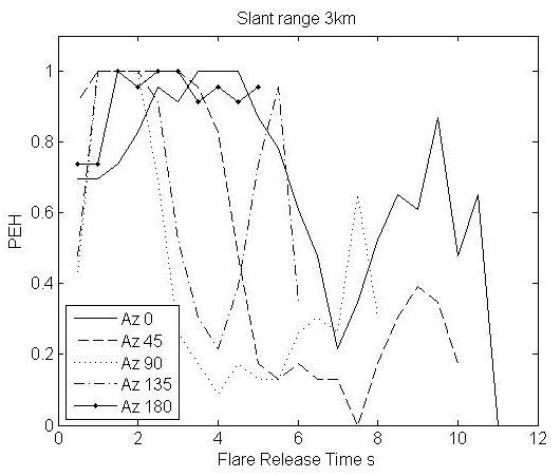

(b)

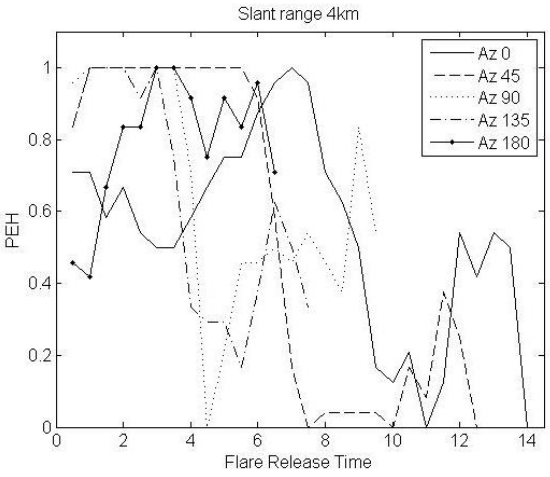

(c)

Figure 11-7 PEH versus flare release time for constant slant ranges of (a) 2km, (b) 3km and (c) 4km.

In the second set of simulations flares are released at half second intervals for constant slant ranges of 2km, 3km and 4km; the results are shown in Figure 11-7. For a slant range of 2km, Figure 11-7 (a), flare release between 1.5s and 2s gives a PEH=1 for azimuths 0°, 45° and 180°. However, for 90° no flare release time gives a high PEH as the spike at 5.5s is due to near misses, i.e. a miss distance less than 10m.

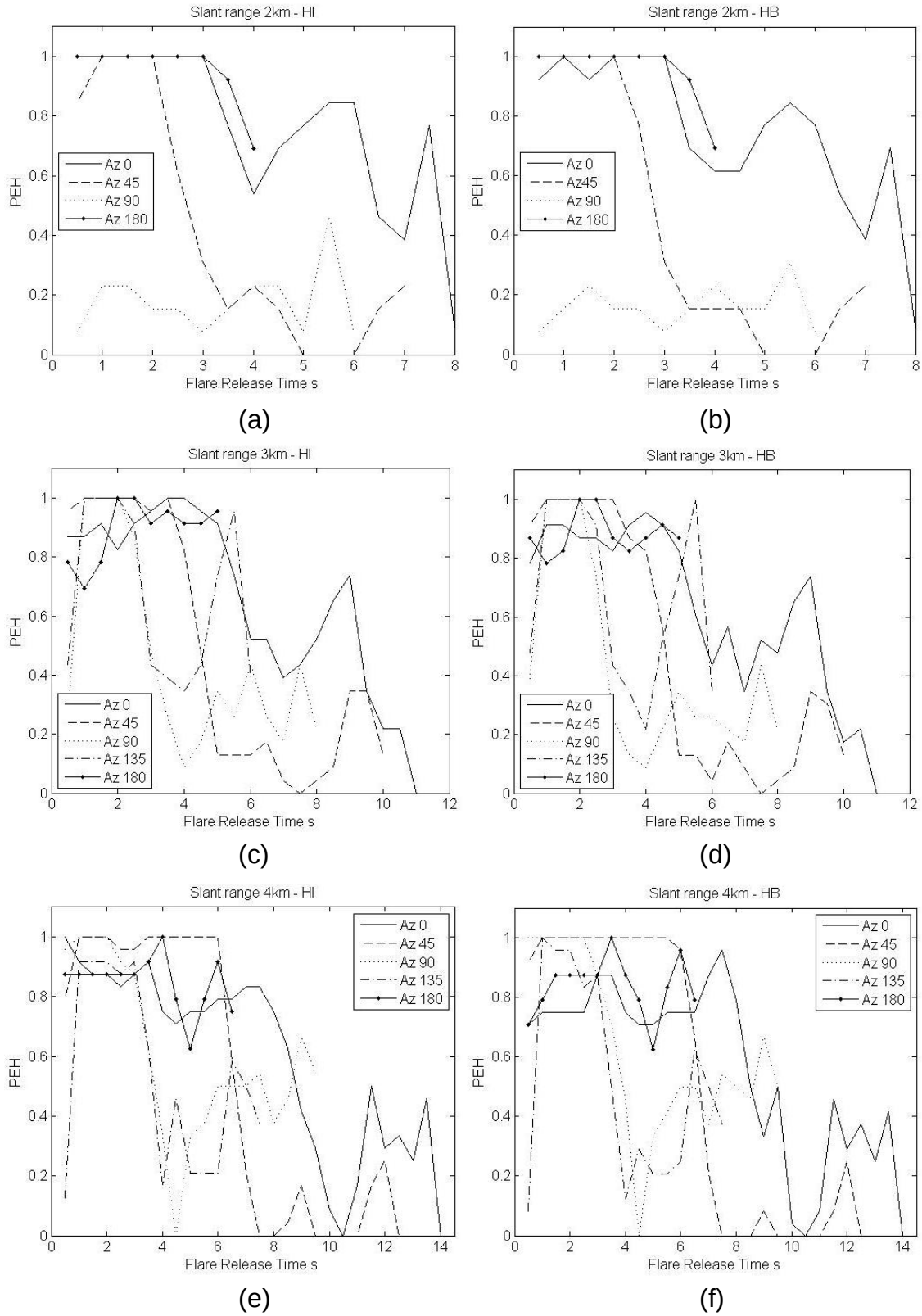

Figure 11-8 PEH versus flare release time for half intensity and half burn time flares.

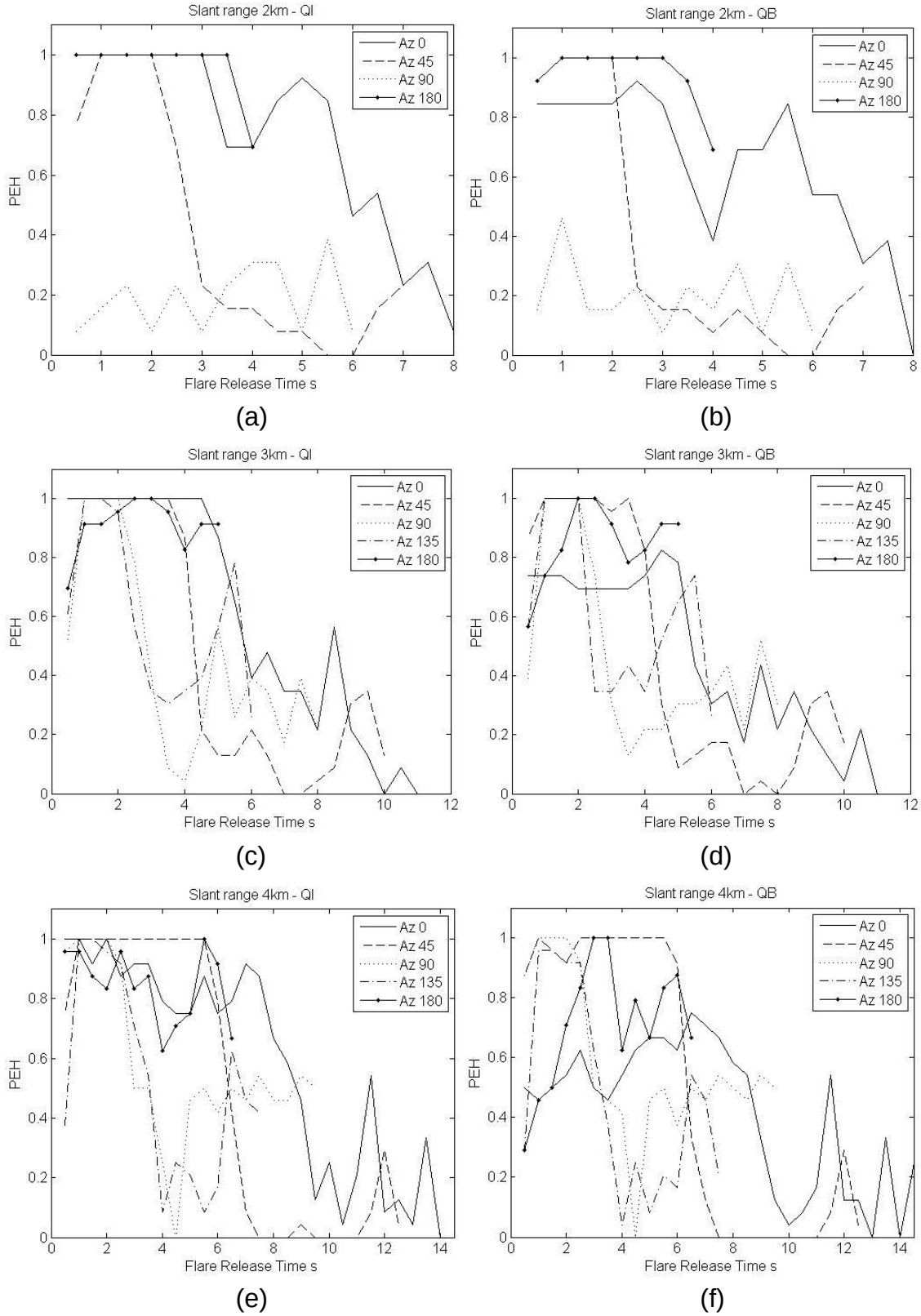

Figure 11-9 PEH versus flare release time for quarter intensity and quarter burn time flares.

For a slant range of 3km, Figure 11-7 (b), flare release around 2s gives a PEH=1 for all but one of the azimuths. The exception is tail-on engagements, 0°, where the PEH=1 at 4s; this time is 7s from the hit point. For a slant range of 4km, Figure 11-7 (c), and 0° azimuth the PEH=1 at 7s, again this is 7s from the hit point. For any engagement with a crossing rate then flare release between 1s and 2s gives a PEH=1. For head-on engagements later flare release at 3s gives a PEH=1. All these flare release times are earlier in an engagement than if they were deployed reactively.

The simulations with constant slant ranges were repeated for the flares with reduced performance. The results for the half intensity and half burn time flares are shown in Figure 11-8. The results for the quarter intensity and quarter burn time flares are shown in Figure 11-9.

The results for each flare type are similar to the standard 218 flare for any engagement with a crossing rate, aircraft azimuths 45°, 90° and 135°. This is also the case for head-on engagements, 180°. The only variation occurs in tail-on engagements, 0°, where the quarter burn time flare gives a lower PEH for all flare release times. Also, for this scenario the quarter intensity flare produces the best results due to the design of the two-colour CCM.

11.3 Two-Colour Conscan CCM and C130 Model

The first simulations for the C130 model were for an aircraft altitude of 1km, all missile ranges and azimuths, and the aircraft releasing no countermeasures; the results are shown in Figure 11-10. Next, the simulations were repeated but this time the aircraft released flares reactively from the front dispensers then the side dispensers at a detection range of 1500m. The results for the front dispensers are shown in Figure 11-11 and the results for the side dispensers are shown in Figure 11-12.

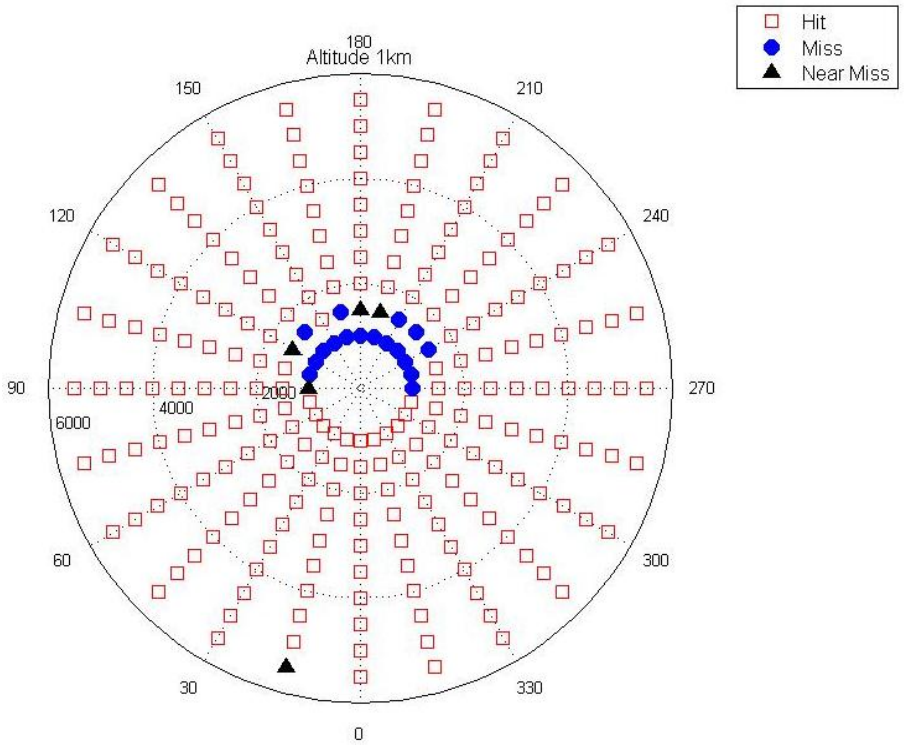

Figure 11-10 Aircraft altitude of 1km with no countermeasures.

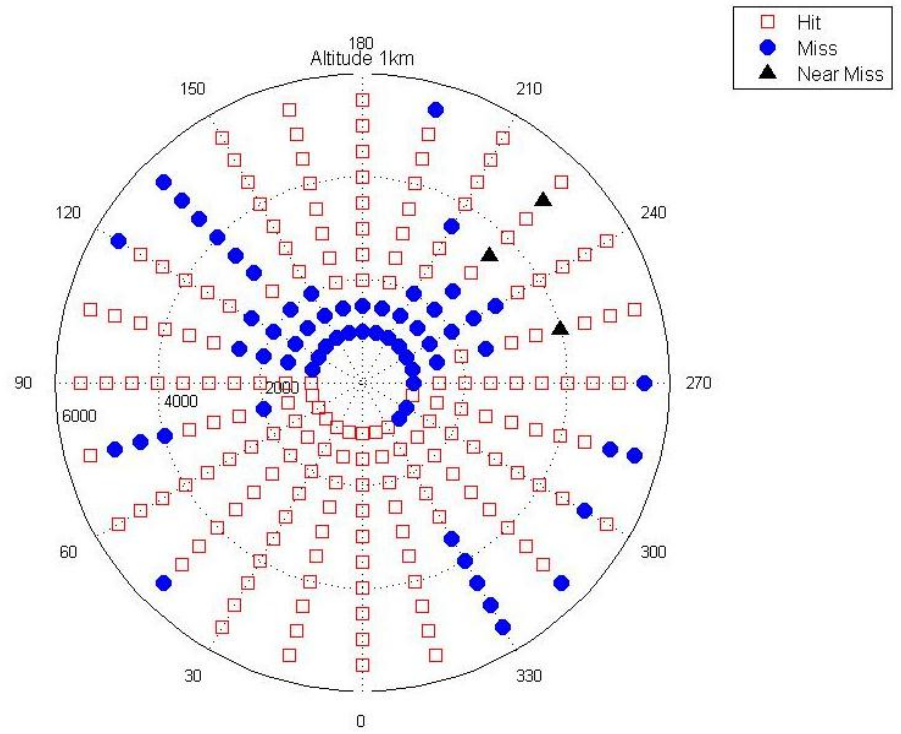

Figure 11-11 Aircraft altitude of 1km with reactive flares fired from the front dispensers.

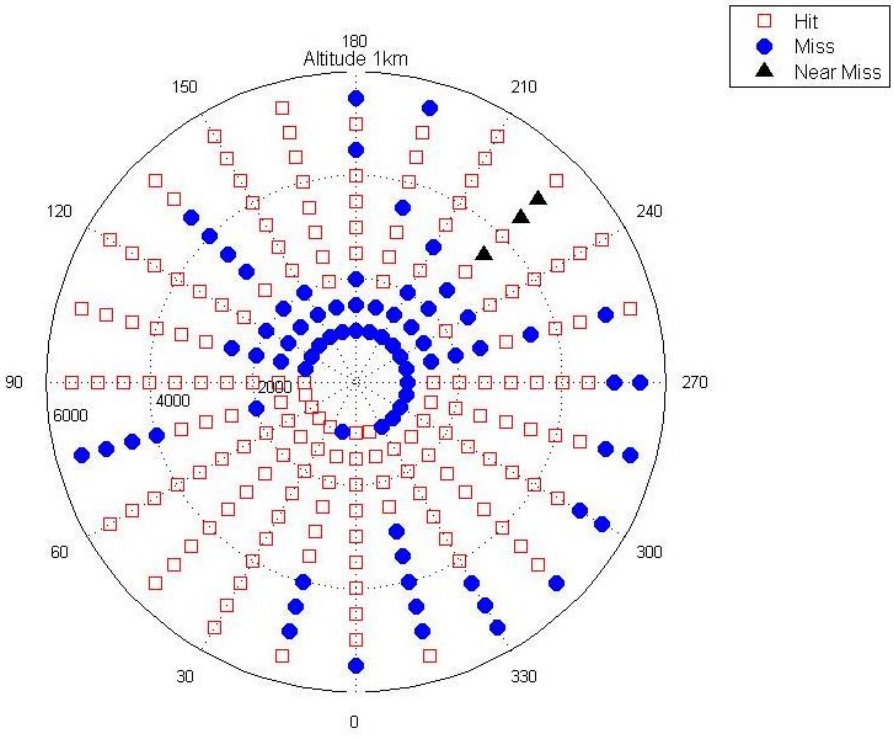

Figure 11-12 Aircraft altitude of 1km with reactive flares fired from the side dispensers.

The PEH when no flares are released is 0.09, compared to 0.05 for a single detector conscan seeker, a slight increase due to a few more close range head-on hits. For a single detector conscan seeker and reactive flares released from the front and side dispensers the PEH=1. When a two-colour conscan CCM is included in the seeker the PEH is 0.27 for the front dispensers and 0.33 for the side dispensers. The small difference is that the side dispensers offer slightly better protection in tail-on aspect engagements. In the second set of simulations flares are released from the front dispensers and side dispensers at half second intervals for constant slant ranges of 2km, 3km and 4km; the results are shown in Figure 11-13. It is clear that flares perform best in tail-on engagements whether released from the front or side dispensers. The maximum PEH for 0° azimuth and 2km, 3km and 4km slant ranges occurs at 2s, 3s and 5s respectively regardless of flare dispensers. All the other aircraft azimuths have a reduced PEH but the amount is dependent on the dispensers. The optimum flare release time is also dependent on the aircraft azimuth.

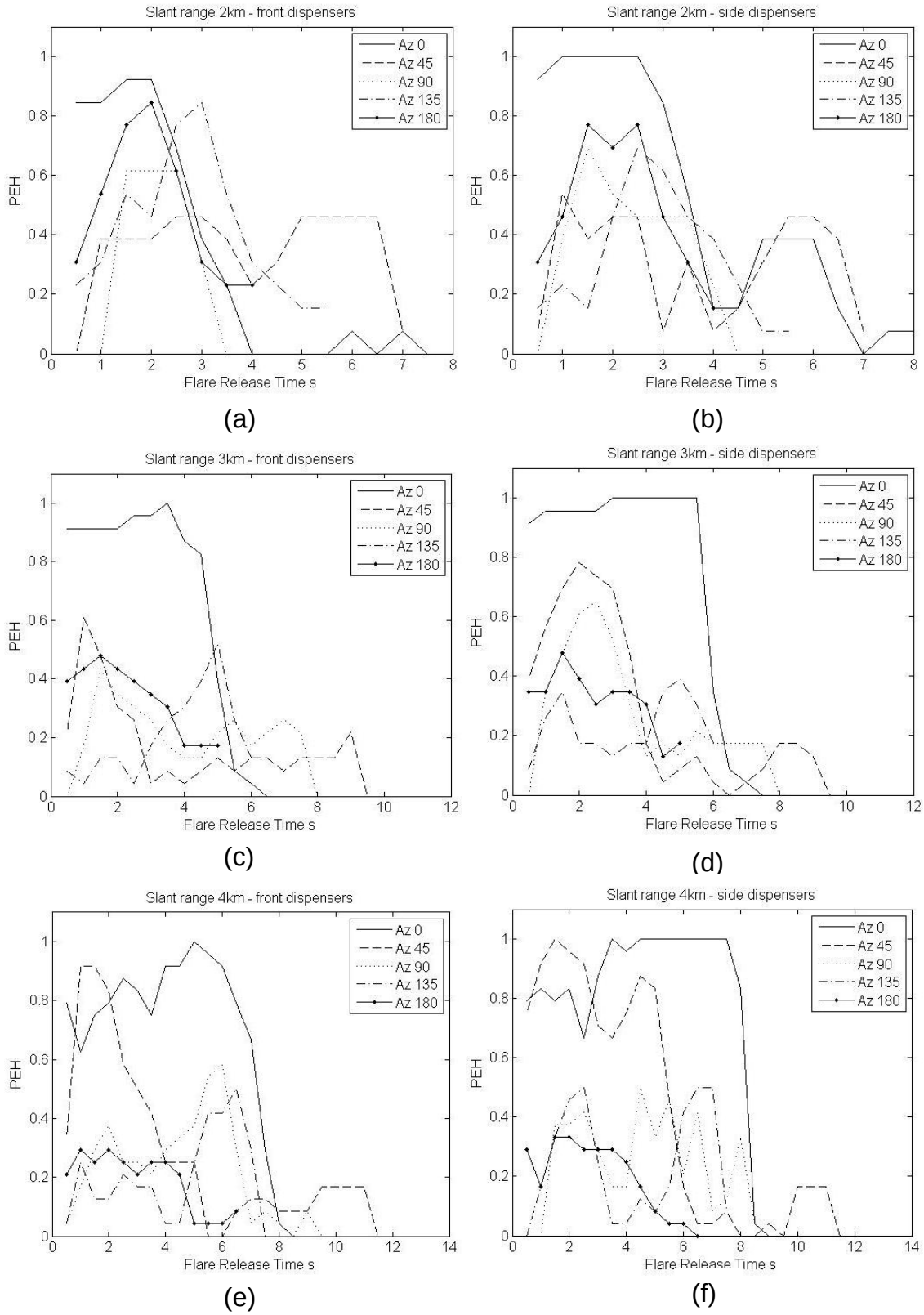

Figure 11-13 PEH versus flare release time for constant slant ranges 2km, 3km and 4km for flare release from the front and side dispensers.

For a slant range of 2km, Figure 11-13 (a) and (b), flare release between 2s and 3s gives the maximum PEH regardless of azimuth or flare dispensers. Azimuths 90°, 135° and 180° have a maximum PEH of between 0.6 and 0.8, but for an azimuth of 45° the PEH is always less than 0.5. For a slant range of 3km, Figure 11-13 (c) and (d), the front dispensers perform worst than the side for azimuths 45° and 90°. The side dispensers still show a peak at the 2s flare release time. Both dispensers give similar results for the other azimuths of 135° and 180°. For a slant range of 4km, Figure 11-13 (e) and (f), the maximum PEH for an azimuth of 45° is around 1.5s. All other azimuths give an unacceptably low PEH of less than 0.5 for any flare release time.

11.4 Conclusions

An IR conscan seeker has been modelled with a two-colour CCM and has shown a good capability of flare rejection. The PEH for each aircraft model releasing reactive flares is 0.33 for the AMX-A1, 0.27 for the C130 using the front dispensers and 0.33 for the C130 using the side dispensers. The next simulations released flares throughout an engagement to find the optimum flare release time for different slant ranges and aircraft azimuths.

For the AMX-A1 model and engagements with a crossing rate flare release around the time of missile launch gives the highest PEH. The only exception is an aircraft azimuth of 90° and a slant range of 2km where no flare release time gives a high PEH. For head-on engagements flare release slightly later, around 3s, gives a high PEH. For tail-on engagements flare release 7s before the hit point is the optimum flare release time. The simulations were repeated for the reduced performance flares which again confirmed the poor performance of the quarter burn time flare in tail-on engagements. Surprisingly, the quarter intensity flare performed the best in the same scenario which is probably due to the two-colour CCM. It is based on the intensity of the signal from different targets and was designed to defeat the standard flare. This also highlights the need for detailed knowledge on the possible threats faced by an aircraft and the fact that

countermeasures have to be effective against this possible range of MANPAD systems.

For the C130 model only tail-on engagements have a high PEH with flare release also around 7s before the hit point. For all other aircraft azimuths the PEH is greatly reduced. Because of this the simulations were not repeated for the reduced performance flares. Using single flares as a countermeasure protection for a larger, slower aircraft against a more sophisticated two-colour conscan seeker is not very effective irrespective of when they are released. This indicates one possible area for future work on the patterns and timing of multiple flare release.

12 CM CONTROLLER

In this chapter the previous results from Chapters 8 to 11 are analysed in further detail so that the information could be utilised in a CM controller for the two types of aircraft. To achieve this aircraft azimuths have to be looked at individually for each slant range and the results plotted with regard to possible threats and flare types.

12.1 Possible Threats

To illustrate, for the five azimuths between 0° and 180° different slant ranges were chosen and the PEH versus flare release time plotted for various threats. The first is a constant slant range of 2km and an azimuth of 45°. In the simulations the altitude ranges from 300m to 1500m therefore the distance ranges from 1323m to 1977m, from Pythagoras theorem. Figure 12-1 shows the positions of the distances on the polar plot and the PEH versus flare release time for the two aircraft models and four possible threats. Again, 0° is a tail-on engagement and the aircraft are positioned at the centre of the polar plot.

For a MANPAD with a conscan seeker and no CCM, then flare release anytime up to 1s prior to the hit point is effective as a decoy for both aircraft models. When a TAB CCM is included in the conscan seeker the time interval where the PEH=1 is significantly reduced with flare release after 3s too late. For the two-colour spinscan seeker the results are similar for both aircraft models, but for the C130 flare release up to 4s from the front dispensers is effective. For the two-colour conscan seeker and the AMX-A1 model the interval where the PEH=1 is further reduced.

In the majority of cases flare release between 1s and 2s from the start of the simulations gives a PEH=1. This time period covers missile launch, the half second ignition delay and the start of the boost thrust motor. The only exception is for the C130 model and a MANPAD with a two-colour conscan seeker where the maximum PEH is roughly 0.5.

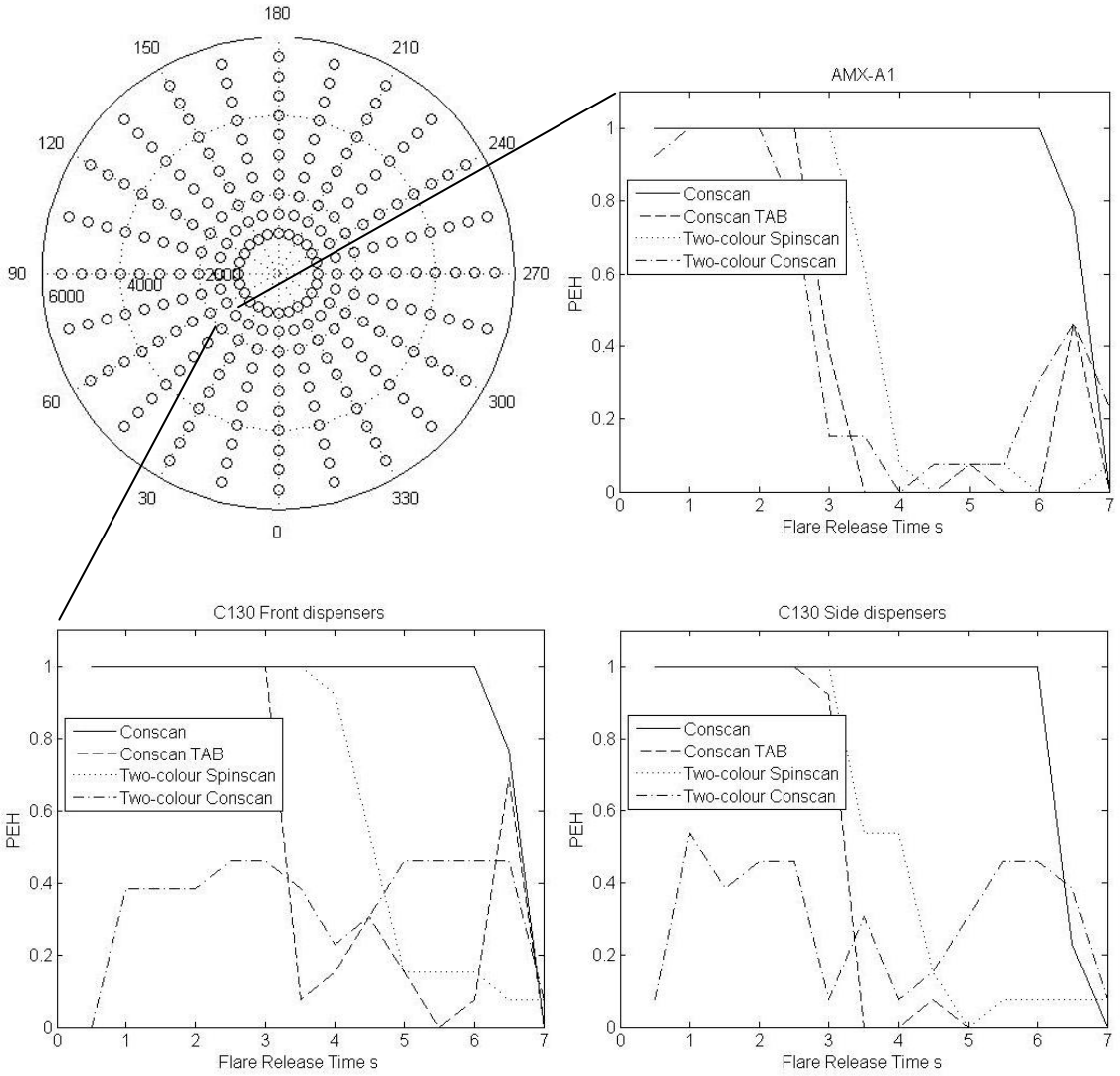

Figure 12-1 PEH versus flare release time for a constant slant range of 2km and an azimuth of 45°.

The second scenario is an azimuth of 90° and a constant slant range of 3km; the results are shown in Figure 12-2. For a slant range of 3km the altitude ranges from 500m to 2700m, giving the distance range of 1308m to 2958m shown on the polar plot. The results also show that flare release between 1s and 2s from the start of the simulation gives a PEH=1 for the majority of cases. Again, the exception is the C130 aircraft model and the two-colour conscan MANPAD model. In this instance the side dispensers give a higher PEH than the front dispensers for the two-colour conscan seeker. The conscan seeker with a TAB gives a slightly better performance than the two-colour spinscan

seeker. This could be due to the better tracking provided by a conscan system and the engagement being beam-on, which a TAB CCM is specifically designed for.

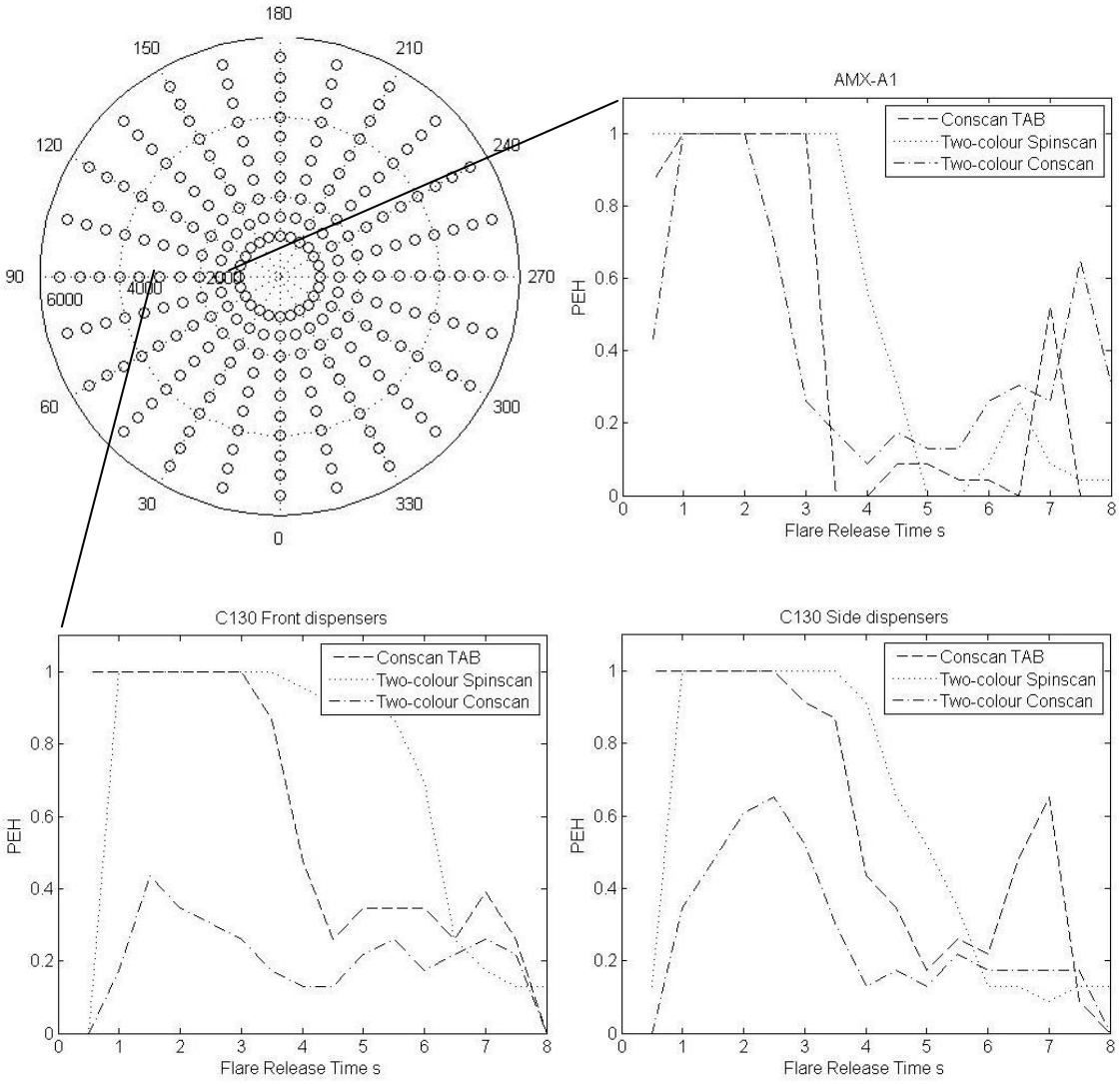

Figure 12-2 PEH versus flare release time for a constant slant range of 3km and an azimuth of 90°.

The third scenario is an azimuth of 0° and a slant range of 4km; the results are shown in Figure 12-3. For a slant range of 4km the altitude ranges from 700m to 300m, giving the distance range of 2646m to 3938m. In these simulations the conscan seeker with a TAB does not perform well, as expected due to the fact that there is no crossing rate in the engagements. For both aircraft models the two-colour spinscan seeker outperforms the two-colour conscan seeker. Flares

have to be released prior to 2s from the start of the simulation to give a high PEH. This was unexpected but the result is a consequence of the signal processor design for the two-colour spinscan seeker being particularly effective in tail-on engagements. The CCM models developed in this thesis may not be used in real systems and highlights the need to have detailed knowledge of the potential threats faced by an aircraft.

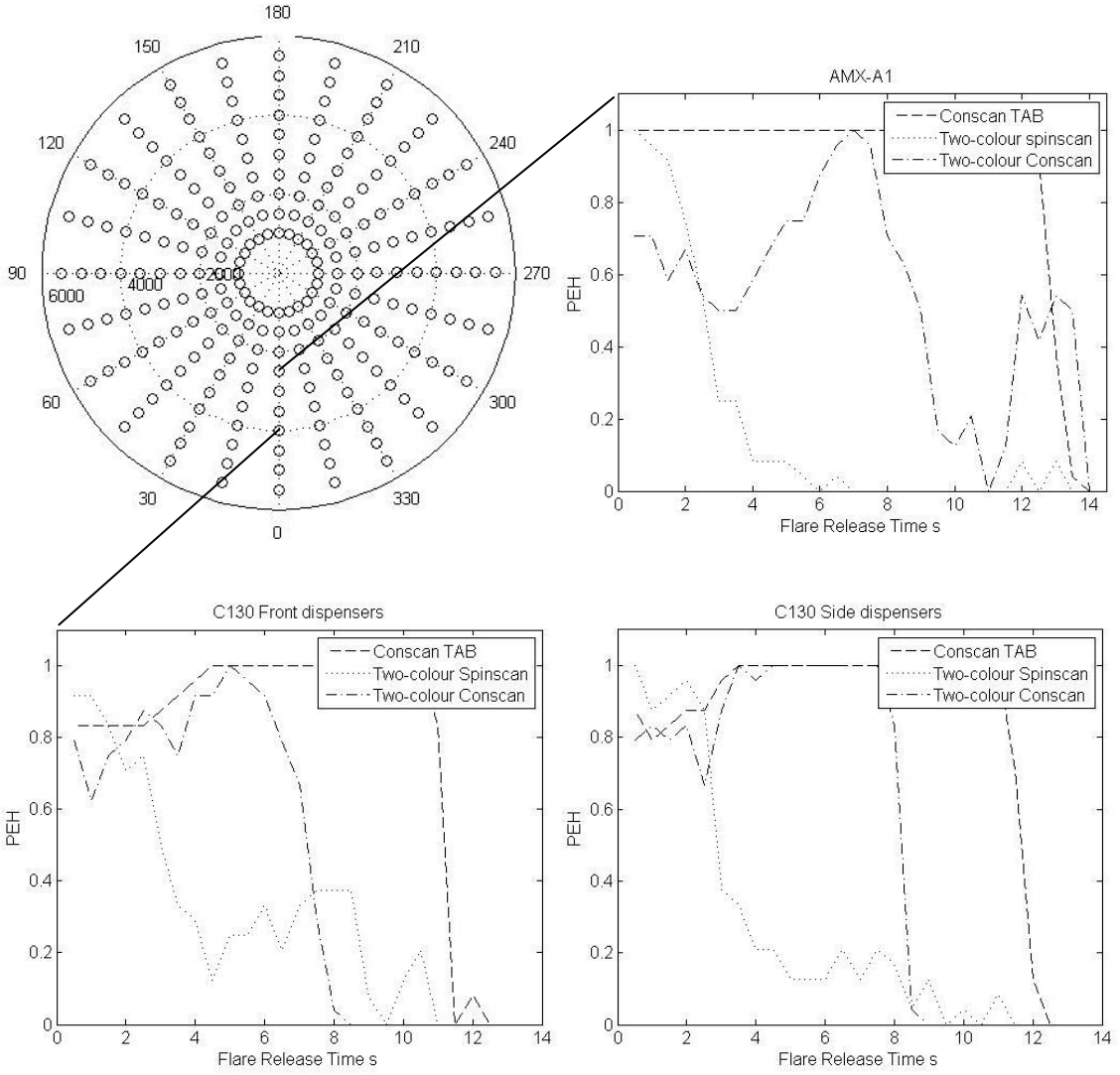

Figure 12-3 PEH versus flare release time for a constant slant range of 4km and an azimuth of 0°.

The fourth scenario is an azimuth of 135° and a slant range of 3km; the results are shown in Figure 12-4. For the AMX-A1 aircraft model flare release between 1s and 2s gives a PEH=1 for all MANPAD models. For the C130 aircraft model

flare release between 1s and 3s gives a PEH=1 for the conscan TAB and two-colour spinscan seekers. The front dispensers perform slightly better than the side against the conscan TAB seeker. Again, no flare release time for the C130 model is effective against the two-colour conscan seeker.

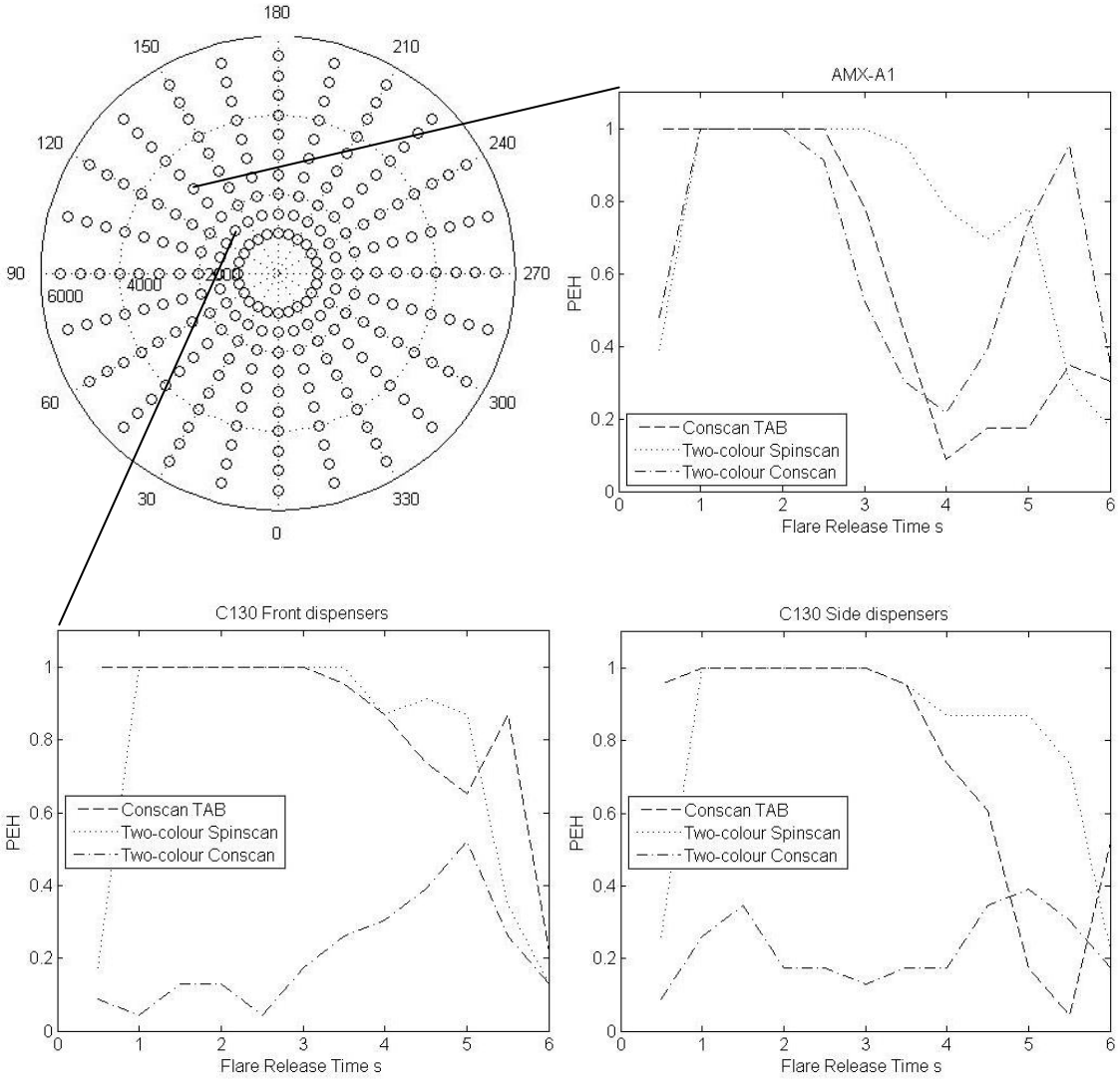

Figure 12-4 PEH versus flare release time for a constant slant range of 3km and an azimuth of 135°.

The fifth scenario is an azimuth of 180° and a slant range of 4km; the results are shown in Figure 12-5. For the AMX-A1 model flare release around 3s is effective against both two-colour seekers. For the C130 model flare release around 2s to 4s gives a high PEH against the two-colour spinscan seeker.

Again, no flare release time for the C130 model is effective against the two-colour conscan seeker.

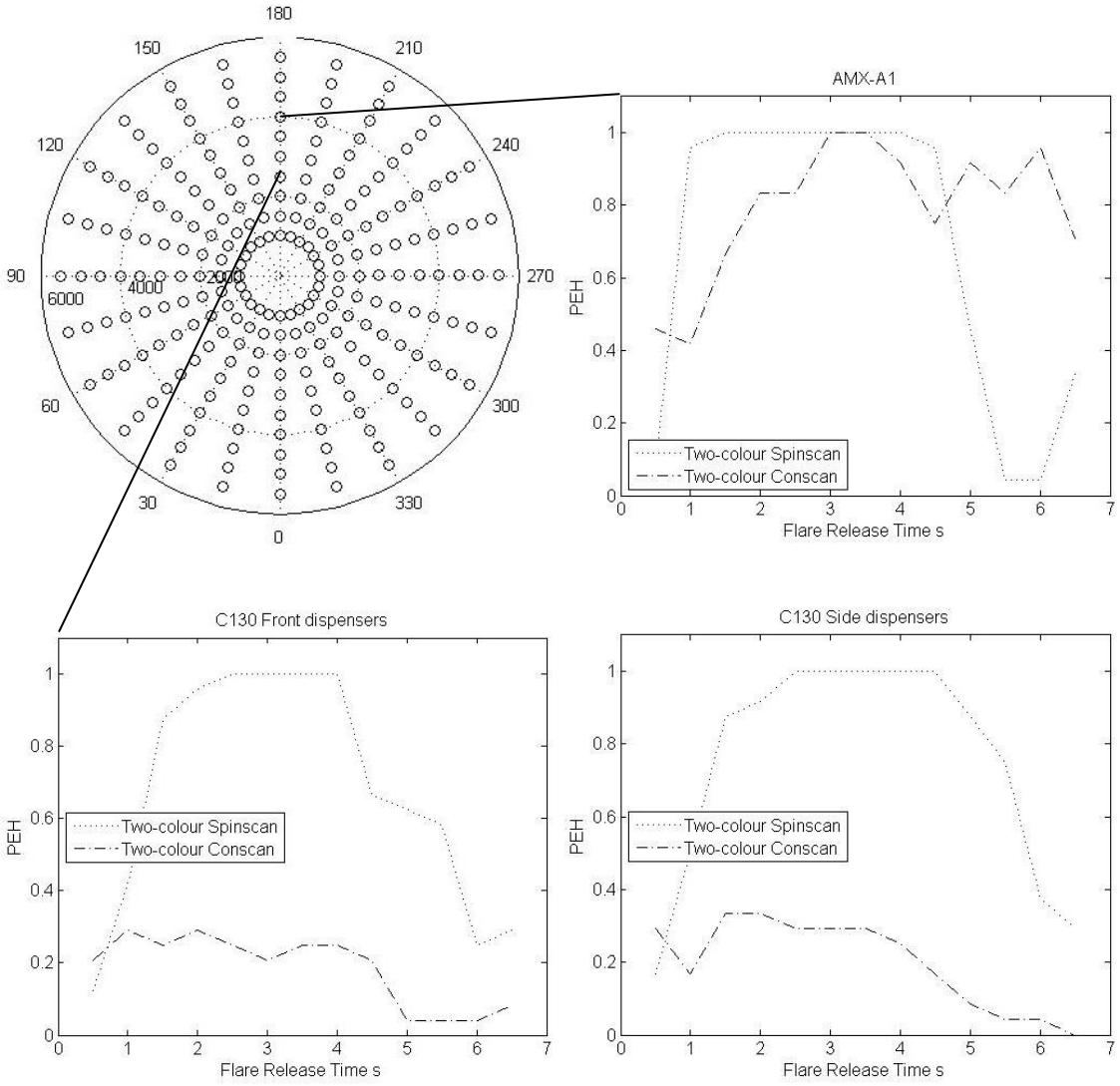

Figure 12-5 PEH versus flare release time for a constant slant range of 4km and an azimuth of 180°.

12.2 Flare Types

The analysis can be repeated but this time for the five different flare types to investigate whether reduced performance flares can offer the same level of protection. Again, individual slant ranges and azimuths have been chosen then flare release time versus PEH plotted for all flare types with regards to a single threat.

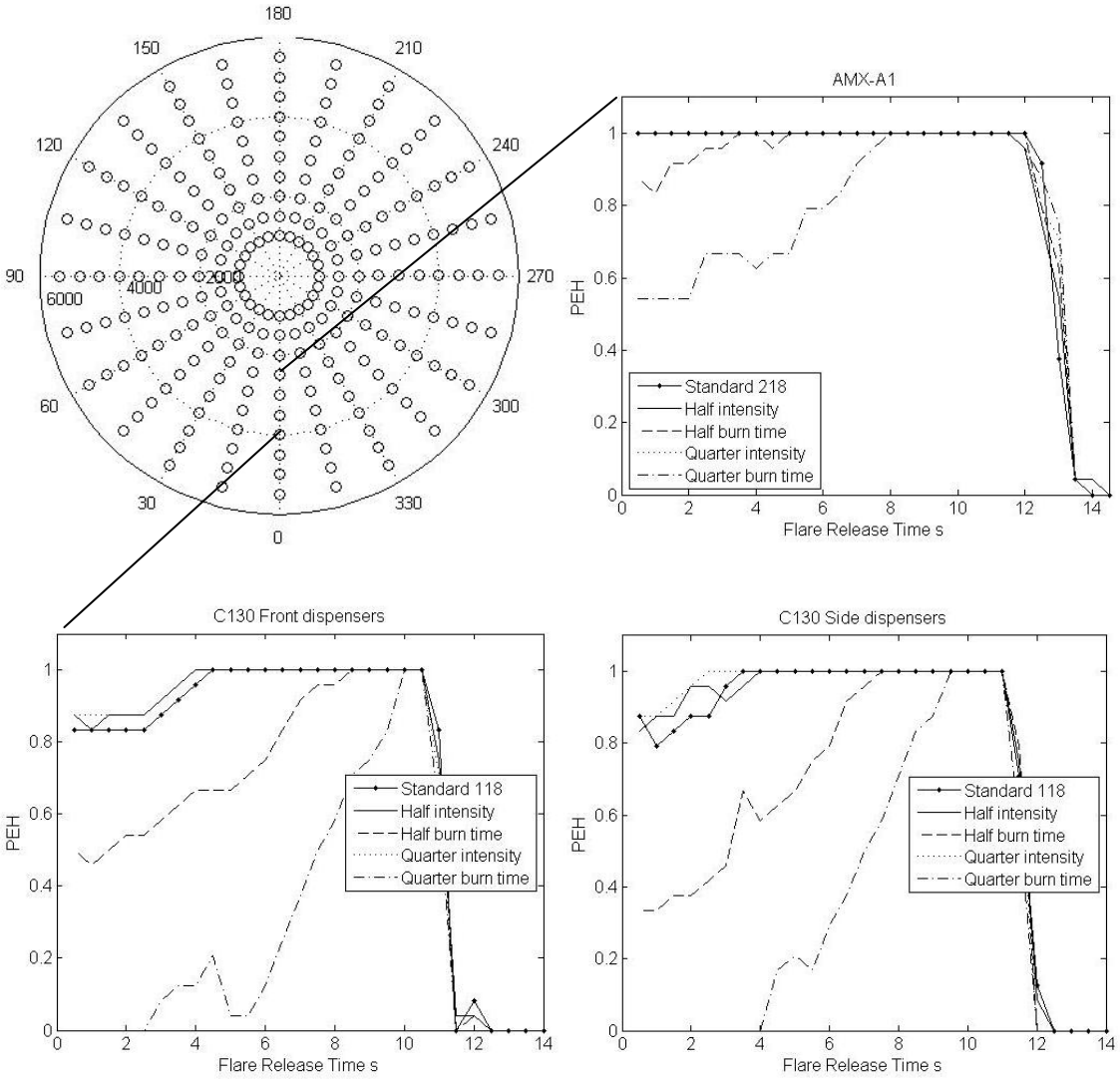

Figure 12-6 PEH versus flare release time for a constant slant range of 4km and an azimuth of 0° with regard to a conscan seeker with a TAB CCM.

The first scenario is a slant range of 4km and an azimuth of 0° for a conscan seeker with a TAB CCM, shown in Figure 12-6. The results show that the standard flares and the reduced intensity flares give similar values of the PEH for all flare release times. The reduced burn time flares perform less well with the quarter burn time flare the worst. To have the PEH=1 the quarter burn time flares have to be released around 10s for both of the aircraft models.

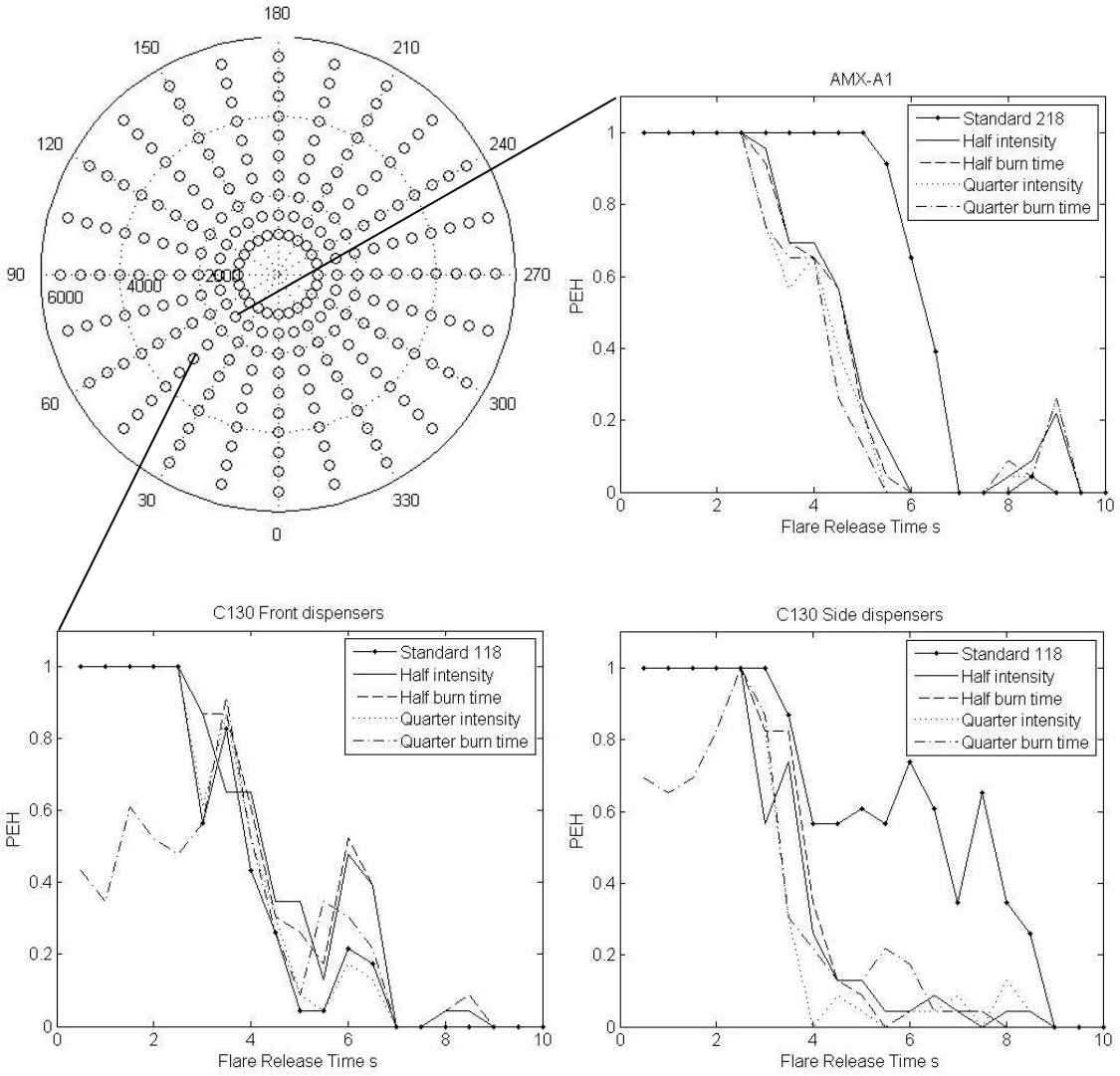

Figure 12-7 PEH versus flare release time for a constant slant range of 3km and an azimuth of 45° with regard to a conscan seeker with a TAB CCM.

The second scenario is a slant range of 3km and an azimuth of 45° for a conscan seeker with a TAB CCM, shown in Figure 12-7. For the AMX-A1 aircraft model the standard 218 flare performs the best with flare release up to 5s giving a PEH=1. All the reduced flare types give similar performance with flare release up to 3s giving a PEH=1. For the C130 aircraft model the standard 118 released from the side dispensers perform the best with the highest PEH for all flare release times. The reduced intensity and half burn time flares

perform roughly the same for both sets of dispensers. Again, the quarter burn time flare gives the worst performance for both dispensers.

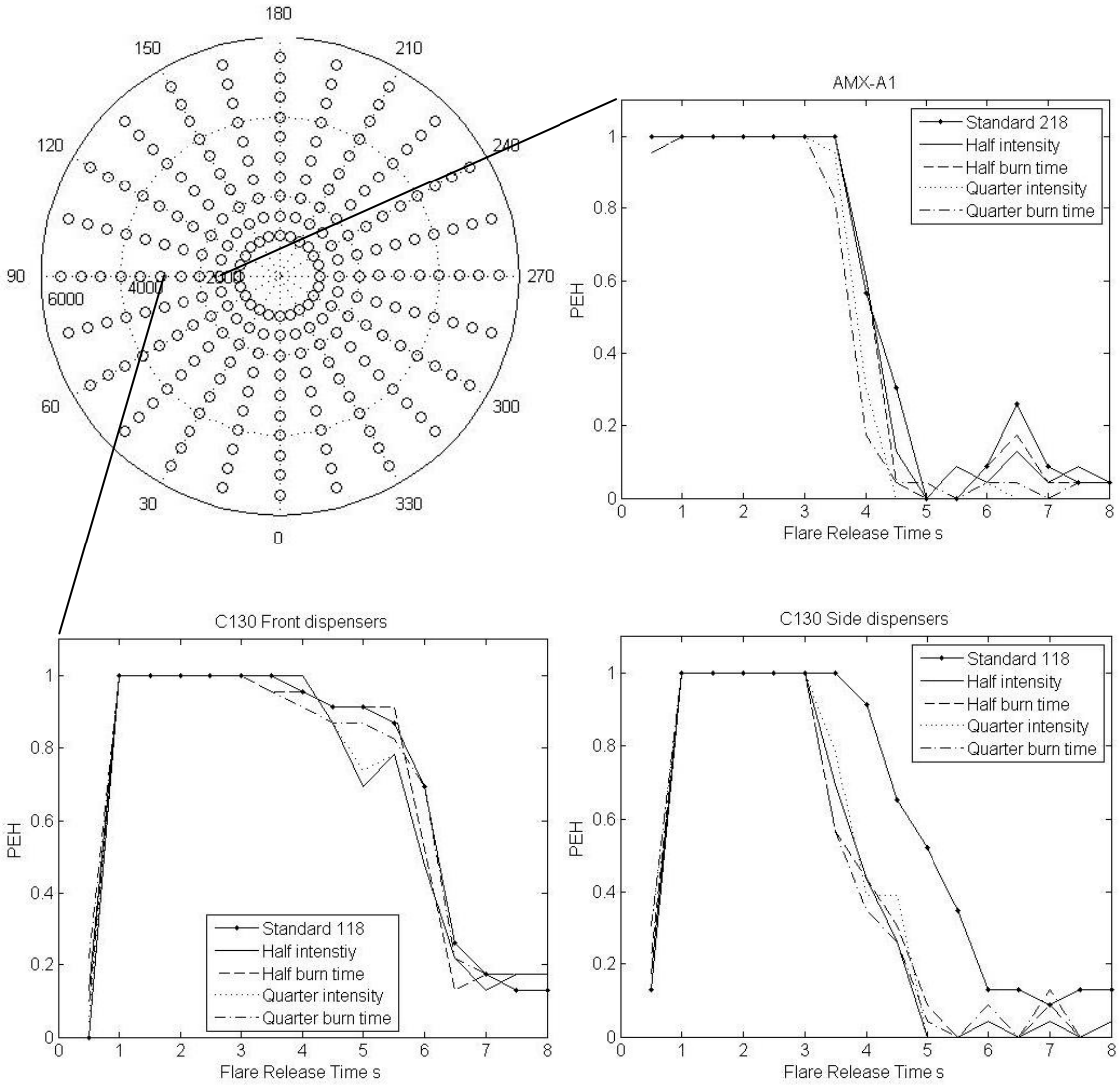

Figure 12-8 PEH versus flare release time for a constant slant range of 3km and an azimuth of 90° with regard to a two-colour spinscan seeker.

The third scenario is a slant range of 3km and an azimuth of 90° for a two-colour spinscan seeker, shown in Figure 12-8. For the AMX-A1 all flare types give similar values for the PEH for all flare release times. This is also the case for the C130 model and flares release from the front dispensers. For the side dispensers the standard 118 flare performs better than the reduced flares, which all give similar results. In this scenario the front dispensers offer a higher PEH for more flare release times than the side dispensers.

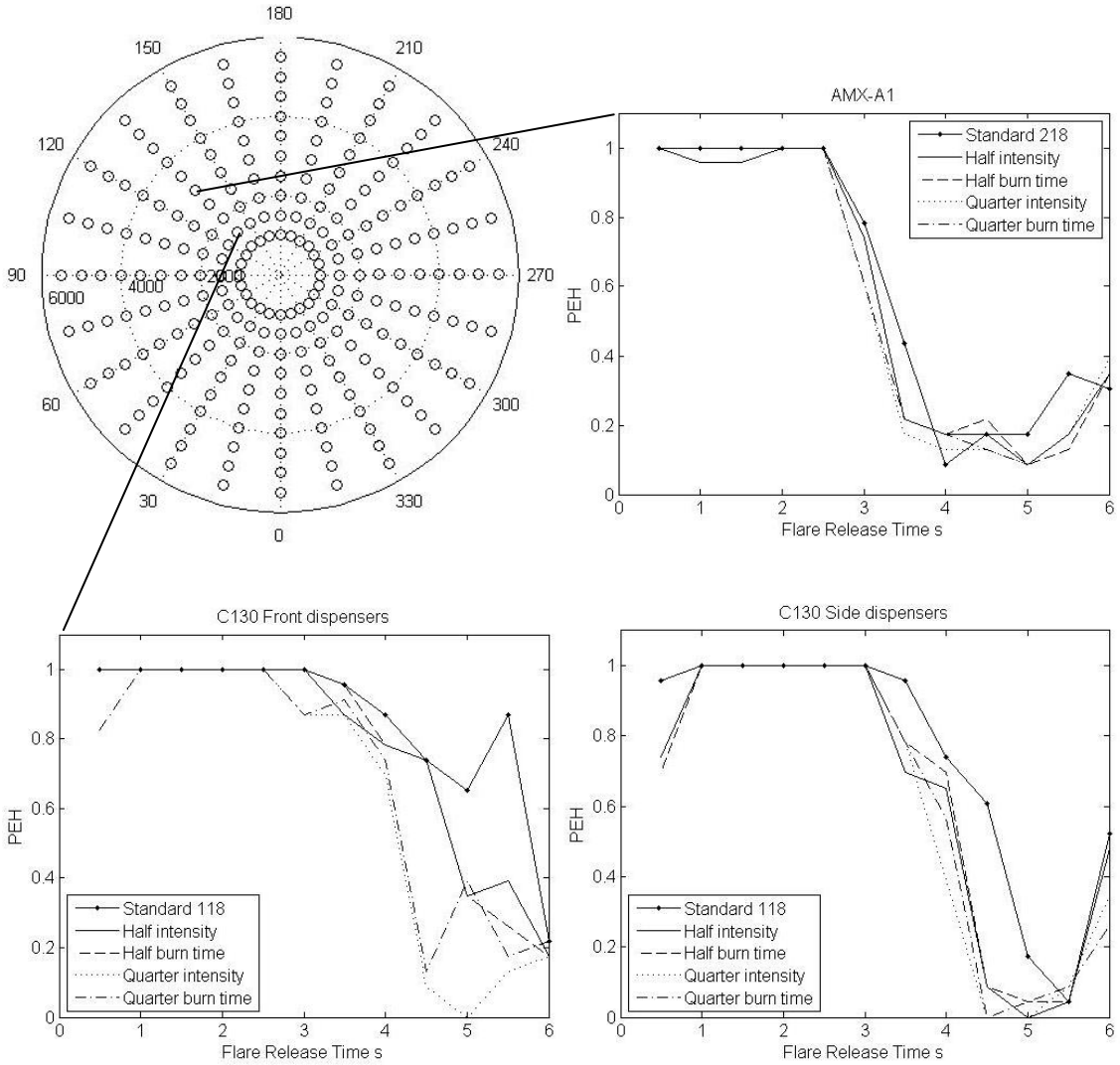

Figure 12-9 PEH versus flare release time for a constant slant range of 3km and an azimuth of 135° with regard to a conscan seeker with a TAB CCM.

The fourth scenario is a slant range of 3km and an azimuth of 135° for a conscan seeker with a TAB CCM, shown in Figure 12-9. Again, for the AMX-A1 all flare types give similar values for the PEH for all flare release times. For the C130 model the standard 118 flare gives the best results for both sets of dispensers with the front dispensers performing slightly better than the side. Also, the reduced performance flares give similar results for all the flare release times.

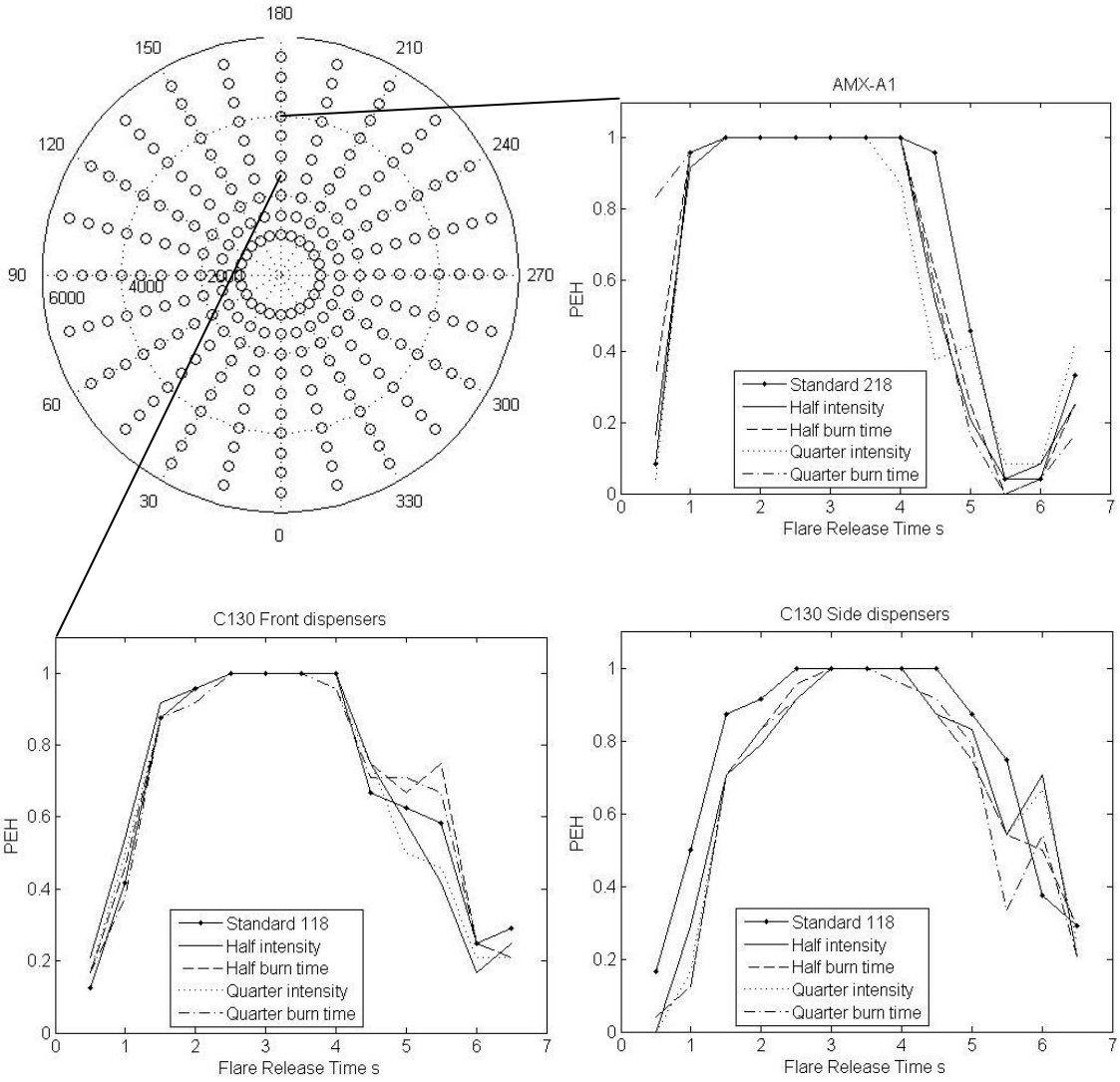

Figure 12-10 PEH versus flare release time for a constant slant range of 4km and an azimuth of 180° with regard to a two-colour spinscan seeker.

The fifth scenario is a slant range of 4km and an azimuth of 180° for a two-colour spinscan seeker, shown in Figure 12-10. For both aircraft models all flare types give similar results with the optimum release time around 3s. The window where the PEH=1 is slightly longer for the AMX-A1 model, about 2s, compared to 1s for the C130 model. For the C130 both dispensers give similar results.

12.3 Conclusions

The PEH versus flare release time has been plotted for some slant ranges and azimuths with regard to possible threats and flare types. It indicates that the

optimum flare release time is dependent on the angle of attack and the threat faced. Also, that reduced performance flares can offer the same level of protection in certain situations.

The previous analysis can be performed in more detail for each slant range and azimuth to design an algorithm for a CM controller. This would be dependent on a MAWS being able to detect the missile launch and providing directional information on the threat, Figure 12-11.

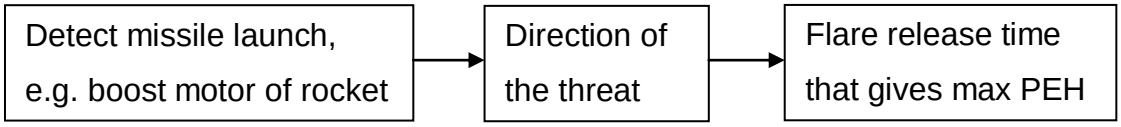

Figure 12-11 Logic for a CM controller.

Another outcome of the analysis is the possibility of flares released at timed intervals(94). (Appendix B discusses a simulation with flares released at timed intervals.) In the majority of case there is a window where the PEH=1 and if this window is 2s then flare release every 2s would protect the aircraft. Furthermore, if the reduced flares offer the same level of protection, then the aircraft could carry more and prolong the flight time. This is especially the case for a quarter intensity flare which shows better results than the quarter burnt time flare.

13 CONCLUSIONS AND FUTURE WORK

In this thesis different types of MANPAD have been modelled and they have utilised a spinscan or a conical scan IR seeker. Base runs were carried out where the aircraft released no countermeasures to give an indication of the underlying performance of the MANPAD models. Flares were then released at the start of the simulations, t=0s, and delayed up to t=1s in intervals to test pre-emptive countermeasures as missile launch occurs after this time. Reactive flares were also released at a specific detection range for comparison. Next, CCMs were included in the IR seeker; a TAB with a rise rate trigger and a two-colour CCM. The use of pre-emptive and reactive flares was again compared but this time against these more capable threats. Table 13-1 gives a summary of the PEH for each type of seeker for the two aircraft models releasing no flares and reactive flares. The PEH is for an aircraft altitude of 1km and consists of 240 simulations each (10 missile ranges x 24 aircraft azimuths).

Table 13-1 Summary of the PEH for each IR seeker and CCM.

	AMX		C130		
	No Flares	React Flares	No Flares	React Flares	
				Front	Side
Spinscan	0.19	1.00	0.27	1.00	1.00
Conscan	0.11	1.00	0.05	1.00	1.00
Conscan TAB	0.11	0.47	0.05	0.61	0.48
Spinscan Two Colour	0.23	0.38	0.17	0.63	0.45
Conscan Two Colour	0.20	0.34	0.09	0.27	0.33

Having shown that reactive flares are less effective against more advanced MANPADs with a CCM capability the next simulations looked at when flares are fired. Firing flares throughout an engagement will give the optimum release time for each aircraft azimuth and distance and for each threat the aircraft might face.

The results show that if flares are released earlier in an engagement than reactively they still offer high protection for the aircraft. The window of release covers the application of lead and super elevation, missile launch, the half second ignition delay after launch and the half second after boost thrust ignition. For the transport aircraft using both the front and side dispensers is inefficient. The side dispensers are generally better in tail-on engagements and the front dispensers for engagements with a crossing rate. Flares of reduced intensity give similar results to the standard flares but flares of reduced burn time perform worse. For the reduced burn time flares and the fast jet model only the tail-on engagements are worse with the window of flare release still present in engagements with a crossing rate. For the reduced burn time flares and the transport aircraft the majority of aircraft azimuths are worse with no window of flare release giving maximum protection to the aircraft.

The results for the optimum flare release time could be used in the CM controller of a Common Defensive Aids Suite (CDAS). Where simultaneous release of two flares is not effective, e.g. against a two-colour conscan CCM, future work could look at multiple flares fired in patterns or in a timed sequence. Different flare models could also be used that have varying rise time. These, coupled with an aircraft manoeuvre after flare release, may offer a greater level of protection. Another aspect of future work could look at the operational analysis of aircraft. The results indicate that releasing 2 flares every 2s is effective in the majority of situations. For example, if a transport aircraft can carry 300 flares then this gives a protected flight time of 150 (300 flares/2) x 2s, which is 5 minutes. This can then be compared to the needs stated in the operational analysis. Is this flight time long enough, or would more flares need to be carried or the interval timings extended?

There are several provisos to the simulations, the main one being that they are just simulations with models based on open source literature. The results may or may not be indicative of real life but they illustrate that significant conclusions can be made from studies of this type. The next step is verification and validation using models with accurate input data, hardware in the loop (HWIL)

simulations and live field trials. However, the conclusions from the modelling work could clearly be used to reduce the number of field trials which are extremely costly.

The simulations for varying flare release time did not include noise of any type or atmospheric attenuation. This therefore represents the best possible case for the IR seeker and the window of flare release where the PEH=1 may be longer.

The standard flares give a J/S ratio of 40:1 for the AMX-A1 and 10:1 for the C130. The reduced intensity flares will therefore still offer a high level of protection, especially for the AMX-A1. To further test flares of reduced payload size future simulations will need to have a greater level of fidelity. This includes accurate radiant intensities for the aircraft models, validated models for the IR seekers and full scene simulation (e.g. atmospheric attenuation, background, solar reflectance).

REFERENCES

1. *The anatomy of the MANPAD.* **Richardson, M.** 2006, Technologies for optical countermeasures IV, Proc. of SPIE, p. 6738.

2. **Bureau of Political-Military Affairs.** *The MANPADS Menace: Combating the Threat to Global Aviation from Man-Portable Air Defense Systems Fact Sheet* : U.S. Department of State, September, 2005.

3. **Congressional Research Service Report for Congress RL31741.** *Homeland Security: Protecting Airliners from Terrorist Missiles.* 2006.

4. *Wikileaks releases 'confirm Afghanistan MANPADS threat'.* **Wasserbly, Daniel.** 28 July 2010, Jane's Defence Weekly.

5. **Jane's Intelligence Review.** *Mombasa Attack Highlights Increasing MANPADs Threat.* February, 2003.

6. *The Proliferation of MANPADS.* **Hunter, Thomas B.** November 28, 2002, Jane's Intelligence Review.

7. *RAF Tristars upgraded with defensive systems.* **Ripley, T.** April 13 2005, Jane's Defence Weekly.

8. [Online] http://www.driir.com/technical2.html (accessed August 2011).

9. **Hudson, R.D.** *Infrared System Engineering.* London : Wiley, 1969.

10. **Driggers, Ronald, Cox, Paul and Edwards, Timothy.** *Introduction to Infrared and Electro-Optical Systems.* 1999 : Artech House.

11. [Online] http://www.enseki.or.jp/e_tokusei.html (accessed August 2011).

12. **Rogatto, William D.** Electro-Optical Componenets Volume 3. *The Infrared & Electro-Optical Systems Handbook* : SPIE Press, 1993.

13. **Richardson, M.A.** *Electro Optics and Infrared Sensors course notes.* Cranfield University, Defence Academy of the UK : GW/MESE MSc, 2008.

14. **Klocek, P.** *Handbook of Infrared Optical Materials.* London : Marcel Dekker, 1991.

15. **Zissis, Geaorge J.** Sources of Radiation Volume 1. *The Infrared & Electro-Optical Systems Handbook* : SPIE Press, 1993.

16. **Dudzik, Michael C.** Electro-Optical Systems Design, Analysis, and Testing Volume 4. *The Infrared & Electro-Optical Systems Handbook* : SPIE Press, 1993.

17. **Campana, Stephen B.** Passive Electro-Optical Systems Volume 5. *The Infrared & Electro-Optical Systems Handbook* : SPIE Press, 1993.

18. [Online] http://mail.gpacademy.org/~rochter/ELECTRO-OPTICS.htm (accessed August 2011).

19. **Smith, Frederick G.** Atmospheric Propogation of Radiation Volume 2. *The Infrared & Electro-Optical Systems Handbook* : SPIE Press, 1993.

20. **Biberman, L.M.** *Reticles in Electro Optical Devices.* Elmsford, NY : Pergamon Press, 1966.

21. *Electro-Optic and Infrared Sensors.* **May, John and Van Zee, M.E.** September, 1983, Microwave Journal.

22. *The technique of spatial filtering.* **Aroyan, Geaorge F.** Paper 4.3.2 p.1561, September 1959, Proceedings of the IRE.

23. *Digital simulation of reticle systems.* **Craubner, S.** 1981, Optical Engineering, Vol. 20(4), pp. 608-615.

24. *Infrared Systems: I. Expressions for signal and background induced noise with space filters.* **Samuelsson, Hans.** January 1971, IEEE Transaction on Aerospace and Electronic Systems, Vols. AES-7 No.1.

25. *Infrared Systems: II. Accuracy of angle measurement.* **Samuelsson, Hans.** January 1971, IEEE Transactions on Aerospace and Electronic Systems, Vols. AES-7 No.1.

26. *The interaction in the development of optical missile seekers and jammer technology.* **Titterton, D.H.** October 2010, The Imaging Science Journal, Vol. 58.

27. **Hong, Hyun-Ki et al.** Reticles-Rotating Systems. *Encyclopedia of Optical Engineering* : Marcel Dekker, 2003.

28. *Simulation of reticle seekers by means of an image processing system.* **Olsson, Gustaf.** March 1994, Optical Engineering, Vol. 33(3), pp. 730-736.

29. *Optimum modultaion characteristics for amplitude-modulated and frequency-modulated infrared systems.* **Butterweiler, T.B.** 1961, Journal of the Optical Society of America, Vol. 51(9), pp. 1011-1015.

30. *Comparison of AM and FM reticle systems.* **Carpenter, R.** 1963, Applied Optics, Vol. 2(3), pp. 2229-236.

31. *Parameters of spinning AM reticles.* **Driggers, R.G. et al.** 1991, Applied Optics, Vol. 30(19), pp. 2675-2684.

32. **Deyerle, Craig M.** Reticle Based Missile Seekers, Encylcopedia of Optical Engineering : Marcel Dekker, 2003.

33. **Pollock, David H.** Countermeasure Systems Volume 7. *The Infrared & Electro-Optical Systems Handbook* : SPIE Press, 1993.

34. *Strela-2.* 2011, Jane's Land-Based Air Defence.

35. [Online] http://www.fas.org/man/dod-101/sys/missile/row/sa-7.htm (accessed August 2011).

36. [Online] http://www.globalsecurity.org/military/world/russia/sa-7.htm (accessed August 2011).

37. *Strela-2M.* 2011, Jane's Land-Based Air Defence.

38. [Online] http://www.fas.org/programs/ssp/asmp/MANPADS.html (accessed August 2011).

39. **Jahng, Surng-Gahb et al.** Reticles-Nutating Systems. *Encyclopedia of Optical Engineering* : Marcel Dekker, 2003.

40. *Parameters of spinning FM reticles.* **Driggers, R.G. et al.** 1991, Applied Optics, Vol. 30(19), pp. 887-895.

41. *Parameter analysis for frequency-modulation reticle design.* **Chao, Z.W. et al.** 1988, Optical Engineering, Vol. 27(6), pp. 443-451.

42. *Target position extraction based on instantaneous frequency estimation in a fixed-reticle seeker.* **Han, S.H. et al.** 2000, Optical Engineering, Vol. 39(9), pp. 2568-2573.

43. [Online] http://www.fas.org/man/dod-101/sys/missile/row/sa-14.htm (accessed August 2011).

44. *Strela-3.* 2011, Jane's Land-Based Air Defence.

45. [Online] http://www.globalsecurity.org/military/world/russia/sa-14.htm (accessed August 2011).

46. *KBM Kolomna 9M313 Igla-1 (SA-16 'Gimlet) man-portable antiaircraft missile.* 2011, Jane's Electro-Optic Systems.

47. [Online] http://www.globalsecurity.org/military/world/russia/sa-16.htm (accessed August 2011).

48. [Online] http://www.fas.org/man/dod-101/sys/missile/row/sa-16.htm (accessed August 2011).

49. [Online] http://www.fas.org/man/dod-101/sys/land/stinger.htm (accessed August 2011).

50. [Online] http://www.globalsecurity.org/military/systems/ground/stinger.htm (accessed August 2011).

51. [Online] http://www.fas.org/man/dod-101/sys/land/row/mistral.htm (accessed August 2011).

52. [Online] http://www.globalsecurity.org/military/world/russia/sa-18.htm (accessed August 2011).

53. [Online] http://www.fas.org/man/dod-101/sys/missile/row/sa-18.htm (accessed August 2011).

54. *KBM Kolomna 9M39 Igla (SA-18 'Grouse') man-portable anti-aircraft missile.* 2011, Jane's Electro-Optic Systems.

55. *KBM Kolomna 9M342 Igla-S (SA-24 'Grinch') man-portable anti-aircraft missile.* 2011, Jane's Electro-Optic Systems.

56. *Raytheon FIM-92 Stinger man-portable anti-aircraft missile.* 2010, Jane's Electro-Optic Systems.

57. **Boreman, Glenn D.** *Modulation Transfer Function in Optical and Electro-Optical Systems.* Bellingham WA : SPIE Press, 2001.

58. **Zarchan, Paul.** *Tactical and Strategic Missile Guidance.* Reston, Virginia : American Institute of Aeronautics and Astronautics, 1997.

59. [Online] http://www.globalsecurity.org/military/systems/aircraft/systems/an-alq-156.htm (accessed August 2011).

60. [Online] http://www.chemringcm.com/Products/AirProducts/Flares/SquareFormat/ (accessed August 2011).

61. **Baqar, S.** *Low-cost PC-based high fidelity infrared signature modelling and simulation.* Cranfield Defence and Security : PhD Thesis, 2007.

62. *Infrared countermeasure flares.* **Withey, M.D.** October 2010, The Imaging Science Journal, Vol. 58.

63. *Dynamic simulations of infrared reticle seekers and an efficient counter-countermeasure algorithm.* **Han, Sung-Hyun et al.** August 1997, Optical Engineering, Vol. 36(8), pp. 2341-2345.

64. *Analysis of the spinning CAR reticle seeker and an effective counter-countermeasures algorithm.* **Hong, H. et al.** 1998. Proc SPIE 3365, 169.

65. *Novel adaptive digital signal processing algorithm for a staionary reticle seeker.* **Oh, J.S. et al.** 2000, Optical Engineering, Vol. 39(10), pp. 2797-2803.

66. *Simulation of target detection in ultraviolet and infrared bands.* **Doo, Kyoung-Soo et al.** November 2001, Optical Engineering, Vol. 40(11), pp. 2646-2654.

67. *Adaptive infrared counter-countermeasures for two-color spinning concentric-annular-ring reticle seeker.* **Hong, H.K. et al.** 2001, Optical Engineering, Vol. 40(6), pp. 1093-1099.

68. *New two-color cancellation algorithm for counter-countermeasures of infrared seekers.* **Oh, J.S. et al.** 2001, Optical Engineering, Vol. 40(8), pp. 1699-1708.

69. *Two-colour infrared counter-countermeasures based on the signal ratio between two detection bands for a crossed-array tracker.* **Oh, Jeong-Su et al.** September 2005, Optical Engineering, Vol. 44(9).

70. *Assessment of the performance of a new decoy dispenser pod against 2nd generation IR MANPADs.* **D'Amico, P. et al.** 2011, Journal of Battlefield Technology, Vol. 14(1).

71. *Northrop Grumman AN/AAQ-24(V) Nemsis Directional Infra-Red CounterMeasures (DIRCM) and Large Aircraft Infra-Red Countermeasures (LAIRCM) systems.* 2011, Jane's Electro-Optic Systems.

72. [Online]
http://www.globalsecurity.org/military/systems/aircraft/systems/ircm.htm
(accessed August 2011).

73. *The future of airborne expendables.* **Knowles, J.** May 2010, The Journal of Electronic Defense.

74. [Online]
http://www.chemringcm.com/AboutUs/TechnologyServices/ModellingSimula/
(accessed February 2010).

75. **General, Dynamics.** *The world's missile systems eighth edition.* Pomona : Pomona Division, General Dynamics, 1988.

76. **Rouse, J.F.** *Guided Weapons Fourth Edition.* London : Brassey's Land Warfare, 2000.

77. **Birchenall, R.** *Reactive and Pre-Emptive Countermeasures Against IR Man Portable Air Defence Systems.* Cranfield Defence and Security : MSc Thesis, 2008.

78. **Hock, N.** *The MANPAD Threat to Commercial Aircraft.* Cranfield Defence and Security : MSc Thesis, 2004.

79. *The MANPAD threat to commercial aircraft.* **Hock, N. et al.** Novemeber 2002, Journal of Battlefield Technology, p. 5(3).

80. **Johnson, H.** *The use of Flare Countermeasures on Large Civilian Aircraft.* Cranfield Defence and Security : MSc Thesis, 2005.

81. *Modelling the improved protection of fast jets from the IR MANPADs threat.* **Tranquillino-Minerva, N et al.** 2006, Technologies for Optical Countermeasures III, Proc. SPIE, pp. 6397-17.

82. *The alpha-beta-gamma tracking filter with a noisy jerk as the maneouvre model.* **Sudano, J.** 30(3), July 1994, IEEE Transactions on Aerospace and Electronic Systems.

83. [Online] http://www.modtran.org (accessed January 2010).

84. **Metropolitan Police.** *MANPADS Forensic Report SA-7.*

85. **Metropolitan Police.** *MANPADS Forensic Report SA-14.*

86. [Online] http://www.enemyforces.net/aircraft/amx.htm (accessed August 2011).

87. [Online] http://www.belgian-wings.be (accessed August 2011).

88. *Analysis of first generation MANPAD attacks on fast jets.* **Jackman, James et al.** 2009. Proc. SPIE 7483, 74830I.

89. [Online] http://local.wasp.uwa.edu.au/~pbourke/geometry/lineline3d/ (accessed February 2010).

90. *The effect of pre-emptive flare deployment on first generation man-portable air-defence (MANPAD) systems.* **Jackman, James et al.** 2010, The Journal of Defense Modeling and Simulation, pp. vol. 7 no.3 181-189.

91. *Effect of payload size on pre-emptive flare countermeasures against MANPAD system.* **Jackman, James et al.** 2010. Proc SPIE 7836, 78360M.

92. *Effect of pre-emptive flares on MANPAD systems with a track angle bias CCM.* **Jackman, James et al.** 2010. Proc SPIE 7836, 78360N.

93. *Simulating pre-emptive countermeasures of varying performance against a Man-Portable Air-Defence (MANPAD) system with a track angle bias counter-countermeasures (CCM).* **Jackman, James et al.** 2011, Infrared Physics & Technology, Vol. 54, pp. 121-129.

94. *Pre-emptive Vs reactive infrared countermeasures.* **Taylor, B.** March 2000, Journal of Electronic Defense.

95. [Online] https://simdis.nrl.navy.mil (accessed August 2011).

APPENDICES

Appendix A Asymmetry of Polar Plots

Producing the polar plots for different aircraft and MANPAD models indicated some asymmetry around the 0° axis. The effect is not very evident where the aircraft release no countermeasures. Figure A-1 (a) is for the AMX-A1 model at an altitude of 1km against a spinscan IR seeker with the reticle rotating anticlockwise. In that instance only two MANPAD firing positions give different results. The simulations were repeated but this time the only change was the reticle rotating in the clockwise direction, the results are shown in Figure A-1 (b). Again, there are only a few positions where the results are different about the 0° axis.

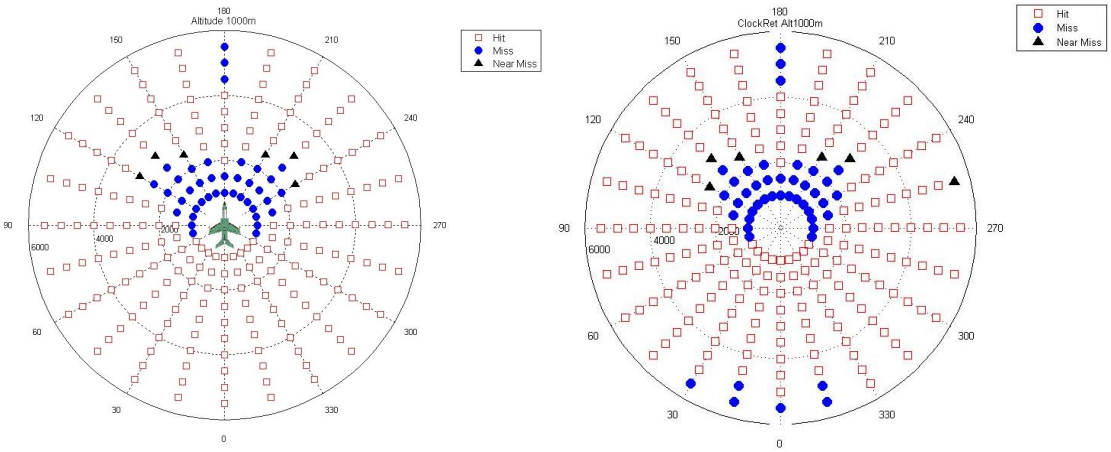

(a) (b)

Figure A-1 AMX-A1 model with no countermeasures against a spinscan IR seeker with reticle rotating (a) anticlockwise and (b) clockwise.

To investigate possible reasons for the different results two engagements were chosen that are mirror images about the 0° axis. They are from Figure A-1 (b) for a distance of 5500m and azimuths 30° and 330°. Given the symmetrical nature of the two engagements both should have the same result, however, the one for 30° was a miss and the one for 330° was a hit. The path of the missile projected on to the x-z plane was plotted for the two engagements and is shown

in Figure A-2 (a). The missile path for the miss, 30°, shows a slightly higher initial trajectory. In the engagement the missile looses lock at 9s so the tracking provided by the seeker was looked at in detail. The largest difference between the hit and the miss was found in the amplitude of the tracking error, shown in Figure A-2 (b), which provides the guidance information. This has an effect on the acceleration commands and the angle of the gimbal in the seeker, shown in Figure A-3 for the miss and Figure A-4 for the hit.

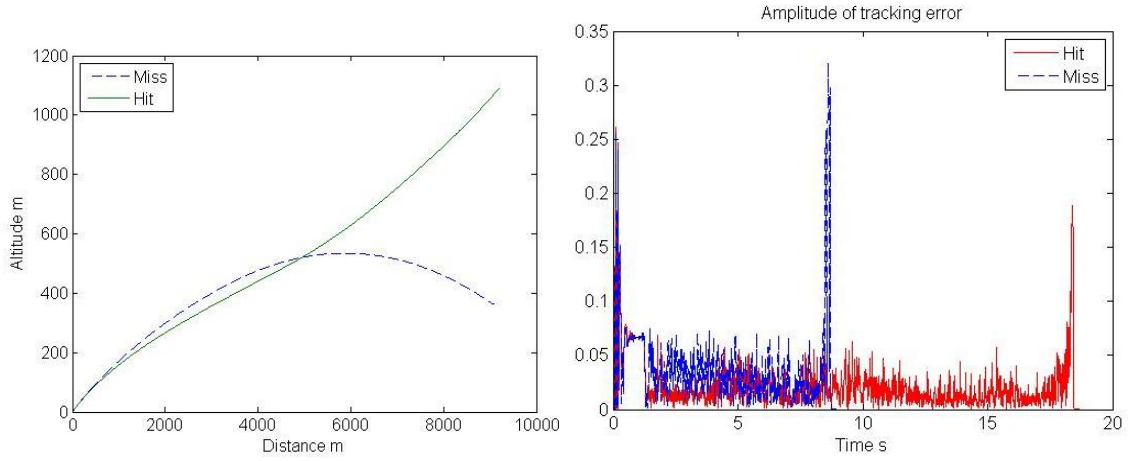

(a) (b)

Figure A-2 (a) Path of the missile projected on to the x-z plane and (b) amplitude of the tracking error.

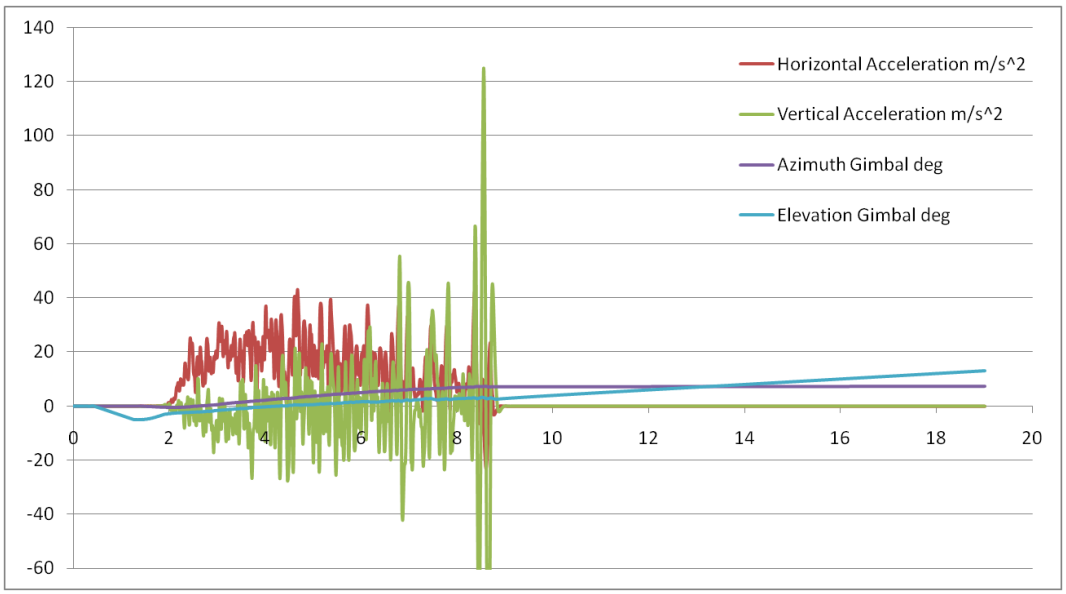

Figure A-3 The 30° azimuth engagement that resulted in a miss.

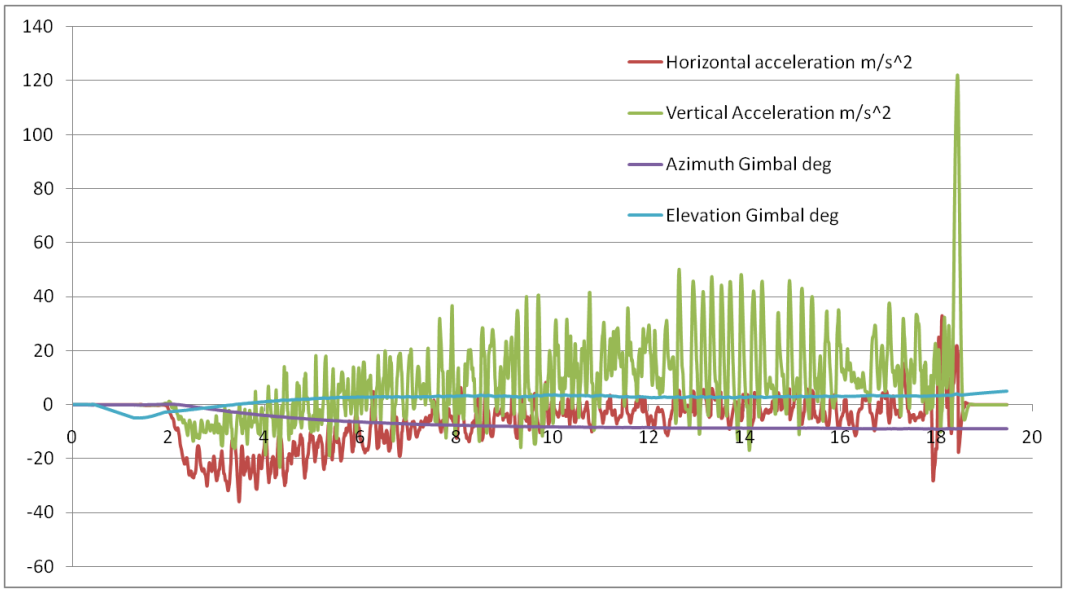

Figure A-4 The 330° azimuth engagement that resulted in a hit.

The azimuth of the gimbal and the horizontal acceleration in Figures A-3 and A-4 should be symmetrical about the time axis; this is roughly the case up to the time when the seeker looses lock at 9s. If both engagements were to hit then the vertical acceleration and elevation of the gimbal should be the same. The greater amplitude of the tracking error for the miss results in larger vertical acceleration and gimbal elevation. This produces the higher trajectory and the loss of the target from the seekers FOV. Given that both engagements were expected to have the same result this indicates that the simulations are sensitive to where the target is located in the FOV. The position of the target in the FOV generates the signal into the signal processor which then gives the amplitude and angle of the tracking error.

The two engagements are possibly unrealistic scenarios given the distance of 5.5km and flight time of the hit at 18s. There is also the lack of atmospheric attenuation and noise that means this represents the best possible results for the missile. However, it does illustrate that the signal processing has a significant effect on the outcome of an engagement. The signal processing is designed by the user and there is no detailed information in the open source environment. Therefore, any MANPAD model developed may or may not represent a possible in theatre threat.

When countermeasures are deployed by the aircraft there is a much greater variation in the asymmetry of the polar plots. To illustrate this, the two-colour conscan model was chosen and used against the AMX-A1 and C130 aircraft models releasing reactive flares. Figure A-5 shows the results for the AMX-A1 and the optics rotating (a) anticlockwise and (b) clockwise.

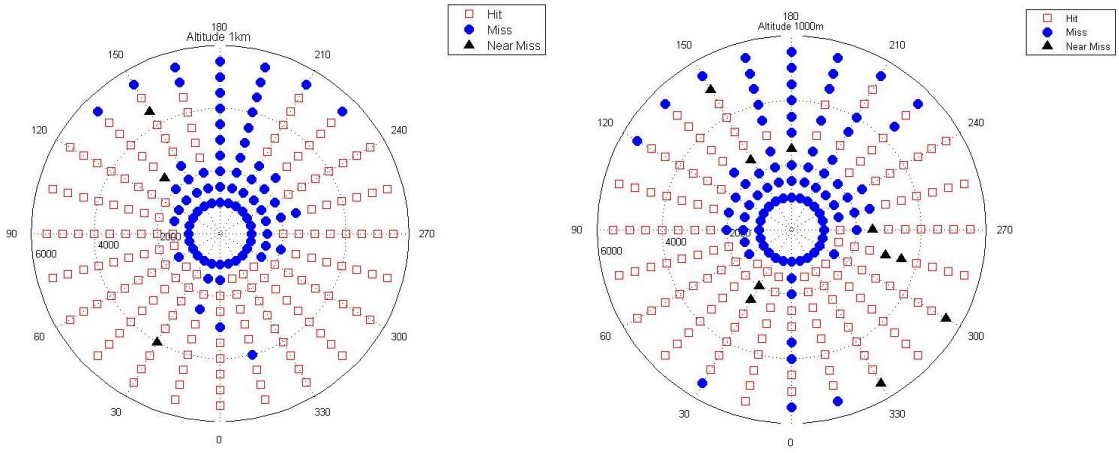

(a) (b)

Figure A-5 AMX-A1 model releasing reactive flares against a two-colour conscan IR seeker with the optics rotating (a) anticlockwise and (b) clockwise.

The results are not mirror images about the 0° axis; therefore, individual engagements were looked at in more detail. The two chosen from Figure A-5 (a) were for a distance of 2500m and azimuths 15°, a miss, and 345°, a hit. Figure A-6 shows where the targets are located in the FOV when the flares are released and a plan view of the engagement in the x-y plane. The left side is for an azimuth of 15° and the right side for an azimuth of 345°. The aircraft is in the same position within the FOV, the left half, when the flares are released. However, the aircraft is travelling from right to left in the FOV for the 15° azimuth and left to right for the 345° azimuth. The two-colour CCM tries to pull the flare to the edge of the FOV which results in the missile missing the aircraft in the 15° azimuth scenario.

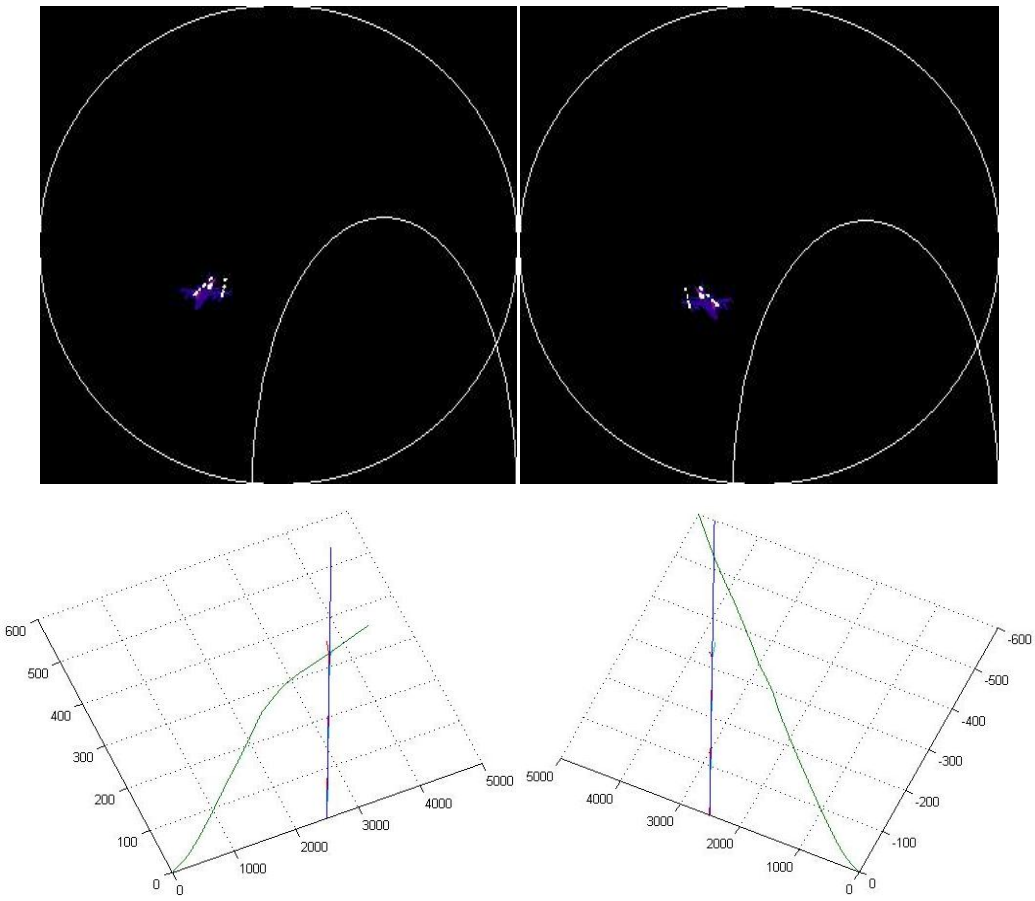

Figure A-6 Engagements for a distance of 2500m and 15° azimuth left side and 345° azimuth right side.

The next simulations used the C130 aircraft model releasing reactive flares from the front dispensers against the two-colour conscan model. Figure A-7 shows the results for the optics rotating (a) anticlockwise and (b) clockwise. Again, there are obvious differences about the 0° axis. The two scenarios chosen from Figure A-7 (a) were a distance of 3500m and azimuths 30°, a hit, and 330°, a miss. When the flares are released the aircraft are located in similar positions within the FOV, Figure A-8. On this occasion they are in the right half so the 30° scenario where the aircraft travels from right to left results in a hit. The 330° azimuth scenario where the aircraft travels from left to right results in a miss. This indicates that the position of the target in the FOV when countermeasures are deployed has a significant effect on the outcome of an engagement.

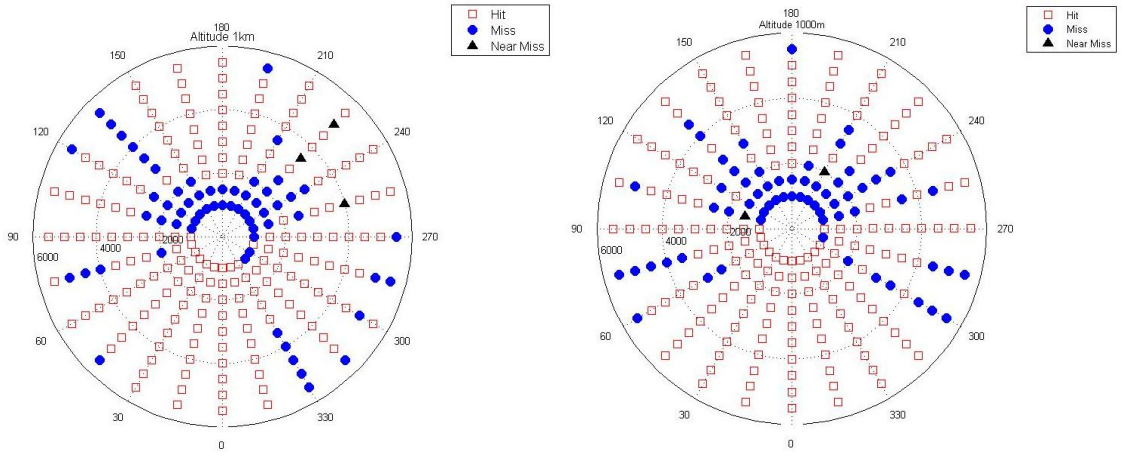

(a) (b)

Figure A-7 C130 model releasing reactive flares from the front dispensers against a two-colour conscan IR seeker with the optics rotating (a) anticlockwise and (b) clockwise.

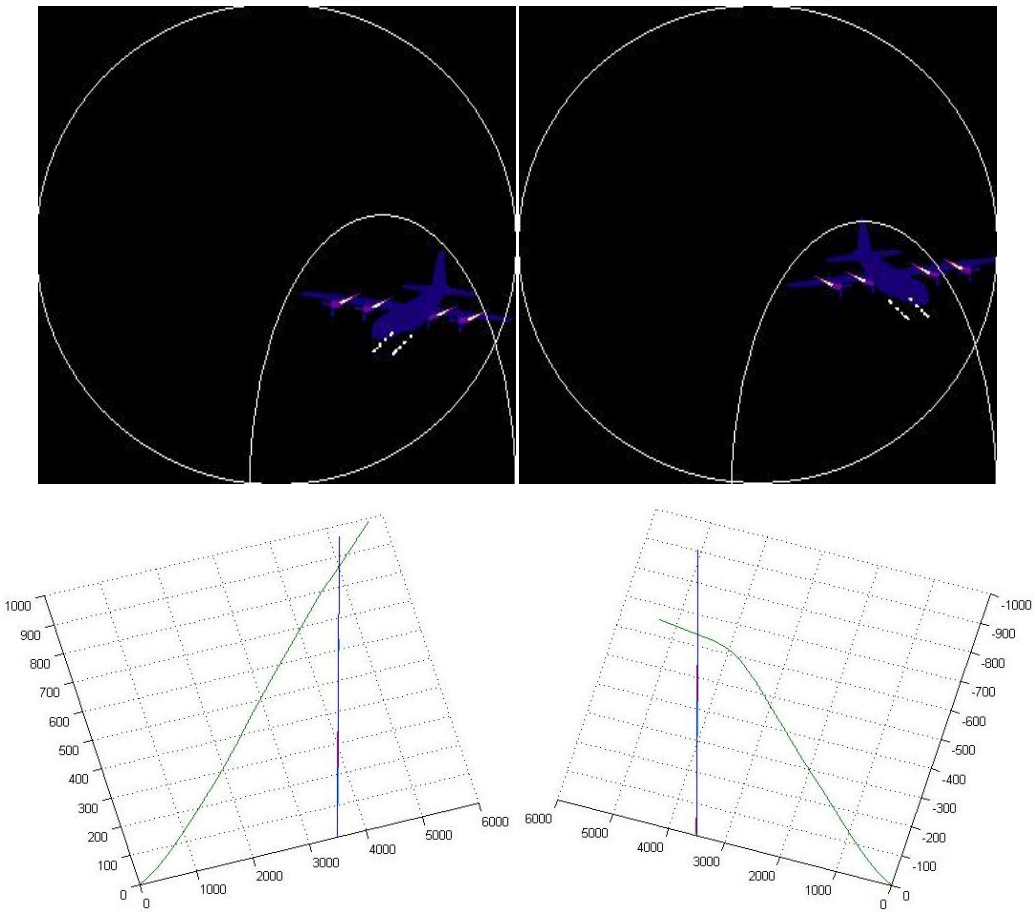

Figure A-8 Engagements for a distance of 3500m and 30° azimuth left side and 330° azimuth right side.

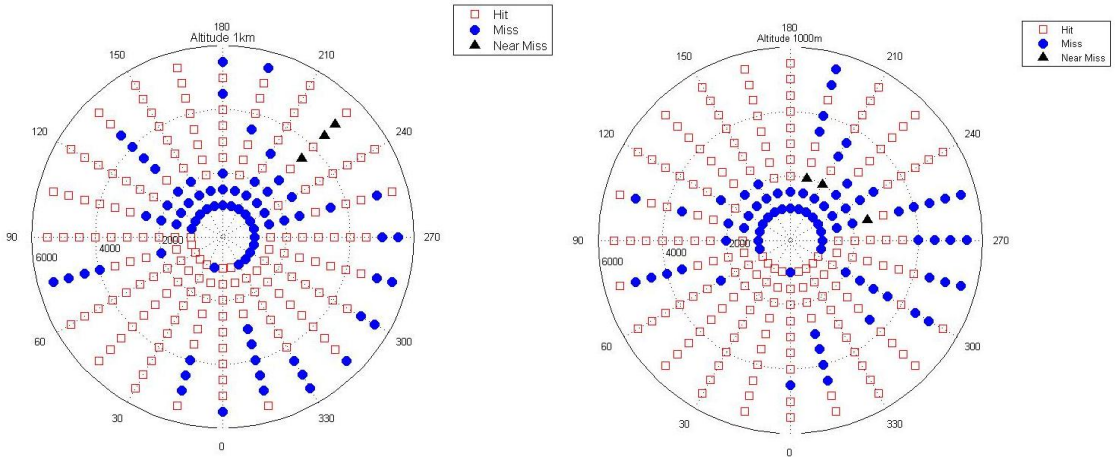

(a) (b)

Figure A-9 C130 model releasing reactive flares from the side dispensers against a two-colour conscan IR seeker with the optics rotating (a) anticlockwise and (b) clockwise.

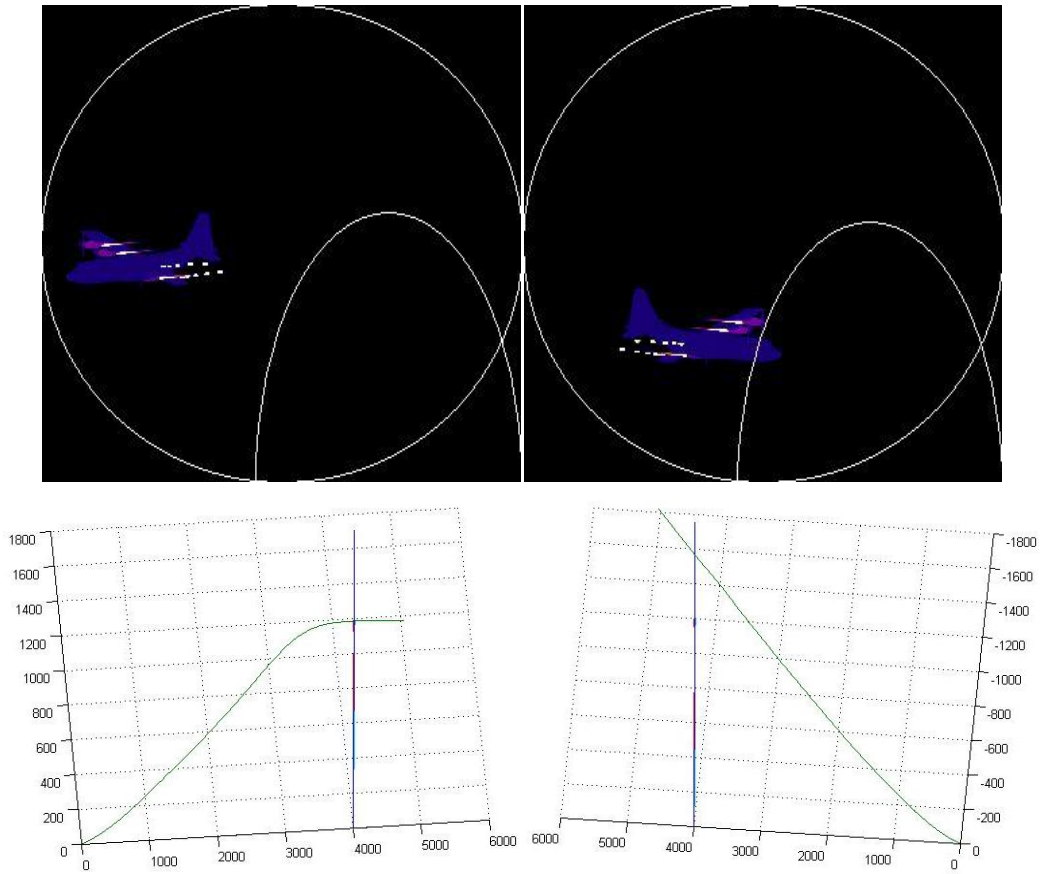

Figure A-10 Engagements for a distance of 4000m and 75° azimuth left side and 285° azimuth right side.

The final scenario used the C130 aircraft model releasing reactive flares from the side dispensers against the two-colour conscan model. Figure A-9 shows the results for the optics rotating (a) anticlockwise and (b) clockwise. Again, because of the obvious difference two scenarios were chosen from Figure A-9 (a). They are for a distance of 4000m and azimuths 75°, a miss, and 285°, a hit. The position of the aircraft in the FOV when flares are released is slightly different, Figure A-10, but both are still in the left half. For the 75° azimuth scenario the aircraft travel from right to left in the FOV and the engagement results in a miss. For the 285° azimuth scenario the aircraft travel from left to right in the FOV and the engagement results in a hit. This reinforces the importance of the location of the target in the FOV when flares are deployed.

In all the simulations there is no noise or atmospheric attenuation and the only differences are where the targets and flares are located in the seeker FOV. This would then change the signal entering the signal processor and from the static gain curves slight changes across the FOV have a large outcome on the measured error, which gives the tracking information. The signal processor designs used in the simulations are all from open sources so may not be representative of the real systems. An actual IR seeker is designed to track the target in the centre of the FOV by using the guidance commands to slave the seeker head. Therefore, this is probably a side effect of the two-colour CCM design. A more detailed knowledge of the threat is needed and also Hardware-in-the Loop (HWIL) simulations to obtain a greater confidence in the results and conclusions.

Appendix B Missile Grid

In addition to the simulations with individual MANPADs a scenario was set up with MANPADs positioned on a grid. There was an area of 10km x 10km with first generation MANPADs placed at 1km intervals, giving 121 in total. The AMX-A1 aircraft model flew at an altitude of 1km through the centre of the grid as shown in Figure B-1. The aircraft released a pair of flares at 4s from the start of the simulation and then in 4s intervals. As the aircraft travelled the MANPAD systems could track and lock-on then launch against the target. The result was that no missile hit the target.

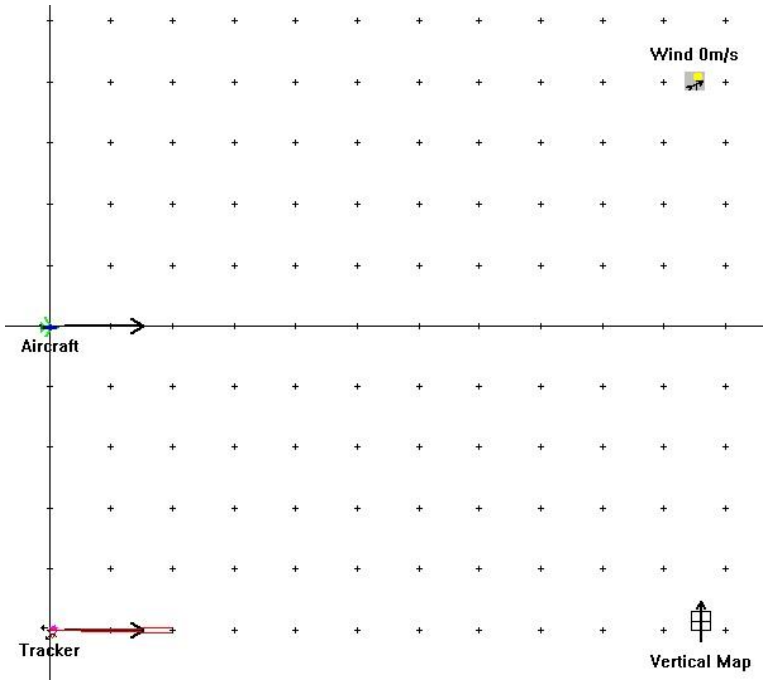

Figure B-1 MANPADs were placed at 1km intervals in a 10km x 10km grid and the aircraft flew along the centre.

To illustrate, Figure B-2 was produced using SIMDIS(95) for a smaller grid with only 9 missile systems. The blue line represents the path of the aircraft, the yellow circles are the flares and the green cones the FOV of the seekers. The MANPADs closest to the aircraft have launched but track the first pair of flare released. The MANPADS positioned at a greater distance lock-on to the second pair of flares as they have a much greater intensity in the FOV. The result of no

hits indicates that flares released at timed intervals could be an effective countermeasure against multiple MANPAD threats fired at a target from different angles and distances.

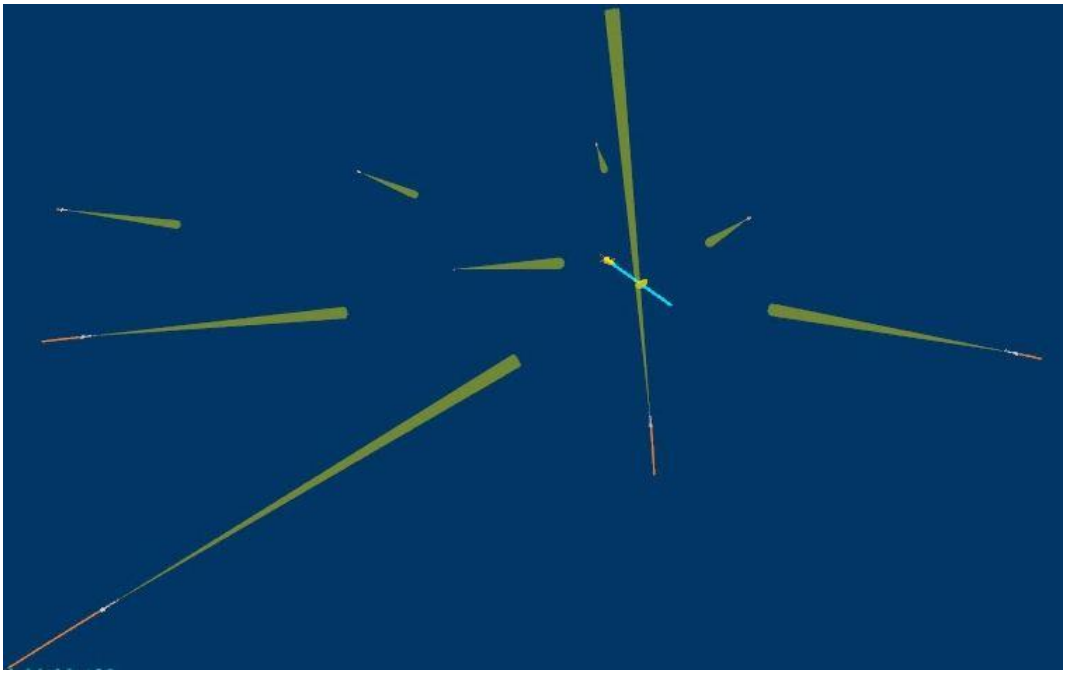

Figure B-2 A figure produced using SIMDIS of a smaller grid with 9 MANPADs.

Appendix C List of Publications

C.1 Journal papers

The effect of pre-emptive flare deployment on first generation man-portable air-defence (MANPAD) systems. **Jackman, James et al.** 2010, The Journal of Defense Modeling and Simulation, pp. vol. 7 no.3 181-189.

Simulating pre-emptive countermeasures of varying performance against a Man-Portable Air-Defence (MANPAD) system with a track angle bias counter-countermeasures (CCM). **Jackman, James et al.** 2011, Infrared Physics & Technology, Vol. 54, pp. 121-129.

Countermeasure effectiveness against a man-portable air-defence system containing a two-colour spinscan infrared seeker. **Jackman, James et al.** 2011, Optical Engineering (50), 126401 DOI:10.1117/1.3657507.

Assessment of the performance of a new decoy dispenser pod against 2nd generation IR MANPADs. **D'Amico, P., Richardson, M., Jackman, J., Butters, B., Millwood, N.** 2011, Journal of Battlefield Technology, Vol. 14(1).

C.2 Conference papers

Analysis of first generation MANPAD attacks on fast jets. **Jackman, James et al.** 2009. Proc. SPIE 7483, 74830I.

Effect of payload size on pre-emptive flare countermeasures against MANPAD system. **Jackman, James et al.** 2010. Proc SPIE 7836, 78360M.

Effect of pre-emptive flares on MANPAD systems with a track angle bias CCM. **Jackman, James et al.** 2010. Proc SPIE 7836, 78360N.

Modelling a MANPAD system with a conical scan two-colour IR seeker. **Jackman, James et al.** 2011, Proc. SPIE 8187-25.

Modelling a MANPAD system with a TAB CCM. **Jackman, James.** 2010, 8th EO/IR Classified conference, Cranfield Defence and Security, Defence Academy of the UK.

Two-colour CCM modelling. **Jackman, James.** 2011, 9th EO/IR Classified conference, Cranfield Defence and Security, Defence Academy of the UK.